A Test of Lepton Flavour Universality in the Decays of the Top Quark and Data driven validation of the Hard Scatter Vertex Selection Efficiency at ATLAS

Emma Jane Marshall, MPhys

Department of Physics

Lancaster University

A thesis submitted for the degree of

Doctor of Philosophy

February, 2025

A Test of Lepton Flavour Universality in the Decays of the Top Quark and Data driven validation of the Hard Scatter Vertex Selection Efficiency at ATLAS

Emma Jane Marshall, MPhys.

Department of Physics, Lancaster University

A thesis submitted for the degree of *Doctor of Philosophy*. February, 2025.

Abstract

The first part of the thesis covers the work done for the 'qualification task' at ATLAS, contributing to the maintenance of the experiment, measuring the efficiency of Hard Scatter identification in isolated lepton events: $Z^0 \to e\bar{e}$, $Z^0 \to \mu\bar{\mu}$ and $t\bar{t} \to e\mu$. Code was developed to extract the HS efficiency, the efficiency at which the 'true' first interaction of an event is identified by ATLAS software , with an 'estimation' method and a 'fitting' method in Release 21 of AnalysisBase. It was found that the Z^0 decay processes have a large discrepancy in the percentage of misidentified Hard Scatter vertices between Monte Carlo simulation and data unlike in the $t\bar{t}$ channel where Monte Carlo and data agreed. The percentage of misidentified Hard Scatter vertices was also found to be far greater in Z^0 decays than $t\bar{t}$. The fitting method was then developed for Release 22, and found that the HS efficiency was much better than Release 21, with the HS efficiency for $Z^0 \to \ell\ell$ events comparable to the efficiency of $t\bar{t}$ events in Release 21.

The second part is the main physics analysis, aiming to test a fundamental axiom of the Standard Model, Lepton Flavour Universality, the hypothesis that the couplings of each lepton flavour to the electroweak gauge bosons are the same regardless of flavour. The aim of the analysis presented is to test lepton flavour universality through the measurement of the of the rate of decay of W bosons to τ-leptons and electrons, $R(\tau/e) = B(W \to \tau\nu_\tau)/B(W \to e\nu_e)$. Di-leptonic $t\bar{t}$ events are based on $139 fb^{-1}$ of data recorded with the ATLAS detector in proton–proton collisions at $\sqrt{s} = 13TeV$. The analysis follows a 'tag and probe' method; one lepton is the tag to select events, the other a probe to determine if the lepton comes from a 'prompt' decay, $W \to e\nu_e$, or an intermediate τ lepton, $W \to \tau\nu_\tau \to e\nu_e\nu_\tau\nu_\tau$. The result of the analysis is still blinded as it is still in the approval process by the ATLAS collaboration. The expected precision of the measurement of $R(\tau/e)$ is 0.0234.

Acknowledgements

I would like to thank my supervisor, Professor Guennadi Borissov, for his guidance throughout my PhD, including the Qualification Task and the analysis. Guennadi has always been a very attentive and supportive which has made my PhD experience incredibly enjoyable and relatively painless. In addition, I would like to thank the ATLAS collaboration as a whole for allowing me to complete my studies at such a renowned and world-leading experiment. In particular, special thanks to the Vertexing and Top groups for giving feedback and guidance for my Qualification Task and analysis work respectively. All of particle physics research is a collaborative effort, and all work I have done is with the support and many years of research of many talented physicists working on so many aspects of the experiment from hardware, software and analysis. My thanks go towards Lancaster University and the physics department, with whom I also completed my Undergraduate studies and has been my home for the last 7 years. I would also like to thank the STFC for funding my studies. I also thank my friends, in particular Harry Scott, and family for their constant support in my PhD and beyond.

Declaration

The material of this thesis has not been submitted, either in whole or in part, for a degree at this, or any other university.

The thesis presented is, to the best of my knowledge and belief, original and my own work. As part of working with an international particle physics collaboration such as ATLAS, internal notes are created at ATLAS in order to describe work to members of the ATLAS community that allow work to be approved for publishing. Due to being an internal document, these are therefore not published. The chapter concerning the Qualification Task (Chapter 4) is based on an internal note written by myself for the vertexing group. As a collaborative analysis, myself and my supervisor, Guennadi Borissov, worked together to produce the final result of the analysis of $R(\tau/e) = B(W \to \tau\nu\tau)/B(W \to e\nu e)$. The main analysis chapter (Chapter 5) is based on the internal note sections written by myself for the ATLAS experiment. The thesis also summarises work Guennadi Borissov performed for the analysis for a more complete understanding. A detailed description of which work was performed by myself, Guennadi and jointly between myself and Guennadi is described in more detail in Chapter 5.

This thesis does not exceed the maximum permitted word length of 80,000 words including appendices and footnotes, but excluding the bibliography. A rough estimate of the word count is: 27106

Emma Jane Marshall

Publications

Only one publication has been produced from the analysis of $R(\tau/e) = Br(W \to \tau\nu_\tau)/Br(W \to e\nu_e)$ [1], which is based on work in this thesis. The analysis was not fully complete by the completion of the thesis, therefore there are some differences between the plots and measurements in this thesis and the final paper. The thesis is written with the results available at the time of the completion of the PhD, however the final result found in [1] will be included for completeness.

Contents

List of Tables

List of Figures

Chapter 1

Introduction

The last 50 years have brought about many new discoveries in particle physics, all of which fit into the picture described by the SM of particle physics [2]. This aims to describe all particle interactions in our universe. Some of these studies that confirm SM theories include the discovery of the Higgs Boson in 2012 [3][4], the tau (τ) neutrino in 2000 [5] and the top quark in 1995 [6] [7]. However, there are some discoveries that have disagreed with the Standard Model such as the observation of neutrino flavour oscillations in recent years [8]. There are also many other unanswered questions for the SM itself, one of which concerns an assumption of the Standard Model known as Lepton Flavour Universality (LFU) [9]. This is the assumption W bosons couple to each lepton flavour (e, μ, τ) with the same strength. Currently, there is no theoretical model that would explain this assumption of the Standard Model, therefore testing this assumption is of interest. If any evidence was found to go against this assumption, this would be new, Beyond the Standard Model (BSM) physics. Other measurements have already been performed that show tension with the SM, such as a recent LHCb measurement showing possible LFU violation with a significance of 3.1σ in the decay of b quarks [10], which was later superseded by a result showing agreement with the SM [11] .

Lepton Flavour Universality can be tested using the decays of top quarks to W bosons and their subsequent decay to leptons. The comparison of the decay to one lepton flavour to another lepton flavour allows the test of LFU, where the expectation is that the same fraction of leptons will be produced regardless of the flavour. Tests such as this have been performed, for example at ATLAS the comparison of the decay fractions of tau lepton to muons was measured to be in agreement with the Standard Model [12]. This analysis resolved a previous tension with the SM measured by

LEP [13], by measuring the ratio of the decay fractions of the decay to τ leptons and muons much more precisely. Other recent measurements of many different decay fraction ratios was performed by CMS [14], also showing agreement with the SM. In the case of this thesis, the decay fraction of top quark pairs to tau leptons and top quark pairs to electrons is considered, following a similar method to this recent ATLAS measurement. Top quarks are a good choice for analysis such as this due to the large number that are detected at ATLAS and the purity of their identification. In addition, an analysis using the decay of top quark pairs probes the coupling of the W boson to a third generation quark.

Working on a PhD at ATLAS requires the completion of a Qualification Task (QT), this is a technical project of around a year on an aspect of the ATLAS experiment itself. For this thesis, the QT will also be presented alongside the main analysis, as this was a significant portion of the total PhD duration. The QT presented here analyses the efficiency of the selection of Hard Scatter (HS) vertices. This work was done with the help of the Vertexing group at ATLAS, as well as my supervisor Guennadi.

The structure of this thesis will therefore be: chapter 2 describes the theoretical background for the main analysis, chapter 3 will describe the ATLAS experimental setup in detail, chapter 4 will describe the work done for the Qualification Task, chapter 5 will describe the main analysis and chapter 6 will describe the conclusions of the thesis.

Chapter 2

Theoretical Background

2.1 Review of the Standard Model

The Standard Model [15] (SM) is a framework that aims to describe all of the fundamental particles and forces in the universe. Currently, the Standard Model encompasses almost all of these forces, except gravity. The SM is based on quantum field theory, a collection of related Gauge Theories that satisfy Local Gauge Invariance (Quantum Electrodynamics [16], Electroweak Unification [9] and Quantum Chromodynamics [17]), with particles defined by their interactions with other particles. Fundamental properties of each particle are known as quantum numbers. These are properties such as charge, mass, spin or flavour.

In the SM particles are separated into many different categories based on their properties. The first distinction between particles is if they are fermions or bosons. Fermions have half-integer 'spin' and obey Fermi-Dirac statistics [15] .

The fermions are then divided into into leptons and quarks. The first, leptons, are colourless fermions divided into three further groups of electrons, muons and tauons which are the charged leptons and neutral leptons being the neutrinos, which are the electron neutrino, muon neutrino and tauon neutrino. Quarks are coloured fermions, meaning they can undergo strong interactions unlike leptons. Quarks are divided into two types, up-type and down-type particles. Up-type quarks have positive charge and down-type quarks have negative charge. The up-type quarks are split into three flavours: up, charm and top, while the down-type quarks are split into three different flavours: down, strange and bottom. The top quark, which is used as the particle of interest in the analysis described in this thesis, is the heaviest of all the quarks by a considerable margin with

a mass of 172 GeV [18] . Fermions have an anti-particle counterpart for each with the opposite charge and spin, but the same mass.

Bosons have integer 'spin' and obey Bose-Einstein statistics [15] . Gauge Bosons are 'force carrying' particles, that mediate interactions between fermions. These gauge bosons are γ (photon) mediating electromagnetic interactions, g (gluon) mediating strong interactions, Z^0, $W^{\pm}$ mediating weak interactions and the Higgs boson (H) the quanta of the Higgs scalar field that gives particles mass. The Higgs boson was the last SM particle discovered by ATLAS ([19]) and CMS ([4]) in 2012 . However, the Standard Model does not include the gravitational force. Currently there is no evidence for a boson carrying the gravitational force (e.g. a graviton).

Figure 2.1 shows the SM particles and their respective groupings.

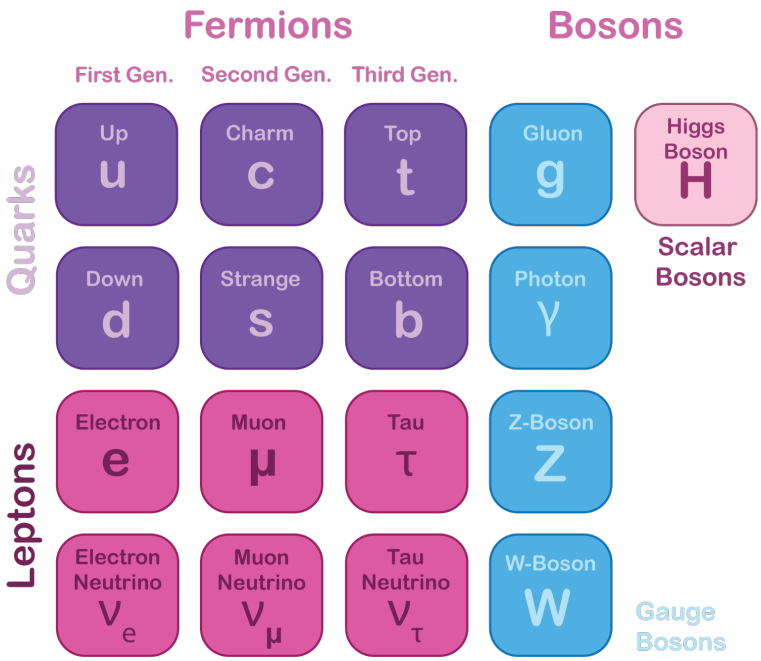

Figure 2.1: The Standard Model, showing the different groupings of the fermions and bosons.

The Standard Model is largely successful in describing large parts of particle physics phenomena, however there are some limitations to its predictivity currently. Physics that cannot be described by the Standard Model is known as Beyond the Standard Model (BSM) physics. There has been much research into BSM physics in recent years, most prominently is that of neutrino oscillations which describe the change of flavour of neutrinos from one to another despite their predicted lack of mass [20]. Another possible instance of BSM physics is that of Lepton Flavour Universality violation. This BSM phenomena, if found would disprove the SM assumption that

all lepton flavours couple to a gauge boson (except the Higgs boson) with the same strength.

2.2 Lepton Flavour Universality

Lepton Flavour Universality is an assumption of the Standard Model that the weak interaction couples to all three of the charged lepton generations with the same strength. Therefore, it would be expected that each lepton flavour (e, μ, τ) interacts with the same gauge boson in the same way. While this is an assumed property of the Standard Model, it is only a consequence of accidental flavour symmetry of the SM lagrangian.

Lepton Flavour Universality is an assumption of the Standard Model, therefore evidence of LFU would imply the existence of new physics beyond the standard model.

Therefore it is important to test this assumption, and look for any deviation from it. In particular, a measurement of LFU comparing the branching ratios of the decay of the W-boson to τ and the W-boson to e has not been performed by the ATLAS experiment until the analysis presented in this thesis.

There have been many tests of LFU from studies at LEP ([21]), to more recent studies at LHCb [10], [11] as well as studies at ATLAS such as the study preceding this one [12] and a very recent CMS study [22], using the decay $b \to s\ell\ell$ from B mesons . Studies at LHCb look at the decays of b-hadrons for signs of LFU, which initially showed a tension with the SM of 3.1σ [10]. However, more recent studies now show agreement with the SM at the level of 0.2σ [11]. Further to this, previous studies at LEP also showed tension with the standard model for various lepton pairings, however further study at ATLAS disproved this tension for the $\tau - \mu$ pairing measuring $R_{\tau/\mu}$ as 0.992 ± 0.013 [12] as well as similar results in a more recent CMS study measuring $R_{\tau/\mu}$ as 0.985 ± 0.020 [14]. This study also measured the parameter of interest of this study, $R_{\tau/e}$ as 0.994 ± 0.021. This measurement is of a similar level of precision as expected in this study. Particularly when looking at LEP results, it can be seen that improvement can be made on the precision of these measurements, which is largely the aim of this study.

2.3 The Top Quark

The top quark is the heaviest of the quarks at 172 GeV [23]. This presents the question of why the mass of the top quark is so much larger than any other quark, as demonstrated in figure 2.2. The

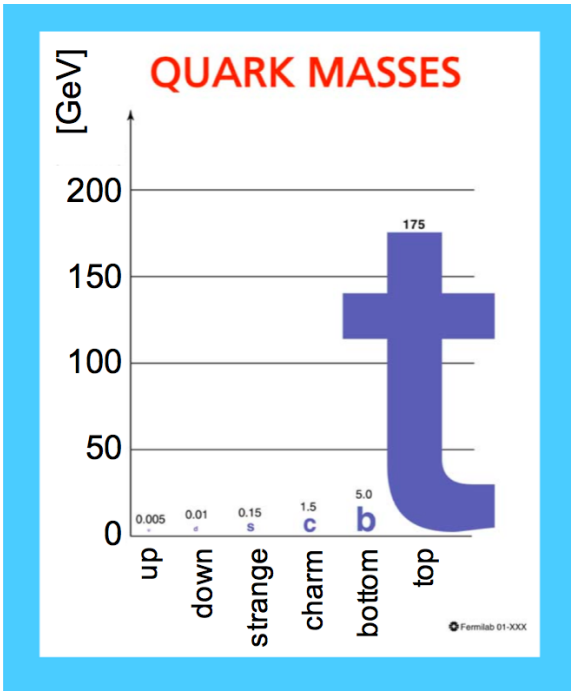

Figure 2.2: The top quark has a much larger mass than any of the other quarks. [24]

large mass of the top quark presents the possibility of new physics that explains its large mass as well as new physics brought about as a consequence of its large mass.

The top quark is a good choice for studies such as these due to its very large cross section of $t\bar{t}$ at the LHC as well as the relatively simple and clean selection of $t\bar{t}$. The majority of top quarks decay to a W boson and a bottom quark with a branching ratio of 0.957 ± 0.034 [23]. Therefore in $t\bar{t}$ events, there are two W bosons in each event. The decay semi-leptonic decay of this W boson can then be measured.

2.3.1 Production

The top quark can be produced by the LHC in two ways: pair production and single-top production. Pair production is the most common, producing a quark-antiquark pair ($t\bar{t}$) via the strong interaction. This mostly occurs through the production of a gluon, either from gluon-gluon fusion as seen in Figure 2.3 or through quark-antiquark annihilation as seen in Figure 2.4. Pair production can also occur through the the t-channel, shown in Figure 2.5. Single-top production occurs via the weak interaction, the most common single-top process is the 't-channel', where a b quark transforms into a t quark through the exchange of a W boson, shown in Figure 2.6. The

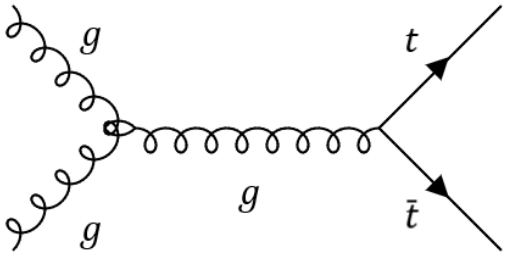

Figure 2.3: Top quark pair production from gluon fusion

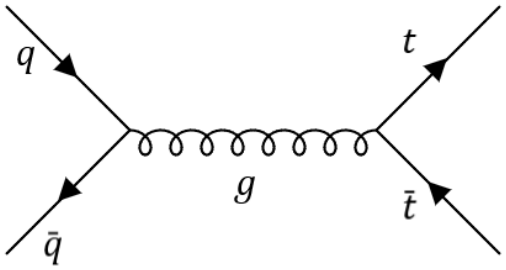

Figure 2.4: Top quark pair production from quark-antiquark annihilation

'Wt-channel' single top process is the next most common, occurring when a b quark interacts with a gluon to produce a top quark and a W boson, as seen in Figure 2.8. The 's-channel' single-top process is the least common, where two quarks annihilate to form a W boson which decays to form a t quark and a b quark, as seen in Figure 2.7.

2.3.2 Decays

The top quark decays via the weak interaction to a W boson and a bottom quark. This decay happens very quickly due to the high mass of the top quark. Because of this, the top quark is unable to form into a hadron with another quark, making the top quark an interesting quark to measure due to its existence outside of a hadron. The W boson from this top quark decay is then able to decay into leptons, as shown in Figure 2.9. In the case of this analysis, the W boson decays to τ or e

The weak force is mediated by W^+, W^- and Z^0 bosons, which have mass due to the electroweak symmetry breaking interaction with the Higgs scalar field. The W^+ and W^- bosons are charged and therefore mediate 'charged current' interactions, whereas the Z^0 boson has no

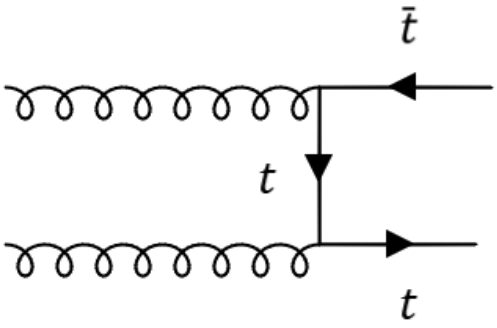

Figure 2.5: t-channel top quark pair production

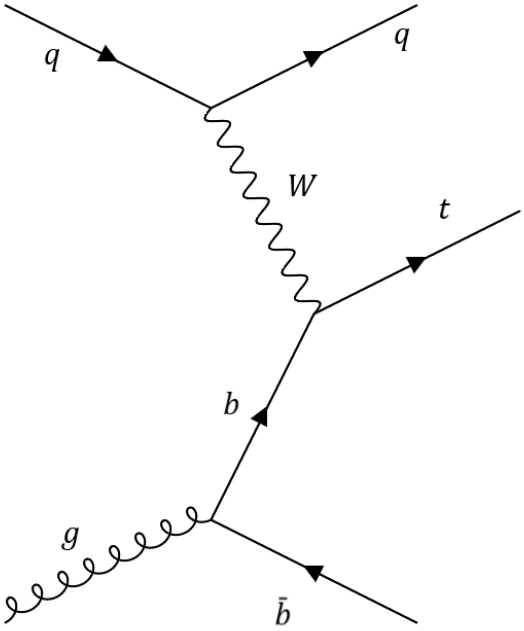

Figure 2.6: t-channel single top production

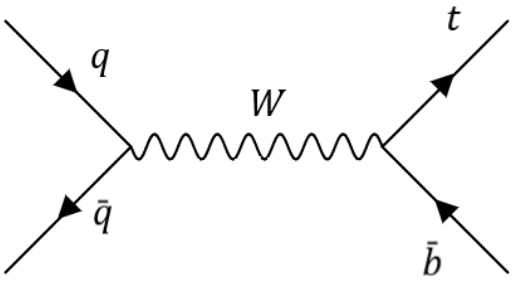

Figure 2.7: s-channel single top production

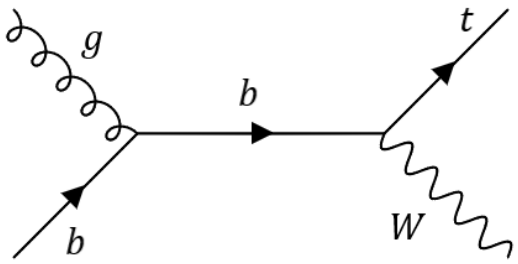

Figure 2.8: Wt-channel single top production

charge and therefore mediates neutral current interactions. The signal events for this analysis come from charged current weak decays of the top quark, however a significant portion of the background includes the decay of the Z^0 boson.

2.4 The Weak Interaction

The weak interaction follows the rule that the strength of any interaction involving the W boson should only depend on its weak charge. This weak charge is 1 and is the same for all fermions. However, this is not the case for the quarks due to their mass eigenstates. Cabbibo [25] proposed that the W boson couples with weak eigenstates that is a mixture of the quark's mass eigenstates, this is represented by the Cabbibo matrix. This proposition was only describing the relative probability of down and strange quarks decaying into up quarks. This was then extended to the CKM matrix, created by Kobayashi and Maskawa [26] which can be written as:

$$\begin{pmatrix} d' \\ s' \\ b' \end{pmatrix} = \begin{pmatrix} V_{ud} & V_{us} & V_{ub} \\ V_{cd} & V_{cs} & V_{cb} \\ V_{td} & V_{ts} & V_{tb} \end{pmatrix} \begin{pmatrix} d \\ s \\ b \end{pmatrix} \tag{2.1}$$

The CKM matrix is unitary, this means that the number of quarks is consistent. If the unitarity of the CKM matrix is violated, this would imply that there are more than 3 generations of quarks or that there is another, BSM, interaction involved. Each parameter in the CKM matrix corresponds to a mass eigenstate. This element will be present in every vertex of a Feynman diagram of an interaction where a W boson and quark is involved, for example with the decay of a top quark:

It can be seen at the first vertex this would correspond to the V_{tb} element in the CKM matrix. The matrix element is given by $\mathscr{M} \propto g_w V_{tb}$

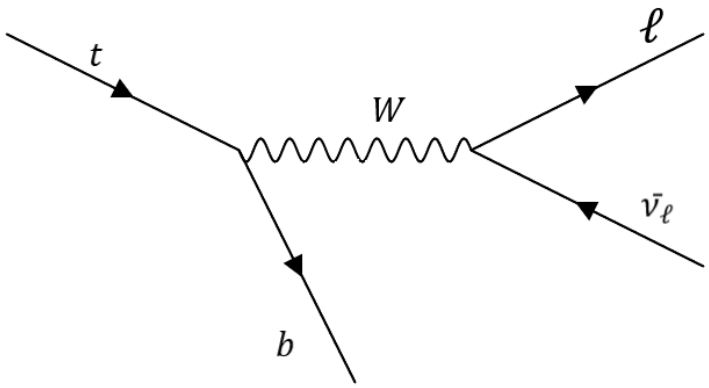

Figure 2.9: Example of the decay of a top quark, the anti-top quark can decay in the same way, producing an anti-b quark and a W boson. The W boson can decay to an anti-ℓ and ν_ℓ, too.

Representing the CKM matrix as a rotation in 3 dimensions, a model can be created for what it represents:

$$V_{CKM} = \begin{pmatrix} 1 & 0 & 0 \\ 0 & c_{23} & s_{23} \\ 0 & -s_{23} & c_{23} \end{pmatrix} \begin{pmatrix} c_{13} & 0 & 0 \\ 0 & 1 & 0 \\ -s_{13} & 0 & c_{13} \end{pmatrix} \begin{pmatrix} c_{12} & s_{12} & 0 \\ -s_{12} & c_{12} & 0 \\ 0 & 0 & 1 \end{pmatrix} \tag{2.2}$$

$$= \begin{pmatrix} c_{12}c_{13} & s_{12}c_{13} & s_{13} \\ -s_{12}c_{23} - c_{12}s_{23}s_{13} & c_{12}c_{23} - s_{12}s_{23}s_{13} & s_{23}c_{13} \\ s_{12}s_{23} - c_{12}c_{23}s_{13} & c_{12}s_{23} - s_{12}c_{23}s_{13} & c_{23}c_{13} \end{pmatrix}$$

There is a hierarchy in the rotations, which is observed experimentally:

$$s_{12} >> s_{23} >> s_{13} \tag{2.3}$$

Which implies that the most likely transitions between quarks occur in the same generation. I.e. $u \to d$, $c \to s$, $t \to b$.

2.5 τ decays

This analysis looks at the ratio between $W \to \tau\nu_\tau$ and $W \to e\nu_e$. In the decay of $W \to \tau\nu_\tau$ the τ lepton can undergo further decay , fully leptonic, decay to an electron, $\tau \to e\nu_e\nu_\tau$. This is known

in this analysis as an intermediate decay, and used as one of the signals in this analysis. The branching ratio for this decay is 17.82 ± 0.04 % [23].

2.6 The Strong Interaction

The strong interaction is mediated by the gluon. In electromagnetic interactions, QED [27] describes the electromagnetic interaction as being mediated by photons coupling to a conserved charge (electric charge). Similarly, the strong interaction is described by QCD [28] as being mediated by gluons coupling to a conserved charge, colour charge. Unlike QED, which has a single electric charge, QCD describes three colour charges: red, green and blue. These colour charges also have anti-colour charges (anti-red, anti-green and anti-blue). Gluons can be considered as carrying colour and anti-colour and therefore come in 8 different colour configurations. As gluons carry colour charge, they can also interact with themselves, unlike electric charge in the electromagnetic force. The strong force only affects particles with non-zero colour charge. Quarks have colour charge, and can have a charge of red, green or blue (or anti-red, anti-green or anti-blue for anti-quarks). Colour symmetry is exact in QCD, and therefore strength of strong interactions is not dependent on the colour charge of the quark it is interacting with. This also means the strong interaction is flavour independent, as all of the quark flavours exist in the same colour states. Two important properties of the strong force are asymptotic freedom and colour confinement. The strong interaction gets weaker at shorter distances. At the scale of hadrons, the strong force is incredibly strong, which allows the binding of quarks into hadrons. However, at distances smaller than this, the strong force is weaker. Colour confinement is the hypothesis that non-zero colour charged particles cannot exist as independent particles. Therefore, quarks cannot be observed by themselves. Particles made up of quarks are known as hadrons. Baryons (e.g. the protons collided at the LHC) are made up of 3 quarks of each colour charge (red, green, blue) and mesons are made up of quarks of opposite colour charge (e.g. red and anti-red, green and anti-green and blue and anti-blue).

2.7 Latest Experimental Results

This section gives a summary of some of the latest experimental results of tests lepton flavour universality violation. The focus of this section will be looking at results coming from the decay

of B mesons and W bosons. The most significant results from the decay of B mesons come from BaBar, Belle and LHCb. The most significant results from the decay of W bosons come from LEP, ATLAS and CMS. Results for all analyses studying LFU with the measurement of $Br(W \to \tau)/Br(W \to e)$ (the ratio studied in this thesis) are shown in figure 2.10.

2.7.1 Results from BaBar

The BaBar experiment at the Stanford linear accelerator (SLAC) measured the ratio of branching ratios $R(D^{(*)}) = Br(\bar{B} \to D^{(*)}\tau^-\bar{\nu}_\tau)/Br(\bar{B} \to D^{(*)}\ell^-\bar{\nu}_\ell)$. These results showed possible evidence of BSM physics [29]. These results are summarised in Table 2.1. The significance of these results were reported as 2.0σ for the measurement of $R(D)$ and 2.7σ for the measurement of $R(D*)$. Together, these results deviate from the SM prediction by 3.4σ. These results were then corroborated by results from Belle and LHCb, which are presented in their own sections further on.

Ratio of Branching Ratios	Result
$Br(\bar{B} \to D\tau^-\bar{\nu}_\tau)/Br(\bar{B} \to D\ell^-\bar{\nu}_\ell)$	$0.440 \pm 0.05 \pm 0.042$
$Br(\bar{B} \to D^*\tau^-\bar{\nu}_\tau)/Br(\bar{B} \to D^*\ell^-\bar{\nu}_\ell)$	$0.332 \pm 0.024 \pm 0.0187$

Table 2.1: A table summarising the results of the semi-leptonic decay $R(D^{(*)}) = Br(\bar{B} \to D^{(*)}\tau^-\bar{\nu}_\tau)/Br(\bar{B} \to D^{(*)}\ell^-\bar{\nu}_\ell)$ from the BaBar experiment [29]

2.7.2 Results from Belle

The Belle experiment has also measured the ratios $R(D^{(*)}) = Br(\bar{B} \to D^{(*)}\tau^-\bar{\nu}_\tau)/Br(\bar{B} \to D^{(*)}\ell^-\bar{\nu}_\ell)$ [30]. The results of which are summarised in Table 2.2. These results are in agreement with the results seen from the BaBar experiment, with a deviation from the SM prediction of 0.2σ for the ratio $R(D)$ and 1.1σ for the ratio $R(D^*)$. The combined result has a significance of 0.8σ.

Ratio of Branching Ratios	Result
$Br(\bar{B} \to D\tau^- \bar{\nu}_\tau)/Br(\bar{B} \to D\ell^- \bar{\nu}_\ell)$	$0.307 \pm 0.037 \pm 0.016$
$Br(\bar{B} \to D^*\tau^- \bar{\nu}_\tau)/Br(\bar{B} \to D^*\ell^- \bar{\nu}_\ell)$	$0.283 \pm 0.018 \pm 0.014$

Table 2.2: A table summarising the results of the semi-leptonic decay $R(D^{(*)}) = Br(\bar{B} \to D^{(*)}\tau^- \bar{\nu}_\tau)/Br(\bar{B} \to D^{(*)}\ell^- \bar{\nu}_\ell)$ from the Belle experiment [30]

2.7.3 Results from LHCb

LHCb has measured LFU violation in the decay of B mesons into kaons (measuring R_{K^*}) as well as B mesons into D mesons (measuring R_{D^*}). LHCb observed tension with the SM prediction in the decay of B mesons to D mesons, similar to the results from Belle and BaBar [31]. In the decay of B mesons to kaons, while previously results suggested a tension with the SM [10], more recently the LHCb experiment found agreement with the SM [11]. The LHCb experiment has also measured the ratio $Br(W \to \mu)/Br(W \to e)$, in agreement with the SM. A summary of the most recent LHCb LFU tests are shown in table 2.3.

Ratio of Branching Ratios	Result
$Br(\bar{B} \to D^0\tau^- \bar{\nu}_\tau)/Br(\bar{B} \to D^0\ell^- \bar{\nu}_\ell)$	$0.441 \pm 0.060(stat) \pm 0.066(syst)$ [31]
$Br(\bar{B} \to D^{*+}\tau^- \bar{\nu}_\tau)/Br(\bar{B} \to D^{*+}\ell^- \bar{\nu}_\ell)$	$0.281 \pm 0.018(stat) \pm 0.024(syst)$ [31]
$Br(\bar{B} \to K\tau^- \bar{\nu}_\tau)/Br(\bar{B} \to K\ell^- \bar{\nu}_\ell)$	Low-q^2 $0.994^{+0.090}_{-0.082}(stat)^{+0.029}_{-0.027}(syst)$ Central-q^2 $0.949^{+0.042}_{-0.041}(stat)^{+0.022}_{-0.022}(syst)$ [11]
$Br(\bar{B} \to K^*\tau^- \bar{\nu}_\tau)/Br(\bar{B} \to K^*\ell^- \bar{\nu}_\ell)$	Low-q^2 $0.927^{+0.093}_{-0.036}(stat)^{+0.087}_{-0.035}(syst)$ Central-q^2 $1.027^{+0.072}_{-0.027}(stat)^{+0.068}_{-0.026}(syst)$ [11]

Table 2.3: A table summarising the results of lepton flavour universality studies from the LHCb experiment

*There are no LHCb measurements of this ratio as of the time of submitting this thesis.

2.7.4 Results from LEP

LEP was a predecessor to the LHC, colliding electrons and positrons instead of protons, reaching energies of 209 Gev [32]. The LEP experiment measured the branching ratio of $Br(W \to \mu)/Br(W \to e)$, $Br(W \to \tau)/Br(W \to e)$ and $Br(W \to \tau)/Br(W \to \mu)$. These are summarised

in Table 2.4.

Ratio of Branching Ratios	Result
$Br(W \to \mu)/Br(W \to e)$	0.993 ± 0.019
$Br(W \to \tau)/Br(W \to e)$	1.063 ± 0.027
$Br(W \to \tau)/Br(W \to \mu)$	1.066 ± 0.025

Table 2.4: A table summarising the results of leptonic W boson decay branching ratios from the LEP experiment [33].

It can be seen that the results from LEP are in tension with the the SM expectation of unity.

2.7.5 Results from CMS

The CMS detector is another detector at CERN, positioned along the LHC. Similar to the ATLAS detector, it is also a multi-purpose detector with similar physics goals as ATLAS. Measurements from both CMS and ATLAS allow for the validation of physics phenomena, such as the joint discovery of the Higgs Boson.

Ratio of Branching Ratios	Result
$Br(W \to \mu)/Br(W \to e)$	1.009 ± 0.019
$Br(W \to \tau)/Br(W \to e)$	0.994 ± 0.021
$Br(W \to \tau)/Br(W \to \mu)$	0.985 ± 0.020

Table 2.5: A table summarising the results of leptonic W boson decay branching ratios from the CMS experiment [14].

The measurement of the ratio of branching ratios of the W-boson decays done at CMS was performed differently than the analysis presented in this thesis. In the measurements in Table 2.5, the measurement was performed directly finding the branching ratio for each decay and then taking the ratio of the branching ratios.

2.7.6 Results from ATLAS

Measurements of LFU in W-boson decays have been studied very recently at ATLAS. The measurement of $Br(W \to \tau)/Br(W \to \mu)$ was performed in a similar way to the analysis outlined

in the thesis, showing agreement with the SM prediction within 1σ. The measurement of $Br(W \to \mu)/Br(W \to e)$ was done using measurements of the $t\bar{t}$ production cross-section in the ee, $e\mu$ and $\mu\mu$ di-lepton final states and was found to be in agreement with the SM prediction within 1σ .

Ratio of Branching Ratios	Result
$Br(W \to \mu)/Br(W \to e)$	0.9995 ± 0.0045 [34]
$Br(W \to \tau)/Br(W \to e)$	- *
$Br(W \to \tau)/Br(W \to \mu)$	0.992 ± 0.013 [12]

Table 2.6: A table summarising the latest results of leptonic W boson decay branching ratios from the ATLAS experiment. *Prior to this analysis, there were no measurements of this from ATLAS

Prior to this analysis, there were no measurements $Br(W \to \tau)/Br(W \to e)$ from ATLAS.

2.7.7 Results for $Br(W \to \tau)/Br(W \to e)$

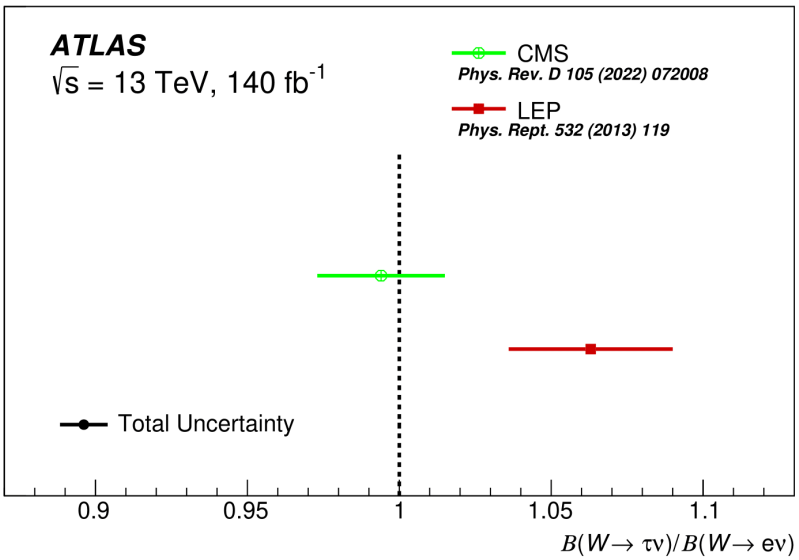

Figure 2.10: Results for all analyses measuring LFU with $Br(W \to \tau)/Br(W \to e)$. Results are currently from CMS [14] and LEP [33]. This plot will be updated to include the result of this analysis, at the end [1].

Chapter 3

The ATLAS Experiment

This section gives a summary of the ATLAS experiment [35] . The ATLAS experiment is one of several detectors on the LHC, where the the protons accelerated by the LHC are collided and detected in ATLAS. Physicists working at ATLAS can then use the data collected from these collisions to test the Standard Model.

3.1 The LHC

This section is based on information from LHC design reports [37], [38], [39]. The Large Hadron Collider (LHC) is a particle accelerator consisting of a 26.7 km ring of superconducting magnets that accelerate protons to close to the speed of light. The LHC is housed in the tunnel made for the Large Electron Positron collider (LEP) [40] , with the LHC able to provide much higher energy collisions than LEP due to colliding protons instead of electrons and positrons.

Two beams of protons are made from ionised hydrogen gas injected into two separate beam pipes. The two beams of protons are accelerated in opposite directions and then collide in the four collision points around the LHC. The pipes are kept at in an ultrahigh vacuum such that collisions only occur in the collision points. The beams are accelerated using superconducting electromagnetic coils cooled to 0.15 K to create a magnetic field which directs the beams around the beam pipes. With this, due to a series of upgrades from 2018-2022, the LHC can now accelerate protons allowing them to collide with a centre of mass energy $\sqrt{s}$ of up to 13.6 TeV [41].

The collision points on the LHC have the particle physics experiments surrounding them, the main four are:

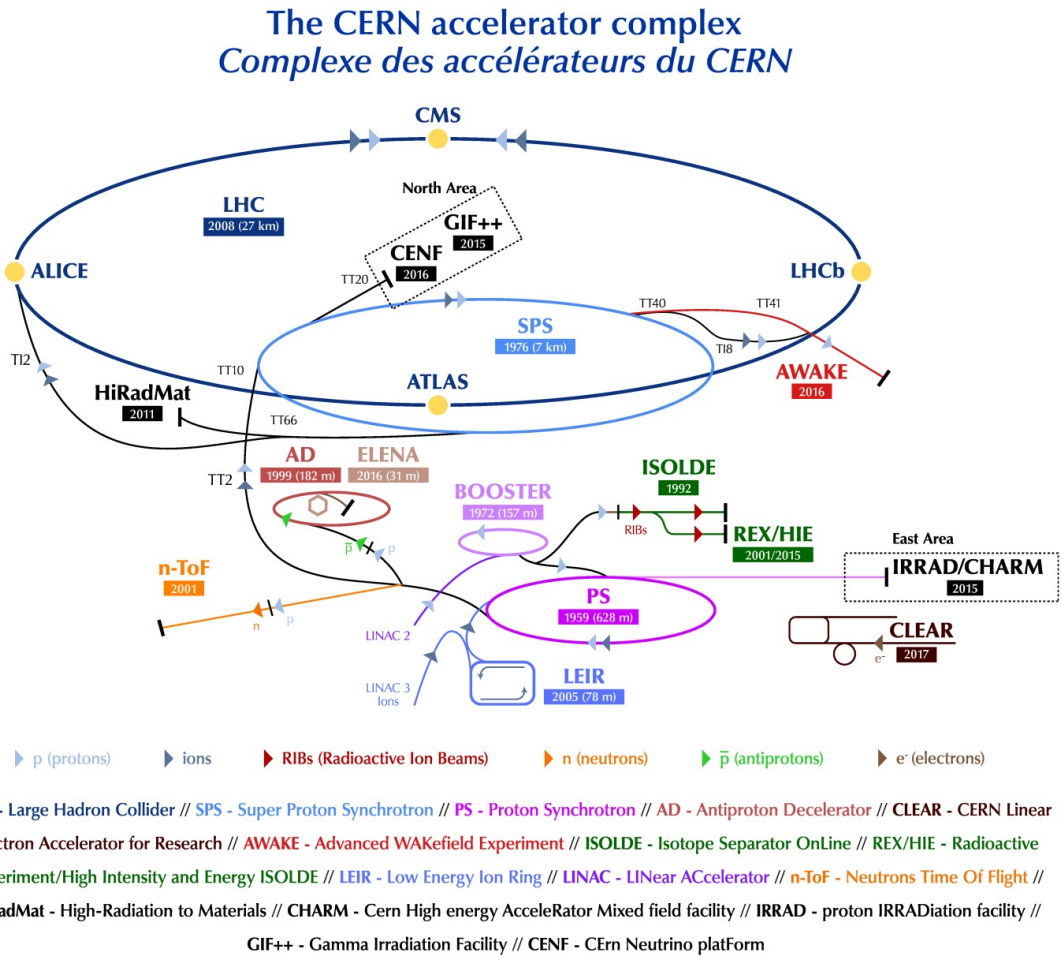

Figure 3.1: A schema of the CERN accelerator complex [36].

- ALICE: (A Large Ion Collider Experiment) designed to study strongly interacting matter in quark-gluon plasma, where energy density is high. [42]

- ATLAS: (A Torodial LHC ApparatuS) a general purpose detector looking at a wide range of particle physics phenomena. [35]

- CMS: (Compact Muon Solenoid) a general purpose detector looking at a wide range of particle physics phenomena. [43]

- LHCb: (LHC Beauty) designed to study beauty quarks. [44]

3.2 The ATLAS Detector

The ATLAS detector is a 46m long, 25m diameter general purpose detector at the LHC. As a general purpose detector, many areas of particle physics can be probed. The content of this chapter based on the ATLAS design report (and subsequent upgrade design reports) [35], where a more detailed description of ATLAS can be found. The ATLAS detector is made up of six different subsystems that work together to detect physics events. The subsystems are 'wrapped' around the beamline and each other in a cylinder such that particle physics events can pass through each one after the other. These subsystems can be seen in figure 3.2. These will be covered in detail below.

3.2.1 Inner detector

The inner detector, shown in figures 3.4 and 3.5, is at the core of ATLAS, and itself is made up of three separate components. These are the Pixel Detector, Semiconductor Tracker (SCT) and Transition Radiation Tracker (TRT). These components are covered in more detail below.

3.2.1.1 Pixel detector (PIX)

The Pixel detector (PIX) is the first layer of the ATLAS detector. Four layers of silicon pixels surround the beamline 3.3 cm away and detect particles by the small energy deposits particles leave as they pass through the layers of pixels. This allows the position and momentum of the particles to be determined to a precision of 10 μm.

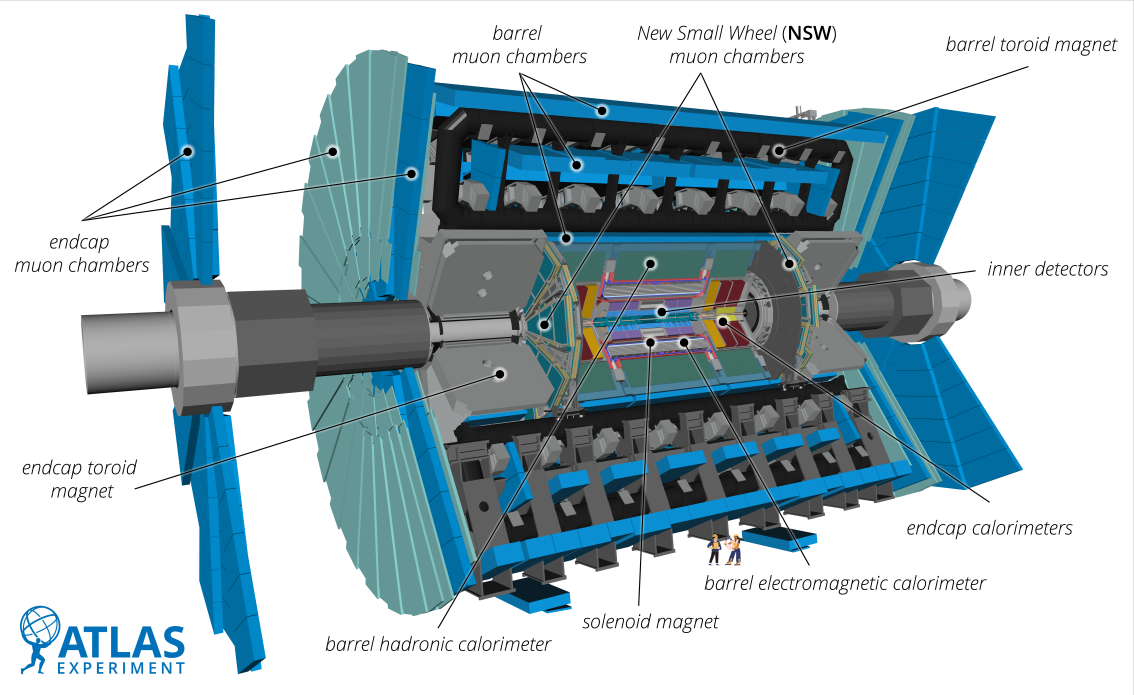

Figure 3.2: A diagram of the ATLAS detector [45]

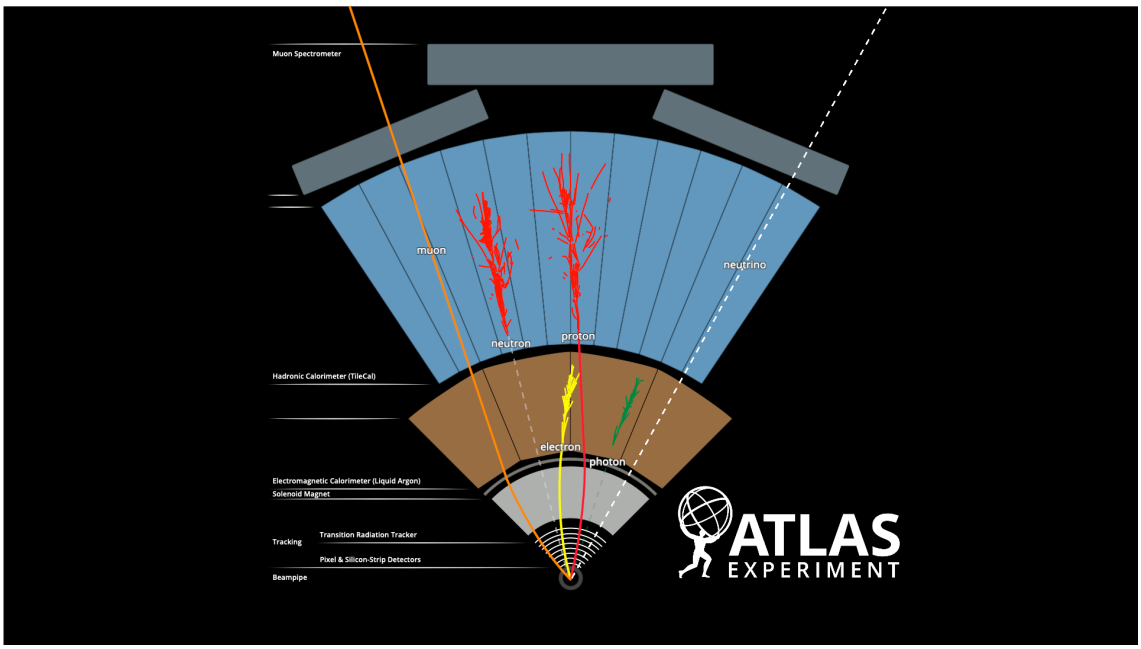

Figure 3.3: A diagram showing the different paths of particles through the ATLAS detector [46]. Particles are distinguished by their different behaviour though each section of the detector.

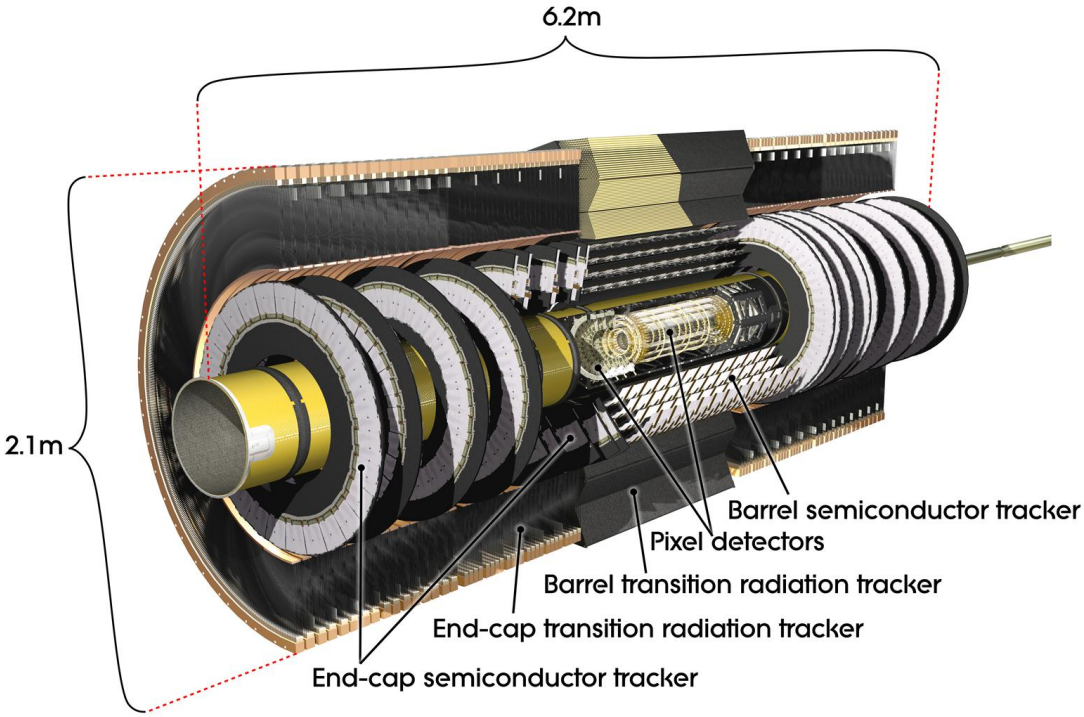

Figure 3.4: A diagram of the inner detector [47].

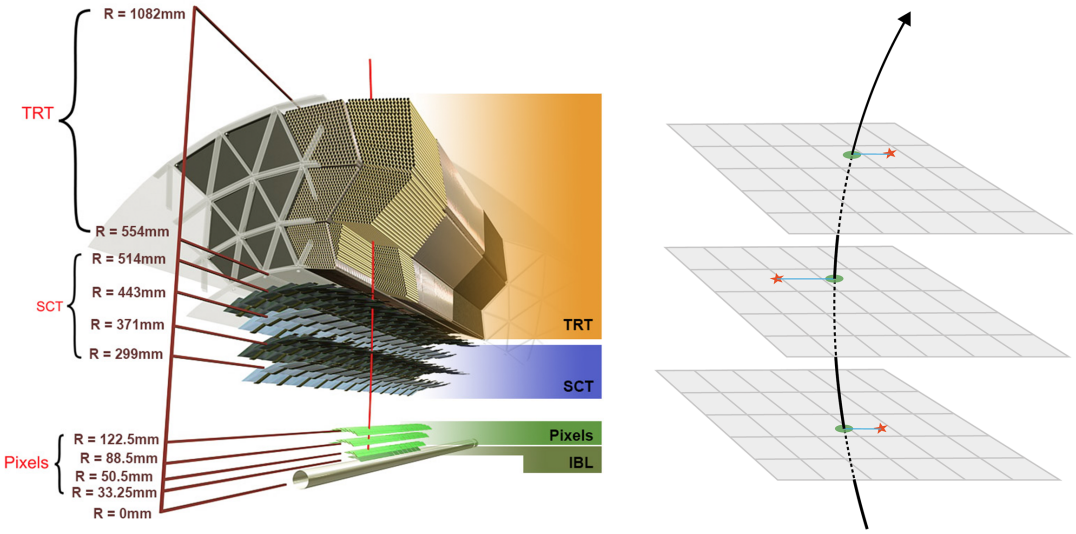

Figure 3.5: A diagram showing a cross section of the inner detector [48].

3.2.1.2 Semiconductor Tracker (SCT)

The next part of the inner detector is the semiconductor tracker (SCT). This surrounds the pixel detector and detects the tracks of charged particles. It is particularly important in the measurement of transverse momenta of charged particles [49]. This section of the detector is made up of 4000 modules of 6 million silicon sensors. These are arranged such that a particle will always pass through 4 layers of sensors. With this the position of charged particles at different points in the detector can be measured and their paths reconstructed.

3.2.1.3 Transition Radiation Tracker (TRT)

The final layer, surrounding the SCT, is the transition radiation detector (TRT). The TRT uses 300,000 straw shaped drift tubes filled with either xenon or an argon-mixture and a thin gold-plated tungsten wire. When a charged particle passes through a tube, it ionises the gas in the tube and releases electrons. The electrons are accelerated toward the charged wire, ionising more gas as they travel and creating an electrical signal in the wire. These signals can then be used to reconstruct the tracks of the particle events, as well as identifying the type of electron . The TRT is considered a complementary detector to the pixel based PIX and SCT, as while it is not as precise as the PIX and SCT, the TRT can detect many more hits per track.

3.2.2 Calorimetry

The next section of the detector is the calorimetry, 3.6 . This section stops most particles from exiting the detector, the exceptions to this are muons and neutrinos, as seen in figure 3.3. The calorimetry in ATLAS is made up of two sections, the liquid argon calorimeter and the tile hadronic calorimeter. The different sections of the calorimeter in ATLAS allow for the type of particle in the event to be determined, with particles behaving in different ways in each. This is demonstrated in figure 3.3 where, for example, electrons will stop and undergo showering in the liquid argon calorimeter whereas protons will pass through the liquid argon calorimeter and stop and shower in the hadronic calorimeter.

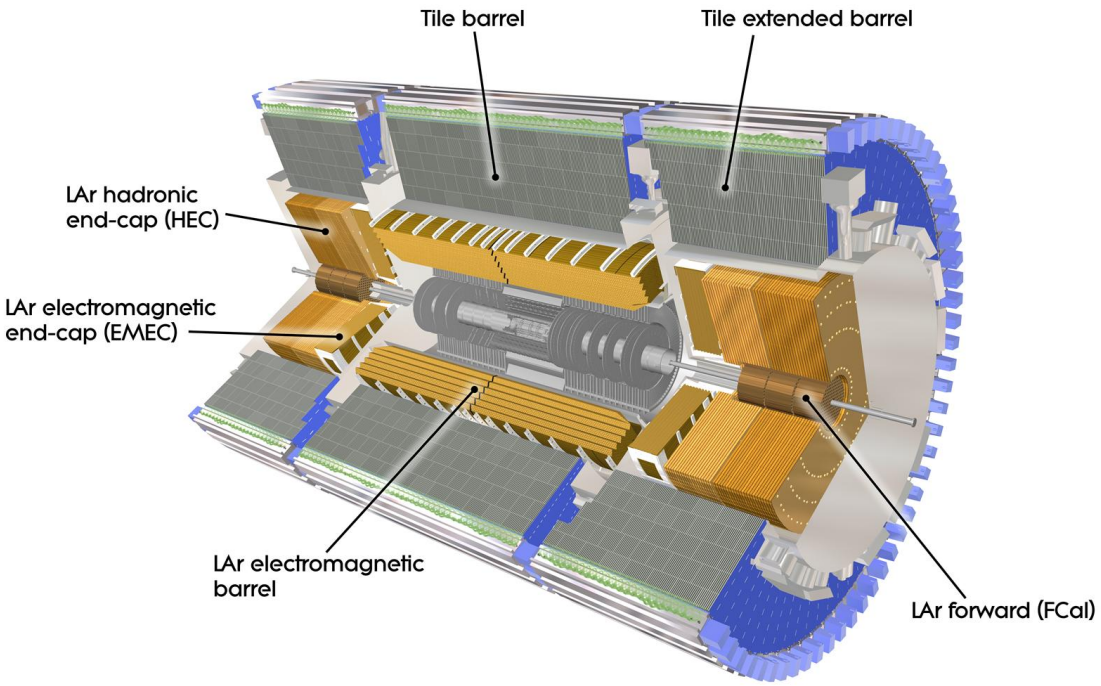

Figure 3.6: A diagram of the calorimeters in the ATLAS detector [50].

3.2.2.1 Liquid Argon calorimeter

The first layer of the calorimetry at ATLAS is the liquid argon (LAr) calorimeter. Liquid argon is sandwiched between layers of tungsten, copper or lead. Non-hadronic particles entering the detector are absorbed by the metal, causing them to produce many particles of lower energy, these particles in turn also produce more lower energy particles, this is known as an electromagnetic shower. The particles in the shower ionise the liquid argon, which produces an electric current. From this current, the energy of the origin particle of the shower can be determined. Particles that shower in the liquid argon calorimeter are electrons and photons. In order to capture data about all such particles in the calorimeter, the calorimeter is structured as an 'accordion' with a 'honeycomb'-like pattern. In order to remain a liquid, the argon must be kept at at least -184 °C.

3.2.2.2 Tile Hadronic Calorimeter

The second layer of the calorimetry is the tile hadronic calorimeter. This section of the calorimeter measures hadronic particles that were not absorbed in the LAr. The tile hadronic calorimeter

consists of layers of steel and plastic scintillators (a material that emits photons when excited by ionised particles). When the hadrons hit the steel, they induce a showering of new lower energy particles. These particles then interact with the plastic scintillator and the scintillator emits photons. These photons are then converted into an electric current with a combination of photomultiplier tubes and wavelength shifting fibres. This current is then used to determine the origin particle's energy.

3.2.3 Muon Spectrometers

As seen in figure 3.3, muons can pass through all of the previous detector subsystems. In order to measure the properties of muons in the detector, five different technologies are used: thin gap chambers, resistive plate chambers, monitored drift tubes, small-strip thin-gap chambers and micromegas. The positions of these technologies can be seen in figure 3.7.

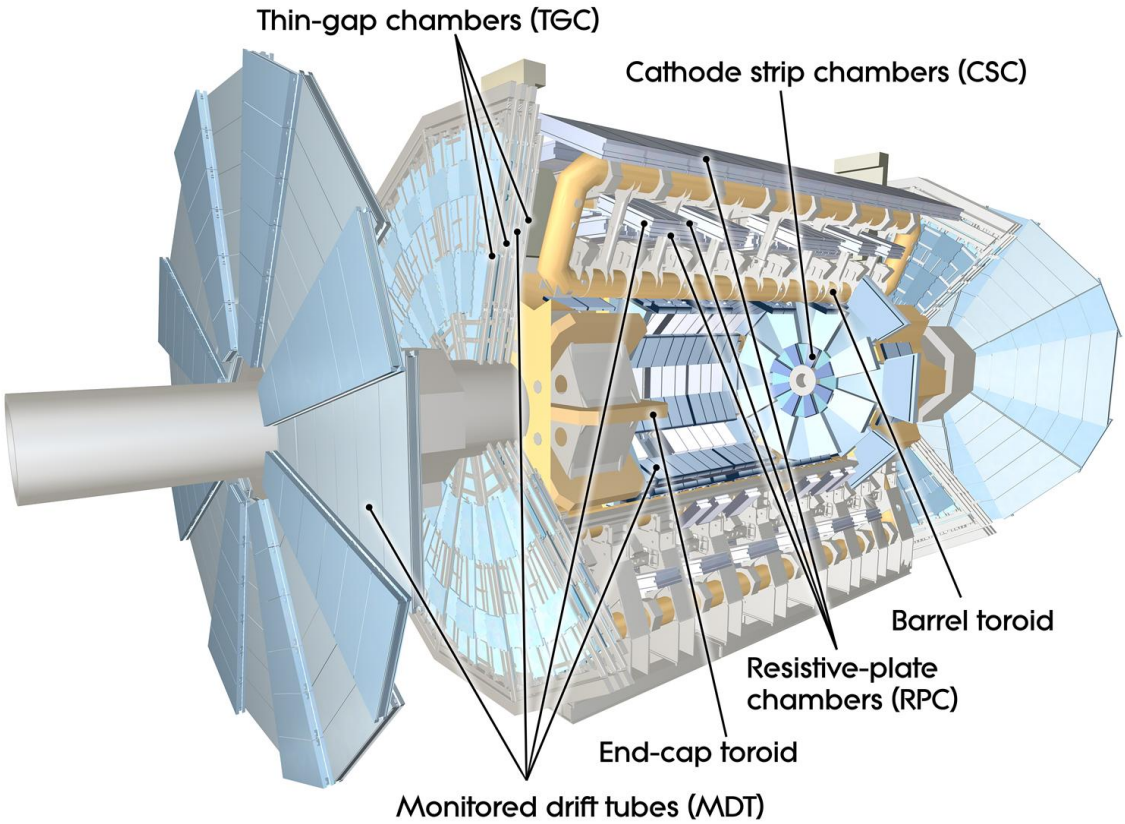

Figure 3.7: A diagram showing the muon spectrometers in the ATLAS detector [51].

3.2.4 Magnet System

Powerful super-cooled magnets are used in the ATLAS detector in order to measure the charge and momentum of particles. This is due to the Lorentz force acting on the particle:

$$F = q\mathbf{E} + \mathbf{q}(\mathbf{v} \times \mathbf{B}), \tag{3.1}$$

F is the force on the particle, q is the charge of the particle, E is the strength of the electric field the particle is in, v is the velocity of the particle and B is the strength of the magnetic field. As can be seen from the equation, a higher magnetic field strength produces a higher force on the particle. Therefore , it is beneficial to have a high magnetic field strength, as the particle will be curved to a more extreme degree making it easier to measure. As can also be seen in the equation, the charge of the particle also affects the degree to which it experiences the Lorentz force. Therefore, the amount of deflection of the particle in the same magnetic field strength can be used to determine the charge and therefore the type of hadron in the detector.

The magnet system at ATLAS is comprised of three different magnet types: the central solenoid magnet, the barrel toroid and the end-cap toroids. The solenoid magnet surrounds the inner detector, as seen in figure 3.2. The barrel toroid surrounds the centre of the experiment, while the end-cap toroids cover each end. The end-cap toroids allow for the magnetic field to be extended to the particles leaving the detector close to the beam pipe.

3.2.5 Coordinate System

The ATLAS detector coordinate system defines the origin as the interaction point in the detector. The z-axis follows the beamline with the x-y plane as perpendicular to the beamline. The positive z-axis is defined as the direction towards 'side-A' of the ATLAS detector. The positive x-axis is then defined as the direction towards the centre of the LHC, while the positive y-axis is upwards. The azimuthal angle, ϕ is measured around the z-axis and the polar angle, θ, is defined along the z-axis. The pseudorapidity is defined as $\eta = -ln(\tan\theta/2)$. Properties such as transverse momentum p_T, missing transverse energy E_T^{miss} and transverse energy E_T are defined in the x-y plane [35].

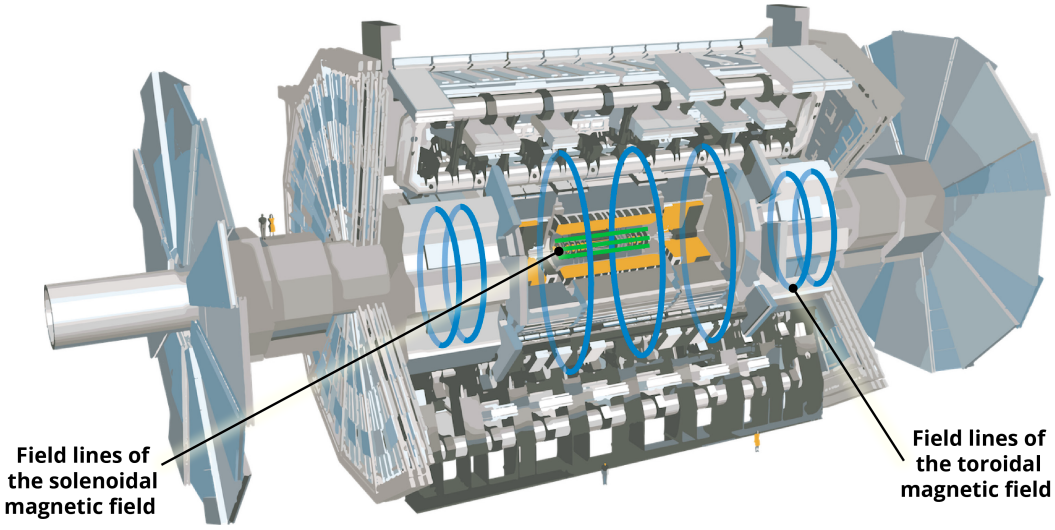

Figure 3.8: A diagram showing the positions of the magnets in the ATLAS detector [52].

3.2.6 Trigger and DAQ

During Run 2, the ATLAS detector saw a bunch crossing every 25 ns [53], with each crossing having multiple proton-proton collisions. Creates an incredibly large amount of data. Due to the large amount of data being produced by ATLAS, the experiment needs a way to filter out 'uninteresting' physics events from those events that are useful in physics analysis. It is not feasible to physically store all of the data that comes out of the detector, so only those events that contain useful information are recorded . This is the purpose of the Trigger and Data Acquisition system. This system works in two stages, the first stage is the Level 1 trigger , the trigger hardware. This is built into the detector, using information from the calorimeters and muon spectrometer to run simple algorithms to choose events . The trigger hardware allows for a smaller number of events to then be passed to the second stage, the High Level Trigger , the trigger software. This software analyses each event and picks those that satisfy the triggers chosen by the collaboration. The events that pass these two stages are then stored to be used for analysis. It can be seen in Figure 3.9 how the stages of the trigger reduce the amount of data into a more manageable amount for data analysis, with the data rate starting at 40 MHz before the triggers to 1.5 kHz after the trigger.

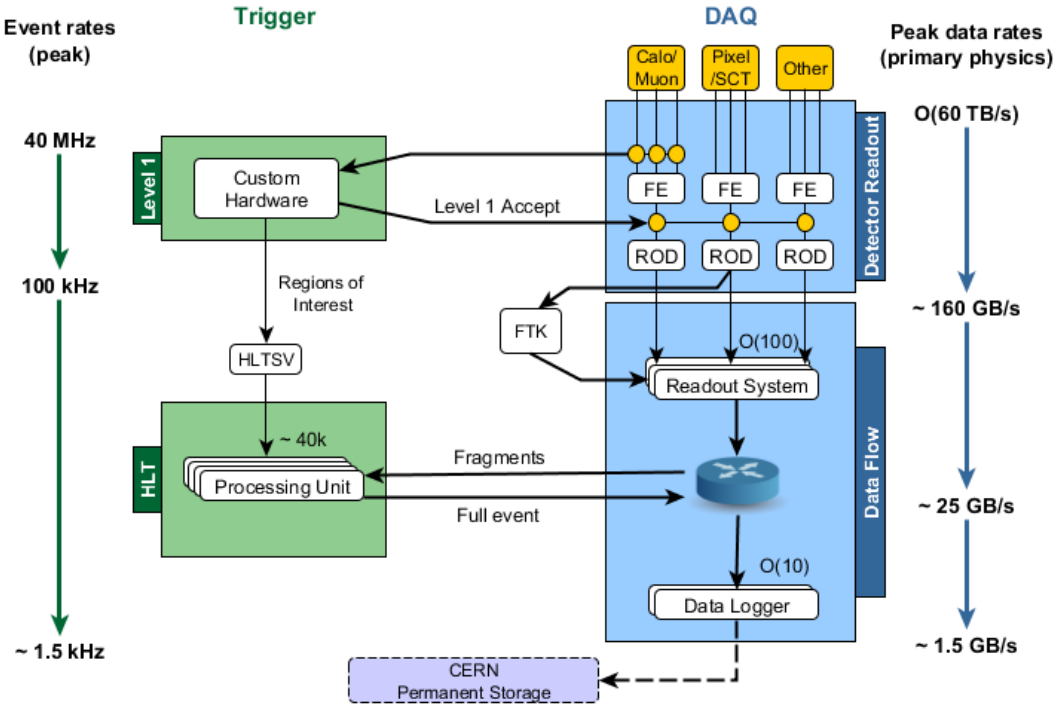

Figure 3.9: A flow diagram showing the different stages of the trigger and data acquisition (DAQ) system at ATLAS [54].

3.3 Software

Even after the trigger hardware and software removes uninteresting physics events, there is still a vast amount of data left to be analysed. All of this data must be stored somewhere, for ATLAS this is done with the Grid [55]. The Grid is a number of sites around the world that process and store data produced at CERN. This allows for the usage of many different data sets, as well as running code remotely on large datasets that would usually take a long time locally. This data is stored as a file called a 'Analysis Object Data' (AOD), in Run 2, these are then used to generate derived Analysis Data Objects (DAOD) which provide smaller data samples to work on offline.

The ATLAS experiment uses the code framework Athena [56] to reconstruct and simulate ATLAS data. In order to compare real data to physical expectations, simulations of data are used. These are Monte Carlo (MC) simulations of the same interactions being studied in data. The data and MC store physics objects to allow for analysis. In data and MC many different properties of the particle interactions are stored, such as their energy and position. In this analysis, these properties are then analysed using the code framework AnalysisBase [57]. Important physics objects stored by data and MC in this analysis are described in section 3.4. A demonstration of the flow of data from the LHC and MC generation to physics analysis is shown in figure 3.10.

3.4 Object Reconstruction

Particles in the ATLAS detector are reconstructed and identified through the signals they leave in the detector. These objects are explained to aid understanding throughout the rest of the thesis. Some of the objects reconstructed at ATLAS are as follows:

- Electrons - Electrons are reconstructed using information from the electron calorimeter and from the track information in the inner detector. The reconstructed electrons are categorised in to three groups (working points) describing their discrimination from background: tight, medium and loose. The tight category has the highest background rejection and loose with the lowest. The loose category contains the largest number of events as it contains all of the events from the previous two categories, with medium containing events from the tight working point also and the tight category only containing tight events [59].

- Muons - Muons are reconstructed using information from the muon spectrometers and track

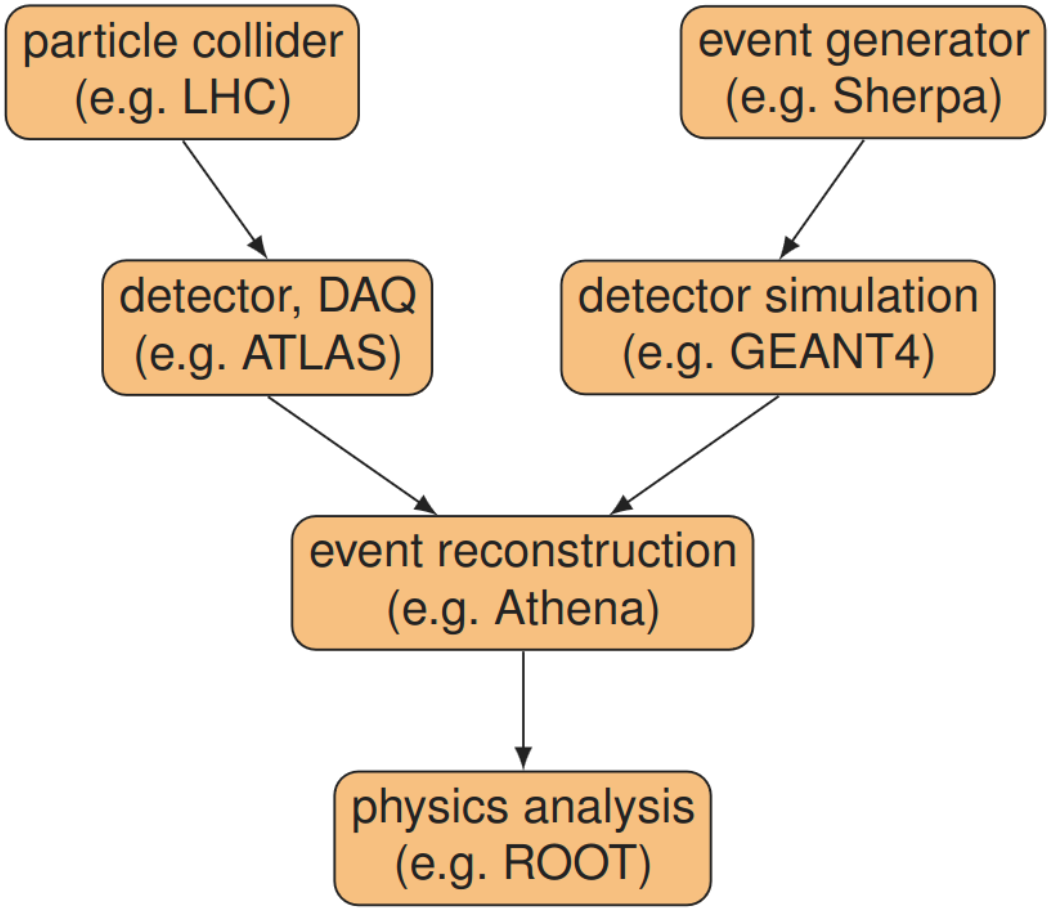

Figure 3.10: A diagram showing the flow of data from the LHC and MC generation to physics analysis [58].

information from inner detector [60].

- Photons - Photons are reconstructed when a track is found but cannot be matched with a cluster in the electronic calorimeter [61].

- Tracks - Tracks are a representation of the movement of each particle in the detector. Tracks are reconstructed using the 'hits' in the inner detector. These hits are information produced when particles hit the detector [62].

- Vertices - A vertex is where a particle interaction takes place. Vertices are reconstructed using the iterative vertex finding algorithm. A particle can make multiple vertices due to further decays after the initial particle interaction. Only one of these is considered the primary vertex, this is defined as the vertex associated with the highest $\sum p_T^2$ and is the first particle interaction to occur in an event. The other vertices are 'secondary' vertices, which come from the secondary decay of the primary particle interaction. The qualification task describes in this thesis will look in more detail at vertex selection [63].

- Jets - Jets are a cone shaped spray of hadrons from the process of hadronisation. Jets are reconstructed from clusters of energy deposits in the hadronic calorimeter using the anti-k_t algorithm [64] . In both analyses shown in this thesis, b-tagged jets are used as a selection. These are jets coming from the hadronisation of a b-hadron [65].

- Missing Transverse Momentum - Missing Transverse Momentum is not reconstructed, but is a term added as a correction to account for the momentum imbalance in the transverse plane when a particle leaves the ATLAS detector undetected (e.g. neutrinos, which ATLAS cannot measure) [66].

3.5 Instantaneous and Integrated Luminosity

The instantaneous luminosity is a measurement of the probability of particles colliding in a bunch crossing. It is defined as,

$$\frac{dN}{dt} = \mathscr{L}\sigma \tag{3.2}$$

where N is the number of events occurring in a time t, $\mathscr{L}$ is the instantaneous luminosity and *sigma* is the cross section. Bunch crossings with a more tightly packed group of particles will have a higher instantaneous luminosity as particles are more likely to collide.

The integrated luminosity is a measure of the total number of events in the detector over a run period. In particle physics, it is obviously beneficial to have the maximum amount of data possible from any measurements done. Therefore, it is aimed to have as high of a luminosity as possible. With the increased luminosity in data, there are more background events known as 'pile-up'. Over the course of Run 2 (the run used in this thesis), the integrated luminosity was $139 fb^{-1}$ [67]

3.6 MC Simulation

Monte Carlo simulation is heavily used in particle physics research, as it allows comparison of expected particle physics events to real data. Monte Carlo simulation at ATLAS is done using the GEANT4 [68]. Geant4 simulates the passage of particles through matter and therefore can be used to simulate the particles passing through the ATLAS detector. The various processes involved in particle interactions are simulated with different generators, for example Pythia [69], Herwig [70], Sherpa [71], Powheg Box [72] and Madgraph [73] . The algorithms of LHC event generation are done in this order: Hard Scatter processes, radiative processes, multiple parton interactions, hadronisation, hadron decays and then photon radiation [58]. A full explanation of MC generation is beyond the scope of this thesis. The detailed simulation choices for each sample in the analysis is given in section 5.3. Monte Carlo simulations for each year in Run 2 are given as MC16a (2015 and 2016), MC16d (2017) and MC16e (2018). These need to be separated by year as there are differences in the data taken from each year such as luminosity and pile-up and therefore need different scale factors applied to the MC for each year. The choice of MC generator will be discussed in more detail in section 5.6. Each MC generator will have slight differences due to different ways of simulating particle interactions, therefore the impact of MC generator choice is a systematic uncertainty that needs to be applied in analysis.

Chapter 4

Data-driven validation of the Hard Scatter Vertex Selection Efficiency

4.1 Introduction

When analysing particle interactions in data from the ATLAS detector it is possible to have interactions associated with many different origin points (vertices) in the detector. This is due to how interaction vertices are reconstructed using the available data, where multiple different vertices can match with the measured properties of the particle interaction. In order to correctly associate an event as a particular particle interaction, the signal hard-scatter (HS) vertex must be selected amongst many other background vertices. The hard-scatter vertex is where the first particle interaction occurs. In ATLAS, the hard-scatter (HS) vertex is currently calculated as the vertex in the event with the highest sum of the squared transverse momentum (P_T) of tracks associated with the vertex. There are other ways to determine the hard scatter vertex, however this is currently considered the most efficient way to determine the HS vertex for most interaction types. Correctly identifying the HS vertex is important to many physics analyses at ATLAS, a large portion of incorrectly identified events could affect the quality of the data used for analyses and lead to errors in any results and conclusions from these analyses. Having a good understanding of the efficiency of this selection and the dependencies of this efficiency allows for the opportunity to improve Monte Carlo simulations of interactions as well as the definition of the hard-scatter vertex.

The purpose of this study was to validate the performance of the current hard-scatter vertex

selection on data. This was done on processes with isolated leptons, as the current HS selector at ATLAS does not use the identified leptons information. This allows these leptons to be used as a probe and cleanly select on data. In this study the processes $Z^0 \to ee$, $Z^0 \to \mu\mu$ and dilepton $t\bar{t}$ were used. A method for extracting the HS selection efficiency was developed and used to compare the efficiency HS selection on Monte Carlo and data. At ATLAS, there are many versions of the analysis framework, Athena (see section 3 for information on Athena). Each version is given a release number, with each latest release generally being considered an improvement on the older release. In this analysis, two releases of Athena are studied upon, release 21 [74] and release 22 [75]. This was first done in release 21 of Athena, then with a different method in release 21 and then a new analysis performed on release 22.

4.2 Background

In order to measure the efficiency of the HS selection at ATLAS, a method for identifying which events contain a wrongly identified hard scatter vertex. One such method is what will be referred to as the 'estimator method'. This method is based on the knowledge that the vertex closest to both lepton tracks in an event will be the hard scatter vertex. Therefore, this method aims to calculate the distance of each vertex in an event to each of the lepton tracks and determine the vertex that is closest. A full description of this method is provided in 4.3. This method has the benefit of being relatively quick to run over many events, however, it could be prone to inaccuracy due to relying on the precision of the track and vertex positions.

In order to validate the estimator method, another method is used to compare the results. This comparison method will be referred to as the 'vertex fitting method'. For this method, software developed by the ATLAS vertexing group is used to determine the hard scatter vertex. While more likely more accurate due to its more complicated algorithm, this complexity also increases the analysis time for the programme. In addition, at the time of the qualification task, the vertex fitting method was only able to analyse events with two muons. Therefore, the vertex fitting method could not study the HS selection efficiency for the $Z^0 \to ee$ and $t\bar{t} \to e\mu$ channels.

Part of the qualification task, along with validating the HS selection efficiency, was to determine if the estimator method was a valid approach to determining the HS selection efficiency. If it was, this would allow for further study into the HS selection efficiency, at least as a first

estimate, to be much faster than using more complicated algorithms such as the vertex fitting method.

4.3 Analysis for Release 21 - The Estimator Method

4.3.1 Strategy

In order to determine the efficiency of the HS selection, a method for identifying incorrectly selected HS vertices was developed. This method was based on the fact that the closest vertex to the particle tracks from the hard-scatter event is the HS vertex. Therefore, the vertex closest to the two lepton tracks associated with the event being analysed was found and if the closest vertex is not considered the HS vertex (the vertex with highest sum squared p_T), the HS vertex was considered as incorrectly identified . The vertex closest to the two leptons was determined using the track longitudinal impact parameter with respect to the n$^{\text{th}}$ vertex, ξ, and polar angle, θ, as shown in Figure 4.1 and calculating the χ^2 between the particle track and the n$^{\text{th}}$ vertex.

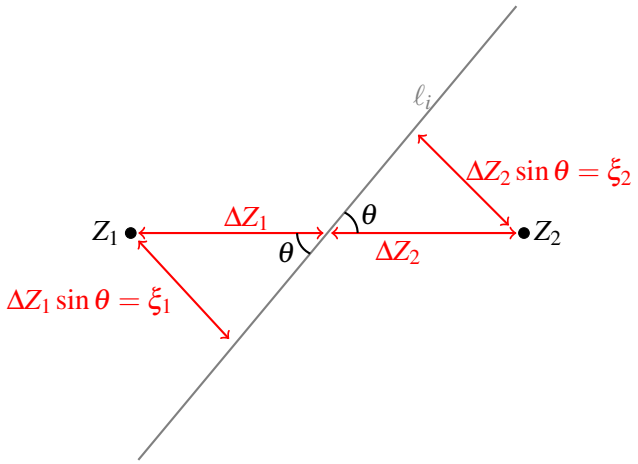

Figure 4.1: A diagram demonstrating distance of a lepton track, ℓ_i, to two vertices, Z_1 and Z_2.

with

$$\xi_n = \xi_0 - (Z_n - Z_0)\sin\theta \tag{4.1}$$

where ξ_n is the longitudinal impact parameter to the n$^{\text{th}}$ vertex, ξ_0 is the longitudinal impact parameter to the HS vertex and Z_0 and Z_n are the vertex Z coordinates of the HS vertex and the vertex n, respectively, and θ is the polar angle of the lepton. In order to find the closest vertex to both tracks in the event, a χ^2 is calculated for each vertex as shown in Equation 4.2.

$$\chi_n^2 = \frac{(\xi_n^1)^2}{\sigma_n^1} + \frac{(\xi_n^2)^2}{\sigma_n^2} \tag{4.2}$$

where σ_n is the associated error of ξ_n.

The χ_0^2 of the HS vertex identified is compared to the χ_i^2 of every other vertex in the event. If the χ_i^2 of a vertex is less than χ_0^2, the event is counted as an incorrectly selected HS vertex. The probability of a wrong vertex being identified as the HS vertex (*PWrong*), is the number of wrongly identified HS vertices divided by the total number of events as shown in equation 4.3.

$$PWrong = \frac{N_{Wrong}}{N_{Tot}}. \tag{4.3}$$

Here, N_{Wrong} is the total number of incorrect HS selections and N_{Tot} is the total number of events. Only events whose first primary vertex (the assumed Hard Scatter vertex) have nTracks greater or equal to 5 are considered. Within these events, only primary vertices with nTracks greater than or equal to 5 are considered for comparison to the fitted vertex. When analysing MC generated events, the weight of each event is used to calculate *PWrong*. Uncertainty was estimated as $\sqrt{\frac{N_{Wrong}}{N_{Tot}^2}}$.

4.3.2 Selection

Three channels were used as signal for this study, corresponding to $Z^0 \to ee$, $Z^0 \to \mu\mu$ and $t\bar{t} \to e\mu + b\bar{b} + \nu_e\nu_\mu$ with centre-of-mass energy of 13 TeV.

For Z^0 decays, events were selected with a single lepton trigger, opposite sign leptons and with a reconstructed Z^0 mass within 85-95 GeV.

A single lepton trigger is a trigger where at least one lepton in an event is able to pass the trigger requirements. By selecting opposite sign leptons, only events where the leptons in the event have the opposite electromagnetic charge are chosen. This is done as the leptons from each channel are expected to have opposite charge due to charge conservation.

The reconstructed mass refers to the mass of the Z^0 boson that is calculated from the energy and momentum of its decay products (in this case two electrons). Only events whose reconstructed Z^0 mass is within 85-95 GeV are considered, as this is the mass of the Z^0 boson is 91.2 GeV [76], encompass a large part of the Z^0 resonant mass peak, reducing background from events that are not from Z^0 decays. This cut will also remove events coming from actual Z^0 decays, however, the number of signal events is high enough that this is not an issue.

For the $t\bar{t}$ channel events were selected with a single lepton trigger, opposite sign leptons and two b-tagged jets and no cut on missing transverse energy (MET). MET refers to the energy that is 'missing' from an event due to particles that were undetected, for example neutrinos. This missing transverse energy can be used to select events if the expected missing energy is known. In the case of Z^0 decays, neutrinos are not produced, so no missing transverse energy is expected. In the $t\bar{t}$ channel, events with a reconstructed mass of 85-95 GeV were removed to avoid Z^0 decay background.

The TightLH electron ID and the FCTight electron isolation [77], medium muon quality [78], PflowTight_FixedRad muon isolation [77] and overlap removal were used [79].

Isolation is a technique used to 'isolate' the lepton of interest from other leptons. This is done by measuring lepton activity around the lepton of interest, and discarding events with neighbouring lepton activity exceeding the chosen isolation working point. The TightLH electron ID. FCTight electron isolation and PflowTight_FixedRad refer to specific ATLAS working points for isolation.

Muon quality is a measure of the accuracy at which a muon is identified, taking into account many different factors such as track reconstruction, purity, efficiency and momentum resolution. Medium quality was used to remove a large number of poor quality muons, while also keeping a reasonable amount of events.

Overlap removal refers to the process of removing multiple events that are identified as separate events, but actually originate from the same interaction point. This effect originates from the limitations of the detector resolution.

Leptons were required to have $p_T > 27GeV$ for consistency between the years of data and at the recommendation of the muon combined performance group at ATLAS.

DAOD (derived AOD) TOPQ1 (top quark processes) derivation for MC and data were used for the analysis with the estimator method.

4.3.3 Background Contributions

The main MC background contributions were added to the MC signal for each channel to better represent the corresponding data, as data will have a contribution from other processes. These contributions are shown in Table 4.1.

$t\bar{t}$ Channel	
Interaction Type	Number of Events
$t\bar{t}$	124926
Wt	4030.32
$Z^0 \to ee$	0.0247443
$Z^0 \to \mu\mu$	3.25703
MC Total	128265.19
Data Total	131747

$Z^0 \to ee$ Channel	
Interaction Type	Number of Events
$t\bar{t}$	10486.7
Wt	972.57
$Z^0 \to ee$	1.42341×10^7
$Z^0 \to \mu\mu$	0
MC Total	1.42491×10^7
Data Total	1.4624×10^7

$Z^0 \to \mu\mu$ Channel	
Interaction Type	Number of Events
$t\bar{t}$	14466.1
Wt	1349.665
$Z^0 \to ee$	0
$Z^0 \to \mu\mu$	2.38958×10^7
MC Total	2.391161577×10^7
Data Total	2.3876×10^7

Table 4.1: Background contributions for each MC signal, compared to the total events in data.

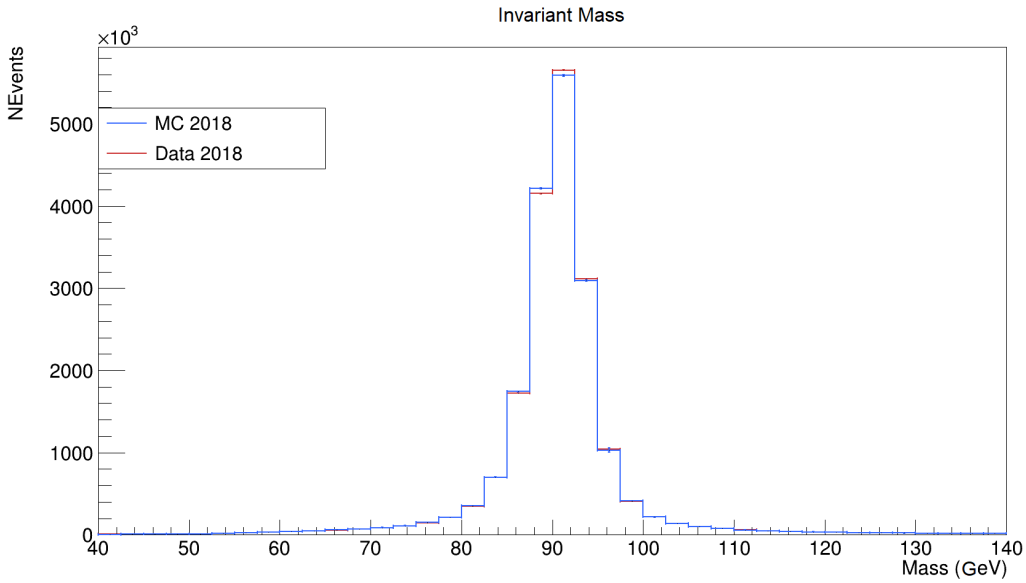

Figure 4.2: The invariant mass distribution of two electrons for 2018 $Z^0 \rightarrow ee$ Monte Carlo (blue) and data (red).

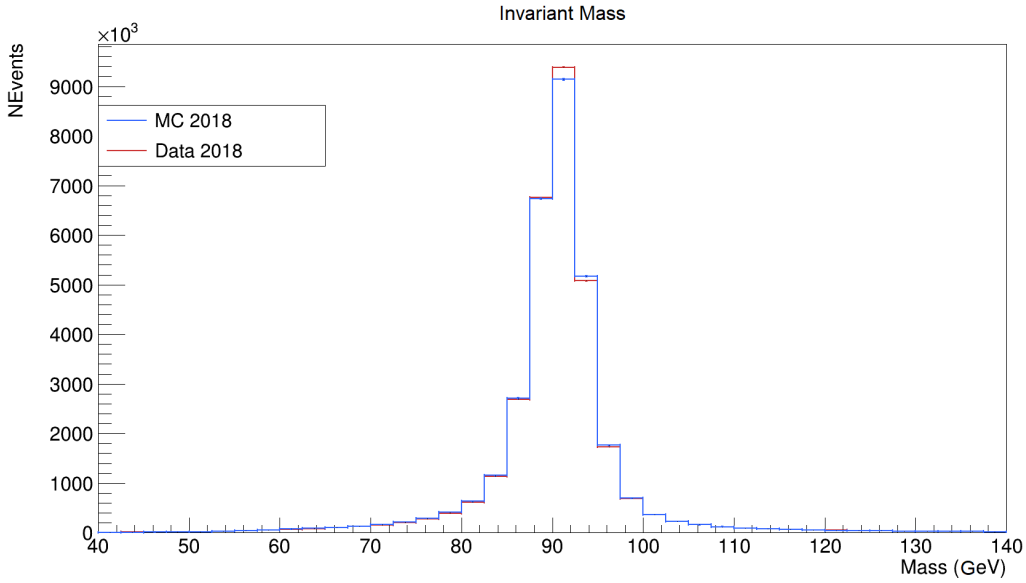

Figure 4.3: The invariant mass distribution of two muons for 2018 $Z^0 \rightarrow \mu\mu$ Monte Carlo (blue) and data (red).

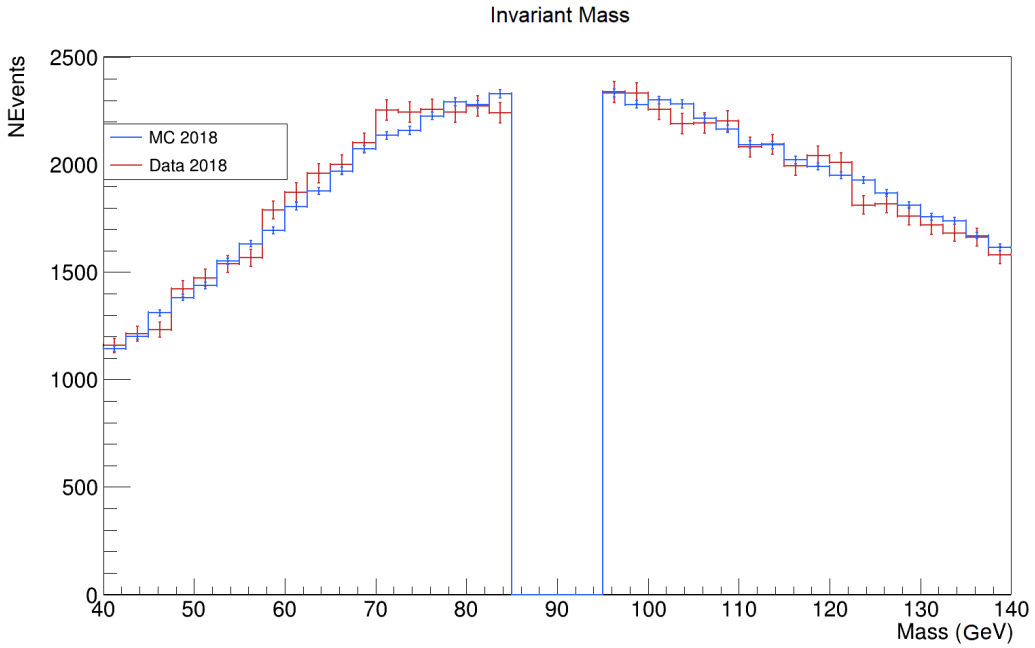

Figure 4.4: The invariant mass distribution of the electron and muon for 2018 $t\bar{t}$ Monte Carlo (blue) and data (red). The region with no events is where the cut of 85-95 GeV was made in the selection.

4.4 Results

4.4.1 $Z^0 \to ee$

PWrong was measured as $1.574\% \pm 0.003\%$ and $0.983\% \pm 0.003\%$ in Monte Carlo and data respectively showing a large discrepancy between MC and data which can be seen in Figures 4.5, 4.7, 4.9, 4.12. The fraction of events that are misidentified as Hard Scatter vertices in both MC and data is relatively high. The $Z^0 \to ee$ channel shows a large dependence vs luminosity, number of tracks and MET. The number of vertices in an event is proportional to luminosity, this is shows why for large pile up the HS selection efficiency is lower. It can be seen in Figures 4.6, 4.8 and 4.10 show good agreement between MC and data when considering all events. Figure 4.2 also shows agreement between MC and data when considering the invariant mass of the two electrons.

Figure 4.14 shows the difference between the χ^2 for the vertex with the minimum χ^2 and the χ^2 for the HS vertex, for incorrectly identified vertices. It can be seen a large portion of the incorrectly identified HS vertices have a χ^2 close to that of the HS vertex, as their difference is small. This suggests that the majority of wrongly identified events are a similar distance away from the two lepton tracks as the HS vertex, possibly implying that a more accurate algorithm might be needed to discriminate better between vertices that are both very close. Figure 4.13 shows that there is a difference in the distribution of nTracks between MC and data for correctly identified events in $Z^0 \to ee$, this could provide explanation for the large discrepancy in *PWrong* for MC and data. The distribution shows the peak of the distribution of nTracks in MC for correctly identified events is lower than that of data. Comparing this to 4.11, where the peak of the distribution of nTracks is about the same for both MC and data, it could be inferred that the MC is not representative of the data when considering the number of tracks in each event. This could be tested by using all the available years in Run 2, instead of just the 2018 sample, or using an alternative MC generator.

4.4.2 $Z^0 \to \mu\mu$

PWrong was measured as $0.589\% \pm 0.002\%$ and $0.331\% \pm 0.002\%$ in Monte Carlo and data respectively showing a large discrepancy which can be seen in Figures 4.15, 4.17, 4.19 and 4.21. The percentage of events wrongly identified as Hard Scatter events is relatively high, although not

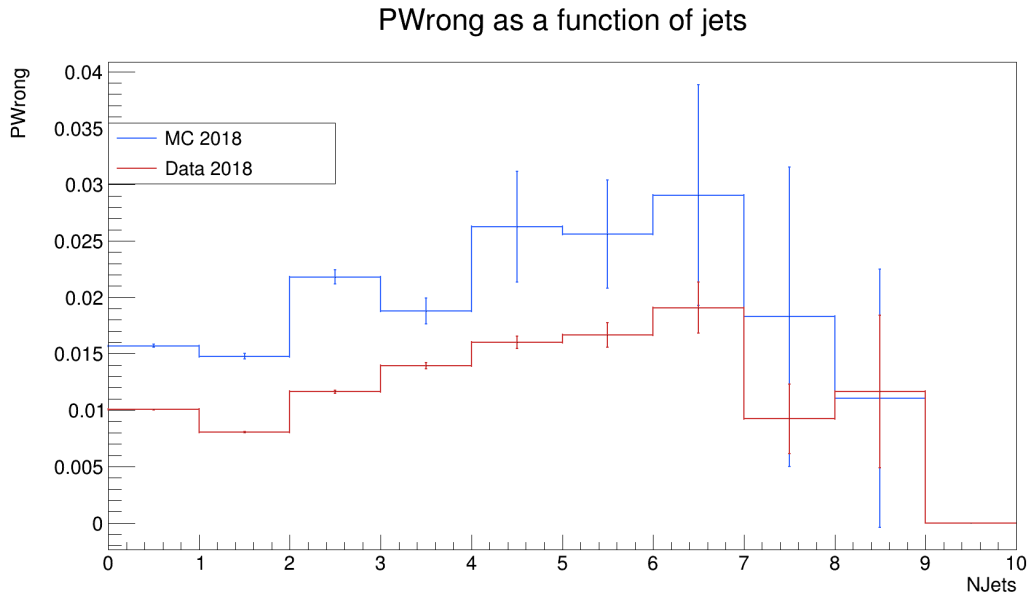

Figure 4.5: Percentage of wrongly identified vertices as a function of the number of jets in an event for 2018 $Z^0 \rightarrow ee$ Monte Carlo (blue) and data (red).

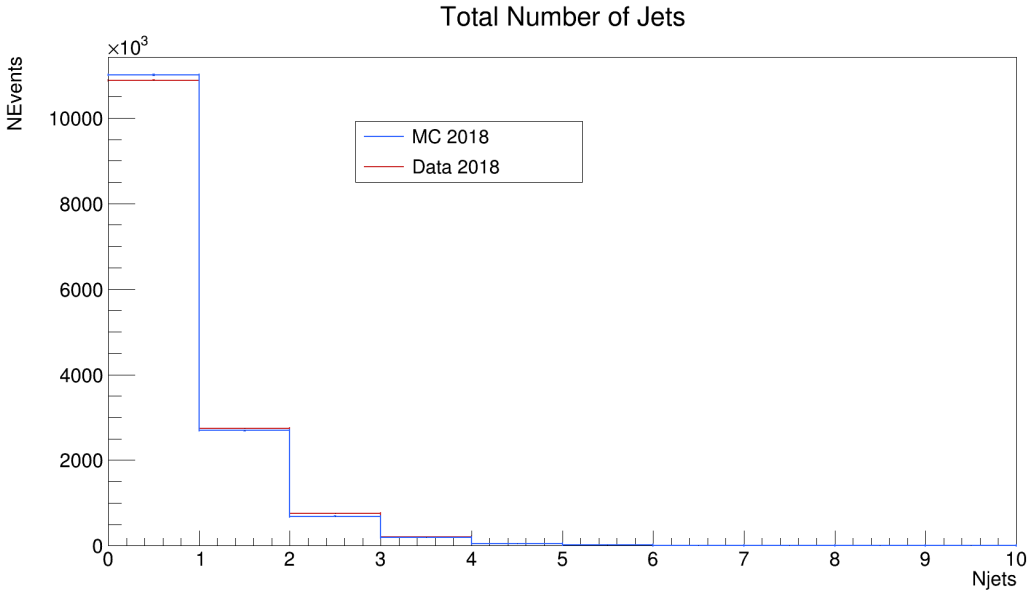

Figure 4.6: Distribution total vertices as a function of the number of jets in an event for 2018 $Z^0 \rightarrow ee$ Monte Carlo (blue) and data (red).

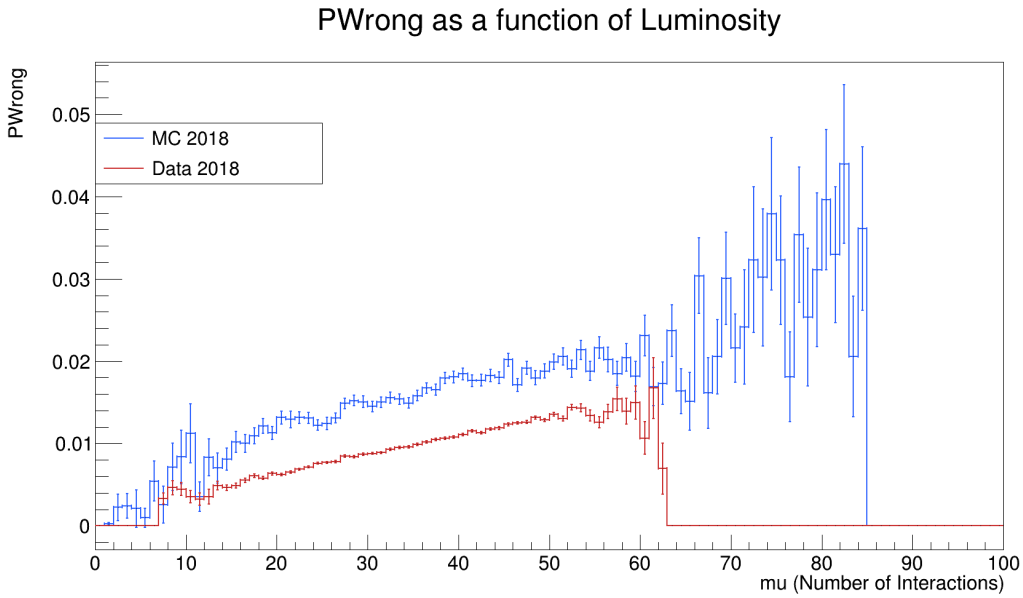

Figure 4.7: Percentage of wrongly identified vertices as a function of mu, the number of vertices in the event, of an event for 2018 $Z^0 \rightarrow ee$ Monte Carlo (blue) and data (red).

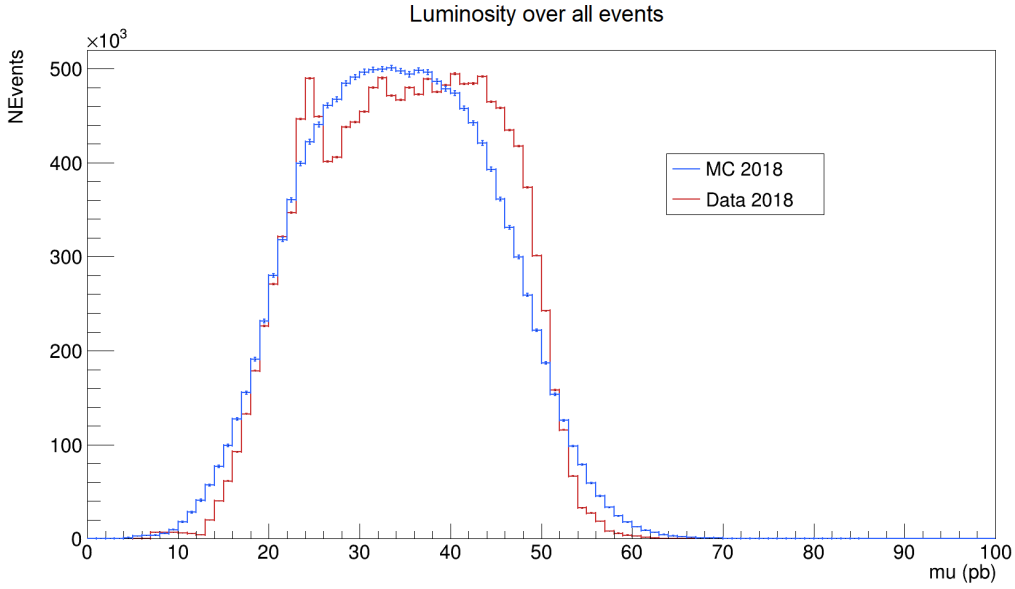

Figure 4.8: Distribution of total vertices as a function of mu, the number of vertices in the event, of an event for 2018 $Z^0 \rightarrow ee$ Monte Carlo (blue) and data (red).

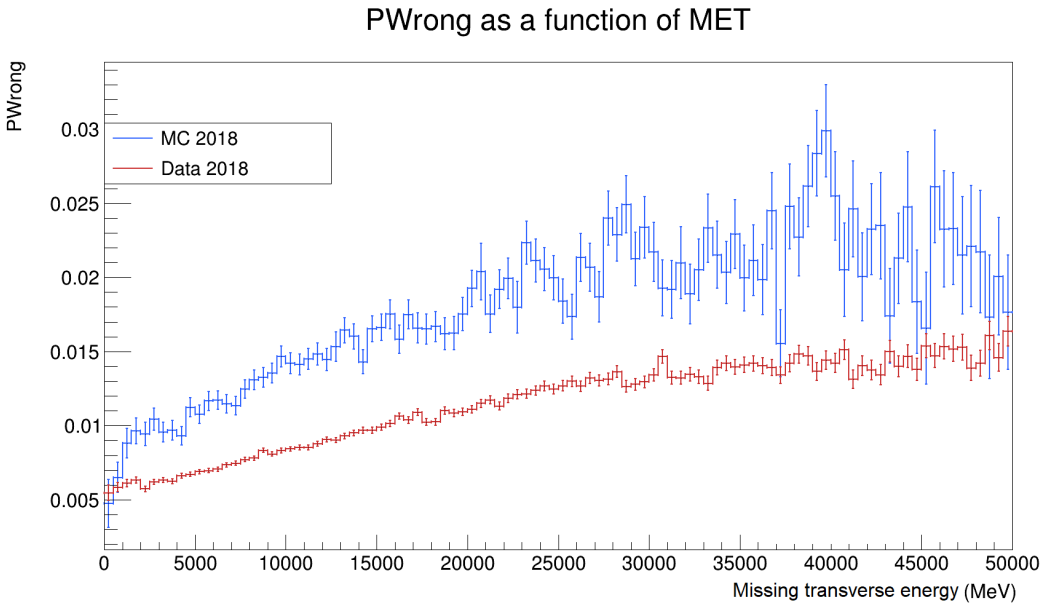

Figure 4.9: Percentage of wrongly identified vertices as a function of the Missing Transverse Energy of an event for 2018 $Z^0 \rightarrow ee$ Monte Carlo (blue) and data (red).

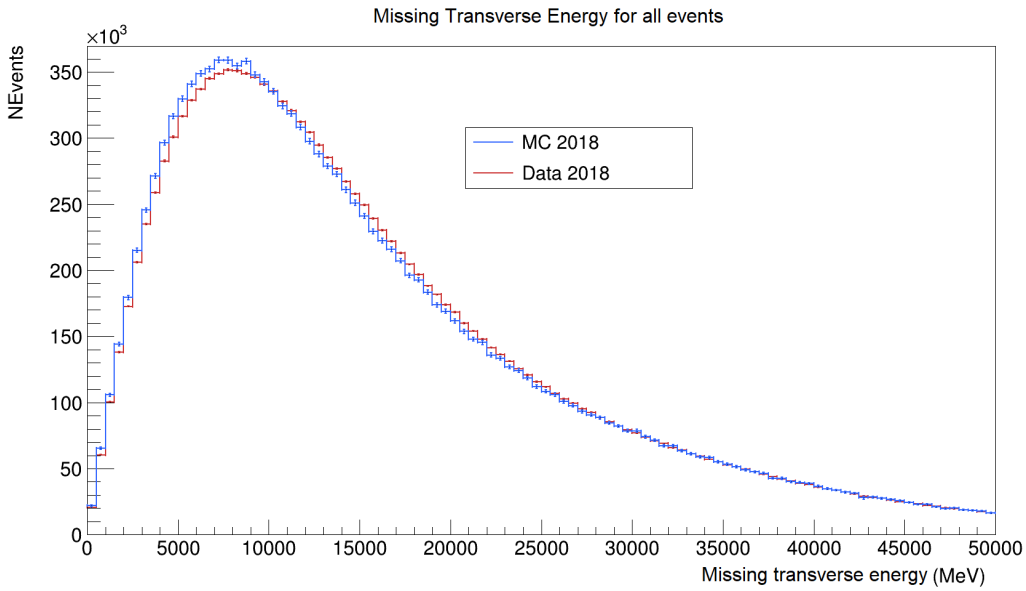

Figure 4.10: Distribution of total vertices as a function of the Missing Transverse Energy of an event for 2018 $Z^0 \rightarrow ee$ Monte Carlo (blue) and data (red).

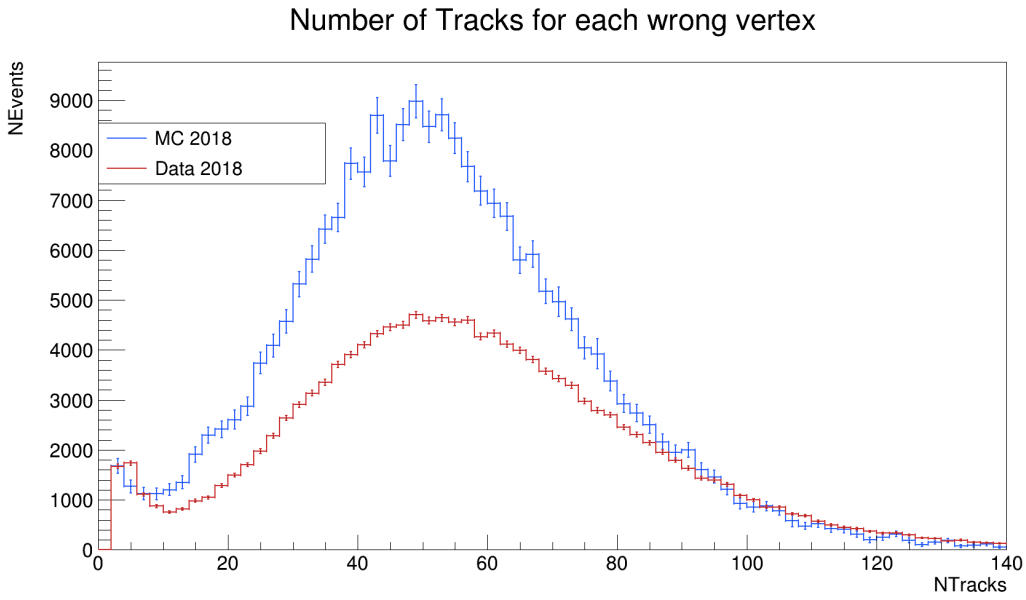

Figure 4.11: Distribution of wrongly identified vertices as a function of the number of tracks in a vertex for 2018 $Z^0 \rightarrow ee$ Monte Carlo (blue) and data (red)

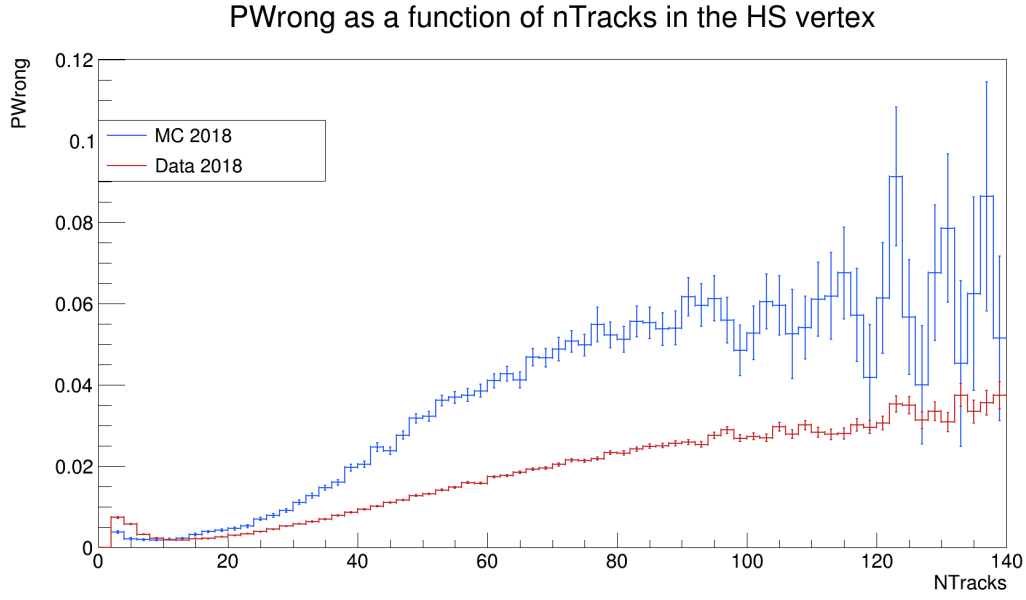

Figure 4.12: Percentage of wrongly identified vertices as a function of the number of tracks in the HS vertex for 2018 $Z^0 \rightarrow ee$ Monte Carlo (blue) and data (red).

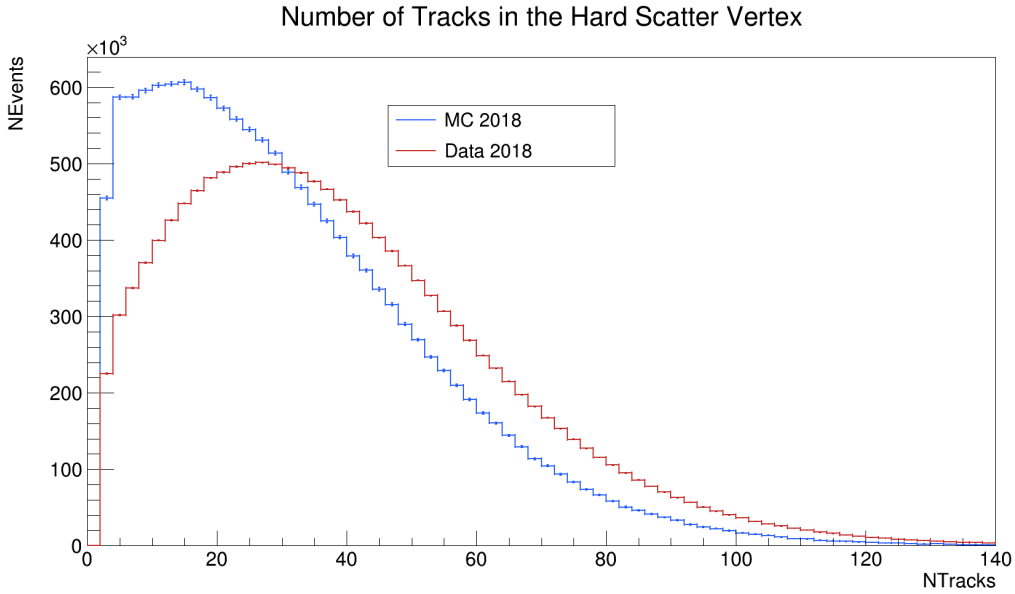

Figure 4.13: Distribution of correctly identified vertices as a function of the number of tracks in the HS vertex for 2018 $Z^0 \rightarrow ee$ Monte Carlo (blue) and data (red).

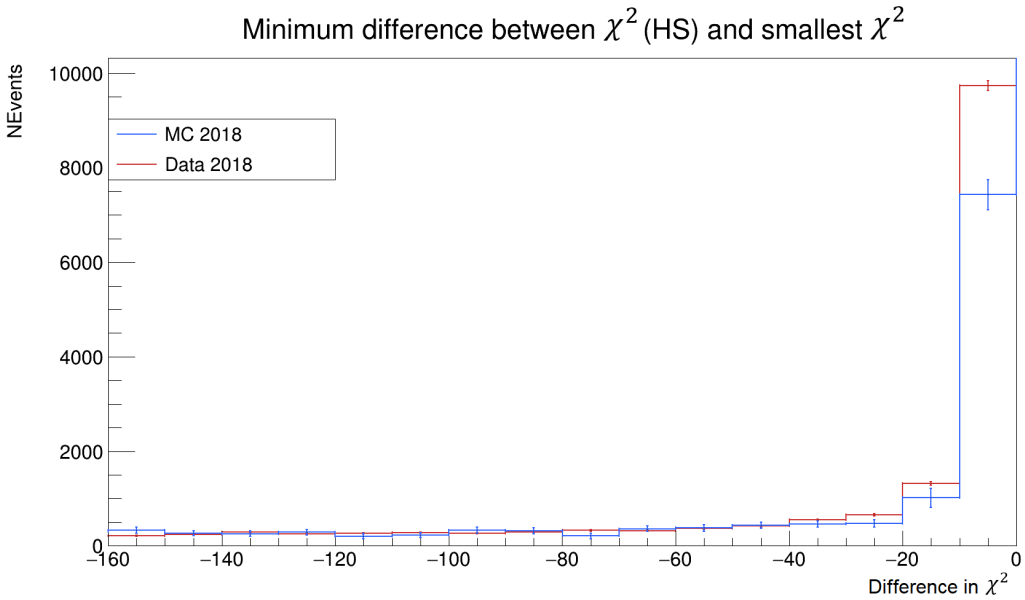

Figure 4.14: The difference between the χ^2 for the correct HS vertex and the χ^2 for the vertex with the smallest χ^2 for 2018 $Z^0 \rightarrow ee$ Monte Carlo (blue) and data (red).

as high as for the $Z^0 \to ee$ channel. Similar to the $Z^0 \to ee$ interaction channel, the $Z^0 \to \mu\mu$ interaction channel is highly dependent upon luminosity, number of tracks and MET, as seen in the figures. Again, suggesting *PWrong* is higher for those events with larger pile-up as expected. It can be seen in Figures 4.16, 4.18 and 4.20 show good agreement between MC and data when considering all events. Figure 4.3 also shows agreement between MC and data when considering the invariant mass of the two muons.

As with the $Z^0 \to ee$ decay channel, Figure 4.23 shows that there is a difference between MC and data for correctly identified events in $Z^0 \to \mu\mu$. Again, as with the $Z^0 \to ee$ decay channel, this could explain the difference in *PWrong*. The distribution shows the peak of the distribution of nTracks in MC for correctly identified events is lower than that of data. Comparing this to 4.22, where the peak of the distribution of nTracks is about the same for both MC and data, it could be inferred that the MC is not representative of the data when considering the number of tracks in each event. This could be tested by using all the available years in Run 2, instead of just the 2018 sample, or using an alternative MC generator.

Again, similarly to that of the $Z^0 \to ee$ interaction channel, a large portion of the incorrectly identified Hard Scatter vertices have χ^2 close to that of the HS vertex as determined by the squared sum p_T as shown in Figure 4.24. The level of *PWrong* in the $Z^0 \to \mu\mu$ was found to be lower than that of the $Z^0 \to ee$. Electron tracking is more inaccurate than muon tracking, therefore the accuracy of the $\sum Z \sin\theta$ estimator becomes imprecise. This would therefore suggest that some of the 'misidentified' HS vertices may actually be a result of inaccuracy in the analysis method. An alternative to this 'estimator method' would be to use the vertex fitting machinery [80] allowing for more accurate measurement of *PWrong*.

4.4.3 $t\bar{t}$

PWrong was measured as $0.031\% \pm 0.005\%$ and $0.032\% \pm 0.003\%$ in Monte Carlo and data respectively showing a very good agreement between Monte Carlo and data. This can be seen in Figures 4.25 to 4.31. It can be seen in Figures 4.26, 4.28 and 4.30 show good agreement between MC and data when considering all events. Figure 4.4 also shows agreement between MC and data when considering the invariant mass of the electron and muon from the decay.

The level of incorrectly identified vertices in the $t\bar{t}$ channel is much lower than that seen in the Z^0 decay channel. This could be due to the accuracy of the analysis strategy being poor for the Z^0

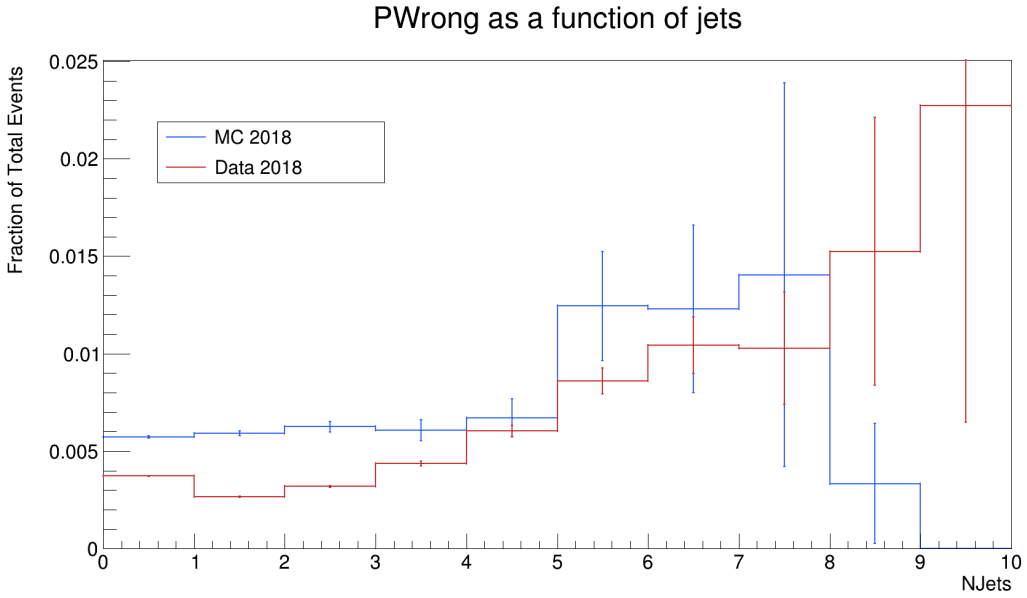

Figure 4.15: Percentage of wrongly identified vertices as a function of the number of jets in an event for 2018 $Z^0 \rightarrow \mu\mu$ Monte Carlo (blue) and data (red).

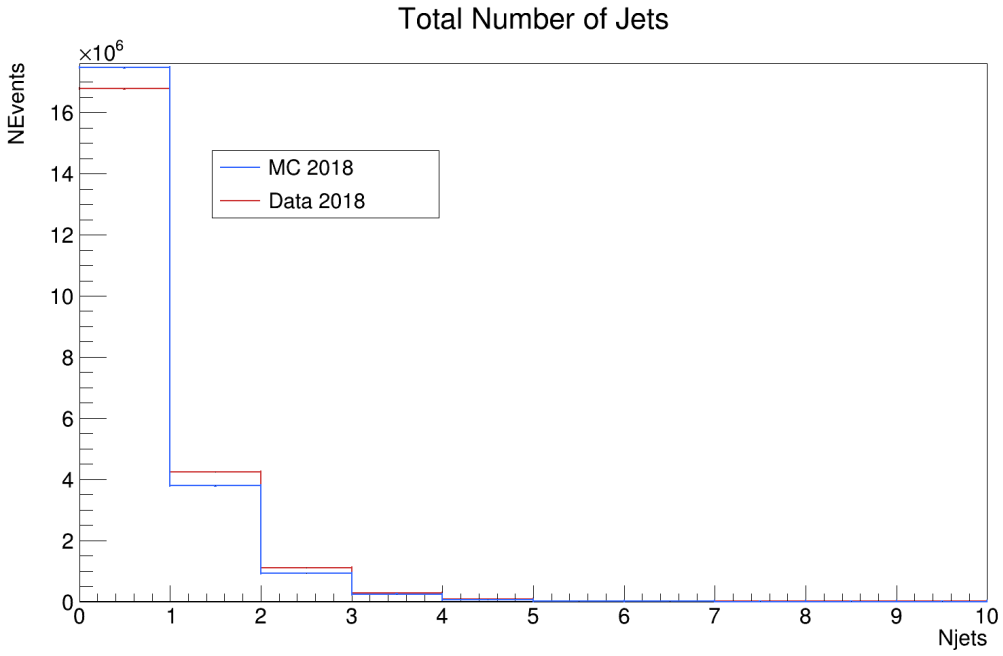

Figure 4.16: Distribution of total vertices as a function of the number of jets in an event for 2018 $Z^0 \rightarrow \mu\mu$ Monte Carlo (blue) and data (red).

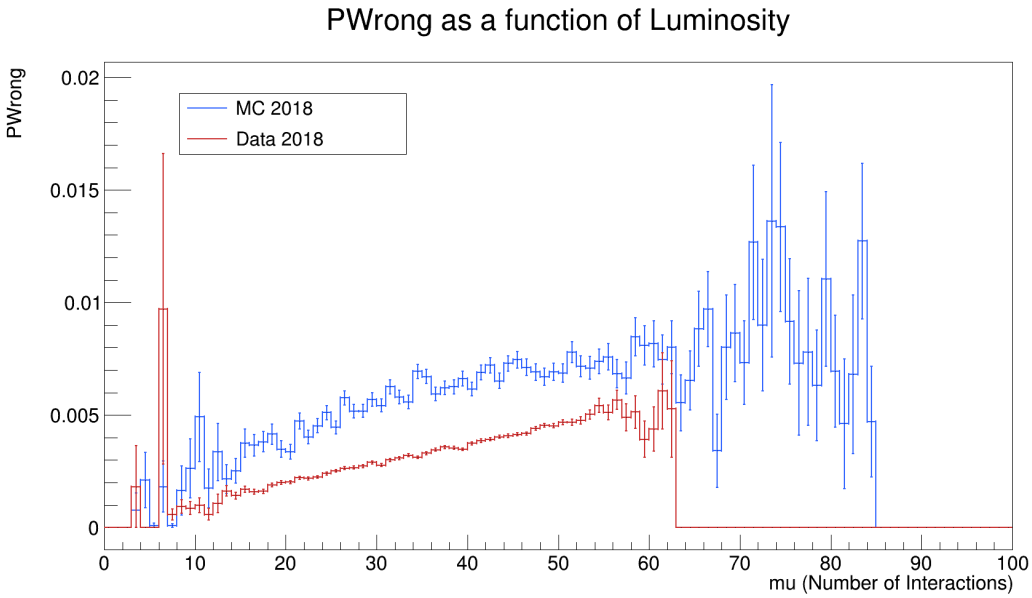

Figure 4.17: Percentage of wrongly identified vertices as a function of mu, the number of vertices in the event, of an event for 2018 $Z^0 \rightarrow \mu\mu$ Monte Carlo (blue) and data (red).

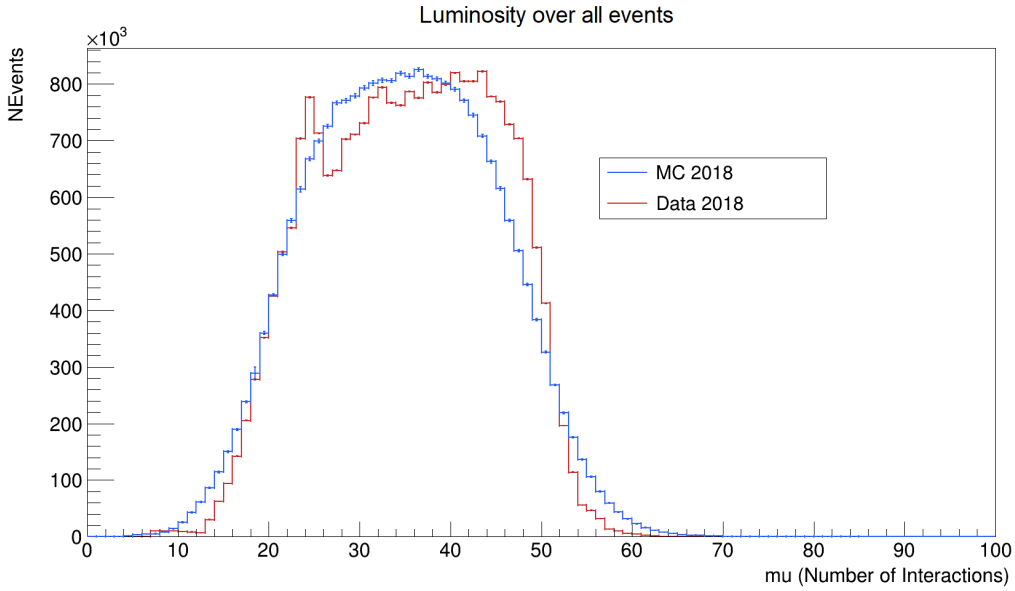

Figure 4.18: Distribution of total vertices as a function of mu, the number of vertices in the event, an event for 2018 $Z^0 \rightarrow \mu\mu$ Monte Carlo (blue) and data (red).

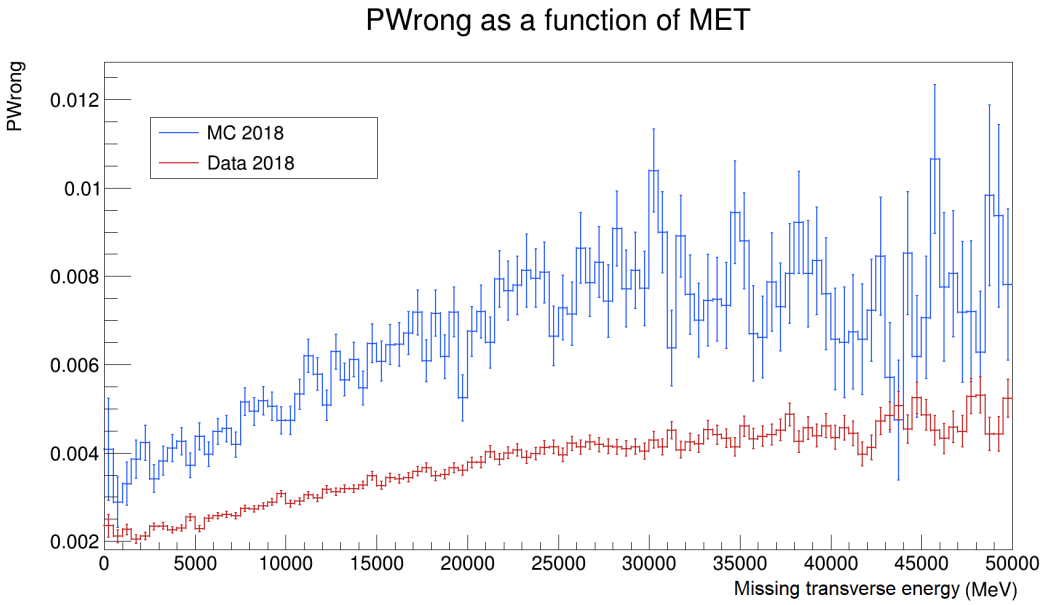

Figure 4.19: Percentage of wrongly identified vertices as a function of the Missing Transverse Energy of an event for 2018 $Z^0 \rightarrow \mu\mu$ Monte Carlo (blue) and data (red)

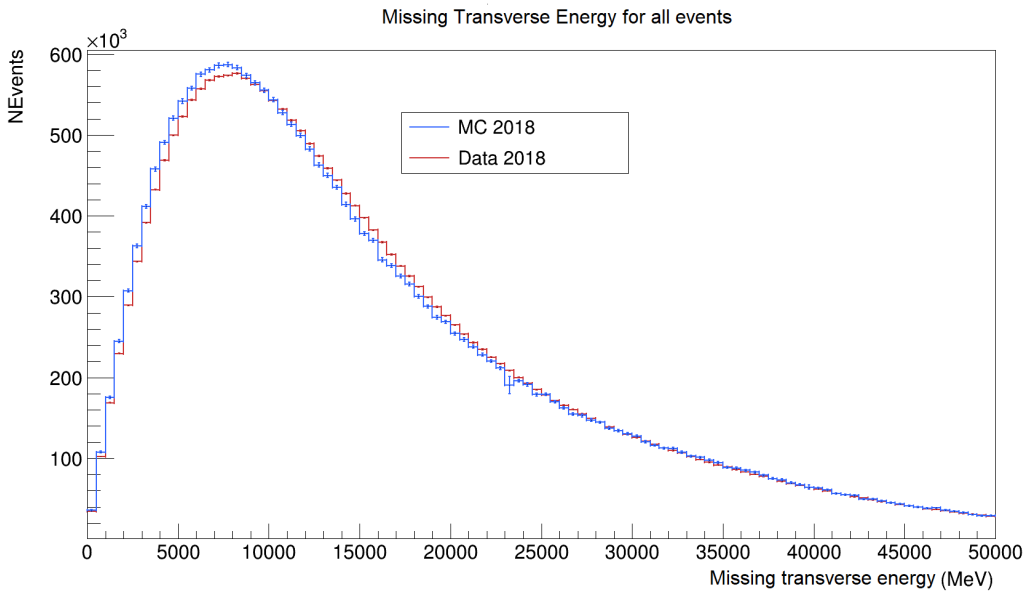

Figure 4.20: Distribution of total vertices as a function of the Missing Transverse Energy of an event for 2018 $Z^0 \rightarrow \mu\mu$ Monte Carlo (blue) and data (red)

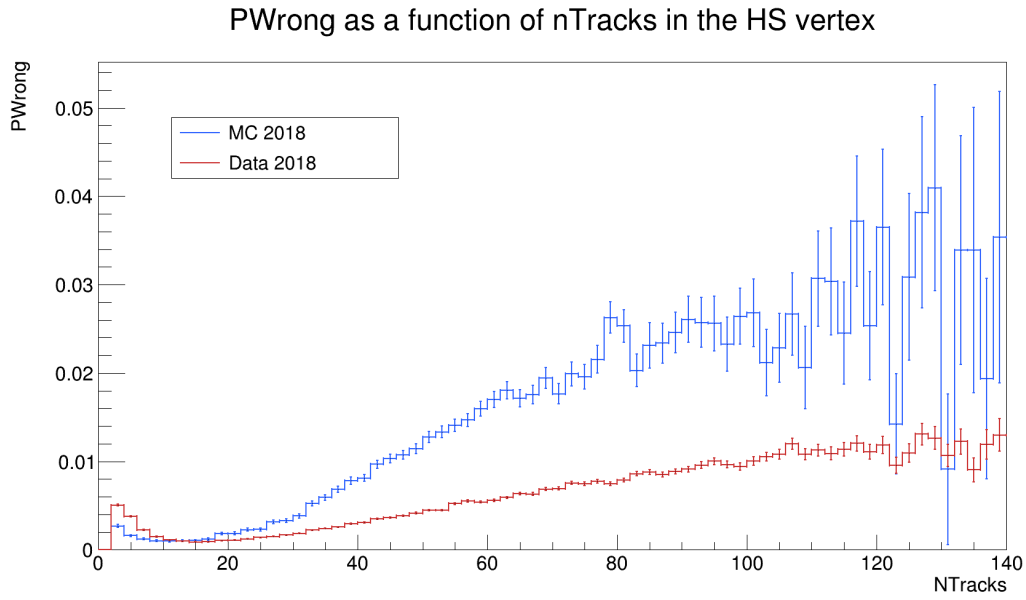

Figure 4.21: Percentage of wrongly identified vertices as a function of the number of tracks in the HS vertex for 2018 $Z^0 \rightarrow \mu\mu$ Monte Carlo (blue) and data (red)

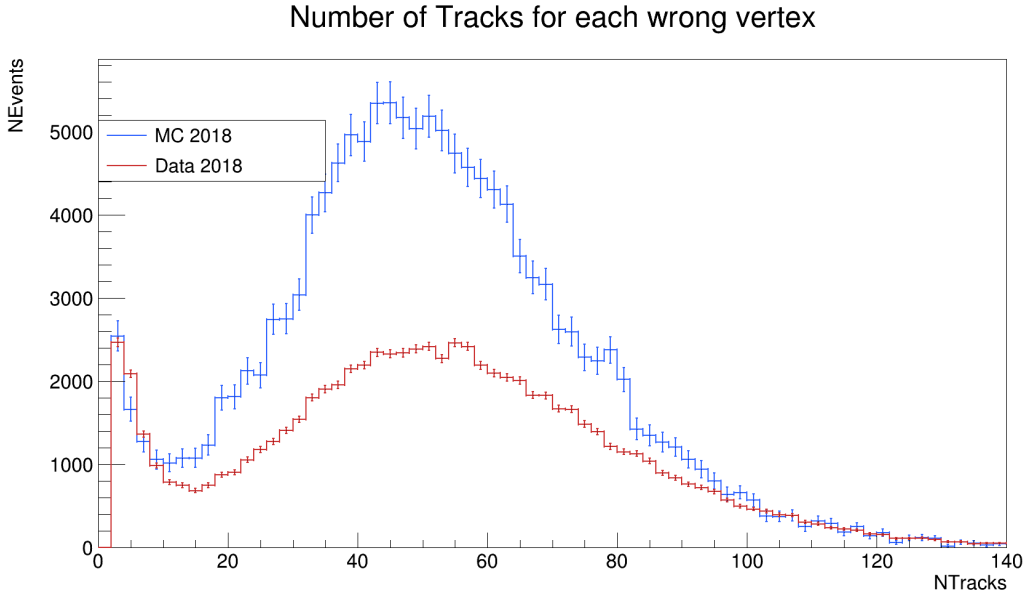

Figure 4.22: Distribution of wrongly identified vertices as a function of the number of tracks in a vertex for 2018 $Z^0 \rightarrow \mu\mu$ Monte Carlo (blue) and data (red)

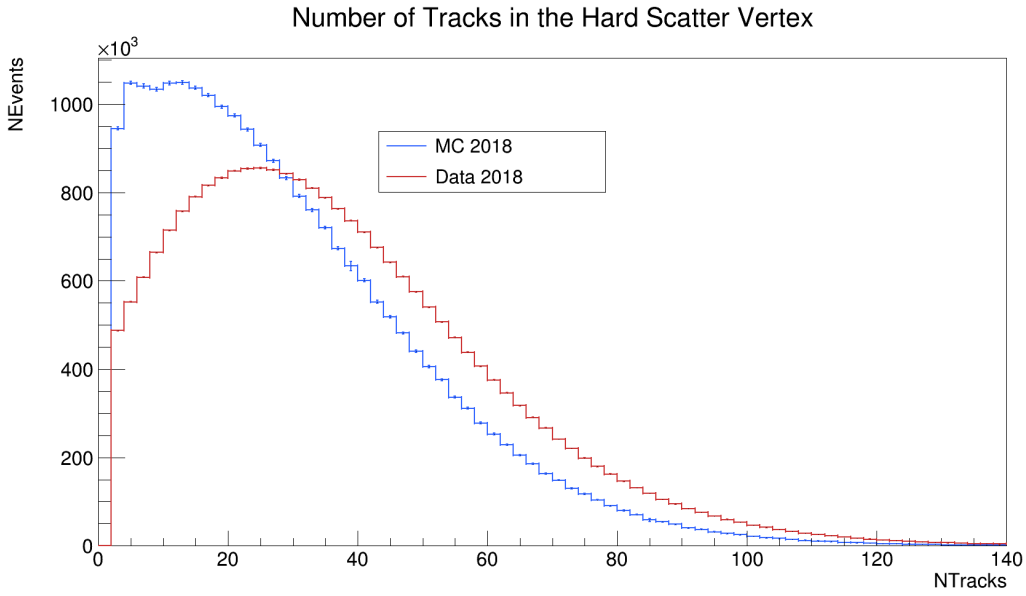

Figure 4.23: Distribution of correctly identified vertices as a function of the number of tracks in a vertex for 2018 $Z^0 \rightarrow \mu\mu$ Monte Carlo (blue) and data (red)

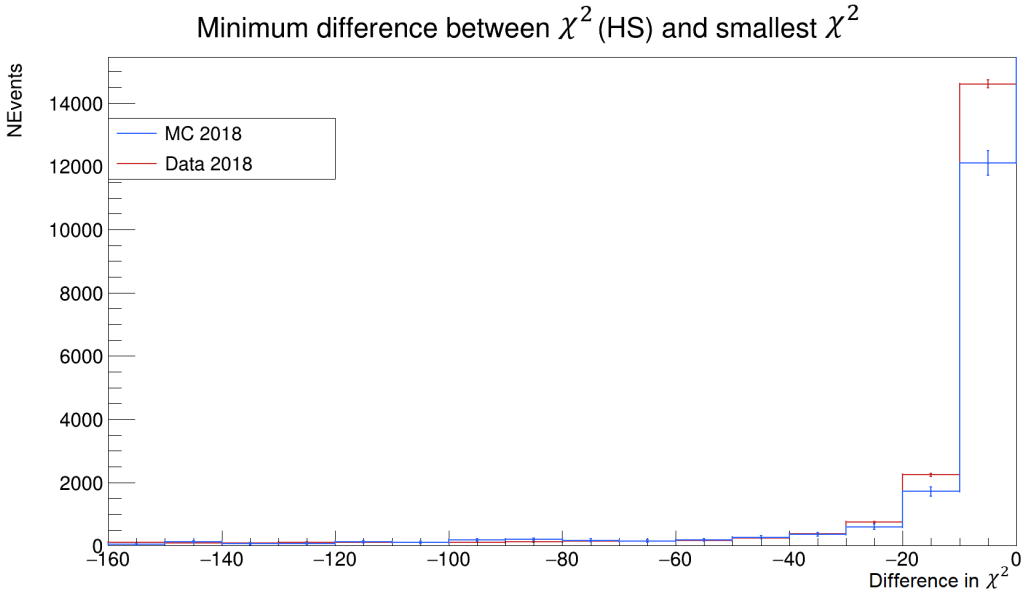

Figure 4.24: The difference between the χ^2 for the correct HS vertex and the χ^2 for an incorrectly identified vertex for 2018 $Z^0 \rightarrow \mu\mu$ Monte Carlo (blue) and data (red).

decay channel, which would further motivate study using the vertex fitting machinery. As can be seen in Figures 4.11, 4.22 and 4.32, $t\bar{t}$ events show very little dependence on the number of tracks in an event, in contrast to Z^0 decays which show a large dependence peaking at around 50 tracks.

It is likely the reason why the $t\bar{t}$ interaction channel gives a much lower value for *PWrong* than the Z^0 decay channels is due to the kinematics of the $t\bar{t}$ channel, the high track multiplicity of $t\bar{t}$ events would allow for efficient HS selection using the normal sum squared p_T method. Figure 4.33 shows good agreement between MC and data for correctly identified vertices, showing agreement with the measured values of *PWrong* that also show an agreement between MC and data. Future work would look at comparing the Z^0 decay channels against $t\bar{t}$ when the Z^0 events have greater than or equal to 2 jets, as this would be a more fair comparison.

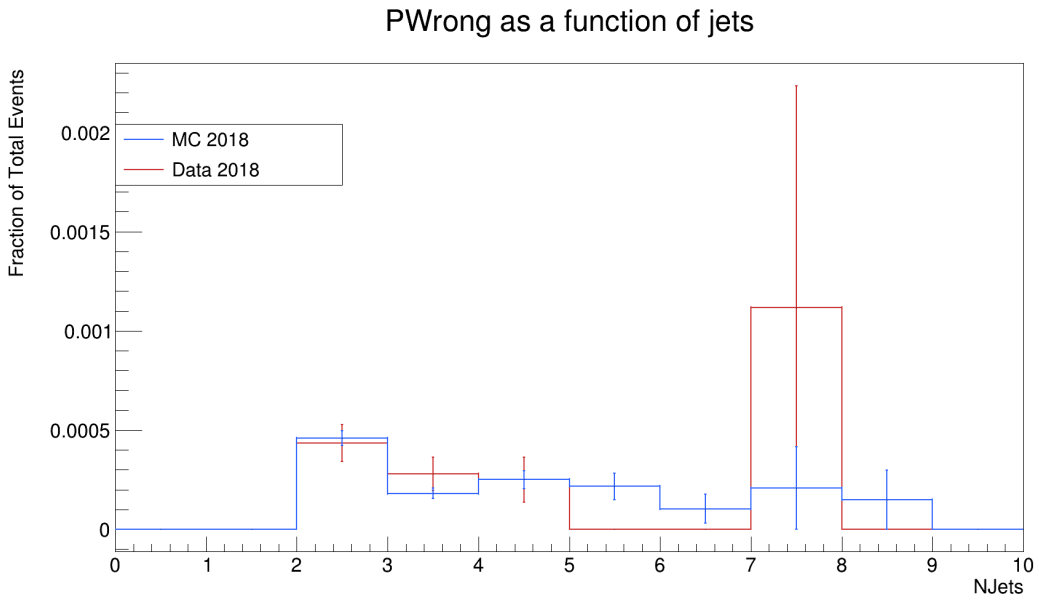

Figure 4.25: Percentage of wrongly identified vertices as a function of the number of jets in an event for 2018 $t\bar{t} \rightarrow e\mu$ Monte Carlo (blue) and data (red).

4.5 Conclusion

From the analysis method presented, good agreement can be seen between Monte Carlo and data for the $t\bar{t}$, with a very low level of wrongly identified Hard Scatter vertices. This is expected as the large track multiplicity in $t\bar{t}$ events it would be expected that the sum squared p_T would be highly efficient. It is therefore unlikely that further scale factor recommendations need to be made for the

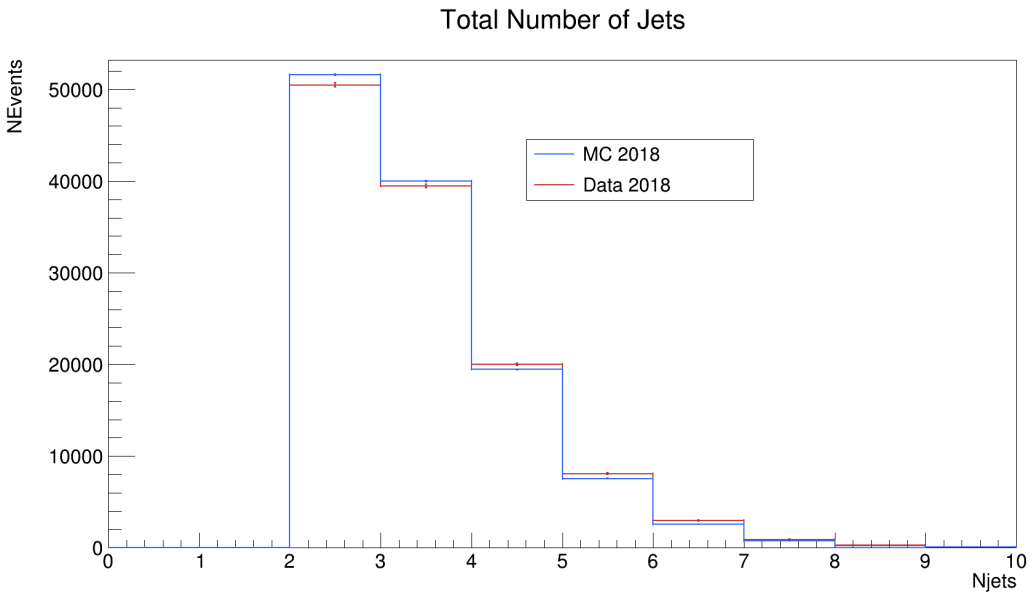

Figure 4.26: Distribution of total identified vertices as a function of the number of jets in an event for 2018 $t\bar{t} \rightarrow e\mu$ Monte Carlo (blue) and data (red).

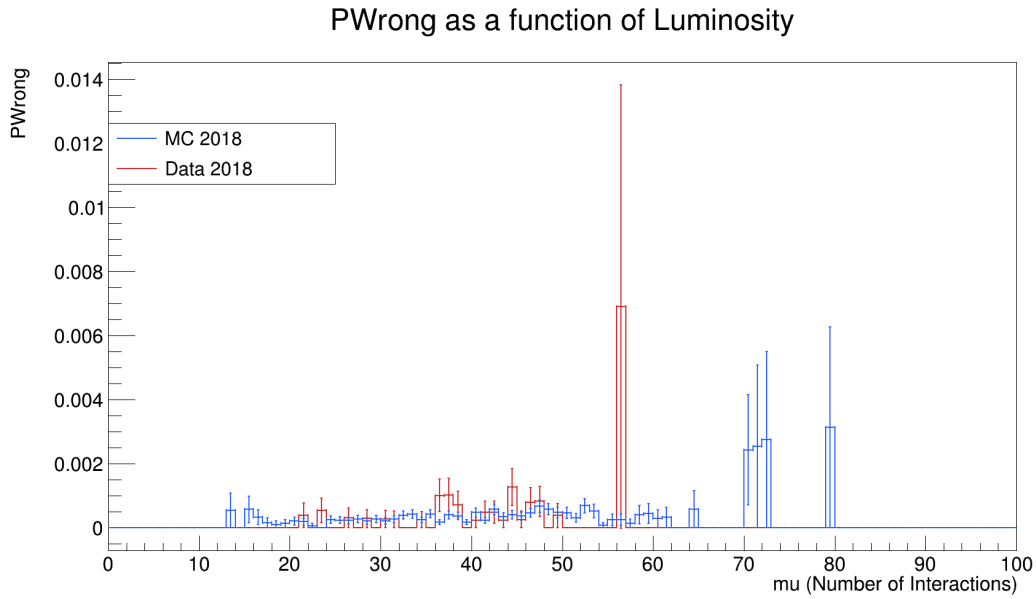

Figure 4.27: Percentage of wrongly identified vertices as a function of mu, the number of vertices in the event, of the event for 2018 $t\bar{t} \rightarrow e\mu$ Monte Carlo (blue) and data (red).

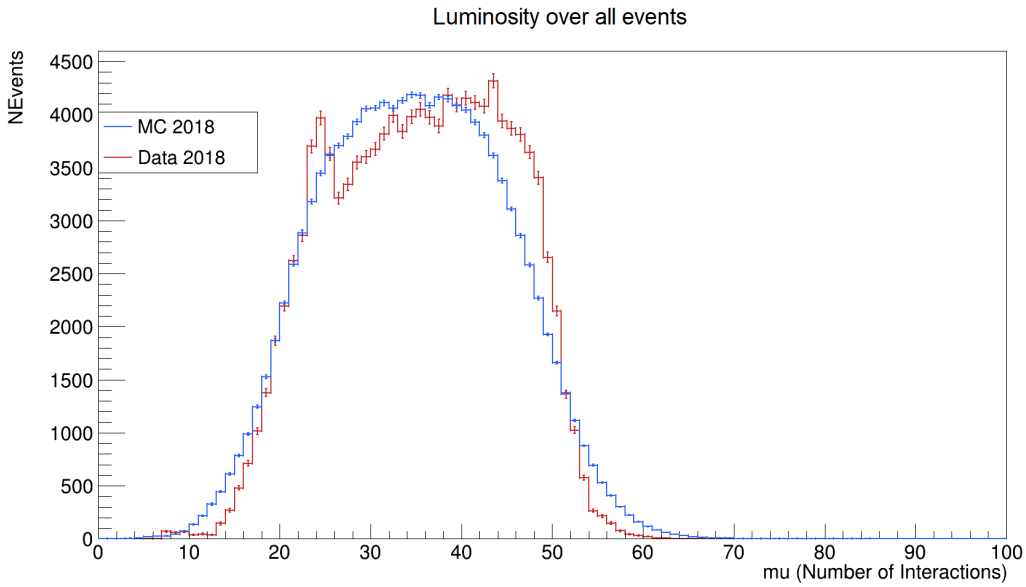

Figure 4.28: Distribution of total vertices as a function of mu, the number of vertices in the event, of the event for 2018 $t\bar{t} \rightarrow e\mu$ Monte Carlo (blue) and data (red).

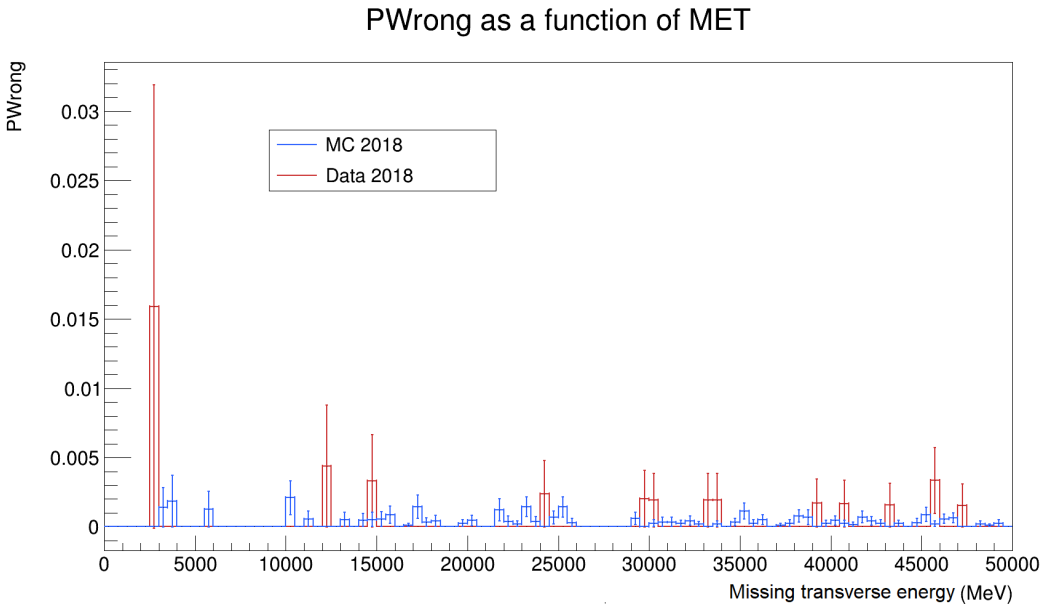

Figure 4.29: Percentage of wrongly identified vertices as a function of the Missing Transverse Energy of the event for 2018 $t\bar{t} \rightarrow e\mu$ Monte Carlo (blue) and data (red).

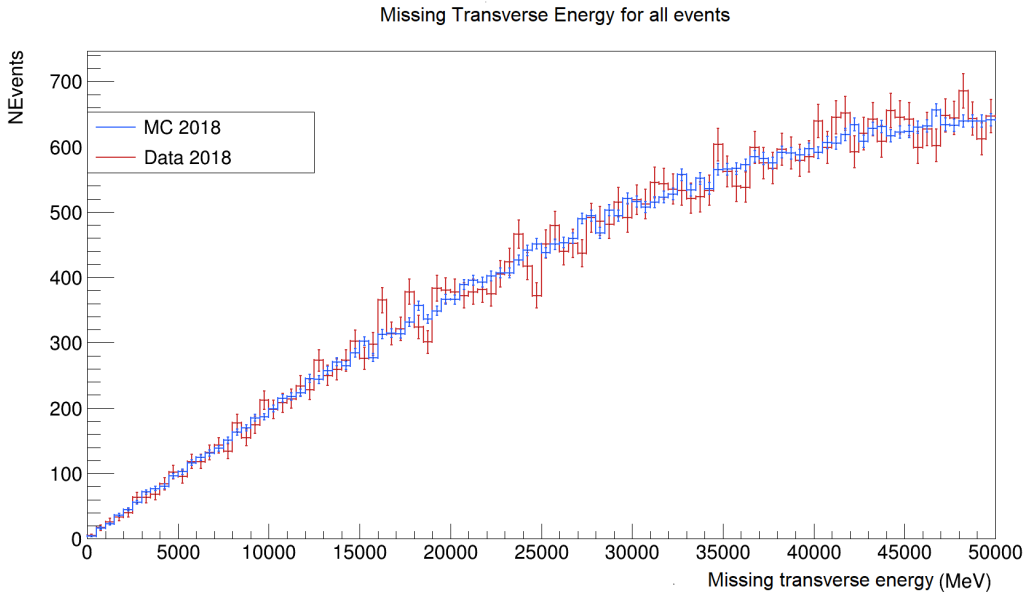

Figure 4.30: Distribution of total identified vertices as a function of the Missing Transverse Energy of the event for 2018 $t\bar{t} \rightarrow e\mu$ Monte Carlo (blue) and data (red).

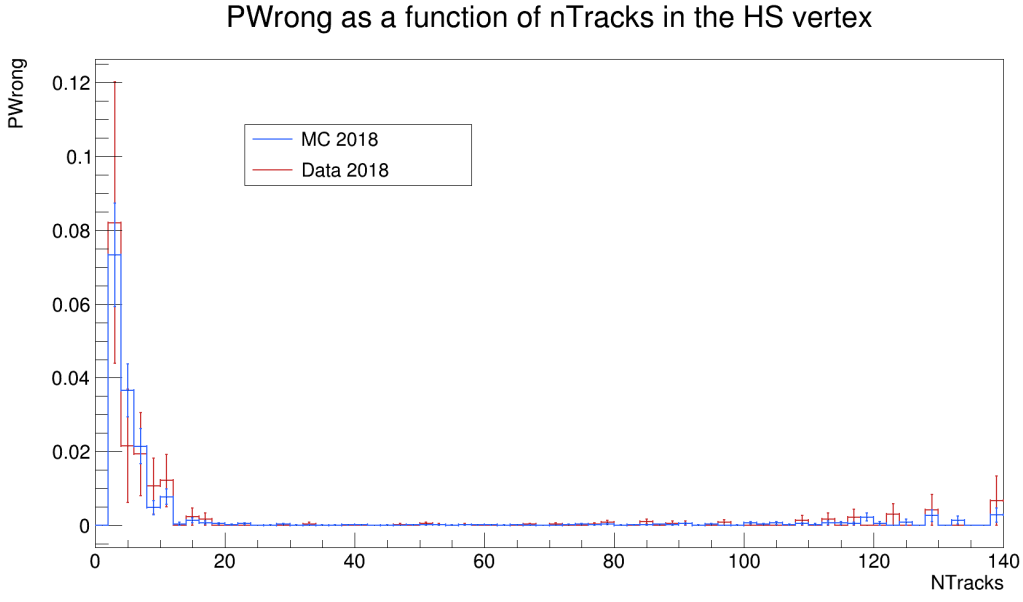

Figure 4.31: Percentage of wrongly identified vertices as a function of the number of tracks in the HS vertex for 2018 $t\bar{t} \rightarrow e\mu$ Monte Carlo (blue) and data (red).

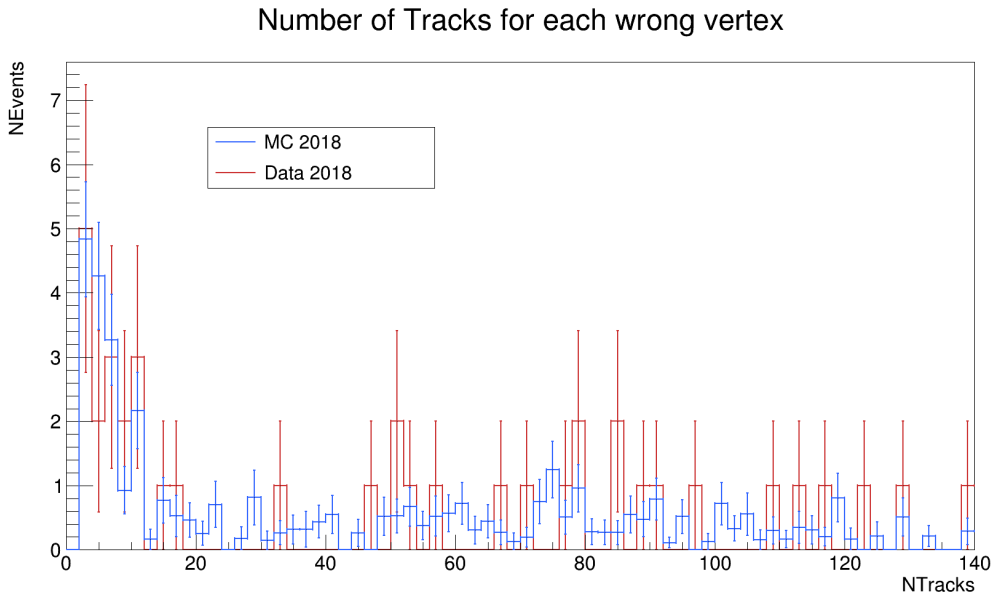

Figure 4.32: Distribution of wrongly identified vertices as a function of the number of tracks in an event for 2018 $t\bar{t} \rightarrow e\mu$ Monte Carlo (blue) and data (red).

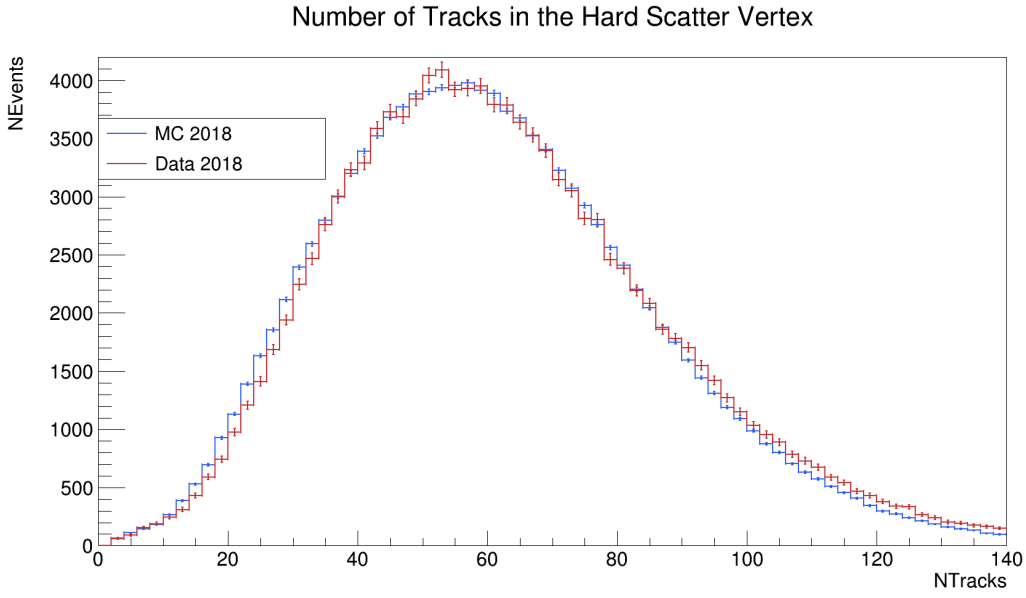

Figure 4.33: Distribution of correctly identified vertices as a function of the number of tracks in an event for 2018 $t\bar{t} \rightarrow e\mu$ Monte Carlo (blue) and data (red).

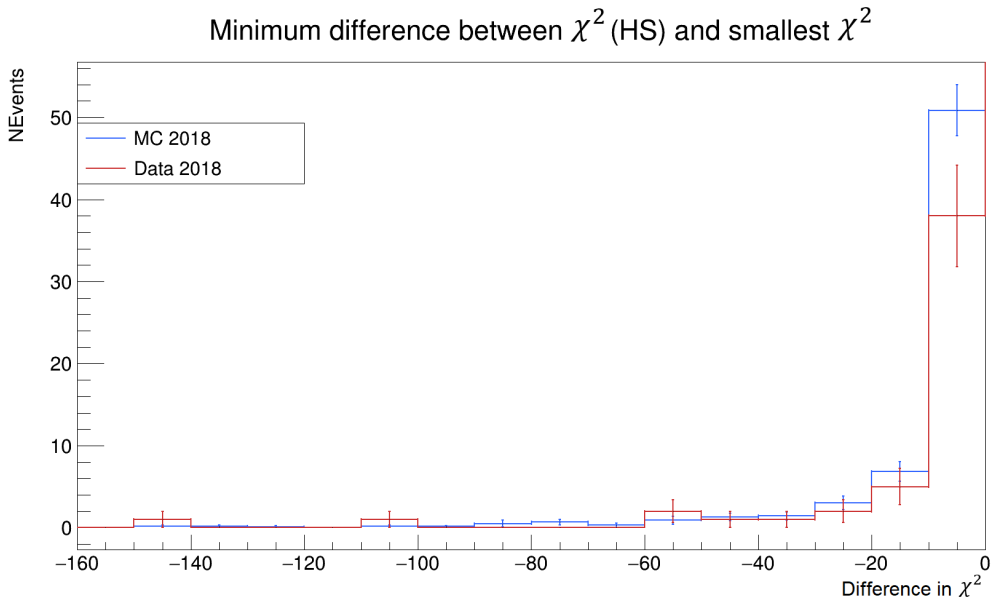

Figure 4.34: The difference between the χ^2 for the correct HS vertex and the χ^2 for an incorrectly identified vertex for 2018 $t\bar{t} \rightarrow e\mu$ Monte Carlo (blue) and data (red).

$t\bar{t}$ Monte Carlo. However, the statistics of the $t\bar{t}$ are low compared to that of the Z^0 decay channels, given the low number of incorrectly identified Hard Scatter vertices. As such, dependences upon luminosity, MET and jets are difficult to discern.

In the Z^0 decay channels, there is a sizeable discrepancy between data and Monte Carlo. In both cases, the Monte Carlo showed more instances of wrongly identified hard scatter vertices, suggesting that the Monte Carlo for the Z^0 channel could be improved to better represent the data. Both channels show a strong dependence upon the number of tracks in the vertex, the number of primary vertices and the MET, suggesting larger pile-up increases the likelihood of a wrongly identified hard scatter vertex.

The analysis method performed is a useful first estimate, however a further, more accurate study is needed in order to confirm the findings. It is possible that the discrepancy between Monte Carlo and data in the Z^0 decay channels and the large difference between the value of PWrong_{Z^0} and $\text{PWrong}_{t\bar{t}}$ is in part due to inaccuracy in the analysis technique. This discrepancy between MC and data is shown by figures 4.13 and 4.23 for $Z^0 \rightarrow ee$ and $Z^0 \rightarrow \mu\mu$. This discrepancy between MC and data should be investigated further as they might explain further the results seen here. The analysis technique might be more favourable to the $t\bar{t}$ process and unfavourable to the Z^0 decay. In

order to validate the results, an alternative method was developed using "vertex fitting machinery" developed at ATLAS [80] which can be used to calculate PWrong for Z^0 decay channels and the $t\bar{t}$ channel and compare the results.

Improvement to this analysis method could be made, including a comparison of the dependence of nJets between the Z^0 decay channels and $t\bar{t}$ where Z^0 events with two or more jets are compared to $t\bar{t}$ events (as $t\bar{t}$ always have two or more jets). This will allow an analysis with more equal footing.

4.6 Validating results using Vertex Fitting Machinery

4.6.1 Introduction

In order to validate the results obtained from this first analysis of HS vertex efficiency, another method of analysis must be performed. In this case, the vertex fitting machinery will be used. The vertex fitting machinery calculates a fitted vertex using information from the muon pair tracks. This can then be used to compare to the measured vertices and decide the closest by calculating a χ^2. This method is more precise than the previously outlined method due to the accuracy of the vertex fitting. It does, however, take much more computing power and therefore more time to process. If the results of this new method agree well with the previously outlined analysis method, it can be concluded that the results of the previous method are valid.

4.6.2 Selection

The $Z^0 \rightarrow \mu\mu$ decay was used as the signal for this analysis method with centre-of-mass energy of 13 TeV. Only $Z^0 \rightarrow \mu\mu$ was used in this analysis as an initial test, to test the method against the estimator method and in the interest of time for this qualification task. Work beyond the qualification task could look to compare both the $Z^0 \rightarrow ee$ and $t\bar{t}$ signals also.

Events were selected with opposite sign leptons, tight muon quality and with a reconstructed Z^0 mass within 85-95 GeV, the same as in 4.3 . AOD 2018 MC was used for the analysis. As AOD contains all muons, unlike the DAODs used in the estimator method, cuts needed to be applied in order to include only isolated muons. This was done by testing the effect on background reduction of three different variables: isolation, muon quality and transverse momentum of the decay products ($\mu\mu$).

Isolation is a technique used to 'isolate' the lepton of interest from other leptons. This is done by measuring lepton activity around the lepton of interest, and discarding events with neighbouring lepton activity exceeding the chosen isolation working point. Isolation was calculated in this study as $\frac{topoetcone20}{p_T}$, where topoetcone20 is the sum of transverse energy of the topological-clusters in a cone where $\sqrt{\Delta\eta^2+\Delta\phi^2}=0.2$ (η is the pseudorapidity and ψ is the angle defining the cone).

Muon quality is a measure of the accuracy at which a muon is identified, taking into account many different factors such as track reconstruction, purity, efficiency and momentum resolution. The standard Tight_FixedRad working point is used which is $\frac{topoetcone20}{p_T} < 0.15$.

Applying a cut on transverse momentum requires looking at the momentum distribution for both the signal and background processes in MC and aiming to observe a transverse momentum region where background is high and signal is low, this region could then be removed from the data sample.

It was found that applying a tight cut on muon quality provided the best background reduction, with cuts on isolation and transverse momentum of the decay products ($\mu\mu$) having little effect on background reduction as shown in figures 4.35, 4.36 and 4.37. Figure 4.35 shows a large decrease in the background events (left hand peak) when applying the tight muon quality cut, with very little removal of the signal events (right hand peak). Figure 4.36 shows that applying a cut on isolation isn't feasible as the majority of background events are where the majority of signal also is. Putting a cut that would remove background would also remove too much signal. Figure 4.37 shows a similar problem with having a cut on transverse momentum, where any p_T cut would remove too much signal.

4.6.3 Strategy

This method follows the estimator method reasonably closeley, but uses the vertex fitting machinery, using the TrkToLeptonPVTool package [80], to calculate a 'fitted vertex' for each set of muon tracks. This fitted vertex is then used to calculate a χ^2, defined below, for each measured vertex in the data set. The vertex associated with the lowest χ^2 is considered the HS vertex. If the vertex associated with the lowest χ^2 is not the HS vertex as calculated with the squared sum p_t, this is considered a wrongly identified vertex. The percentage of total events with wrongly identified vertices is then calculated.

From this, the results from this algorithm are compared to the first HS selection technique

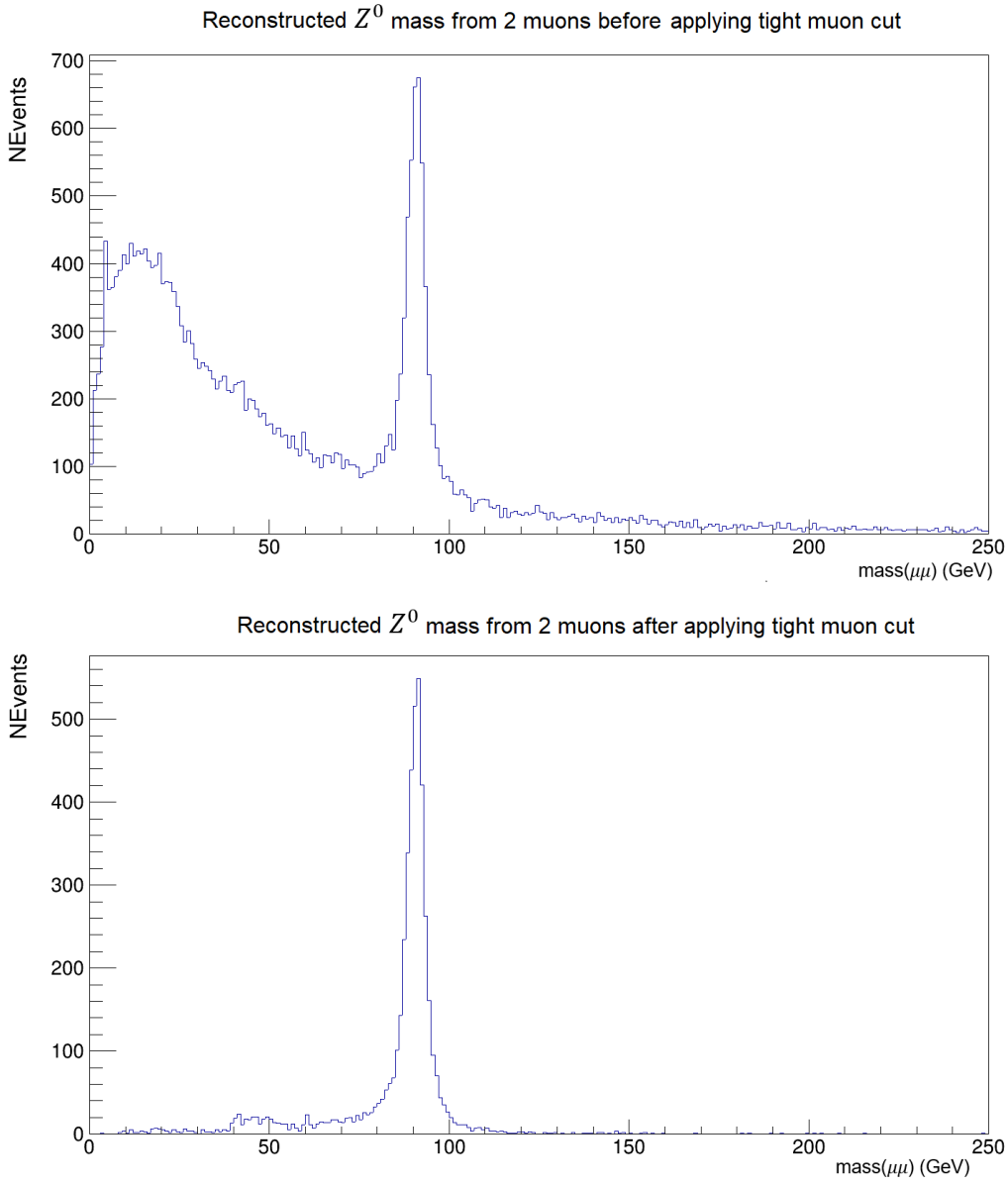

Figure 4.35: Comparison of the effect on the mass distribution of Z^0 before (above) and after (below) applying tight muon cut to events using $Z^0 \to \mu\mu$ sample.

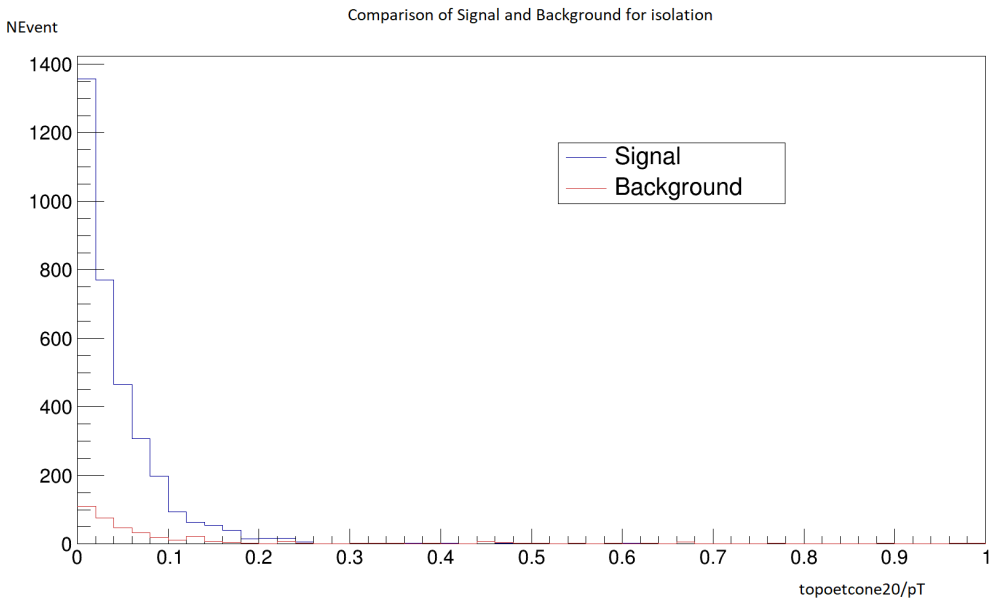

Figure 4.36: Isolation distribution for signal (those events with reconstructed mass between 85-95 GeV) (blue) and background (those events with reconstructed mass of 50-75 GeV) (red) using $Z^0 \to \mu\mu$ MC.

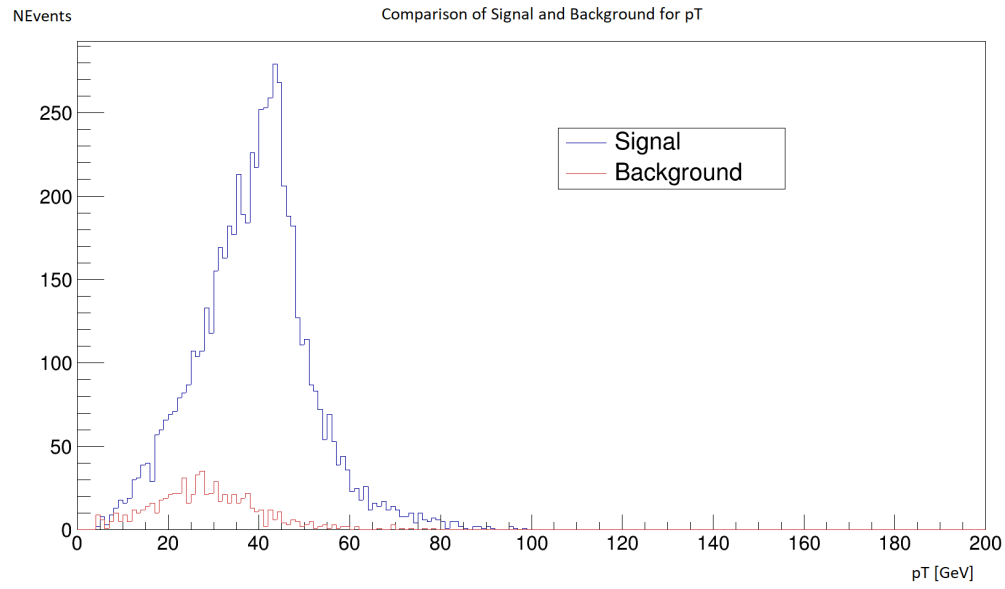

Figure 4.37: Transverse momentum distribution for signal (those events with reconstructed mass between 85-95 GeV) (blue) and background (those events with reconstructed mass of 50-75 GeV) (red) using $Z^0 \to \mu\mu$ MC.

outlined previously in section 4.3. Given the constraints of the vertex fitting machinery, only $Z^0 \to \mu\mu$ MC events are analysed. An agreement in PWrong for $Z^0 \to \mu\mu$ for both analysis techniques would suggest the results for all decay channels for the initial analysis technique were valid. As in the estimator analysis method, only events whose first primary vertex (the assumed Hard Scatter vertex) have nTracks greater or equal to 5 are considered. Within these events, only primary vertices with nTracks greater than or equal to 5 are considered for comparison to the fitted vertex.

The vertex fitting method allowed errors to be accessed from covariance matrices, therefore for this method χ^2 is calculated as:

$$V = V^{PV} + V^{FV} \qquad \chi^2 = \sum_{\substack{i=1,2,3 \\ j=1,2,3}} (\vec{x}_1 - \vec{x}_2)_i V_{ij}^{-1} (\vec{x}_1 - \vec{x}_2)_j, \tag{4.4}$$

where V^{PV} and V^{FV} are the covariance matrices for the primary vertex and the fitted vertex respectively. $\vec{x}_1$ and $\vec{x}_2$ are the vector positions of the muon tracks of the fitted vertex and primary vertex respectively. i and j correspond to the x,y,z coordinates of the vector (i.e. $x = 1, y = 2, z = 3$).

The χ^2 between the fitted vertex and every stored primary vertex is then calculated, and the vertex with the smallest χ^2 is recorded. If this vertex is not the primary vertex with the highest $\sum p_T^2$, the weight of the event is added to a counter. The total of the weighted wrong events is then used to calculate a percentage of the total weighted events, *PWrong*, in the same way as in equation 4.3. The uncertainty was, again, estimated in the same way as the estimator method as $\sqrt{\frac{N_{Wrong}}{N_{Tot}^2}}$.

4.6.4 Results

The χ^2 between the assumed HS vertex and the fitted vertex was plotted for each transverse momentum of generated Z^0 range to confirm the expected distribution, seen in the release 21 study, was obtained as shown in Figures 4.38, 4.39, 4.40 and 4.41. The distribution is the same shape for each transverse momentum range, showing consistency in *PWrong* for each range.

PWrong was found to be qualitatively in agreement between the two analysis methods, as detailed in Table 4.2. Figure 4.42 shows the dependence of *PWrong* on the transverse momentum of Z^0 is also the same for both methods, showing further agreement. This suggests that the results

obtained with the estimator method are valid for showing the HS efficiency for isolated events. The uncertainty on the estimator method is seen as smaller due to the higher statistics that were collected using this method. Given the higher CPU power required for the vertex fitting method (due to its more complex analysis process compared to the estimator method), much more time was required to select and analyse events.

Work further to this study could aim to increase the statistics of the vertex fitting method, with improvements to the speed of the vertex fitting machinery. With a similar volume of events it is expected that the vertex fitting method will be more accurate than the estimator method due to the more precise calculation of fitted vertices and access to the covariance matrices that allowed a more accurate calculation of χ^2.

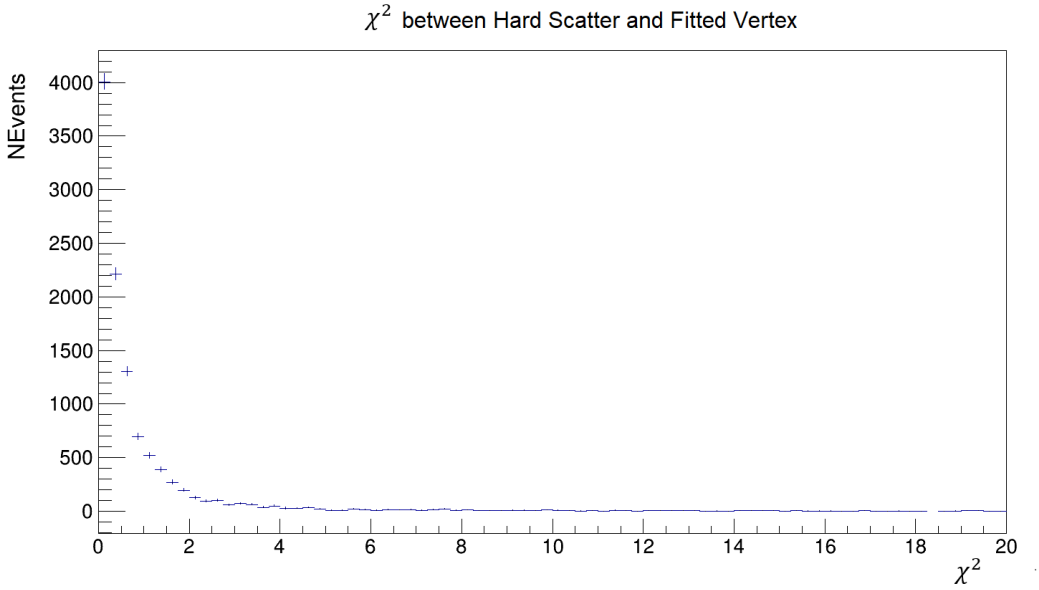

Figure 4.38: χ^2 (HS between fitted vertex) distributions for transverse momentum of generated Z^0 range 0-70 GeV.

4.6.5 Conclusions and Future Work

It was found that the two methods of determining HS selection efficiency agreed, therefore suggesting that full results from the estimator method are valid. As the more detailed vertex fitting method takes longer to analyse data, this allows the use of the conclusions of the quicker estimator method as a benchmark for further study. This further study could include the full analysis using

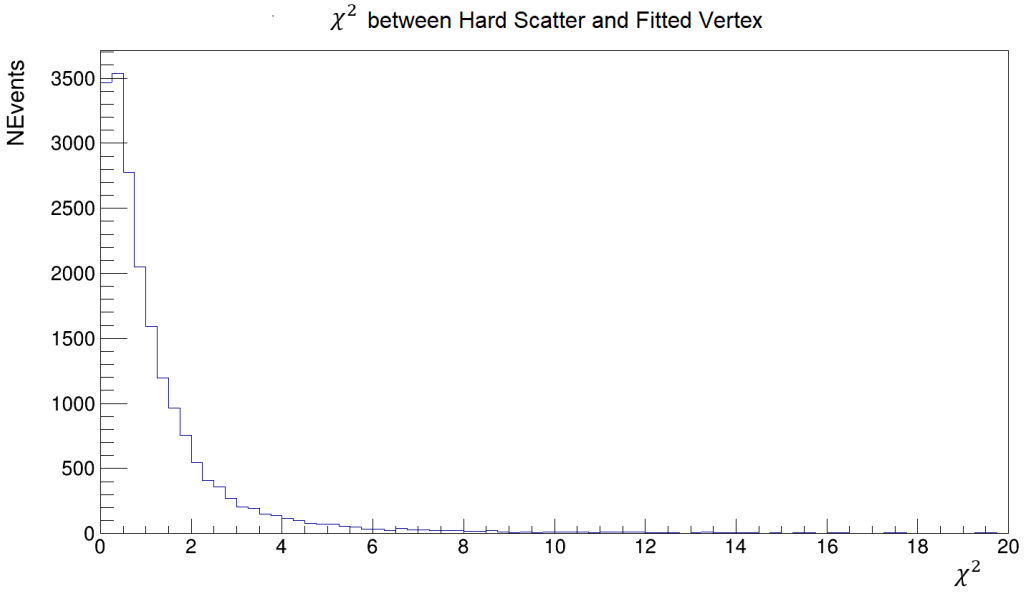

Figure 4.39: χ^2 (HS between fitted vertex) distributions for transverse momentum of generated Z^0 range 70-140 GeV.

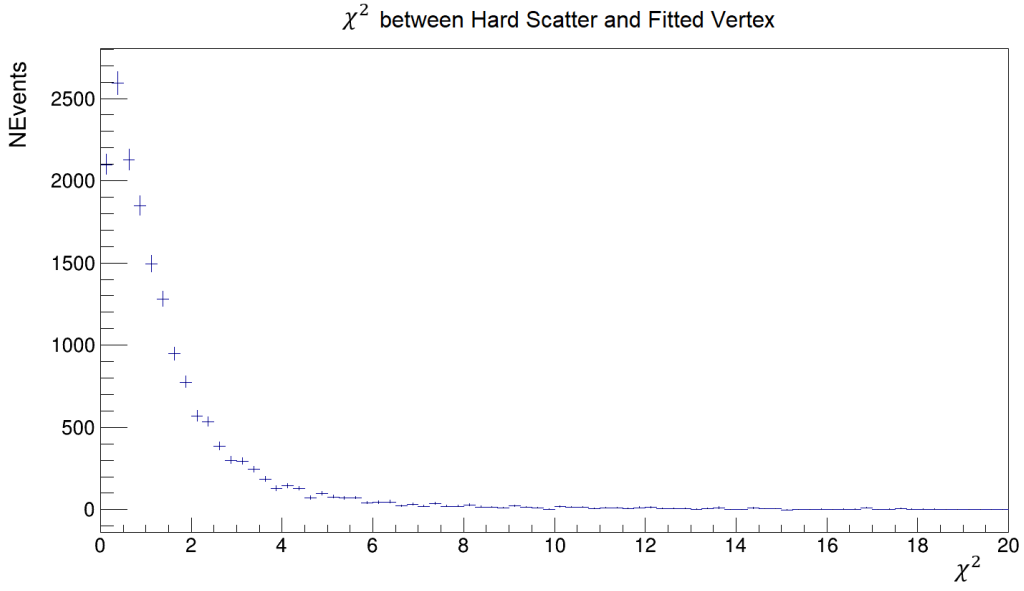

Figure 4.40: χ^2 (HS between fitted vertex) distributions for transverse momentum of generated Z^0 range 140-280 GeV.

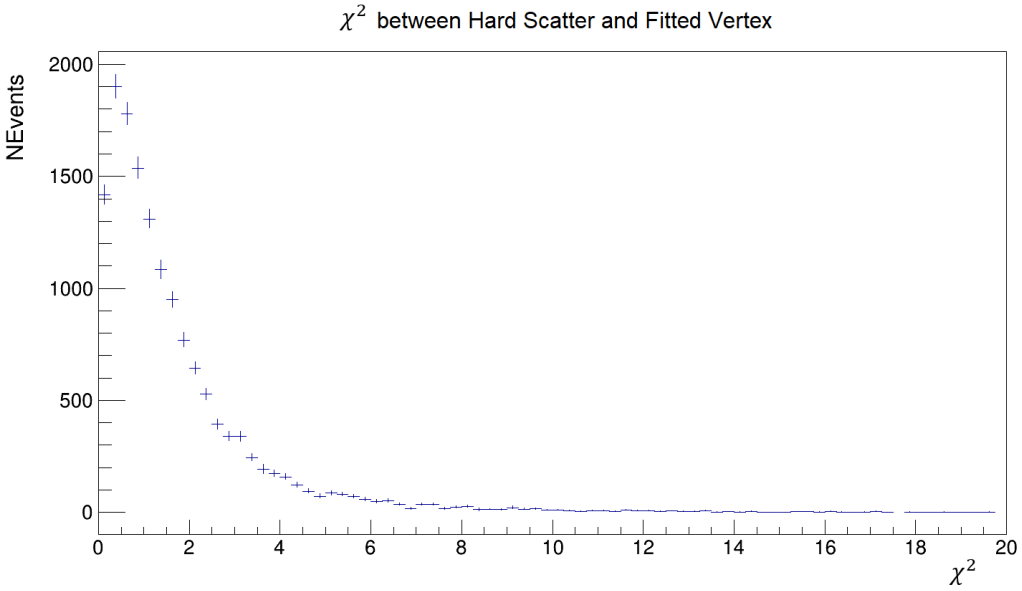

Figure 4.41: χ^2 (HS between fitted vertex) distributions for transverse momentum of generated Z^0 range 280-500 GeV.

	Estimator Method	Vertex Fitting Method
0-70 GeV (DSID 364100)	$0.792 \pm 0.002\%$	$1.057 \pm 0.096\%$
70-140 GeV (DSID 364103)	$0.104 \pm 0.004\%$	$0.136 \pm 0.043\%$
140-280 GeV (DSID 364106, 364107)	$0.050 \pm 0.007\%$	$0.127 \pm 0.027\%$
280-500 GeV (DSID 364109)	$0.028 \pm 0.007\%$	$0.085 \pm 0.024\%$

Table 4.2: Comparison of PWrong for the estimator method and vertex fitting method for $Z^0 \to \mu\mu$ for each transverse momentum of generated Z^0 range

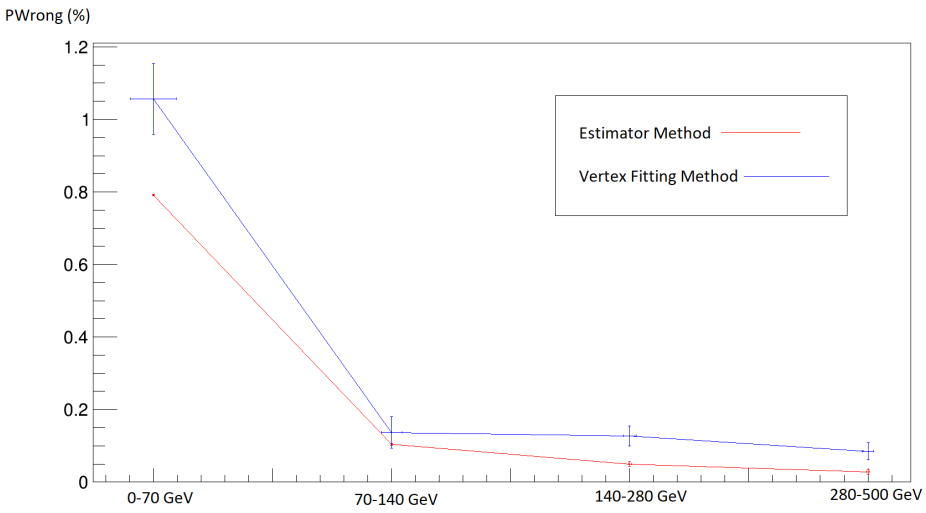

Figure 4.42: Comparison of magnitude of *PWrong* for the estimator and vertex fitting analysis methods for each range of transverse momentum.

the vertex fitting method. This work could include analysing all of the $Z^0 \rightarrow \mu\mu$ MC AODs that are available to improve statistics as well as investigating the dependence of *PWrong* on a variety of variables. Further to this, $Z^0 \rightarrow ee$ and $t\bar{t}$ events should also be investigated using the vertex fitting method. In addition, further study into statistical uncertainty should be done.

As previously discussed, further work into the high magnitude of wrongly identified HS vertices in the Z^0 decay channels should be performed to understand its origin and make recommendations of vertex selection efficiency. This future work should also explore why there is a difference in *PWrong* between MC and data and Z^0 decays and $t\bar{t}$ interactions.

4.7 Analysis for Release 22

As more analysis is ongoing at ATLAS, many analyses are using more recent release, the most commonly used is now release 22. Therefore, it was requested that to repeat the release 21 study for release 22. In order to work within the time constraints of the qualification task, this was only a quick check of the HS selection efficiency using the vertex fitting method.

4.7.1 Analysis Strategy

The code logic of the release 22 analysis follows closely to previous study's method. For this analysis, only muons were considered ($Z^0 \rightarrow \mu\mu$). Two muons were selected, and only those whose first primary vertex (the assumed HS vertex) has a number of tracks greater than or equal to 5, those primary vertices with a number of tracks greater than or equal to 5 and events with reconstructed mass of the two muons was between 85-95 GeV were considered. The fit of the two muon tracks to the assumed HS vertex and each primary vertex that fit the selection criteria was then done with the TrackToBeamTool package [80]. The fit to the assumed HS vertex and every other valid primary vertex was then compared, and those primary vertices that had a better fit to the two muon tracks than the assumed HS vertex were considered 'wrongly identified' HS vertices. χ^2 is calculated for fitted vertex and each primary vertex using position (x) and the covariance matrix (V):

$$\begin{aligned} V &= V^{PV} + V^{FV} \\ \chi^2 &= \sum_{\substack{i=1,2,3 \\ j=1,2,3}} (\vec{x_1} - \vec{x_2})_i V_{ij}^{-1} (\vec{x_1} - \vec{x_2})_j \end{aligned} \tag{4.5}$$

4.7.2 Selection

The same selection as used as in 4.6. The correct selection was confirmed by looking at the reconstructed mass of the two muons to compare to the resonant peak of Z^0 to confirm it was the interaction $Z^0 \rightarrow \mu\mu$ that was being analysed.

4.7.3 Results

It was found that the value of *PWrong* in MC was 0.019% and in data was 0.068% . *PWrong* was found to be much lower in release 22 compared to release 21 (approximately 1 order of magnitude smaller). *PWrong* was found to be higher in data than MC in release 22. This was actually due to poor selection on data, and therefore this was repeated to select properly on data. It was found there was a dependence on the number of tracks in an event, as seen in figure 4.44, when there were more wrongly identified events when the number of tracks was higher.

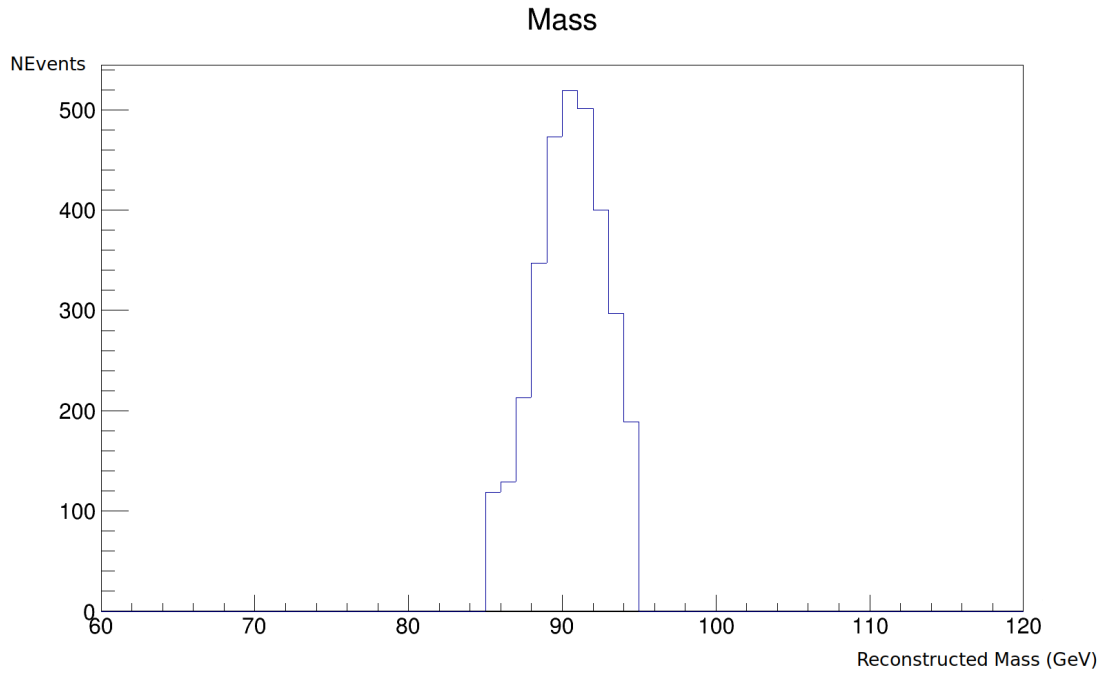

Figure 4.43: The invariant mass distribution of the electron and muon for 2018 $Z^0 \rightarrow \mu\mu$ Monte Carlo (blue) and data (red).

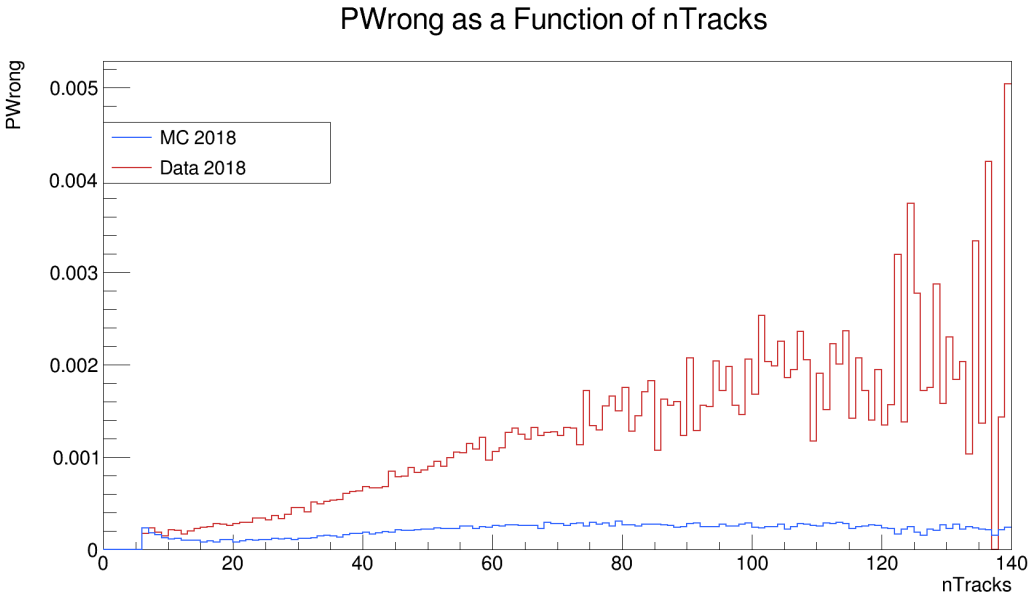

Figure 4.44: Percentage of wrongly identified vertices as a function of the number of tracks in the HS vertex for 2018 $Z^0 \rightarrow \mu\mu$ Monte Carlo (blue) and data (red)

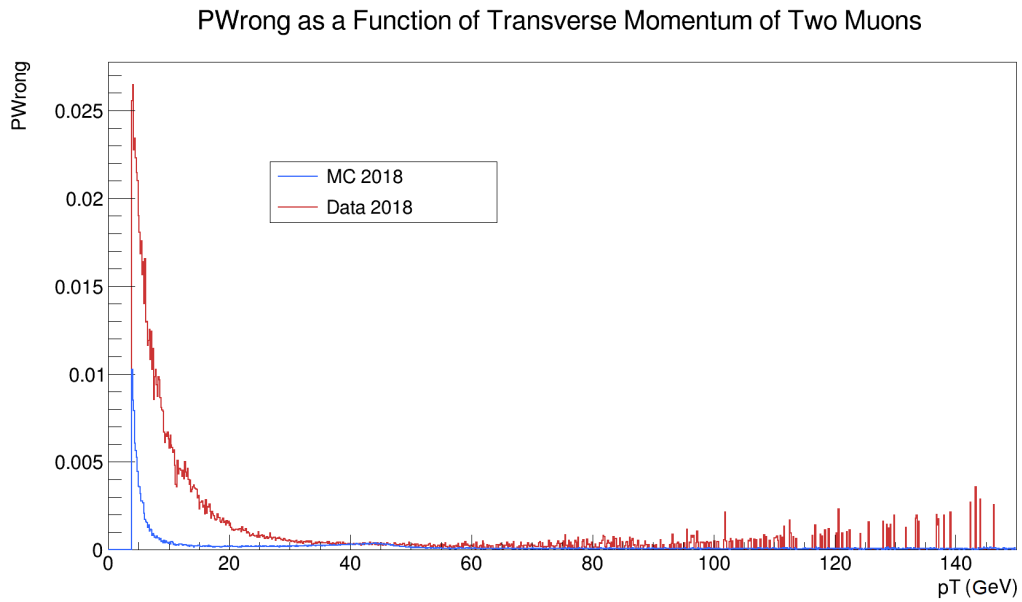

Figure 4.45: Percentage of wrongly identified vertices as a function of p_T in the HS vertex for 2018 $Z^0 \rightarrow \mu\mu$ Monte Carlo (blue) and data (red)

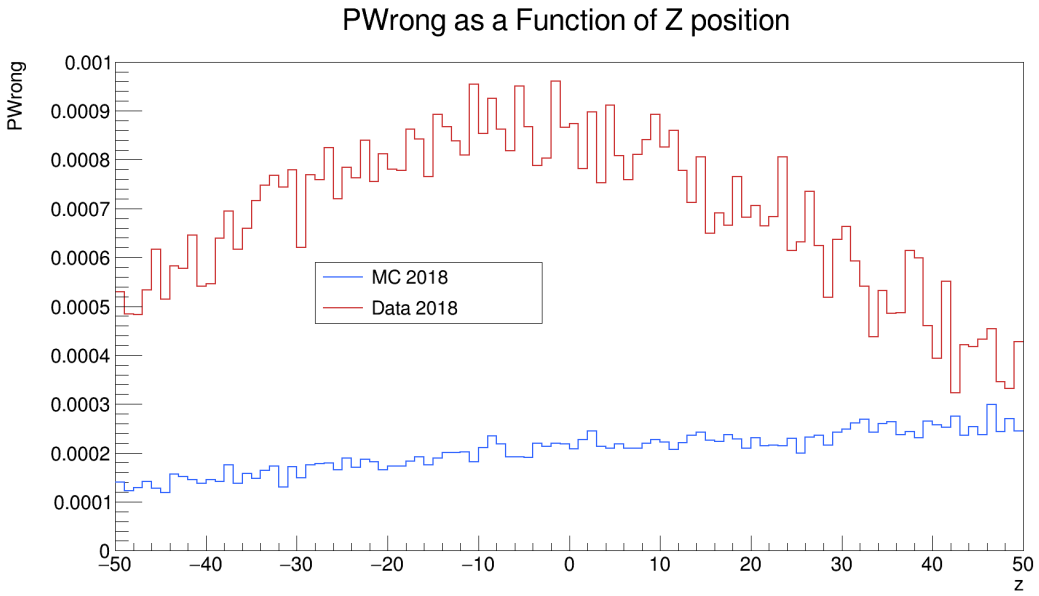

Figure 4.46: Percentage of wrongly identified vertices as a function of the in the HS vertex for 2018 $Z^0 \rightarrow \mu\mu$ Monte Carlo (blue) and data (red)

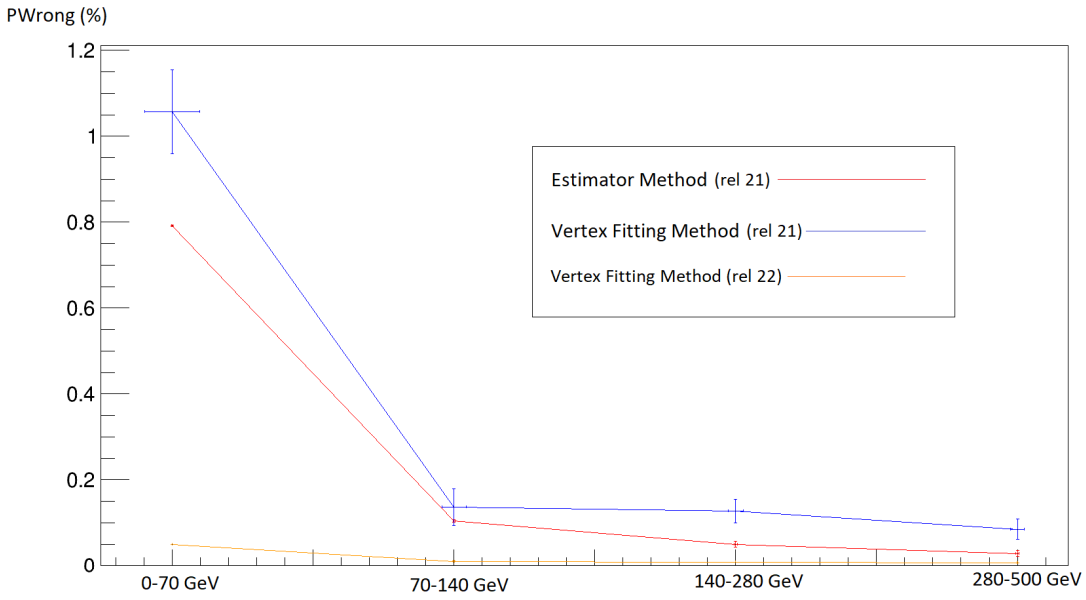

Figure 4.47: Comparison of magnitude of *PWrong* for the estimator and vertex fitting analysis methods for release 21 and the vertex fitting method for release 22 for each range of transverse momentum.

4.7.4 Further Work

All DSIDs for $Z^0 \rightarrow \mu\mu$ (for b-jets and c-jets) can be analysed. The data AOD choice should be checked and appropriate selections made. The $Z^0 \rightarrow ee$ decay channel can be analysed, $t\bar{t}$ decay channel is not feasible with AOD analysis due to the information needed. Other years data can also be studied (not just 2018), including new data from Run 3. Other variable dependencies (nJets etc...) can also be studied.

4.8 Overall Conclusions

It was found that the rate of HS selection inefficiency was relatively high in release 21 for Z^0 decays, although was of an acceptable level in $t\bar{t}$ decays. It was found that the two methods of determining HS selection efficiency; the estimator method and the vertex fitting method agreed, therefore suggesting that full results from the estimator method are valid. As the more detailed vertex fitting method takes longer to analyse data, this allows the use of the conclusions of the quicker estimator method as a benchmark for further study.

Chapter 5

A Test of Lepton Flavour Universality in the Decays of the Top Quark

5.1 Introduction

Section 2 described in detail the motivation for a more precise measurement of the ratio of the branching ratios of leptonic W boson decay. In this analysis, this ratio is between the branching ratios of the W boson decay to the tau lepton and the W boson to the electron. When this analysis started the most precise measurement of this ratio was from LEP around 20 years ago at 1.063 ± 0.027 [13] , in tension with the Standard Model . More recently, CMS has measured this ratio as 0.994 ± 0.021 [22], in agreement with the Standard Model. Further precise measurements of this ratio with an alternative analysis method therefore either validate this measurement, or shows a contesting measurement in disagreement with Standard Model prediction. At its conception, the aim of this analysis was to measure the ratio of Br($W \to \tau\nu$) and Br($W \to e\nu$) , $R(\tau/e)$, with much higher precision than the previous LEP measurement. The recent CMS measurement is in mild tension with the previous LEP measurement. Further measurement by ATLAS allows for validation of either measurement, using high energy events.

The analysis was a joint effort between myself and Guennadi Borissov. In this analysis, the largest contribution of the thesis author is made in the section analysing background events, Section 5.6). Sections 5.5 and 5.7 summarise work largely performed by Guennadi Borissov, my supervisor, and are summarised to be able to describe the analysis in its entirety. All other work is performed jointly between myself and Guennadi.

5.2 Analysis Strategy

The analysis follows the strategy of the previous leptonic lepton flavour universality violation study with top quark decays to either a τ or muon [81]. This study measured the ratio of the branching fractions Br($W \to \tau\nu$) and Br($W \to \mu\nu$) with then world-best precision, resolving the previous 2.7σ deviation from the SM expectation measured by LEP [13].

In this analysis, the decays of the top quark to a τ lepton and electron are used. Leptonic decays ($\tau \to e\nu\bar{\nu}$) are utilised in this analysis, as it is much easier to handle uncertainties in leptonic decays over hadronics decays. In the Standard Model, top quarks decays mainly to the Wb final state (in this study it is assumed 100% of events decay in this way), and by measuring the ratio of branching fractions of top quark to τ and electron we obtain the ratio of the branching fractions Br($W \to \tau\nu$) and Br($W \to e\nu$).

The factor $C(\tau/e)$ is measured which is defined as

$$C(\tau/e) = \left(\frac{Br(W \to \tau\nu \to e\nu\nu\bar{\nu})}{Br(W \to e\nu)}\right)_{\text{data}} / \left(\frac{Br(W \to \tau\nu \to e\nu\nu\bar{\nu})}{Br(W \to e\nu)}\right)_{\text{MC}} \tag{5.1}$$

In simulation the branching ratios of W boson to different leptons are the same as lepton flavour universality is assumed . Therefore, $C(\tau/e)$ matches exactly the parameter of interest $R(\tau/e)$. The result depends on Br($\tau \to e\nu\bar{\nu}$) which has been measured with good precision as $17.82 \pm 0.04\%$ [82]. This value and its associated uncertainty is used in this analysis. Thus, dependence on this branching ratio does not produce a significant impact on the final result.

The $t\bar{t}$ events are used due to their large production cross section (i.e. there are lots of events to analyse) and ease of triggering on (it is easy to select events) . Leptonic decays of both top quarks are used in the analysis. The selection of $t\bar{t}$ events is done by the requirement of at least two b-tagged jets and two leptons of opposite charge. With this selection the 'tag and probe' approach can be used. One lepton (muon or electron) from the $t\bar{t}$ pair is used as the 'tag'. This lepton must have a high p_T (above 27 GeV) and must trigger the selection of the event by a single-lepton triggers. The tag lepton is required to have a high p_T as higher p_T events are less likely to be incorrectly identified as signal. The other lepton in the $t\bar{t}$ pair (electron) is used as the 'probe'. It is allowed to have a much lower p_T and is used to measure $R(\tau/e)$.

Leptons are categorised as follows:

- **prompt (top)** : leptons that come from the decay of a top quark to a W boson to a lepton

- **prompt (non-top)**: leptons that come from Z^0 and W bosons that did not decay from a top quark
- **tau**: leptons that come from the intermediate decay of a W boson to a τ lepton with $\tau \rightarrow e\nu_\tau\bar{\nu}_e$
- **fake**: leptons from every other origin, misidentified as signal

In order to distinguish between electrons coming from prompt decays (immediately from the decay of a W boson) and intermediate decays (from the decay of a W boson to a τ with the following decay $\tau \rightarrow e\nu\bar{\nu}$), the difference in the electron transverse momentum (p_T) spectra and the displacement of intermediate decays from the primary vertex (due to the lifetime of the τ) are used. The quantity reflecting the displacement of the vertex of τ decay from the primary vertex is the electron impact parameter, d_0, which is defined as the distance of closest approach of the extrapolated track to the beamline in the plane perpendicular to the beamline.

The main sources of background in the analysis are from Drell-Yan [83] processes and fakes. Drell-Yan processes are processes where a Z^0 boson is created from the high energy annihilation of a quark and anti-quark, and the Z^0 subsequently decays into two oppositely charged leptons. Fakes are leptons that come from any other process other than the identified background events that are not signal but are misidentified as such. In this analysis, the majority of leptons come from hadron decays (b and c mesons) and photon conversion. These processes will be explained in further detail in 5.6.2

The estimation of Drell-Yan contribution is determined by the calculation of a scale factor from the fit of the data and MC resonant mass of the Z^0 boson. The contribution of fakes is determined by the calculation of scale factors based on the origin of same sign (SS) leptons in 3 p_T bins. The study of fakes in this analysis differs to that of the previous ATLAS analysis using the same method to measure $R(\tau/\mu)$, due to the difference in origin of fakes for the electron channel compared to the muon channel. Due to Bremsstrahlung effects (electromagnetic radiation produced by the deceleration of a charged particle when deflected by another charged particle) in the electron channel, fakes are made up of hadronic decays as well as a significant proportion of photon conversion (pair production from the interaction of a high energy photon with the electromagnetic field of an atom). In the previous analysis, fakes were overall only made up by hadronic decays.

The value of $R(\tau/e)$ is extracted from the two-dimensional fit of the impact parameter, d_0 and transverse momenta, p_T. A constant scaling factor, $C(t\bar{t})$ (a normalisation parameter, the ratio of prompt and intermediate electrons to the number of predicted electrons using the theoretical cross sections for the $t\bar{t}$ and wt processes) , is applied to prompt electrons and $\tau \to e$ from $t\bar{t}$ and Wt events. It is a floating parameter in the fit together with $C(\tau/e)$ (the ratio of the number of probe electrons in data and MC) .The events with μ (tag) and e (probe), and with e (tag) and e (probe) are analysed separately. These channels are denoted as μe and ee.

5.3 Data and Simulation Samples

The analysis is performed on proton-proton (pp) collisions at $\sqrt{s} = 13$ TeV for Run 2, years 2015-2018. Events fulfil the standard data quality requirements specified in the good run lists (GRL). The GRL are provided by ATLAS, which are lists of data where the ATLAS detector is fully operational. The corresponding GRL files and integrated luminosity of the selected samples are provided in Appendix D in Table D.1. Events are selected using TOPQ1 derivation in the main `Physics` stream. This derivation contains all events that have at least one lepton with $p_T > 20$ GeV.

The main signal (both $t\bar{t}$ and Wt) and background samples were processed through the full ATLAS detector simulation based on GEANT4 [84]. Studies on MC generator systematics were done with ATLAS Fast (AF) simulation samples as well as full simulation samples which will be described in more detail in Section 5.6. The full list of the datasets used in the analysis is given in Appendix A. The normalisation cross-sections of all samples is specified in the file is given in Appendix A for the signal samples.

Data and simulation samples were analysed using the AnalysisBase-21.2.268 [57] software framework. The ntuples produced by AnalysisBase were analysed using the custom `ttau` package.

5.3.1 Monte Carlo Generators

5.3.2 Signal Simulation Samples

Leptonic $t\bar{t}$ and Wt (whose final states are W bosons decaying to e, or decaying to τ and then into e) were used as signal in this analysis. This selection allows for a very pure $t\bar{t}$ selection with a small contamination from other processes. The full technical explanation of the samples is found

in Appendix A. The text describing the simulation samples in the appendix is provided by the ATLAS collaboration [85]. Any further details for the samples used in this analysis are described below.

5.3.2.1 $t\bar{t}$

Several additional samples are produced with both ATLAS FAST and the full simulation to estimate the systematic uncertainty due to the choice of MC. These samples are described in more detail in Section 5.6.

In all cases the di-lepton sample is used for the prompt and tau leptons and the non-all-hadronic sample is used for the fakes. Hence, it is ensured that there is no overlap between the samples and that the available MC statistics is maximised.

5.3.3 Background Simulation Samples

The background for this analysis comes from two main sources: high-p_T processes producing two prompt leptons and processes that are misidentified as signal. The first mainly comes from Drell-Yann processes and the second from 'fakes'. The full technical explanation of the background samples is found in Appendix A. The text describing the simulation samples in the appendix is provided by the ATLAS collaboration [85].

5.3.4 Fakes

Fake leptons, as described further in Section 5.4, are events which are misidentified as signal.

5.3.4.1 $t\bar{t}$ and W t-channel single top

The main contribution to the events with at least one fake lepton comes from $t\bar{t}$ or Wt production where only one of the leptons comes from $W \to l\nu$ decay. The simulation of these events was done in the same way as for signal $t\bar{t}$ and Wt-channel single top.

5.3.4.2 s and t-channel single top

Both s- and t-channel single top production can also produce di-lepton events with at least one fake lepton. The full technical explanation the simulation of this sample is found in Appendix A.

5.4 Object and Event Selection

The following describes the definitions used throughout the analysis for various particles and procedures. The selections applied to the events in this analysis are then also described.

5.4.1 Object Definitions

Baseline Muons All of the muons used for analysis must meet the baseline criteria to be used. Baseline muons are required to pass the PFlowTight_FixedRad isolation [77] and medium quality criteria [78]. PFlowTight_FixedRad isolation is defined as $\frac{\text{ptvarcone30\_TightTTVA\_pt500 + 0.4 neflowisol20}}{p_T} <$ 0.045 for $p_T < 50$ GeV and where ptvarcone30 is the sum of transverse momentum of the topological-clusters in a cone where $\sqrt{\Delta\eta^2 + \Delta\phi^2} = 0.3$ (η is the pseudorapidity and ψ is the angle defining the cone) for muons with $pT > 0.5$ GeV and with loose vertex association. ptvarcone has a maximum cone size, to stop it blowing up at low pT, for ptvarcone30 at larger values of p_T ptvarcone30 has a smaller cone size than ptcone30. ptvarcone30 deviates from ptcone30 above 33.3 GeV. newflowisol20 is a correction for core energy subtraction. $\frac{\text{ptcone20\_TightTTVA\_pt500 + 0.4 neflowisol20}}{pT} < 0.045$ for $p_T > 50GeV$ where ptcone20 is the sum of transverse momentum of the topological-clusters in a cone where $\sqrt{\Delta\eta^2 + \Delta\phi^2} = 0.2$ (η is the pseudorapidity and ψ is the angle defining the cone) for muons with $p_T > 0.5$ GeV and with loose vertex association. newflowisol20 is a correction for core energy subtraction.

Baseline Electrons All of the electrons used for analysis must meet the baseline criteria to be used. Baseline electrons are required to pass FixedCutTight isolation requirement and the tight log-likelihood criteria [77]. FixedCutTight is defined such that topoetcone40 $< 0.022pT + 2.45$ GeV (where topoetcone40 is the sum of transverse energy of the topological-clusters in a cone where $\sqrt{\Delta\eta^2 + \Delta\phi^2} = 0.4$ (η is the pseudorapidity and ψ is the angle defining the cone)) and $\frac{\text{ptcone20}}{pT} < 0.05$ where where ptcone20 is the sum of transverse momentum of the topological-clusters in a cone where $\sqrt{\Delta\eta^2 + \Delta\phi^2} = 0.2$.

Tag Muons: Tag muons are required to satisfy the normal baseline criteria [79], be trigger matched, and have $|\eta| < 2.5$. Additional requirement is placed on their p_T to put them above the trigger threshold. To reduce pile-up and remove cosmics and extremely badly reconstructed muons it is required that the distance to the primary vertex along the z axis, z_0, is $|z_0 \sin\theta| < 0.3$ mm. Here θ is the polar angle of the track. It is also required that $|d_0| < 0.5$ mm. For consistency

across years the p_T is required to be greater than 27.3 GeV.

Tag Electrons: Tag electrons are required to satisfy the normal baseline criteria [79], be trigger matched, and have $|\eta| < 2.47$. Additional requirement is placed on their p_T to put them above the trigger thresholds. Electrons in the crack region, $1.37 < |\eta| < 1.52$, are excluded. To reduce pile-up and extremely badly reconstructed electrons it is required that $|z_0 \sin\theta| < 0.3$ mm and $|d_0| < 0.5$ mm. For consistency across years the p_T is required to be greater than 27 GeV.

Probe Electrons: Probe electrons are required to satisfy the normal baseline criteria [79]. As well as this, tag electrons must have $p_T > 7$ GeV and $|eta| < 2.47$. Electrons in the crack region, $1.37 < |\eta| < 1.52$, are excluded. It is also required that $|z_0 \sin\theta| < 0.3$ mm and $|d_0| < 0.5$ mm to avoid poorly reconstructed events near the beamline.

Jets: Jets from the jet collection AntiKt4EMPFlowJets_BTagging201903 which is defined as having an Anti-Kt with R=0.4 and with the b-Tagging trained on PFlow jets[79] are used. The jets in Monte Carlo are smeared to correct for differences in the jet resolution between data and Monte Carlo. For jets with $25 < p_T < 60$ GeV and $|\eta| < 2.4$ pile-up suppression cuts in the form of $JVT > 0.59$ are applied. Only jets with $p_T > 25$ GeV are considered in the analysis.

B-tagging: To classify jets as containing a b-hadron the 70% efficiency working point of the DL1r algorithm (FixedCutBEff_70) is used [79].

Overlap Removal: This is performed using the standard methods provided by the top reconstruction group [79].

5.4.1.1 Event Selection

This selection aims to given a very pure sample of $t\bar{t}$ events while also not being very dependent on the probe lepton spectra. This selection is:

- Exactly two opposite-charge leptons, one satisfying the tag and the second the probe conditions.
- For *ee* events, if both electrons satisfy the tag criteria the event is analysed twice and each electron is considered in turn as the tag or probe.
- At least two b-tagged jets
- The invariant mass of the tag and probe leptons must exceed 15 GeV to exclude low mass resonances

- Events with a resonant mass of $|m_{ee} - m_Z| < 5$ GeV are excluded (such that a symmetric cut of events about the Z^0 resonant peak is taken), to exclude a large amount of events that could come from Z^0 production.

5.5 Calibration and Tuning of Monte Carlo Signal

5.5.1 Weights applied to MC events

Monte Carlo events need to be weighted in order to match data. The weight applied to each Monte Carlo event is computed as the product of the following factors:

- weight, MC – weight produced by the MC generators
- weight, pileup – weight intended to make the pileup distribution in MC to be consistent with that in data. This is unique for each year (2015+2016, 2017 and 2018), and is based on the observed pile-up for each year.
- weight, modified lepton scale factor – modified leptons scale factor. This is modified due to the scale factor provided by the top group is computed assuming that trigger conditions are applied to both leptons in an event. In this analysis, this is not the case, only one lepton in the 'tag and probe' method needs to be above the trigger threshold. Therefore, this weight is modified to be the same as the normal weight scale factor but without the scale factor due to the trigger. This scale factor due to the trigger is biased for low p_T leptons.
- weight, tag trigger scale factor – trigger scale factor on tag lepton. This is only applied to the tag lepton, due to the trigger threshold not needing to be met for the probe lepton.
- weight, b-tagging scale factor – scale factor correcting the b-tagging efficiency
- weight, jet vertex tagging – scale factor correcting the distribution of the JVT variable

All factors are provided by the top reconstruction group, except for the modified lepton scale factor and tag trigger scale factor which were modified from factors provided by the top group to suit the analysis better.

5.5.2 Electron efficiency calibration

All the scale factors recommended by the computing performance groups at ATLAS to correct the efficiency of electron and muon reconstruction and identification are applied. A dedicated study of $Z^0 \to e^+e^-$ decays was also performed to verify that the electron efficiency is correctly reproduced in simulation. Special attention in this study is paid to the electron efficiency as a function of p_T, which impacts significantly the results of the measurement of $R(\tau/e)$. This is because the analysis uses differences in the p_T distributions of leptons to separate prompt and intermediate events. Therefore, the study is sensitive to the variation of lepton efficiency as a function of p_T and not to its absolute normalisation. This consideration determines the strategy in the calibration of lepton identification and reconstruction efficiency. The relative agreement between data and simulation of this global efficiency as a function of lepton p_T is determined using $Z^0 \to l^+l^-$ events.

The selection of events for the study of electron efficiency is the same as for the main analysis except the following modifications:

- require two electrons of the opposite charge;
- instead of rejecting events with $|m_{ee} - m_Z| < 5$ GeV, use only the events with $|m_{ee} - m_Z| < 10$ GeV ;
- instead of requiring at least two b-tagged jets, select events with at least two jets and no b-tagged jets.

The electron selection efficiency depends on the electron isolation, which in turn depends on the number of particles in the event. To keep the track multiplicity around the electron similar to that of the main analysis at least two jets are required. These jets are required to not be b-tagged such that the contribution of $t\bar{t}$ events is reduced.

The study is performed independently for each year of data taking. Using the specified above selections it was found that there were 1.07×10^6 events in 2015-2016, 1.39×10^6 events in 2017, and 1.81×10^6 events in 2018. The details on the composition of the selected events in the 2018 MC are given in Table 5.1. The composition in the other years is similar. In this table, the entry 'Other' includes the decay $Z^0 \to \tau^+\tau^-$. As expected, the main contribution to the selected sample comes from $Z^0 \to e^+e^-$ events while the contribution from other processes is just about 1.7%. The classification of probe electrons into four different categories in the 2018 MC is shown in Table

5.2. These tables confirm a clean selection of $Z^0 \to e^+e^-$ process. Hence, possible systematic uncertainties due to background electrons produce a negligible impact on the results of this study.

Table 5.1: Composition of the events selected for p_T calibration in the 2018 MC.

$Z^0 \to e^+e^-$	0.983
$t\bar{t}+X$	0.003
VV	0.013
Other	0.001

Table 5.2: Classification of the probe electrons in the 2018 MC sample of events selected for p_T calibration.

prompt	0.993
$t \to bW(\to e\nu)$	0.003
$t \to bW(\to \tau(\to e\nu\nu)\nu)$	0.000
fake	0.004

The kinematic parameters of two electrons from $Z^0 \to e^+e^-$ decay are correlated. Therefore, the discrepancy between data and MC in the kinematic properties of the Z^0 boson, such as its transverse momentum or pseudorapidity, could impact the electron selection efficiency. To eliminate this impact, MC events are re-weighted and enforce the agreement between data and MC in the kinematic properties of the e^+e^- pair.

The $p_T(l^+l^-)$ distribution for both muon and electron pairs is different between data and MC. This difference is corrected by applying an additional weight to the MC events depending on the value of $p_T(l^+l^-)$. The agreement in the distribution of $\eta(l^+l^-)$ is good enough and no any additional correction depending on $\eta(l^+l^-)$ is applied.

The agreement between data and MC is poor for electrons with low p_T. This deviation of the electron efficiency in MC from that in data can produce a significant impact on the analysis because the electrons produced in the decays of τ have smaller p_T. To eliminate this impact, in addition to the scale factors recommended by e/gamma CP group the electron efficiency is corrected in MC depending on p_T. An additional systematic uncertainty is applied related to this correction as explained in Section 5.7.

5.5.3 Impact parameter definition

By default in the ATLAS software the impact parameter, d_0, is defined with respect to the beam line. The measurement of the d_0 with respect to the primary vertex position should give a better precision, however, using the primary vertex for the definition of d_0 makes it dependent on the properties of the primary vertex, such as the number of tracks in the primary vertex and their momentum distribution. In this analysis the control sample of $Z^0 \to e^+e^-$ events is used to measure the d_0 resolution as discussed in Section 5.5.4, and the properties of the primary vertex of the control sample are different from that of the signal $t\bar{t}$ events. This is why d_0 is defined with respect to the beam line and thus eliminate any sensitivity of d_0 on the properties of the event.

The test of a possible bias of d_0 due to residual imperfections of the detector alignment was studied in the analysis of $R(\tau/\mu)$ [81]. In the $R(\tau/\mu)$ study it was found that there is a time-dependent and charge-independent bias of d_0 in 2015 and 2016. This bias is corrected by applying a charge-independent shift to the d_0 value

$$d_0' = d_0 + \alpha \tag{5.2}$$

where the value of α is $+4.22\ \mu m$ for 2015 data, $+3.5\ \mu m$ for periods A+B of 2016 data, and $-3.35\ \mu m$ for the remainder of 2016 data.

5.5.4 Calibration of impact parameter of prompt electrons

The impact parameter of electron, d_0, is one of the two quantities used to separate the electrons produced in decays of τ from other sources (along with p_T) and its accurate calibration is essential for the analysis. The d_0 distribution of prompt electrons (i.e. electrons originating from the point of primary interaction) is mainly determined by the detector resolution while the impact of physical processes producing such electrons is small. As such, d_0 of prompt electrons can be obtained using the electrons from $Z^0 \to e^+e^-$ decay. The sample of such decays in data is large and the background contribution to it is small as demonstrated in Tables 5.1 and 5.2. Therefore, the d_0 calibration can be performed using data with a negligible impact from MC. This approach aids in reducing the systematic uncertainties related to d_0.

The same selection of $Z^0 \to e^+e^-$ events is used as in Section 5.5.2 and apply the re-weighting of Z^0 MC events according to $p_T(e^+e^-)$. The d_0 distributions are obtained separately in 39 kinematic bins depending on the value of p_T and $|\eta|$ of the electron, where η is the pseudo-

rapidity of the electron track. The whole p_T range is divided into 13 bins. The $|\eta|$ range is divided into three bins. The details of these divisions are given in Tables 5.3 and 5.4. By definition, the kinematic bin ij contains all electrons with p_T in bin i and $|\eta|$ in bin j. A considerable number of events in the selected calibration samples ensures that appropriate statistics is available in each bin.

Table 5.3: Definition of p_T bins.

p_T bin number (n_{p_T})	p_T range (GeV)	p_T bin number (n_{p_T})	p_T range (GeV)
0	7 – 10	7	45 – 50
1	10 – 15	8	50 – 60
2	15 – 20	9	60 – 75
3	20 – 30	10	75 – 100
4	30 – 35	11	100 – 150
5	35 – 40	12	150 – 250
6	40 – 45		

Table 5.4: Definition of η bins.

$\|\eta\|$ bin number (n_η)	$\|\eta\|$ range
0	0 – 0.8
1	0.8 – 1.5
2	1.5 – 2.47

For each kinematic bin ij, the MC d_0 distributions for fake leptons and for leptons coming from decays of τ leptons produced in various processes, such as $t \to bW(\to \tau(\to e\nu\nu)\nu)$ or $Z \to \tau^+\tau^-$, are subtracted from the d_0 distribution in data. The same binning of d_0 distribution is used. The resulting distribution $F_{ij}^{\mathrm{pr}}(d_0)$ is normalized to unity.

The d_0 distribution of prompt electrons with p_T in a range $p_T^{\min} \leq p_T < p_T^{\max}$, denoted as $F^{\mathrm{pr}}(d_0, p_T\min, p_T^{\max})$, is computed as

$$F^{\mathrm{pr}}(d_0, p_T^{\min}, p_T^{\max}) = \sum_{i=i_{\min}}^{i_{\max}} \sum_{j=0}^{2} r_{ij}^{\mathrm{pr}} F_{ij}^{\mathrm{pr}}(d_0). \tag{5.3}$$

Here r_{ij}^{pr} is the fraction of prompt electrons in the analysis sample which are produced in top-

quark decay and contained in the kinematic bin ij. In this analysis, Wt events are treated as signal together with $t\bar{t}$. Therefore, r_{ij}^{pr} is computed using all processes which produce a prompt electron from top-quark decay. The summation range of the index i in (5.3) is determined by the momentum range $p_{\mathrm{min}} \leq p_T < p_{\mathrm{max}}$. For example, to obtain the d_0 template for electrons with $10 < p_T < 20$ GeV, the summation range of the index i is from one to two. The similar method and the same templates $F_{ij}^{\mathrm{pr}}(d_0)$ are used to obtain the d_0 distribution of prompt electrons from other sources (e.g., from $Z^0 \to e^+e^-$ decays), with the only difference is that the fractions r_{ij}^{pr} correspond to the given source. An additional study is performed to verify that the obtained d_0 templates properly describe the d_0 distribution of prompt electrons produced in $t \to bW(\to e\nu)$ decay. The details of this study are given in Section 5.7.2.1.

5.5.5 Calibration of impact parameter of electrons produced in τ-lepton decays

The d_0 distributions of electrons produced in τ decays are taken from MC. However, these distributions are corrected to take into account the difference in the d_0 resolution between data and MC. To quantify this difference, a fit is performed on the d_0 distribution of the electrons from $Z^0 \to e^+e^-$ decays using a Gaussian function with mean fixed at zero. The selection of $Z^0 \to e^+e^-$ events is described in in Section 5.5.2. The fit is performed in each kinematic bin defined in Section 5.5.4 in the d_0 range 0-0.02 mm. The main difference between data and MC is located at small values of d_0 which justifies the selection of the fitting range. The standard deviation of Gaussian, σ, reflects the d_0 resolution of electrons. In many kinematic bins the resolution in data is better than in Monte Carlo. This effect is increased in the bins with high p_T of the electron. The resolution in data is worse in 2015-2016 and is the best in the 2018 sample. In Monte Carlo, the resolution remains similar for all years. The observed effects are primarily due to the influence of the beam-spot transverse size which is the same in all MC samples but decreases with increasing luminosity such that the data/MC difference grows over the run.

Using the obtained values of the d_0 resolution, the d_0 distributions of the electrons from τ decays in MC is corrected and this distribution is used to obtain the results. It is especially constructed to take into account that in some cases the impact parameter resolution in data is better than in Monte Carlo. For convenience, the details of this procedure are given below.

The d_0 of the probe electron is smeared randomly by a Gaussian distribution for each MC

event. $\sigma_{ij}^{\text{smear}}$, the standard deviation is defined as:

$$\sigma_{ij}^{\text{smear}} = \sqrt{\left|\sigma_{ij}^2(data) - \sigma_{ij}^2(MC)\right|} \tag{5.4}$$

After processing all events, the smeared d_0 distributions are obtained, $f_{ij}^{\text{smear}}(d_0)$, and the difference $\delta_{ij}(d_0)$ between and the non-smeared distributions $f_{ij}^{\text{non-smear}}(d_0)$ is computed:

$$\delta_{ij}(d_0) = f_{ij}^{\text{smear}}(d_0) - f_{ij}^{\text{non-smear}}(d_0). \tag{5.5}$$

To suppress fluctuations related to the process of random smearing, this procedure is repeated 10000 times. The average of all 10000 iterations is computed and used as $\delta_{ij}(d_0)$ going forward.

If $\sigma_i(data) > \sigma_i(MC)$, the template d_0 distributions $F_{ij}^{\tau}(d_0)$ is defined for $t \to bW(\to \tau(\to e\nu\nu)\nu)$ electrons as

$$F_{ij}^{\tau}(d_0) = f_{ij}^{\text{non-smear}}(d_0) + \delta_{ij}(d_0) = f_{ij}^{\text{smear}}(d_0). \tag{5.6}$$

If $\sigma_{ij}(data) < \sigma_{ij}(MC)$, $F_{ij}^{\tau}(d_0)$ is defined as

$$F_{ij}^{\tau}(d_0) = f_{ij}^{\text{non-smear}}(d_0) - \delta_{ij}(d_0) \tag{5.7}$$

By doing this, it is assumed that the variations of the d_0 distribution is symmetric with respect to the change of the sign of $\sigma_{ij}(data) - \sigma_{ij}(MC)$.

The obtained $F_{ij}^{\tau}(d_0)$ distributions are normalised to unity, and the final template d_0 distribution of $t \to bW(\to \tau(\to e\nu\nu)\nu)$ electrons used in the analysis is defined as

$$F^{\tau}(d_0, p_T^{\text{min}}, p_T^{\text{max}}) = \sum_{i=i_{\text{min}}}^{i_{\text{max}}} \sum_{j=0}^{2} r_{ij}^{\tau} F_{ij}^{\tau}(d_0). \tag{5.8}$$

Here r_{ij}^{τ} is the fraction of $\tau \to e$ electrons in the kinematic bin ij in the analysis sample.

The resulting correction due to d_0 resolution is relatively small and variation for different values of d_0 is of the order of 1 %.

5.5.6 Impact parameter of fake electrons

The d_0 distribution of fake electrons is also taken from MC. Consequently, it is also subject to corrections due to the differences in the d_0 resolution. The same method is used as for $\tau \to e$ electrons to determine these corrections.

5.6 Background Efficiencies

In order to accurately measure the parameter of interest, background events that do not make up the signal must be removed. In this analysis, background events mainly come from events from Drell-Yan processes and 'fake' leptons.

5.6.1 Z^0 Correction Factor

Drell-Yann processes are a large background in this analysis. $Z^0 \to ee$ decay processes are removed from the analysis using the resonant mass range of $|m_{ee} - m_Z| < 5$ GeV as a cut. However, a scale factor is needed to account for non-resonant Drell-Yann processes. In the following this is denoted as the Z^0 correction factor. In the study of this scale factor, $Z^0 \to ee$ contribution is included, unlike in the main analysis where this mass window is removed. This study still requires two b-tagged jets in the selection of $Z^0 \to ee$ in the same way as the rest of the analysis. It is assumed non-resonant e^+e^- production scales similarly to $Z^0 \to ee$ decay, and the single correction factor is applied to both resonant and non-resonant Drell-Yann contribution. The Z^0 correction factor also applies to the $Z^0 \to \tau\tau$ background. The calculation of the $Z^0 \to \mu\mu$ scale factor is also presented as an extra check to validate the method.

The Z^0 correction factor is given as

$$R_{Z^0} = \frac{N_{data}}{N_{MC}} \tag{5.9}$$

where N_{data} and N_{MC} are the number of events in the Z^0 resonant peak in data and MC respectively.

In order to calculate the number of events in the peak, a fit is performed using a Voigt profile for the Z^0 contribution and a Chebychev polynominal for background between 50 GeV and 140 GeV. The Voight profile is a convolution of a Breit-Wigner and Gaussian distribution representing the signal and detector resolution respectively. It is given as:

$$V(x,m,\Gamma,s) = \frac{1}{(x-m^2)+\frac{1}{4}\Gamma^2} \otimes e^{-\frac{1}{2}(\frac{x-m}{s})^2} \tag{5.10}$$

where x is an observable, m is the mean, Γ is the width and s is the standard deviation. For the fit, the Z^0 mass (m) was not fixed, while the full width (Γ) was fixed to 2.4952 GeV (PDG value) and

the standard deviation (s) was not fixed. The result of the fit for data and MC for Z^0 decay mode (ee, $\mu\mu$) is shown in figures 5.1 and 5.2. The full list of fit parameters can be found in appendix B.

Sample	R_{Z^0}	Relative Uncertainty	N_Z (data)	N_Z (MC)
$Z^0 \to ee$	1.15	0.79%	33926 ± 267	29611 ± 254
$Z^0 \to \mu\mu$	1.11	0.63%	55297 ± 344	49802 ± 330

Table 5.5: Fitted numbers of $Z^0 \to \ell\ell$ in data and simulation, along with their respective ratios for the full dataset

The systematic uncertainty for the Z^0 correction factor is determined by comparing the result of the used fitting procedure with an alternative fitting procedure. This alternative fitting procedure was chosen as a double Voigt profile. The difference between the two Voigt profiles was the value of s. The double Voigt fit is performed such that the largest difference between the double Voigt fit and the nominal fit is found while still having the double voigt profile fit converge acceptably. This largest difference in the result of the two fitting procedure is then taken as the systematic uncertainty. The systematic uncertainty for $R_{Z^0} \to ee$ was determined as 0.002 (0.167%).

Sample	R_{Z^0}	Relative Uncertainty	N_Z (data)	N_Z (MC)
$Z^0 \to ee$	1.14	0.88 %	34284 ± 261	29879 ± 249

Table 5.6: Double Voigt fitted numbers of $Z^0 \to ee$ in data and simulation, along with their respective ratios for the full dataset used to calculate the systematic uncertainty. $Z^0 \to \mu\mu$ was not calculated as it is not used in this analysis.

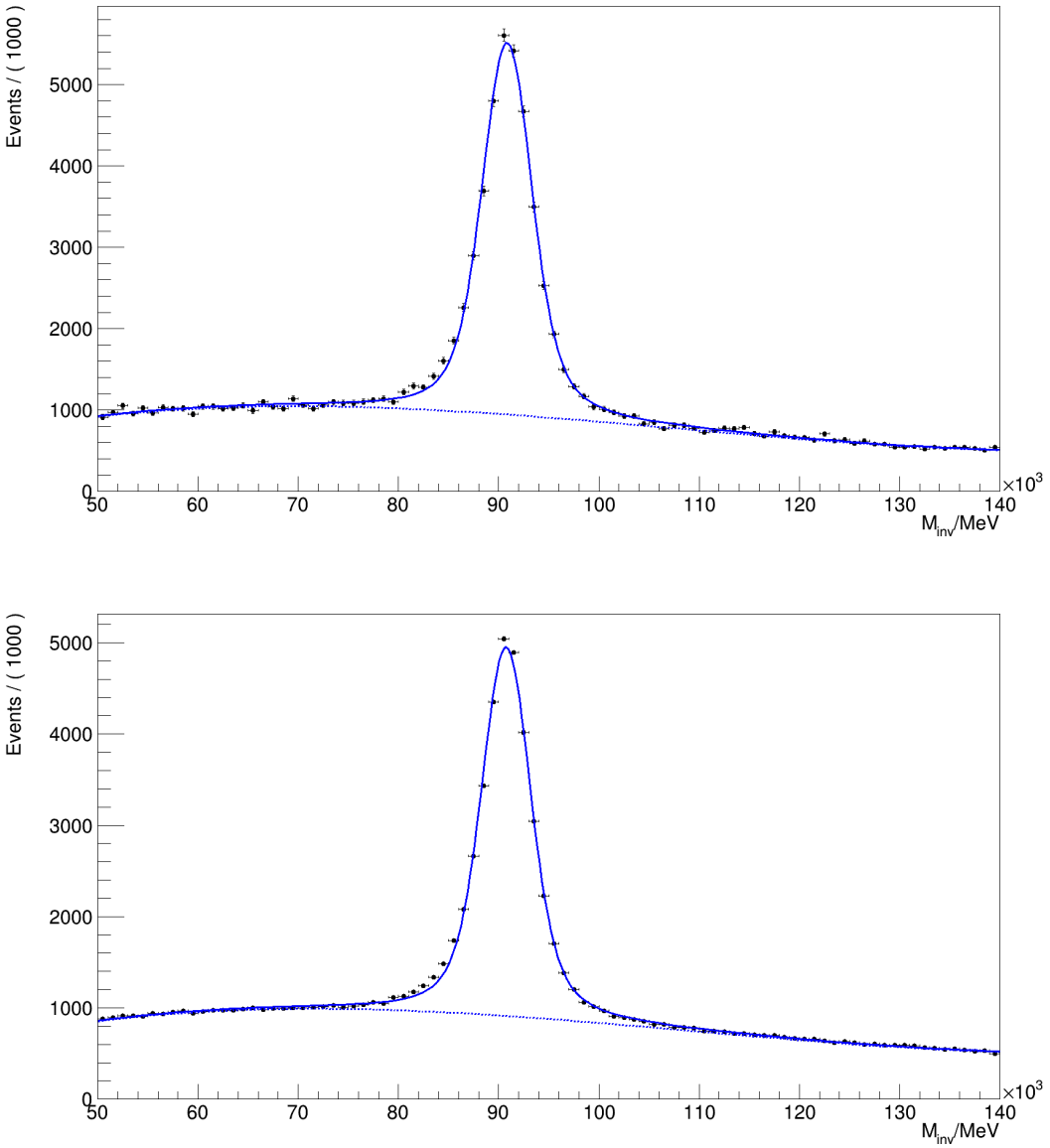

Figure 5.1: Fit of Voigt-profile and Chebychev polynomial to invariant mass distribution of $Z^0 \rightarrow ee$ for data (above) and MC (below). The χ^2/NDF for the data fit is 2.88 and for MC is 22.5. The high χ^2 in MC is due to the high statistics in the MC sample. It can be seen in the left Z^0 peak tail, where it can be seen how the electrons lose energy as they pass through the detector.

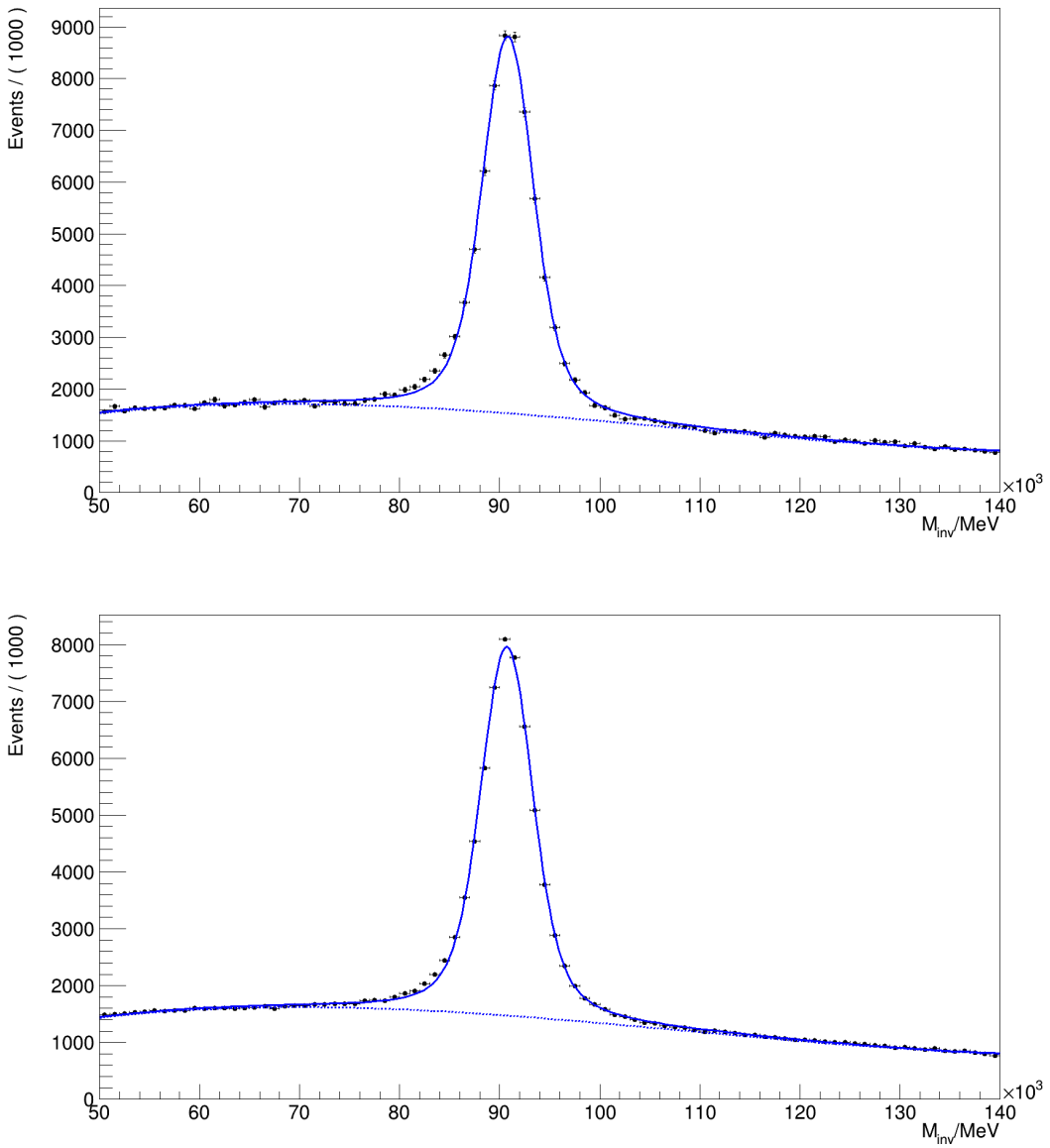

Figure 5.2: Fit of Voigt-profile and Chebychev polynomial to invariant mass distribution of $Z^0 \rightarrow \mu\mu$ for data (above) and MC (below). The χ^2/NDF for the data fit is 4.67 and for MC is 37.0. The high χ^2 in MC is due to the high statistics in the MC sample. It can be seen in the left Z^0 peak tail, where it can be seen how the muons lose energy as they pass through the detector.

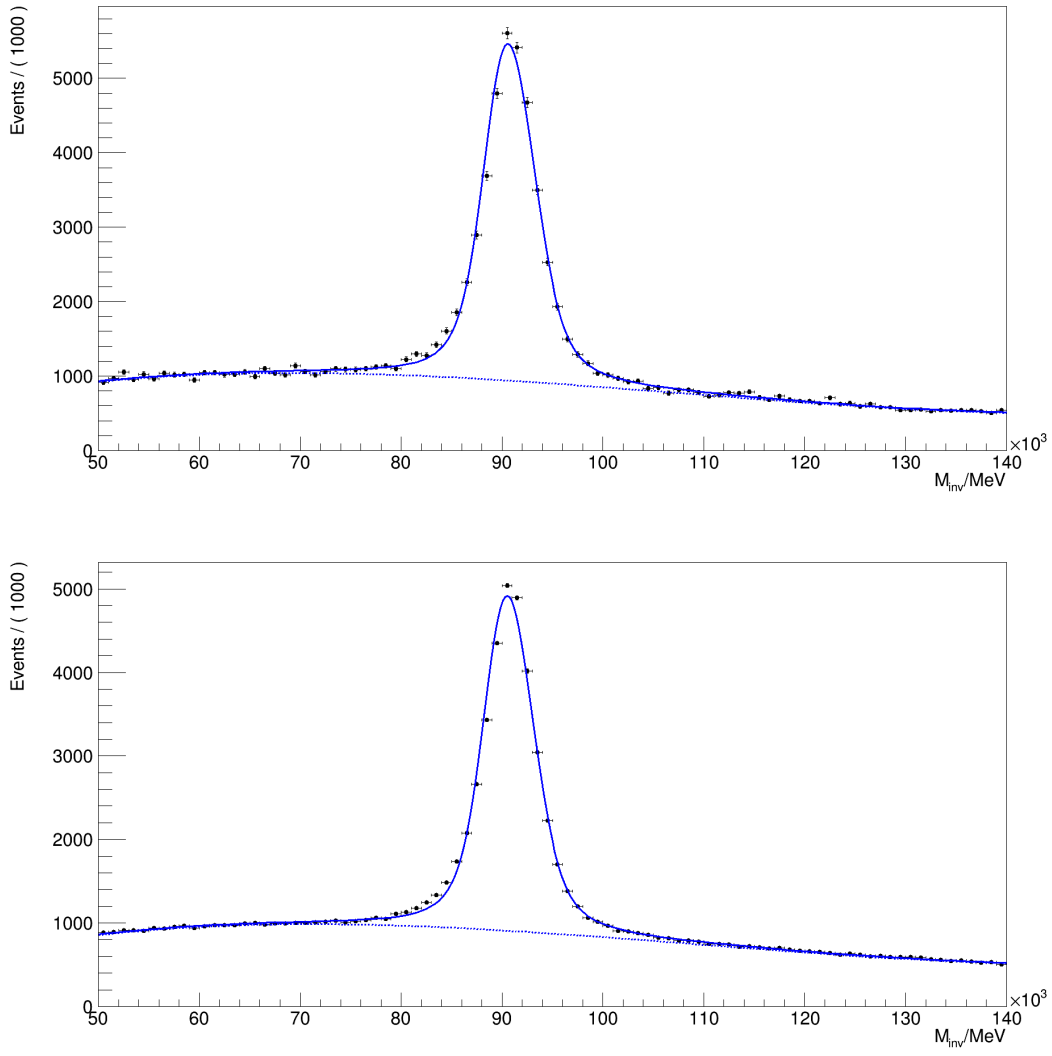

Figure 5.3: Fit of a double Voigt-profile and Chebychev polynomial to invariant mass distribution of $Z^0 \to ee$ for data (above) and MC (below). The χ^2 for the data fit is 2.91 and for MC is 22.2. The high χ^2 in MC is due to the high statistics in the MC sample. It can be seen in the left Z^0 peak tail, where it can be seen how the electrons lose energy as they pass through the detector.

5.6.2 Fakes

Fake electrons are an important source of background. Fake events are events whose origin is not that of the signal, but appear as signal in the data. The number of fake electrons in the signal sample is taken from MC as this contains truth information and corrected by a factor derived from the comparison of data and MC. Fake electrons contribute to both samples containing opposite-sign (*OS*) and same-sign (*SS*) leptons, while the contribution of non-fake leptons to SS sample is suppressed.

Hence, fake leptons dominate in SS events. The fake correction factor is determined by using SS sample of events and it is assumed the same for the OS sample. This assumption is supported by the study of origin of fake electrons presented in Figures 5.4 and 5.5. Here, it can be seen the origin of leptons is similar in OS and SS samples. In the plots, 'Non-defined' events are those coming from unknown sources. Further study was done to determine the origin of these leptons, and these events were found to be mostly originating from hadrons identified as electrons

In the study of $R(\tau/\mu)$ [81] fakes were assumed to come mainly from decays of light, charm, and beauty hadrons. However, the estimation of fakes becomes more complicated in the $\tau - e$ case, as electrons in the detector can come from other sources. A comparison of the origin of the fake probe lepton for ee and $\mu\mu$ channels for all p_T of probe leptons shows a large make-up of fake electrons coming from photon conversion, rather than bottom mesons as in the $\mu\mu$ channel, as shown in Tables 5.7 and 5.8. Photon conversion is the process by which a photon will spontaneously convert into an electron and anti-electron, because of this photon conversion is a process that is only relevant to the electron channels (μe and ee).

The composition of fake lepton origin changes depending on p_T, with higher p_T fake electrons originating mostly from photon conversion and lower p_T originating from B mesons and photon conversion, as shown in Tables 5.9, 5.10, 5.11, 5.12, 5.13 and 5.14.

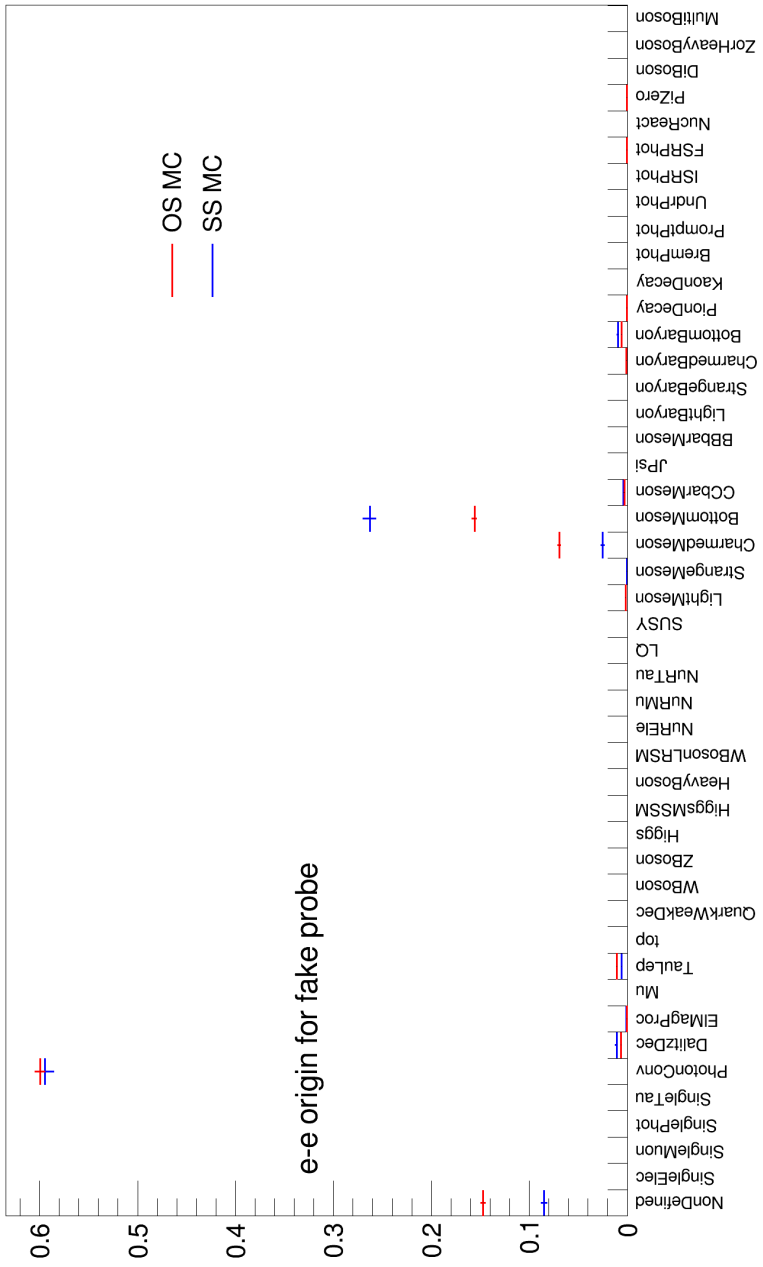

Figure 5.4: Sources of fake probe electrons in SS and OS *ee* events in simulation.

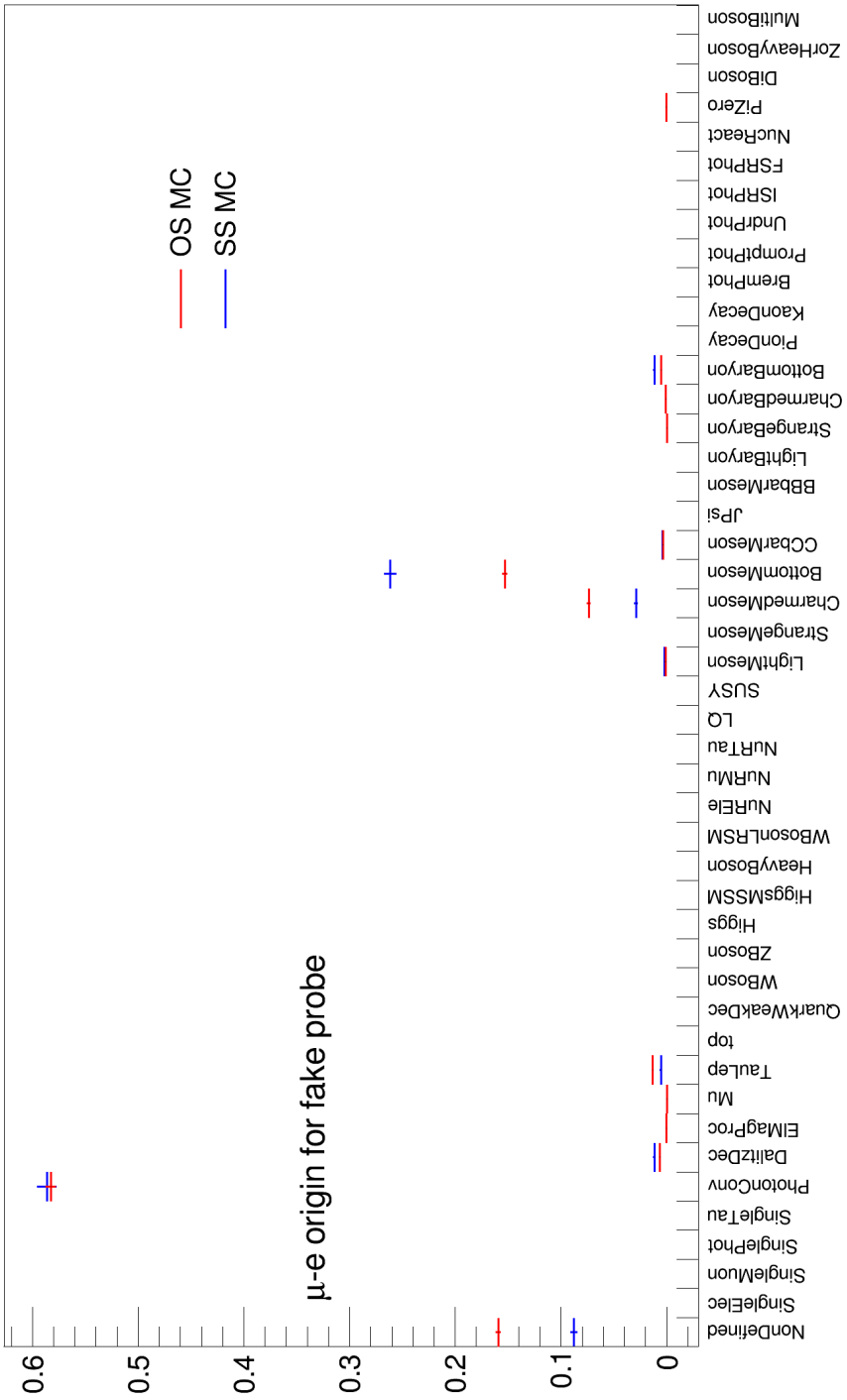

Figure 5.5: Sources of fake probe electrons in SS and OS μe events in simulation.

Origin of lepton	Fraction of total leptons (%)
NonDefined	8.44
PhotonConv	59.5
DalitzDec	1.08
ElMagProc	0.086
TauLep	0.556
LightMeson	0.159
StrangeMeson	0.00581
CharmedMeson	2.47
BottomMeson	26.3
CCbarMeson	0.373
CharmedBaryon	0.0540
BottomBaryon	0.923
PiZero	0.0378
Total	100

Table 5.7: Origin of fake probe electrons in the SS sample with prompt tag electron (all p_T).

Origin of lepton	Fraction of total leptons (%)
NonDefined	6.00
TauLep	1.87
LightMeson	0.926
StrangeMeson	0.749
CharmedMeson	13.1
BottomMeson	66.9
CCbarMeson	1.26
BBbarMeson	0.0324
CharmedBaryon	0.236
BottomBaryon	3.327
PionDecay	3.25
KaonDecay	2.30
Total	100

Table 5.8: Origin of fake probe muons in the SS sample with prompt tag muon (all p_T).

Origin of lepton	N	Fraction of total leptons (%)
NonDefined	20.0 ± 1.4	14.2
PhotonConv	25.5 ± 1.7	18.1
DalitzDec	1.55 ± 0.38	1.10
ElMagProc	0.00162 ± 0.00196	0.00115
TauLep	1.67 ± 0.41	1.18
LightMeson	0.643 ± 0.265	0.455
CharmedMeson	10.5 ± 1.0	7.41
BottomMeson	76.2 ± 2.9	53.9
CCbarMeson	0.757 ± 0.266	0.535
CharmedBaryon	0.409 ± 0.199	0.289
BottomBaryon	3.96 ± 0.65	2.80
PiZero	0.177 ± 0.153	0.125
Total	141 ± 4	100

Table 5.9: Origin of fake probe electrons ($p_T = [7, 10]$ GeV) in the SS sample with prompt tag electron.

Origin of lepton	N	Fraction of total leptons (%)
NonDefined	19.5 ± 1.5	10.1
PhotonConv	61.2 ± 2.7	31.8
DalitzDec	1.73 ± 0.56	0.897
ElMagProc	0.440 ± 0.235	0.228
TauLep	2.03 ± 0.52	1.05
LightMeson	0.145 ± 0.131	0.0751
StrangeMeson	0.0441 ± 0.0441	0.0229
CharmedMeson	7.51 ± 0.95	3.89
BottomMeson	96.0 ± 3.5	49.8
CCbarMeson	1.53 ± 0.46	0.794
CharmedBaryon	0.000306 ± 0.000306	0.000160
BottomBaryon	2.54 ± 0.56	1.32
PiZero	0.110 ± 0.110	0.0572
Total	193 ± 5	100

Table 5.10: Origin of fake probe electrons ($p_T = [10, 20]$ GeV) in the SS sample with prompt tag electron.

Origin of lepton	N	Fraction of total leptons (%)
NonDefined	19.1 ± 1.5	4.64
PhotonConv	358 ± 7	86.8
DalitzDec	4.95 ± 0.80	1.20
ElMagProc	0.218 ± 0.139	0.0528
TauLep	0.523 ± 0.269	0.127
LightMeson	0.418 ± 0.215	0.101
CharmedMeson	0.718 ± 0.286	0.174
BottomMeson	27.6 ± 2.4	6.70
CCbarMeson	0.544 ± 0.257	0.132
BottomBaryon	0.498 ± 0.261	0.121
Total	412 ± 7	100

Table 5.11: Origin of fake probe electrons ($p_T = [20, 250]$ GeV) in the SS sample with prompt tag electron.

Because of a complicated composition of fake electrons, one scale factor can not properly scale SS events. The number of MC events is scaled based on the origin of tag and probe leptons instead. The scale factor C^P is applied to the events in which both tag and probe leptons are prompt. In the SS sample, such events come mainly from VV and $t\bar{t}V$ production. The cross section of these processes is not modelled well in MC, hence this scale factor is found to be large. A scale factor C^C is applied to events in which the charge of tag or probe electrons has changed due to Bremsstrahlung (*charge flip*) resulting in the SS charge combination. It is not applied to events that have a probe muon as muons do not experience Bremsstrahlung. However, the fraction of events coming from this source are very low and this scale factor is set to 1. A composite scale factor $C^{PH} f_{PH} + C^{HAD}(1 - f_{PH})$ is applied to events containing fake tag or probe electrons. Here C^{PH} is the scale factor applied to fake electrons from photon conversion and C^{HAD} is the scale factor applied to leptons produced in hadron decays. The coefficient f_{PH} is the fraction of electrons from photon conversion among all fake electrons. This fraction depends on the p_T of the electron.

All the coefficients applied to different types of SS events are summarised in Table 5.15. The C^{PH} and C^C scale factors are only used for events with an electron. The same scale factors are

Origin of lepton	N	Fraction of total leptons (%)
NonDefined	23.3 ± 1.5	15.7
PhotonConv	24.3 ± 1.6	16.5
DalitzDec	1.91 ± 0.43	1.29
ElMagProc	0.00797 ± 0.04127	0.00539
TauLep	2.01 ± 0.45	1.36
LightMeson	0.812 ± 0.270	0.550
CharmedMeson	12.7 ± 1.1	8.62
BottomMeson	77.1 ± 2.8	52.2
CCbarMeson	1.11 ± 0.34	0.751
CharmedBaryon	0.703 ± 0.259	0.476
BottomBaryon	3.71 ± 0.67	2.51
PiZero	0.0675 ± 0.0659	0.0457
Total	148 ± 4	100

Table 5.12: Origin of fake probe electrons ($p_T = [7, 10]$ GeV) in the SS sample with prompt tag muon.

Origin of lepton	N	Fraction of total leptons (%)
NonDefined	24.8 ± 1.7	11.7
PhotonConv	63.5 ± 2.7	29.8
DalitzDec	1.91 ± 0.46	0.897
ElMagProc	0.131 ± 0.130	0.0615
TauLep	1.86 ± 0.45	0.874
LightMeson	0.512 ± 0.257	0.240
CharmedMeson	9.16 ± 1.01	4.30
BottomMeson	105 ± 4	49.3
CCbarMeson	1.60 ± 0.42	0.752
CharmedBaryon	0.133 ± 0.129	0.0625
BottomBaryon	4.41 ± 0.71	2.07
Total	213 ± 5	100

Table 5.13: Origin of fake probe electrons ($p_T = [10,20]$ GeV) in the SS sample with prompt tag muon.

used, C^P and C^{HAD}, for electron and muons as the origin of prompt leptons and leptons from hadron decays does not depend on the lepton flavour. The scale factor one is applied to several negligible contributions, e.g., subsamples with one fake lepton and one lepton with flipped charge.

Fakes in OS MC are also calculated differently to the previous study. The number of fakes is scaled using C^{HAD} and C^{PH}, obtained in the SS sample using the general expression:

$$C_{OS} = C^{PH} f_{PH}^{OS} + C^{HAD}(1 - f_{PH}^{OS}) \tag{5.11}$$

Where f_{PH}^{OS} is the fraction of fakes from photon conversion in the OS sample. The fraction of events coming from photon conversion scales in the same way in the OS sample as it does in the SS sample, as shown in Tables 5.16, 5.17, 5.18, 5.19, 5.20 and 5.21. The values of f_{PH} for SS and OS events are summarised in Table 5.22.

TRExFitter is used to determine the best fit scale factors. This fit is statistical only, with systematics calculated separately. C^C is fixed to unity in the fit since the fraction of events with charge flip is very small and the fit is not sensitive to this parameter. The fractions f_{PH} in different p_T bins are fixed to the MC values given in Table 5.22. Figures 5.6, 5.7 and 5.8 show the pre and

Origin of lepton	N	Fraction of total leptons (%)
NonDefined	18.8 ± 1.5	4.35
PhotonConv	375 ± 6.8	87.0
DalitzDec	4.61 ± 0.74	1.07
ElMagProc	0.210 ± 0.158	0.0486
Mu	0.00294 ± 0.00294	0.000681
TauLep	0.535 ± 0.237	0.124
LightMeson	0.391 ± 0.208	0.0905
CharmedMeson	1.23 ± 0.39	0.286
BottomMeson	29.1 ± 1.9	6.75
CCbarMeson	0.333 ± 0.188	0.0771
CharmedBaryon	0.00170 ± 0.00170	0.000394
BottomBaryon	0.955 ± 0.335	0.221
Total	431 ± 7	100

Table 5.14: Origin of fake probe electrons ($p_T = [20, 250]$ GeV) in the SS sample with prompt tag muon.

	ee	μe	$\mu\mu$	$e\mu$
prompt-prompt	C^P	C^P	C^P	C^P
prompt-flip	C^C	C^C	1	1
flip-prompt	C^C	1	1	C^C
prompt-fake	$C^{PH} f_{PH}$ + $C^{HAD}(1-f_{PH}))$	$C^{PH} f_{PH}$ + $C^{HAD}(1-f_{PHG})$	C^{HAD}	C^{HAD}
fake-prompt	$C^{PH} f_{PHH}$ + $C^{HAD}(1-f_{PHH})$	C^{HAD}	C^{HAD}	$C^{PH} f_{PHH}$ + $C^{HAD}(1-f_{PHH})$
flip-flip	1	1	1	1
fake-flip	1	1	1	1
flip-fake	1	1	1	1
fake-fake	1	1	1	1

Table 5.15: The scale factor that scales each contribution to SS events for each tag-probe combination and lepton channel. Prompt-fake combination corresponds to prompt tag and fake lepton and so on. f_{PH} is the fraction of events coming from photon conversion and is different for the three p_T bins (7-10, 10-20, 20-250 GeV) used in the analysis. The factor f_{PHH} of high p_T bin (20-250 GeV) is applied to fake tag and prompt probe contribution since the tag electon has $p_T > 27$ GeV.

Origin of lepton	N	Fraction of total leptons (%)
NonDefined	2.73 ± 0.41	11.9
PhotonConv	3.88 ± 0.56	16.9
DalitzDec	0.217 ± 0.123	0.946
TauLep	0.214 ± 0.110	0.930
LightMeson	0.0595 ± 0.0353	0.259
CharmedMeson	2.08 ± 0.46	9.07
BottomMeson	12.6 ± 1.0	54.8
CCbarMeson	0.0320 ± 0.0155	0.140
CharmedBaryon	0.0141 ± 0.0097	0.0612
BottomBaryon	1.12 ± 0.32	4.86
PiZero	0.0376 ± 0.0373	0.163
Total	22.9 ± 1.4	100

Table 5.16: Origin of fake probe electrons ($p_T = [7, 10]$ GeV) in the OS sample with prompt tag electron.

post-fit data and MC agreement for the fakes scaling. Figure 5.9 shows the overall pre- and post-fit data and MC comparison for the yield in different channels of the SS events.The resulting scale factors of this fit are shown in Table 5.23. These scale factors are then used to validate the scaling by comparison of the d_0 and p_T distributions in data and MC as shown in Figures 5.10 and 5.11.

Origin of lepton	N	Fraction of total leptons (%)
NonDefined	3.60 ± 0.56	10.6
PhotonConv	14.1 ± 1.2	41.7
DalitzDec	0.272 ± 0.178	0.804
ElMagProc	0.0456 ± 0.0519	0.135
TauLep	0.334 ± 0.163	0.986
LightMeson	0.0627 ± 0.0329	0.185
CharmedMeson	2.68 ± 0.52	7.90
BottomMeson	11.3 ± 1.1	33.4
CCbarMeson	0.621 ± 0.356	1.83
CharmedBaryon	0.112 ± 0.114	0.332
BottomBaryon	0.948 ± 0.300	2.80
FSRPhot	0.00663 ± 0.00663	0.0196
Total	33.9 ± 1.9	100

Table 5.17: Origin of fake probe electrons ($p_T = [10, 20]$ GeV) in the OS sample with prompt tag electron.

Origin of lepton	N	Fraction of total leptons (%)
NonDefined	8.10 ± 0.89	10.083
PhotonConv	67.9 ± 2.7	84.4357
DalitzDec	0.317 ± 0.120	0.393899
ElMagProc	0.0894 ± 0.0889	0.111301
TauLep	0.0656 ± 0.0270	0.0816405
LightMeson	0.156 ± 0.079	0.192996
CharmedMeson	0.819 ± 0.240	1.01877
BottomMeson	2.84 ± 0.46	3.52859
CCbarMeson	0.0901 ± 0.0586	0.112132
CharmedBaryon	0.0103 ± 0.0103	0.0128154
BottomBaryon	0.0235 ± 0.0186	0.0291859
Total	80.4 ± 2.8	100

Table 5.18: Origin of fake probe electrons ($p_T = [20, 250]$ GeV) in the OS sample with prompt tag electron.

The systematic uncertainty in the expected number of fake electrons in the signal OS sample due to $t\bar{t}$ modelling is determined by comparison with alternative MC generators. POWHEG+PYTHIA8-HDAMP and POWHEG+HERWIG, were compared against the nominal POWHEG+PYTHIA8-AF2 generator. The alternative MC events have been produced using Atlas Fast (AF) simulation, for the POWHEG+PYTHIA8-HDAMP sample therefore the AF simulation of the nominal $t\bar{t}$ MC is used for the systematic study. While full simulation was used for the POWHEG+HERWIG sample, as such full simulation of the nominal sample was used as a comparison. For each alternative MC generator the C^{PH} and C^{HAD} are measured using the method presented in this section and the expected number of fake electrons in the OS sample is obtained for each p_T bin. The maximum relative difference with respect to the nominal MC simulation is taken as the systematic uncertainty from this source. The results of the systematic study are summarised in Tables 5.24, 5.25 and 5.26. Plots showing the fakes scaling fit results and p_T and d_0 distributions for the alternative MC samples can be found in appendix C.

Origin of lepton	N	Fraction of total leptons (%)
NonDefined	2.94 ± 0.52	13.6
PhotonConv	2.56 ± 0.39	11.8
DalitzDec	0.359 ± 0.171	1.66
ElMagProc	0.00147 ± 0.00147	0.00678
Mu	0.00775 ± 0.00775	0.0358
TauLep	0.396 ± 0.170	1.83
LightMeson	0.0335 ± 0.0179	0.155
CharmedMeson	4.74 ± 1.65	21.9
BottomMeson	9.44 ± 1.10	43.6
CCbarMeson	0.184 ± 0.128	0.847
StrangeBaryon	0.000222 ± 0.000222	0.00103
CharmedBaryon	0.0366 ± 0.0345	0.169
BottomBaryon	0.960 ± 0.239	4.43
PiZero	0.0414 ± 0.0240	0.191
Total	21.7 ± 2.1	100

Table 5.19: Origin of fake probe electrons ($p_T = [7, 10]$ GeV) in the OS sample with prompt tag muon.

Origin of lepton	N	Fraction of total leptons (%)
NonDefined	3.30 ± 0.58	12.4
PhotonConv	5.94 ± 0.69	22.3
DalitzDec	0.157 ± 0.074	0.591
ElMagProc	0.0120 ± 0.0096	0.0450
Mu	0.00759 ± 0.00759	0.0286
TauLep	0.815 ± 0.344	3.07
LightMeson	0.370 ± 0.268	1.39
CharmedMeson	2.31 ± 0.43	8.70
BottomMeson	12.5 ± 1.2	46.9
CCbarMeson	0.385 ± 0.156	1.45
CharmedBaryon	0.0317 ± 0.0379	0.119
BottomBaryon	0.836 ± 0.395	3.15
PiZero	0.00765 ± 0.00765	0.0288
Total	26.6 ± 1.7	100

Table 5.20: Origin of fake probe electrons ($p_T = [10, 20]$ GeV) in the OS sample with prompt tag muon.

Origin of lepton	N	Fraction of total leptons (%)
NonDefined	9.38 ± 1.06	20.2183
PhotonConv	33.2 ± 2.0	71.5702
DalitzDec	0.349 ± 0.183	0.751753
ElMagProc	0.000889 ± 0.003376	0.0019164
Mu	0.000292 ± 0.000292	0.00063002
TauLep	0.218 ± 0.148	0.46961
LightMeson	0.144 ± 0.075	0.310678
CharmedMeson	0.845 ± 0.283	1.8222
BottomMeson	2.19 ± 0.38	4.72904
CCbarMeson	0.0250 ± 0.0126	0.0539635
BottomBaryon	0.0332 ± 0.0151	0.0717307
Total	46.4 ± 2.3	100

Table 5.21: Origin of fake probe electrons ($p_T = [20, 250]$ GeV) in the OS sample with prompt tag muon.

p_T bin	Fraction of Photon Conversion (SS)	Fraction of Photon Conversion (OS)
$F_{PH}(7-10)$	0.173	0.143
$F_{PH}(10-20)$	0.308	0.320
$F_{PH}(20-250)$	0.869	0.780

Table 5.22: Fractions of photon conversion in same-sign(SS) and opposite-sign(OS) events. The values for SS sample are used in the fit of the scale factors.

Scale Factor Origin	Scale Factor Fitted Value
C_P	1.36 ± 0.07
C_{HAD}	1.46 ± 0.03
C_{PH}	0.84 ± 0.07
C_C	1 (fixed)

Table 5.23: Scale factors resulting from the fit

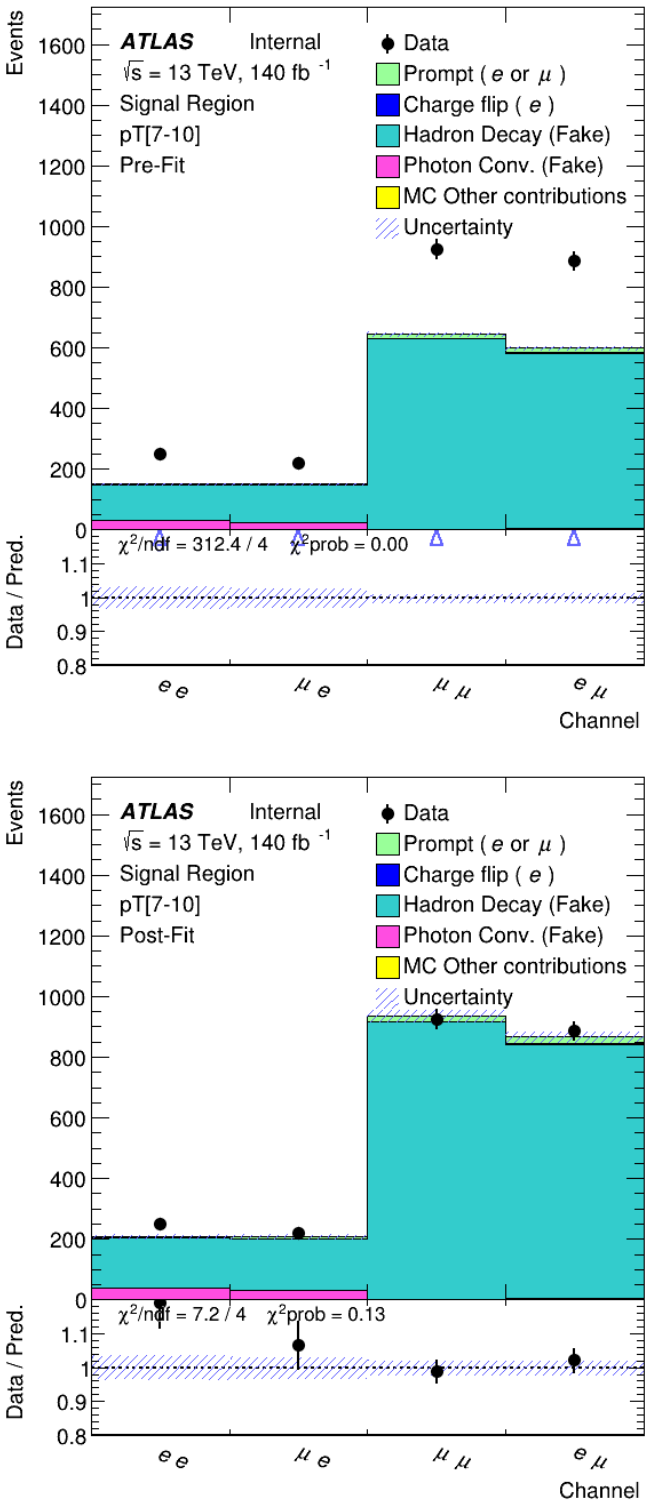

Figure 5.6: Prefit (above) and postfit (below) plots in the same-sign control region showing the data and MC agreement for the 7-10 GeV p_T bin for each decay channel ee, μe, $\mu\mu$ and $e\mu$. The post-fit result shows the calculated scale factors improve the data-MC agreement when applied.

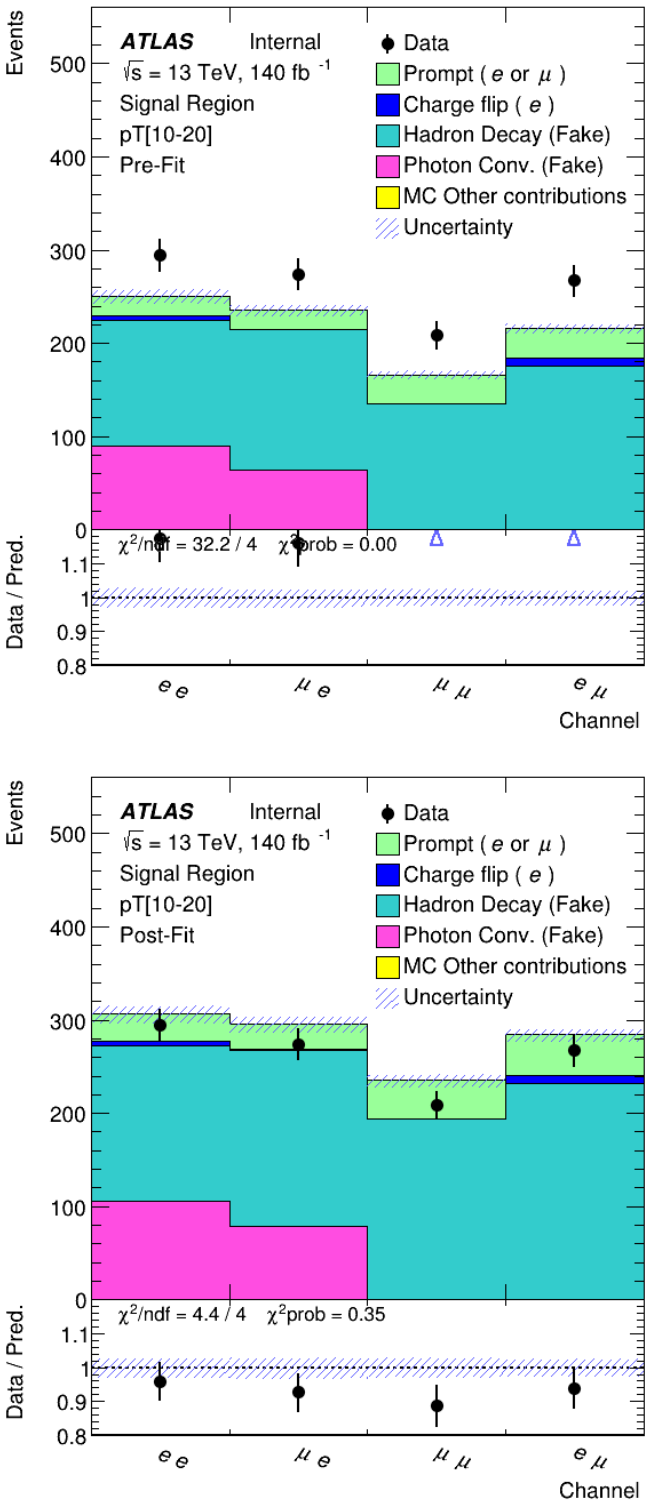

Figure 5.7: Prefit (above) and postfit (below) plots in the same-sign control region showing the data and MC agreement for the 10-20 GeV p_T bin for each decay channel ee, μe, $\mu\mu$ and $e\mu$. The post-fit result shows the calculated scale factors improve the data-MC agreement when applied.

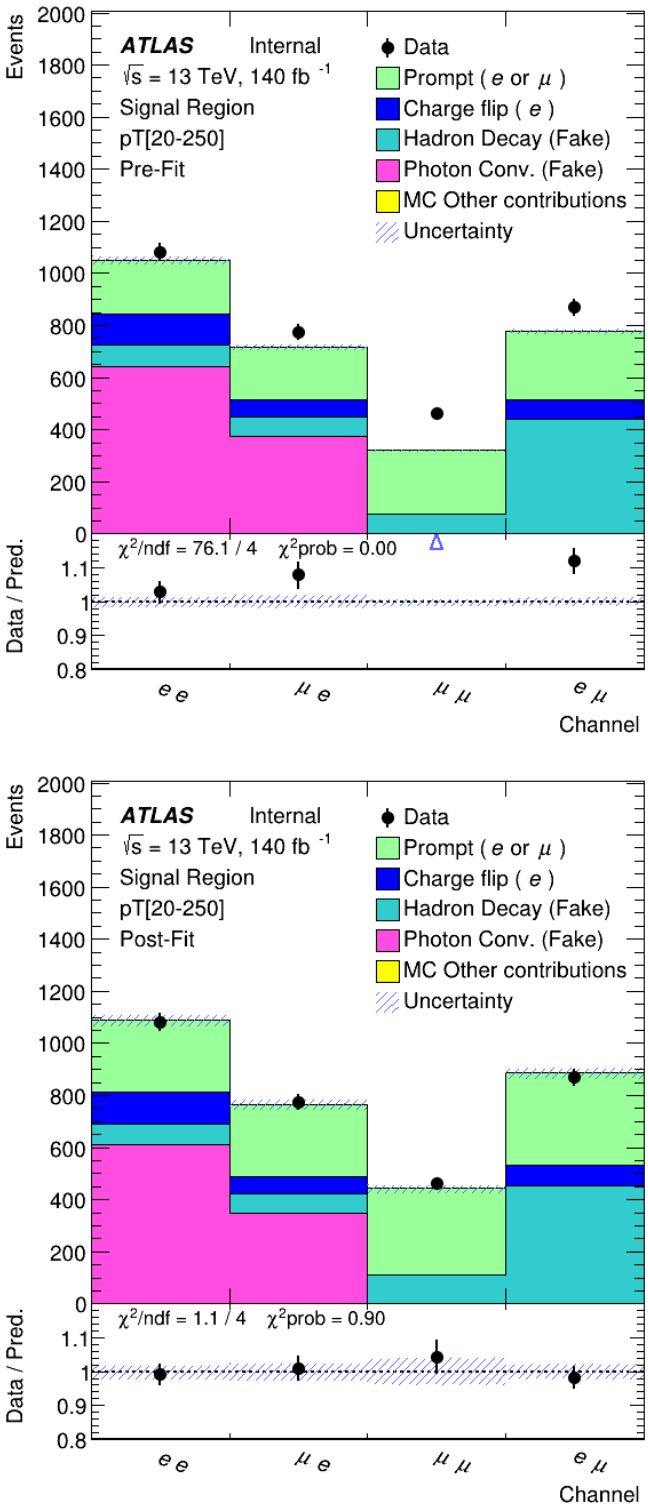

Figure 5.8: Prefit (above) and postfit (below) plots in the same-sign control region showing the data and MC agreement for the 20-250 GeV p_T bin for each decay channel ee, μe, $\mu\mu$ and $e\mu$. The post-fit result shows the calculated scale factors improve the data-MC agreement when applied.

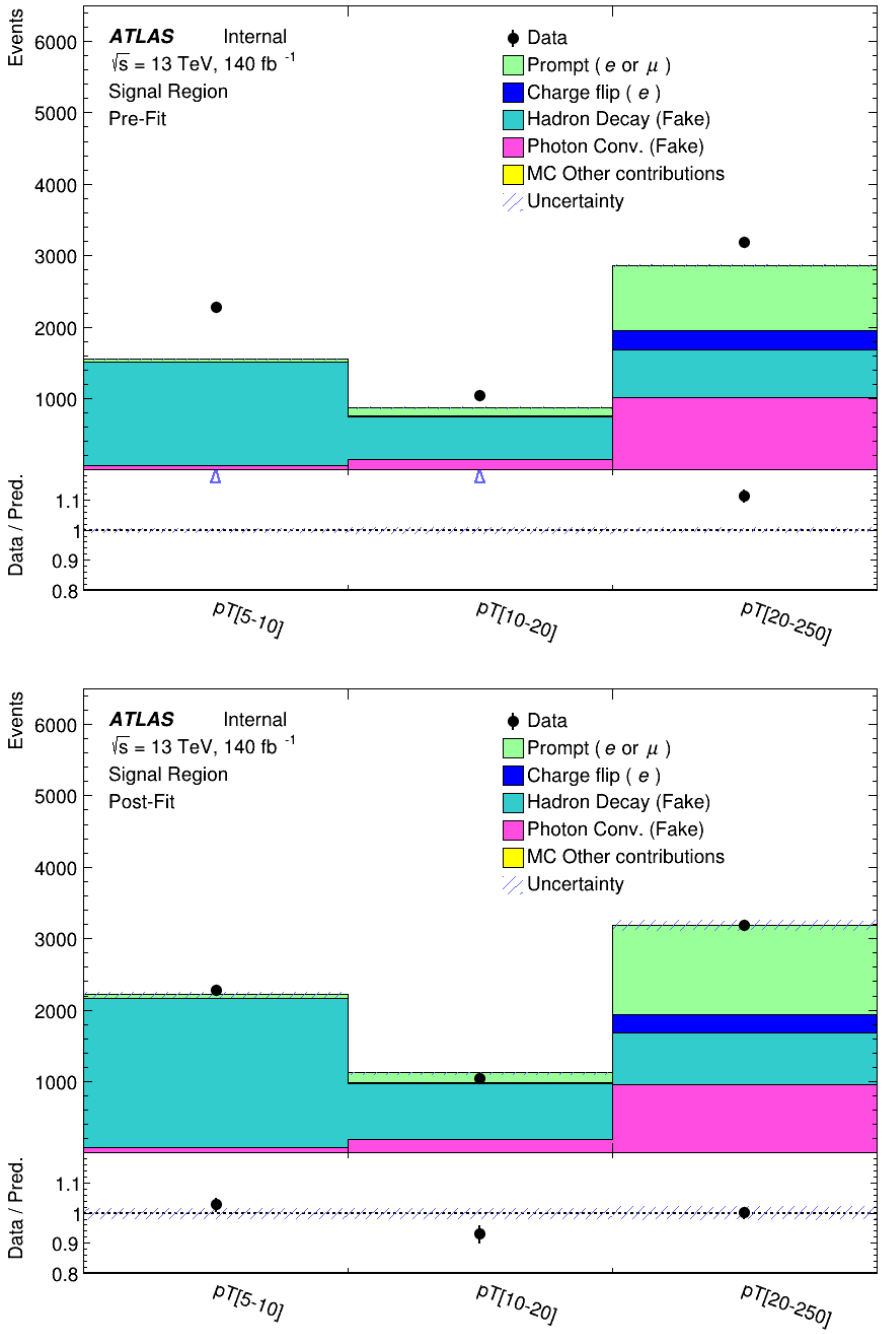

Figure 5.9: Prefit (above) and postfit (below) summary plots in the same-sign control region showing the data and MC agreement for all p_T bins for each decay channel ee, μe, $\mu\mu$ and $e\mu$. The post-fit result shows the calculated scale factors improve the data-MC agreement when applied.

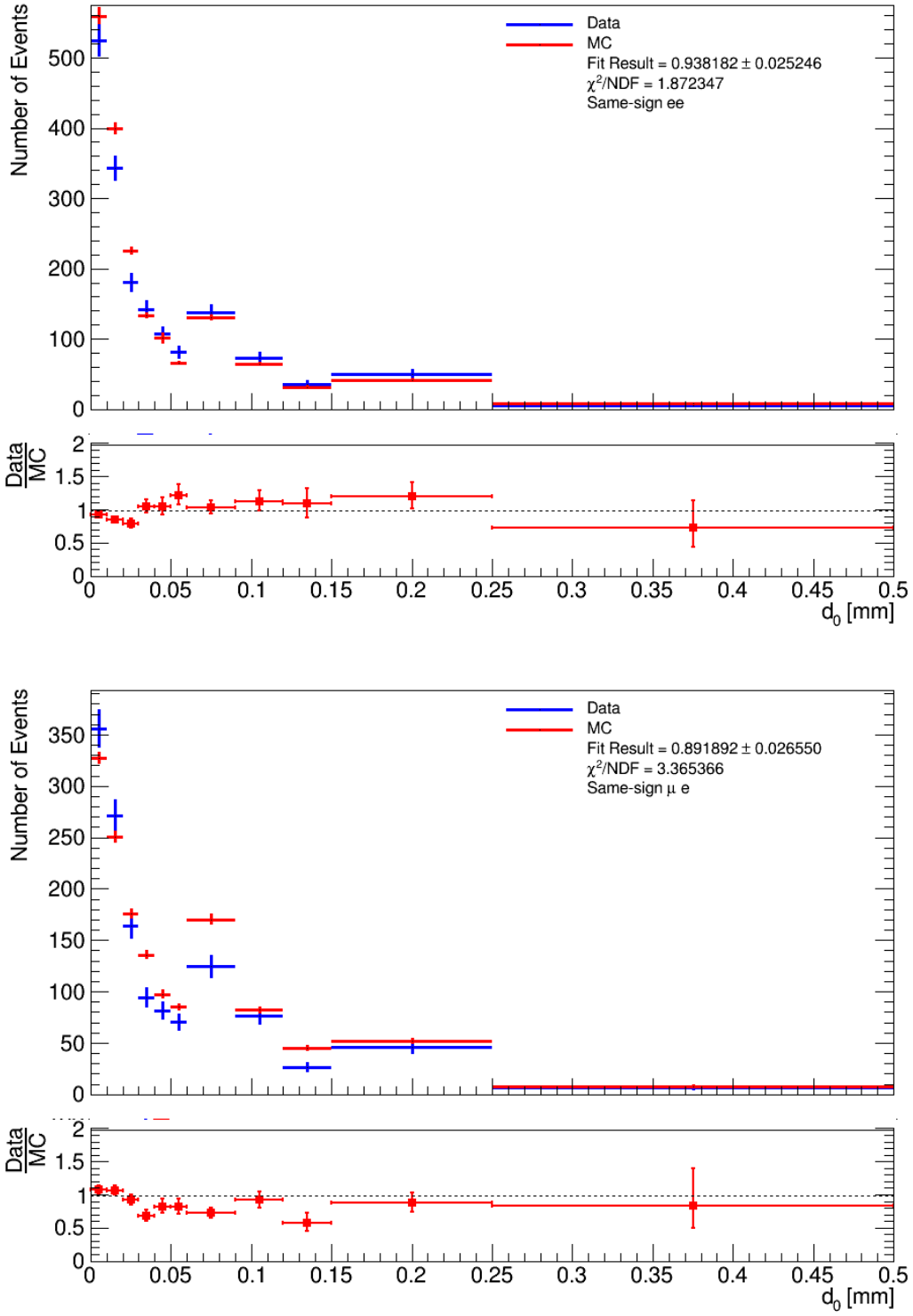

Figure 5.10: Comparison of distributions of d_0 in same-sign ee (a) and μe (b) events in data and simulation for the full dataset.

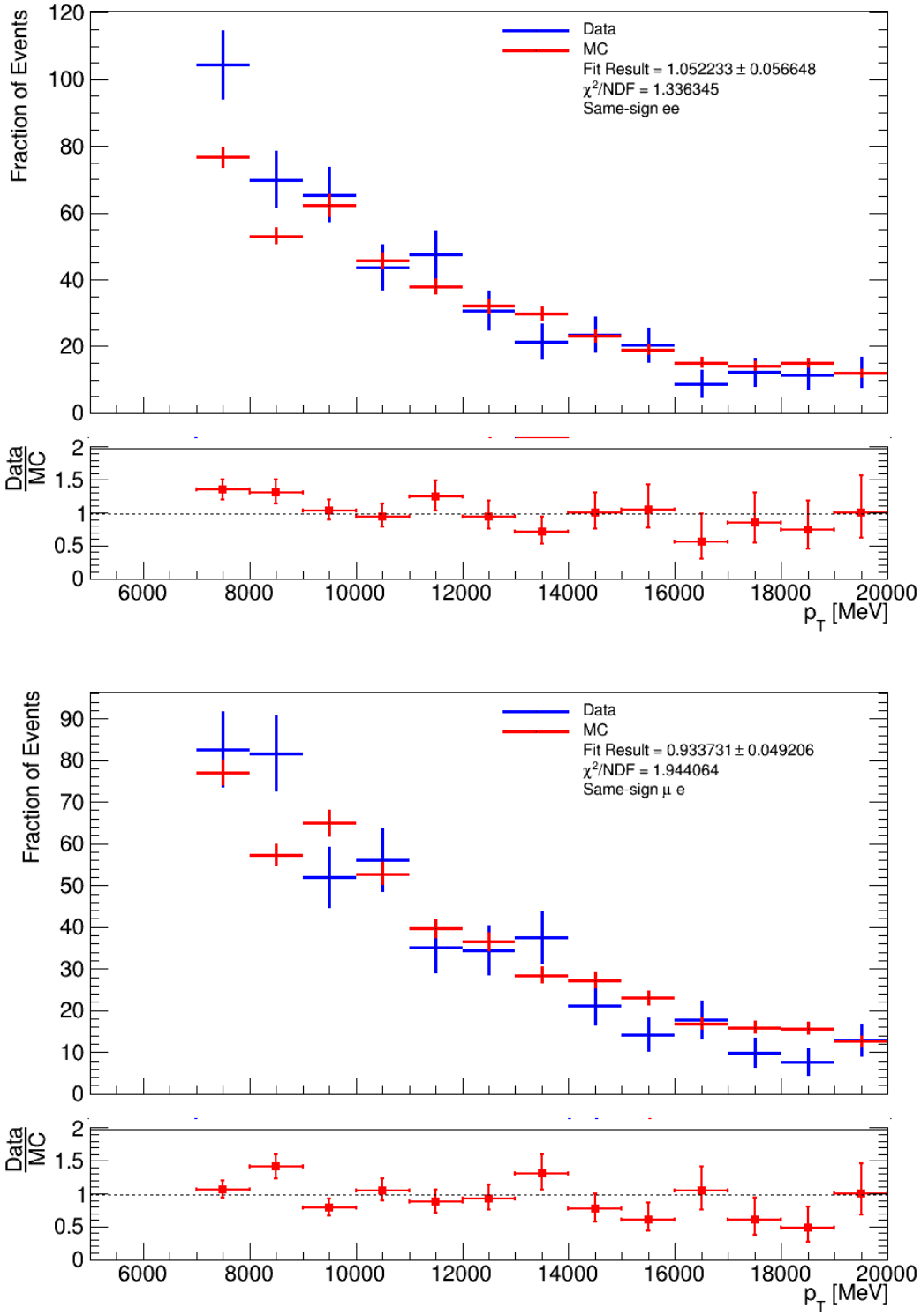

Figure 5.11: Comparison of distributions of p_T in same-sign ee (a) and μe (b) events in data and simulation for the full dataset.

	POWHEG+PYTHIA8 (AF)	POWHEG+PYTHIA8-HDAMP-AF (AF)
C_{PH}	$1.02^{+0.08}_{-0.07}$	$1.00^{+0.07}_{-0.07}$
C_{HAD}	$1.52^{+0.03}_{-0.03}$	$1.50^{+0.03}_{-0.03}$
C_{P}	$1.36^{+0.07}_{-0.07}$	$1.41^{+0.07}_{-0.07}$
C_{FLIP}	1	1
$f_{SS(7-10)}$	0.19	0.19
$f_{SS(10-20)}$	0.36	0.35
$f_{SS(20-250)}$	0.90	0.90
$f_{OS(7-10)}$	0.18	0.17
$f_{OS(10-20)}$	0.35	0.36
$f_{OS(20-250)}$	0.88	0.88
C_{7-10}	1.42	1.41
C_{10-20}	1.34	1.32
C_{20-250}	1.07	1.05
N_{MC}^{7-10}	136	144
N_{MC}^{10-20}	231	230
N_{MC}^{10-250}	981	969
N_{expect}^{7-10}	193	203
N_{expect}^{10-20}	308	305
N_{expect}^{20-250}	988	1017
Difference (7-10)	0	10.2 (5.26%)
Difference (10-20)	0	3.53 (1.14%)
Difference (20-250)	0	29.4 (2.98%)

Table 5.24: Scale factors and numbers used in the fakes systematics study, for the alternative sample Powheg+Pythia8-hdamp. The alternative sample was produced with ATLAS Fast simulation, therefore the nominal sample for comparison is also ATLAS Fast.

	POWHEG+PYTHIA8 (FS)	POWHEG+HERWIG (FS)
C_{PH}	$0.84^{+0.07}_{-0.07}$	$0.90^{+0.08}_{-0.08}$
C_{HAD}	$1.46^{+0.03}_{-0.03}$	$1.67^{+0.04}_{-0.04}$
C_{P}	$1.36^{+0.07}_{-0.07}$	$1.28^{+0.07}_{-0.07}$
C_{FLIP}	1	1
$f_{SS(7-10)}$	0.17	0.18
$f_{SS(10-20)}$	0.31	0.33
$f_{SS(20-250)}$	0.87	0.87
$f_{OS(7-10)}$	0.15	0.14
$f_{OS(10-20)}$	0.32	0.32
$f_{OS(20-250)}$	0.78	0.78
C_{7-10}	1.35	1.53
C_{10-20}	1.27	1.42
C_{20-250}	0.92	1.00
N_{MC}^{7-10}	151	205
N_{MC}^{10-20}	250	215
N_{MC}^{10-250}	1052	1039
N_{expect}^{7-10}	204	225
N_{expect}^{10-20}	317	314
N_{expect}^{20-250}	970	1037
Difference (7-10)	0	20.6 (9.17%)
Difference (10-20)	0	2.86 (0.91%)
Difference (20-250)	0	67.4 (6.50%)

Table 5.25: Scale factors and numbers used in the fakes systematics study, for the alternative sample Powheg+Herwig. The alternative sample was produced with Full Sim simulation, therefore the nominal sample for comparison is also Full Sim.

	Maximum % Difference	Alternative Sample
Difference (7-10)	9.17%	Powheg+Herwig
Difference (10-20)	1.14%	Powheg+Pythia8-hdamp
Difference (20-250)	6.50%	Powheg+Herwig

Table 5.26: Results of fakes systematic study.

5.7 Systematic Uncertainties

The analysis is designed such that many systematic uncertainties are correlated between the $t \to bW(\to e\nu)$ and $t \to bW(\to \tau(\to e\nu\nu)\nu)$ channels, so that an identical variation in both channels cancels out in the ratio $R(\tau/e)$. Therefore, several uncertainties that can have a significant impact on the selection of events, e.g. jet energy scale and b-tagging, do not result in large uncertainties on $R(\tau/e)$.

For the experimental systematic uncertainties the correlation model from the relevant CP groups is used and each uncertainty component across different processes is correlated and this is also done across all of the kinematic bins. Similarly, the theoretical modelling uncertainties are correlated across kinematic bins except the uncertainty due to parton shower and hadronisation, which are considered independently in three kinematic bins and correlate between the $t \to bW(\to e\nu)$ and $t \to bW(\to \tau(\to e\nu\nu)\nu)$ processes. For the analysis specific data-driven uncertainties they only apply to specific processes and their correlation structure is discussed in the sub-sections below.

5.7.1 Pruning and Smoothing of the Systematic Variations

The removal of non-relevant systematic uncertainties before they are inputted to the fit (pruning) and smoothing the input histograms to the fit to remove statistical fluctuations is done using the standard tools of the TRexFitter package [86]. TRExFitter performs a pruning of systematics based on whether the shape and normalisation variations are larger than a given threshold set at 0.001. TRExFitter additionally performs a smoothing of several of the systematic uncertainties to reduce the effect of statistical fluctuations in the varied samples. Additionally the gamma statistical uncertainties which are very small are pruned away.

5.7.2 Systematic Uncertainties from Data-driven Corrections

5.7.2.1 Uncertainties due to d_0 templates for prompt electrons

An uncertainty on the data-driven templates for the d_0 distribution of prompt electrons is derived to account for the fact that the templates are constructed in a Z-enriched selection, but applied to a $t\bar{t}$ final state. This uncertainty is labelled as d_0 template.

The procedure of d_0 calibration consists in using the d_0 distributions of electrons observed in the data sample containing mainly $Z^0 \to e^+e^-$ events as the templates of prompt electrons produced in $t\bar{t}$. In both cases, the electrons come from the primary interaction point. Therefore, the d_0 distributions are expected to be identical to the first approximation. However, the track environment in the processes of Z^0 and $t\bar{t}$ production and decay are considerably different. Additionally there is the effect of the finite binning in p_T and $|\eta|$ which may not be able to encapsulate the full shape information. Therefore, small differences between the used templates and the actual d_0 distributions cannot be excluded.

To verify the procedure of d_0 calibration the d_0 distributions of prompt electrons produced in $Z^0 \to e^+e^-$ and $t\bar{t}$ events are compared using Monte Carlo simulation.

The residual differences between $Z^0 \to e^+e^-$ and $t\bar{t}$ processes in d_0 distributions are propagated to the systematic uncertainty by calculating the ratio of the normalised d_0 distributions of prompt electrons (of $Z^0 \to e^+e^-$ and $t\bar{t}$) in each kinematic bin in MC. This ratio is then used to modify the d_0 distribution in data minus the MC distribution for fake leptons and for leptons coming from decays of τ leptons produced in various processes. The distributions are then normalised to unity and are used to build the modified template d_0 distributions of prompt electrons. The difference in the value of $R(\tau/e)$ obtained with the modified and nominal templates is taken as the systematic uncertainty due to the calibration of d_0 of prompt electrons. This uncertainty is symmetrised.

5.7.2.2 d_0 uncertainty on non-prompt leptons

In Section 5.5.5 corrections on the d_0 resolution are derived which is applied as a smearing to non-prompt electrons coming from τ decay to account for the differences between data and MC. A similar procedure is used to determine the corrections for the fake electrons as described in Section 5.5.6. The statistics used to derive these corrections are extremely high and the difference

between data and MC is understood to be primarily due to the difference in beam spot size at high p_T and material, alignment and modelling at low p_T. For uncertainties on this correction half the size of the full correction is taken and symmetrised. As the statistics are high this is many times ($\sim$5) the statistical uncertainty on the correction so is thought to be highly conservative. The impact of this uncertainty on the final analysis is small such that a more detailed treatment of this is not thought to be required.

5.7.2.3 Sources of uncertainty from data-driven background estimates

The normalisation of the $t\bar{t}$ fake-lepton background and the $Z \to e^+e^-$ background are derived from data control regions as described in Section 5.6. The normalisation factors and their uncertainties are propagated to the fit.

5.7.2.4 $t\bar{t}$ fake-lepton background

Two sources contribute to the fake normalisation uncertainty derivation described in Section 5.6.2. These sources are considered individually for each p_T range of the probe electron. Those are the uncertainty due to the limited size of the *SS* dataset and the uncertainty derived by using different MC generators. The maximum variation in the number of fakes estimated using different generators is taken to form the later uncertainty. The sizes of these uncertainties are shown in Table 5.27. The normalisation factors are derived using Equation 5.11 and the coefficients given in Tables 5.22 and 5.23. The same normalisation factors and uncertainties are applied in *ee* and μe channels.

p_T range [GeV]	Normalisation factor	Statistical	Systematic
$[7,10]$	1.27	$\pm$ 2.9%	$\pm$ 9.2%
$[10,20]$	1.19	$\pm$ 3.2%	$\pm$ 1.1%
$[20,250]$	0.93	$\pm$ 6.1%	$\pm$ 6.5%

Table 5.27: Normalisation factors and the corresponding uncertainties on the fake electron background.

Scale Factor Origin	Scale Factor Fitted Value
C_P	1.38 ± 0.07
C_{HAD}	1.54 ± 0.08
C_{PH}	0.80 ± 0.08
C_C	1 (fixed)
C_{HAD_mu}	0.93 ± 0.05

Table 5.28: Scale factors resulting from the fit

5.7.2.5 Adding systematic uncertainty to validation plots

As described in Section 5.6.2, validation plots were produced to validate the scale factors obtained in the study of fakes. When adding the systematic uncertainty of fakes to the plots, it is found that the χ^2 between MC and data is improved. This is shown in Figure 5.12. The results on these plots show the calculated scale factors for fake contributions are valid and these values were used in the final result of the analysis.

5.7.2.6 Consistency check for fake muon and electron scale factors

In the fakes analysis, it is assumed that the correction factors C^P and C^{HAD} are the same for electrons and muons as the origin of the fakes is the same. The mismodelling between electrons and muons might be different due to reconstruction or isolation. In order to test this, another scale factor is included, C_{HAD_mu} is included as a scale factor only on muons and the effect the other scale factors is observed. With this scale factor included, the scale factors are measured as shown in Table 5.28. It can be seen that the new included scale factor, C_{HAD_mu} is unity within 2σ, while leaving the other scale factors relatively unchanged from their original values. This validates the assumption that the correction factors for C^P and C_{HAD} can be treated the same for electrons and muons.

5.7.2.7 $Z^0 \to e^+e^-$ background

The $Z^0 \to e^+e^-$ background normalisation is strongly constrained using a control region in data. The corresponding normalisation factor and uncertainty for the *ee*-channel is shown in Table 5.29. The details on deriving this factor are given in Section 5.6. The statistical uncertainty comes from

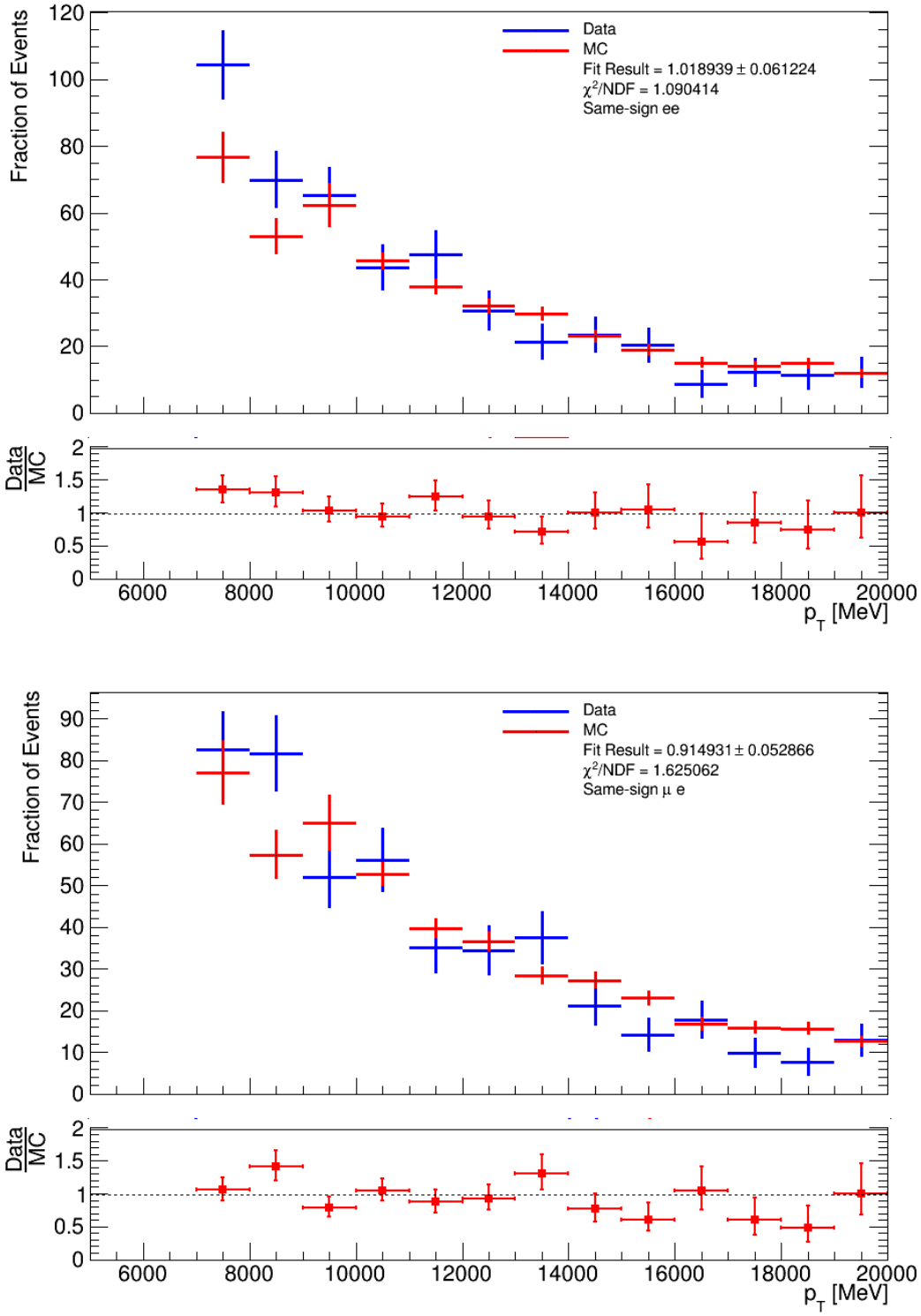

Figure 5.12: The validation plots from section 5.6.2, with the fakes systematic uncertainty included.

the fitted Z^0 yield and is due to the limited size of the Z^0 MC sample and data control region.

A systematic uncertainty on this estimate based on the shape of the choice of fit functions used to extract the Z^0 normalisation was also investigated. Switching the signal model from a single Voigt function to a double Voigt function induces a further small uncertainty.

Channel	Normalisation factor	Statistical	Systematic
ee	1.257	$\pm$ 0.008%	$\pm$ 0.002%

Table 5.29: Normalisation factors and the corresponding uncertainties on the $Z^0 \to e^+e^-$ background.

5.7.2.8 Electron reconstruction and identification

Besides the electron scale factor provided by the EGamma CP group, additional correction of electron efficiency are applied as explained in Section 5.5.2. This correction is derived using the calibration sample of events with the dominant $Z^0 \to e^+e^-$ contribution. The MC $Z^0 \to e^+e^-$ events are generated using Sherpa 2.2.11 MC generator [71]. To estimate the related systematic uncertainty the alternative sample of $Z^0 \to e^+e^-$ events generated using the MadGraph5 + Pythia [87] MC generator is used. The difference in the electron efficiency obtained with these two MC simulations is propagated to the final result and is taken as the systematic uncertainty related to the additional correction of electron efficiency.

5.7.3 Sources of uncertainty from MC modelling

5.7.3.1 $t\bar{t}$ modelling uncertainties

The uncertainties due to the choice of MC generator are estimated by comparing the nominal $t\bar{t}$ sample with several different MC generators and/or sample configurations within the nominal generator described in 5.3.2.

5.7.3.1.1 Matrix element systematic This uncertainty is estimated by comparing the nominal $t\bar{t}$ simulation with the sample generated with Pythia8 and pthard = 1 (DSID 601491) as specified by the ATLAS physics modelling group.

5.7.3.1.2 ISR systematic To estimate the uncertainty on the amount of inital state radiation the Var3c A14 eigen-tune variations [88] of α_s for initial state radiation (ISR), in the A14 tune are applied. The difference between up and down variations divided by 2 is taken as a symmetric uncertainty.

5.7.3.1.3 $\mu_{R,F}$ systematic To simulate changes to the amount of parton radiation and potential missing higher-order corrections, the renormalisation (μ_R) and factorisation (μ_F) scales are varied up by a factor of 2 and down by a factor of 0.5. The difference between up and down variations divided by 2 is taken as a symmetric uncertainty.

5.7.3.1.4 h_{damp} systematic A variations of the Powheg [72] hdamp value to 3.0 mtop is used to vary the resummation scale. This is then symmetrised to form an uncertainty.

5.7.3.1.5 FSR systematic The impact of final-state-radiation (FSR) is evaluated using PS weights which vary the renormalisation scale for QCD emission in the FSR by a factor of 0.5 and 2.0, respectively. This systematic uncertainty suffers form large weights which reduce the statistical power of the sample. Therefore these are restricted to be below 10 times the nominal. The difference between up and down variations divided by 2 is taken as a symmetric uncertainty.

5.7.3.1.6 Gluon recoil systematic The nominal $t\bar{t}$ Monte Carlo employs the recoiling against b quarks to simulate the gluon recoil scheme. The ATLAS physics modelling group recommends to use the recoil to top scheme (DSID 601357) for the estimate of the corresponding systematic uncertainty.

5.7.3.1.7 Parton shower and hadronisation systematic The impact of the parton shower and hadronisation model is evaluated by comparing the nominal generator setup with a sample produced with the POWHEGBOX [89–92] v2 generator interfaced with Herwig 7.2.1 [70, 93, 94]. The difference between the nominal and alternative MC simulations is then symmetrised to form an uncertainty.

5.7.3.1.8 NNLO corrections An additional weight to the $t\bar{t}$ MC is applied to take into account the NNLO corrections to the simulation of $t\bar{t}$ production. The recursive method of correction is used as specified in [95]. Taking into account the NNLO corrections significantly improves the

agreement in p_T distribution of e^+e^- pairs in the signal sample. The improved agreement between data and MC is essential for this analysis as the p_T of the probe electron is used to separate $t \to e$ and $t \to \tau \to e$ electrons. To take into account the systematic uncertainties due to the NNLO corrections the result with and without NNLO re-weighting is compared.

5.7.3.2 PDF systematic

To estimate the systematic uncertainty due to PDF the recommendation of the ATLAS top working group [96] is followed. The weight of the MC events is modified using the sample of 30 different variations of PDF defined by PDF4LHC15 set [97] and propagate this modification to the measurement of $R(\tau/e)$. The standard deviation of the distribution of 30 values of $R(\tau/e)$ is taken as the systematic uncertainty from this source).

5.7.3.3 Extrapolating from $W \to \tau\nu \to e\nu\nu\nu$ to $W \to \tau\nu$

In the analysis the ratio of events where the W-boson decays directly to electrons and where it decays through a τ lepton is fitted. To extrapolate this to the fundamental ratio of W-boson decays an uncertainty on the branching fraction of τ leptons to electrons needs to be accounted for. This is added at the end of the process, rather than in the fit, such that future improvements on the precision of this can be taken advantage of. The uncertainty from the PDG average is used , which is 0.22% [82] and add this in quadrature to the final measurement uncertainty.

5.8 Fitting Procedure

5.8.1 Fit setup

A binned template profile likelihood fit is used to extract the measured value of $R(\tau/e)$, using the TRExFitter package [86].

A global likelihood function is built that includes all measurement bins and all fit parameters. The fit is setup such that a negative-log-likelihood minimization is performed with several unknown parameters, the parameter of interest (POI) for this analysis, $R(\tau/e)$, and systematic uncertainties included as nuisance parameters, θ. The likelihood function is defined in the usual way, as a product of Poisson measurements for each bin of each region and a probability density function for systematics,

$$L(n,\theta^0|R(\tau/e),\theta) = \prod_{i\in\text{bins}} P(n_i|R(\tau/e)(\theta)) \times \prod_{j\in\text{NPs}} G(\theta_j^0|\theta_j) \tag{5.12}$$

where G is a gaussian prior that required continuous interpolation between variations and nominal templates.

The fit is set up with three floating parameters; $R(\tau/e)$, the parameter of interest (POI), $C(t\bar{t})$, and $R(\mu/e)$. $C(t\bar{t})$ is the ratio of the number of both the prompt- and τ-lepton $t\bar{t}$ and Wt processes to the corresponding number of predicted simulated events (using the theoretical cross-sections for the processes). $R(\mu/e)$ takes into account any residual difference in the efficiencies of the tag electron and muon reconstruction. It is applied as an additional factor to all events in the μe sample. $R(\tau/e)$ only affects the τ-lepton contribution. Therefore $R(\tau/e)$ controls the relative contribution of the two lepton templates, i.e. it is the ratio of the two. Note, that the total number of fitted τ-lepton events will be the predicted number scaled by the product of $C(t\bar{t})$ and $R(\tau/e)$. The total number of events from different processes in μe sample is scaled by the product pf $C(t\bar{t})$ and $R(\mu/e)$.

The normalisation of the fake-lepton background is extracted from data, as described in Section 5.6.2, it is treated by a separate nuisance parameter for each p_T region with the nominal value as derived from data and a 1σ uncertainty given by the corresponding uncertainty on the value derived from the method described in the aforementioned section.

The normalisation of the Z+jets background is also extracted from data, as described in Section 5.6.1, it is treated by a nuisance parameter with the nominal value as derived from data and a 1σ uncertainty given by the corresponding uncertainty on the value derived from the method described in the aforementioned section.

All other backgrounds are normalised to higher order cross sections as described in Section 5.3.3 and are also treated as nuisance parameters with 1σ uncertainties given by the uncertainties on these higher order cross sections.

Additional sources of uncertainty can arise from shape and acceptance effects. These are also treated as nuisance parameters in the fit.

The two-dimensional p_T and d_0 fit is performed by splitting the events into 3 p_T regions each of which has a corresponding 1-D d_0 distribution with 8 bins. There are two channels in the fit so the fit is then a 2-D $3 \times 8 \times 2 = 48$ bin fit.

The 3 p_T regions are selected to have significantly different prompt, tau and fake electron

compositions. Optimisation results in bins with $p_T = [7, 10, 20, 250]$ GeV boundaries.

The 8 d_0 bins are optimised to also have different lepton source compositions. The main trade-off here is between having enough bins to extract the best sensitivity to $R(\tau/e)$ whilst not overcomplicating the fit to the extent that it is hard to get good convergence. Optimisation results in bins with $d_0 = [0, 0.01, 0.02, 0.03, 0.04, 0.06, 0.09, 0.15, 0.5]$ mm boundaries.

5.8.2 Fit validation and Asimov fit results

This section discusses the results of the fit to an Asimov dataset [98]. An Asimov dataset is used to evaluate the performance of the fitting procedure and to understand how well the parameter of interest, $R(\tau/e)$, can be fitted. An Asimov dataset is an 'idealised' dataset that is the expected data generated based on 'best fit' parameters. This allows for changes to the fitting procedure to be made without unblinding the result, by identifying issues such as heavily constrained nuisance parameters or parameters with a large correlation.

The extracted value of $R(\tau/e)$ is 1.000 ± 0.0232 [± 0.0126 (stat) ± 0.0195 (syst) $\pm$ 0.0022 (BR)] for the Asmiov dataset. A more detailed breakdown of the components of the systematic uncertainty is given in Table 5.30. The dominant uncertainty comes from the theoretical description of $t\bar{t}$ production. Additionally the extracted value of $C(t\bar{t})$ is $1.0000 \pm +0.0584$ and $R(\mu/e)$ is 1.0000 ± 0.0104. The sum of squares of the specified groups of uncertainties does not give the total systematics because of the correlations. Figure 5.13 shows the nuisance parameter correlation matrix for the Asimov fit with a threshold of 20% for the minimum correlation. This plot shows the correlation between parameters, it is important to understand the correlation between parameters as correlations mean that their systematic uncertainties affect each other.

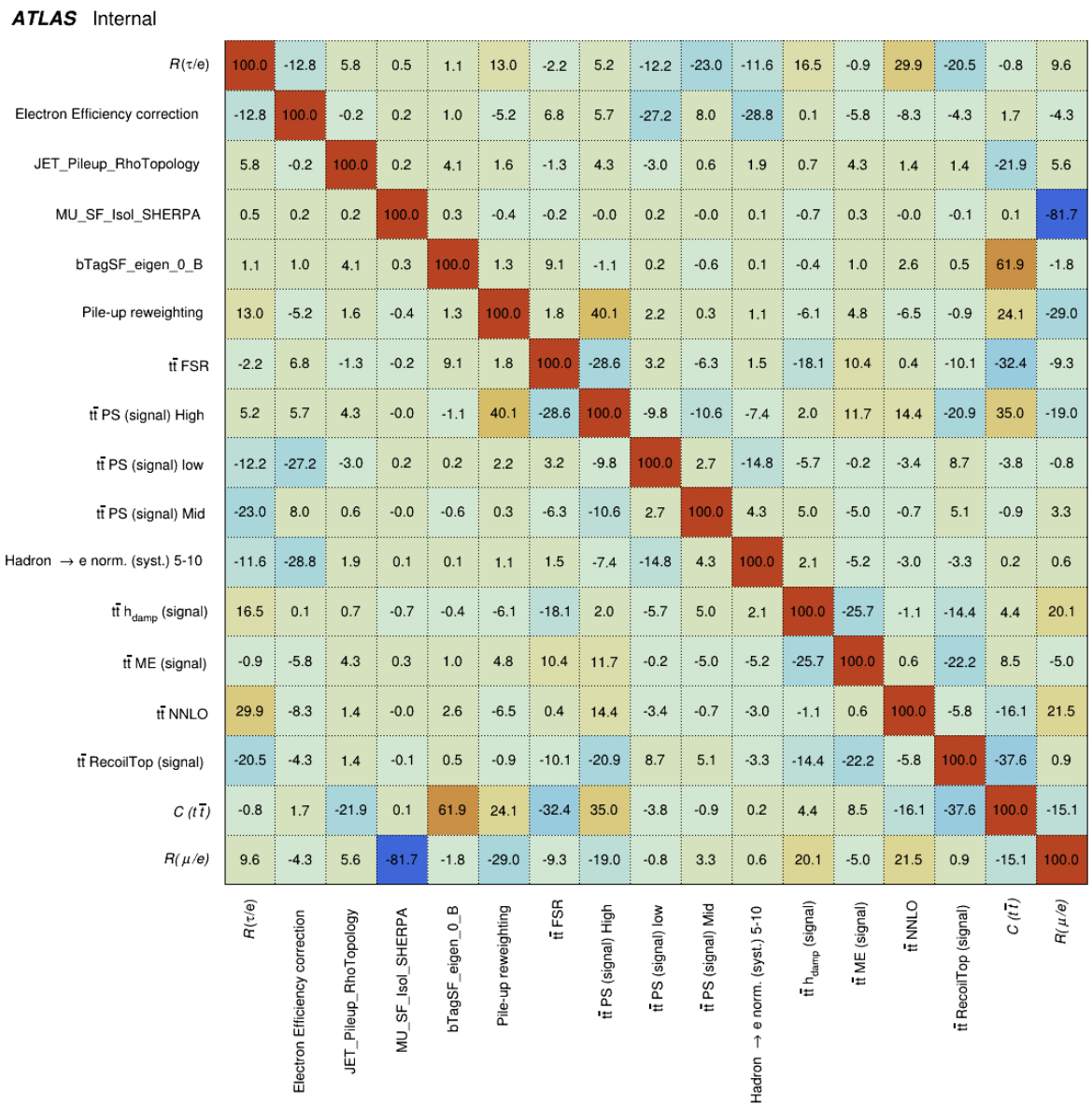

Figure 5.13: Fit parameter correlation matrix for Asimov fit.

Uncertainty group	$\Delta R(\tau/e)$
Data statistics	0.0126
Systematics total	0.0195
- Data-driven	0.0040
- Theory	0.0114
- Electrons resolution	0.0024
- Electrons scale	0.0028
- Electrons reconstruction	0.0031
- Electrons identification	0.0011
- Electrons isolation	0.0004
- Muons	0.0003
- Jets	0.0026
- Jets energy resolution	0.0030
- Jets flavour	0.0014
- Instrumental other	0.0045
- Normalisation factors	0.0001
- Limited MC statistics	0.0031
$BR(W \to \tau\nu \to e\nu\nu\nu)$	0.0022
Total uncertainty	0.0233

Table 5.30: Breakdown of uncertainties in Asimov fit.

5.8.2.1 Nuisance parameter constraints

Figures 5.14, 5.15, 5.17, and 5.19 show the nuisance parameter pulls and constraints for Asimov fit. In particular, Figure 5.17 shows the pulls related to various scale factor modification of electron reconstruction, identification, and isolation.

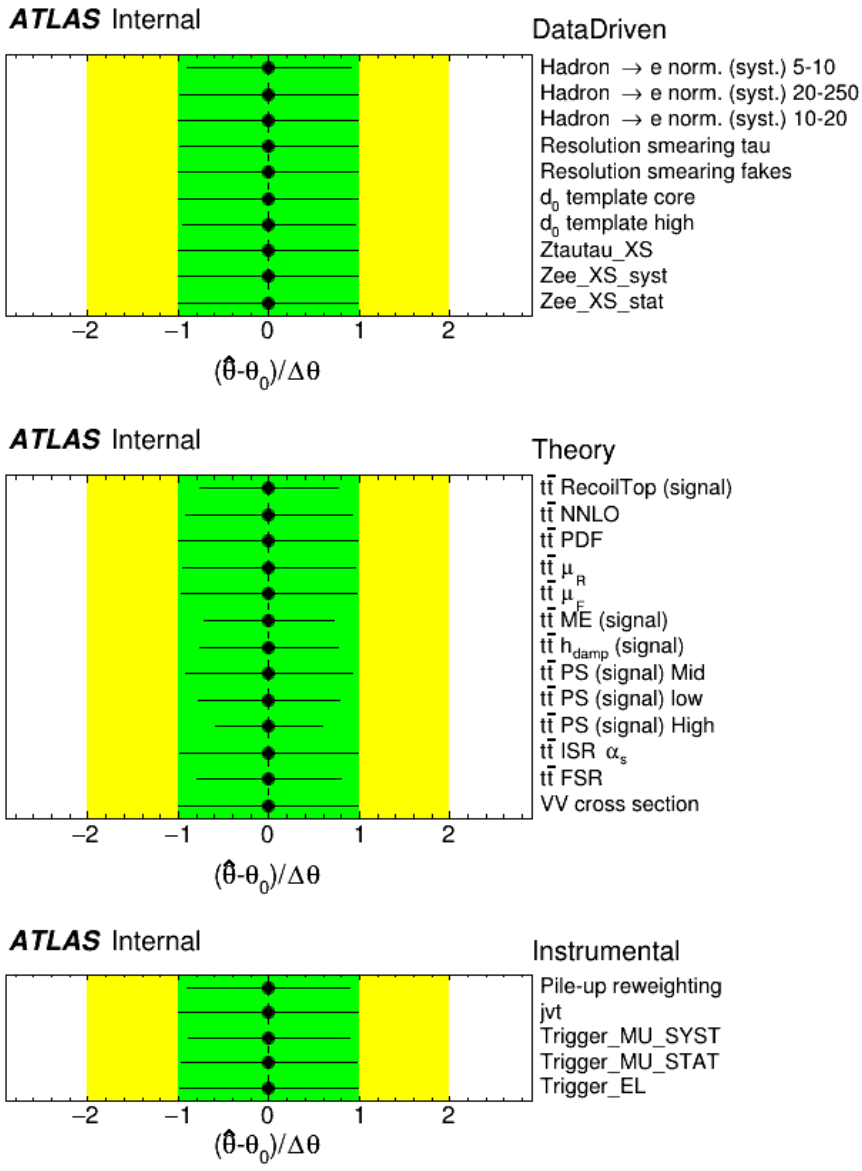

Figure 5.14: Nuisance parameter pulls and constraints for the groups of uncertainties for Data Driven (above), Theory (middle), and Instrumental Other (below) in the Asimov fit.

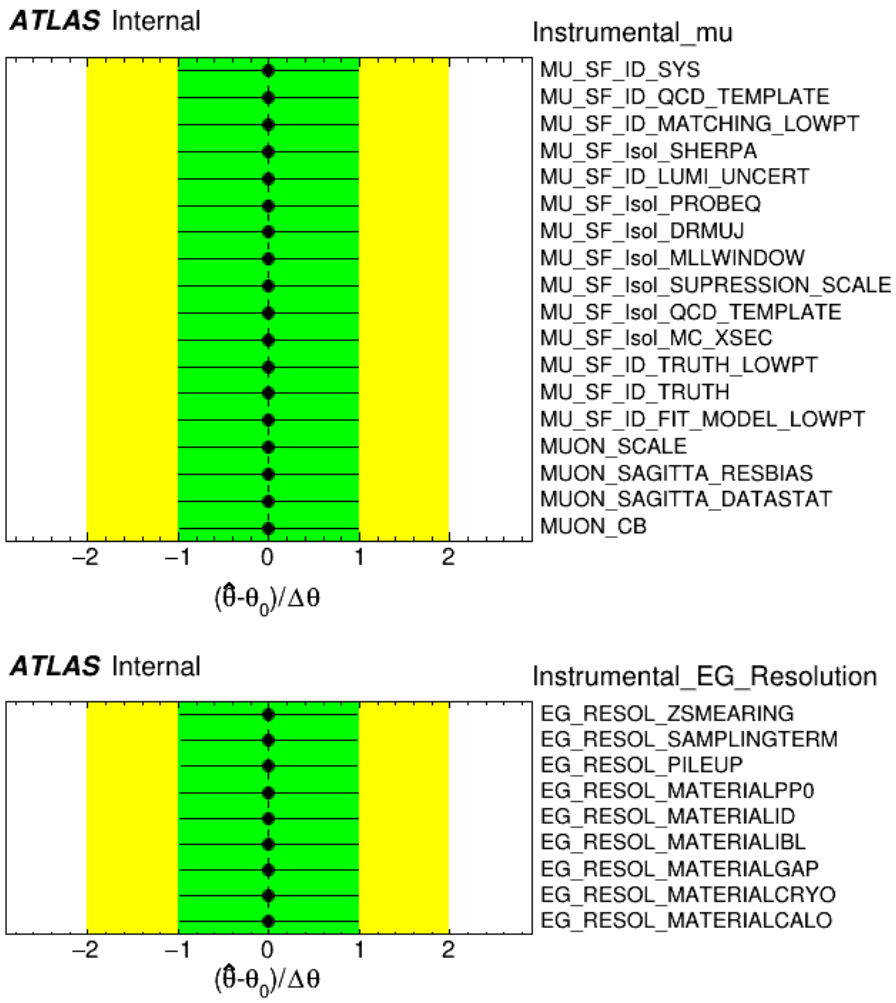

Figure 5.15: Nuisance parameter pulls and constraints for the groups of uncertainties: Muons and Electron resolution in the Asimov fit

The constraints of the most uncertainties are related to their p_T dependence. To confirm this, the fit is performed inclusively in electron p_T (i.e. without division in separate p_T regions) and observe that essentially all the constraints disappear. The corresponding plots of the nuisance parameters from this fit are shown in Figure 5.21. Note that the uncertainties for Hadron $\rightarrow e$ norm. (syst) and $t\bar{t}$ PS (signal) are treated as single components in this alternative fit because there is no splitting into different p_T regions. It can be seen that all the constraints except for the uncertainty$t\bar{t}$ PS (signal) are completely relaxed, and the constraint on the uncertainty $t\bar{t}$ PS (signal) is relaxed to 75%.

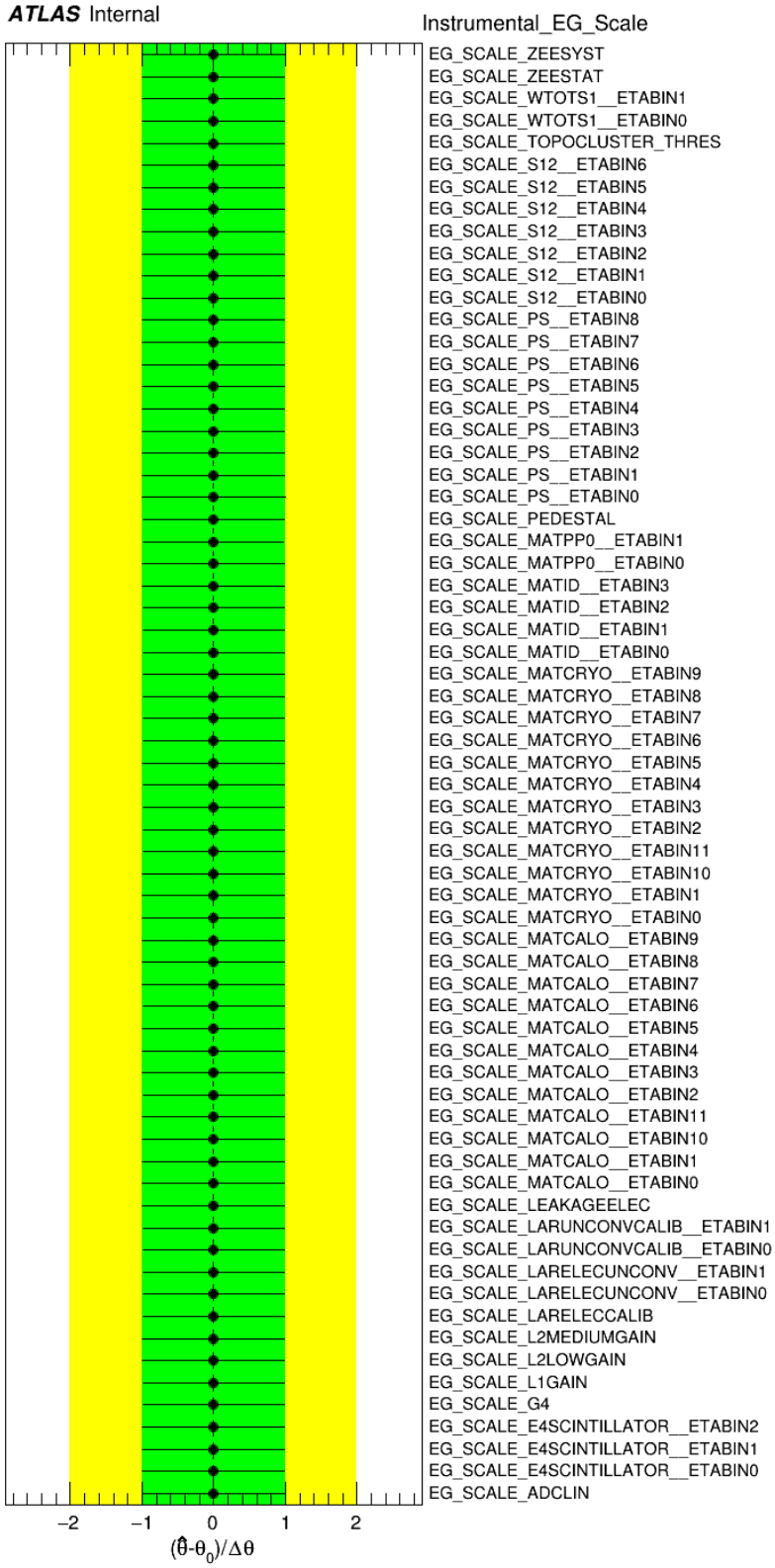

Figure 5.16: Nuisance parameter pulls and constraints for Electron scale in the Asimov fit

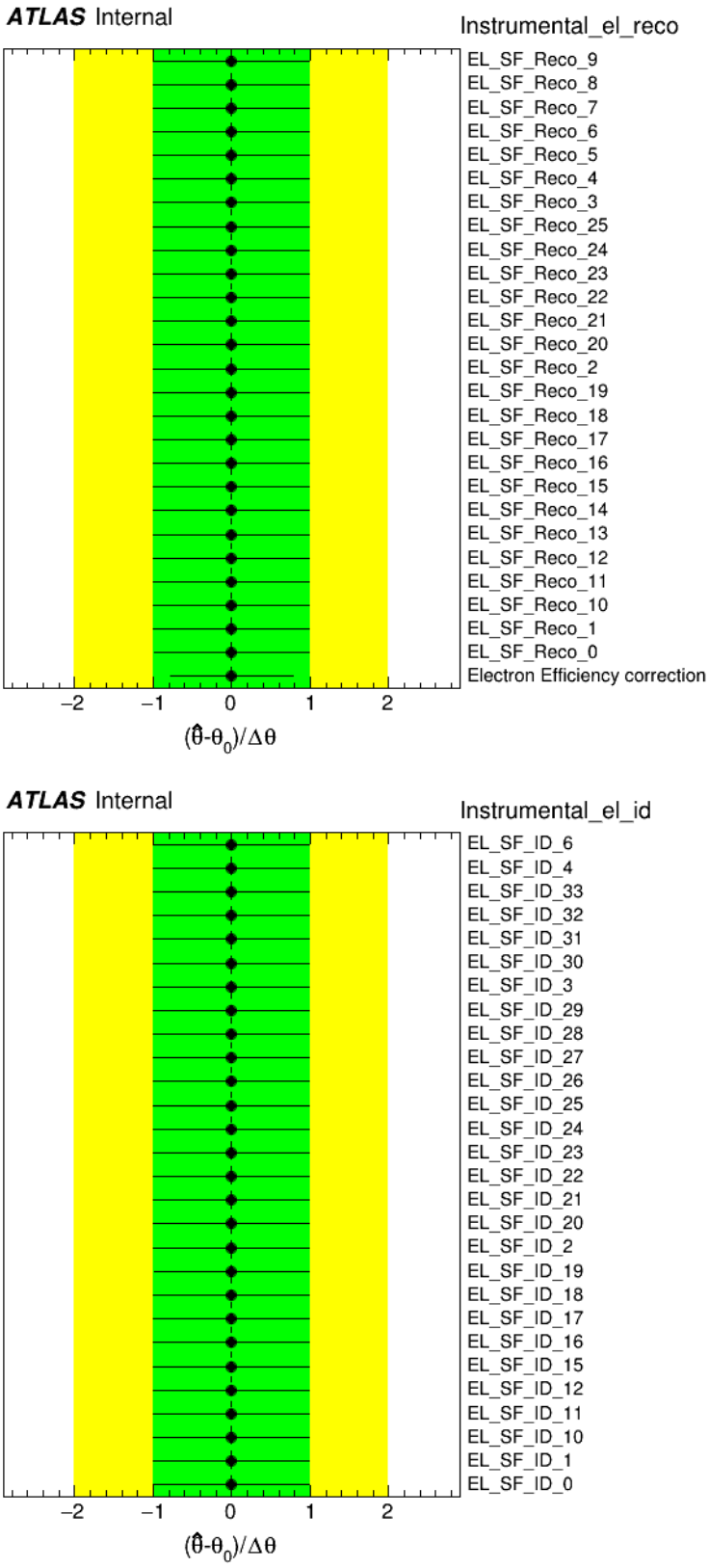

Figure 5.17: Nuisance parameter pulls and constraints for the groups of uncertainties Electron reconstruction and Electron identification in the Asimov fit.

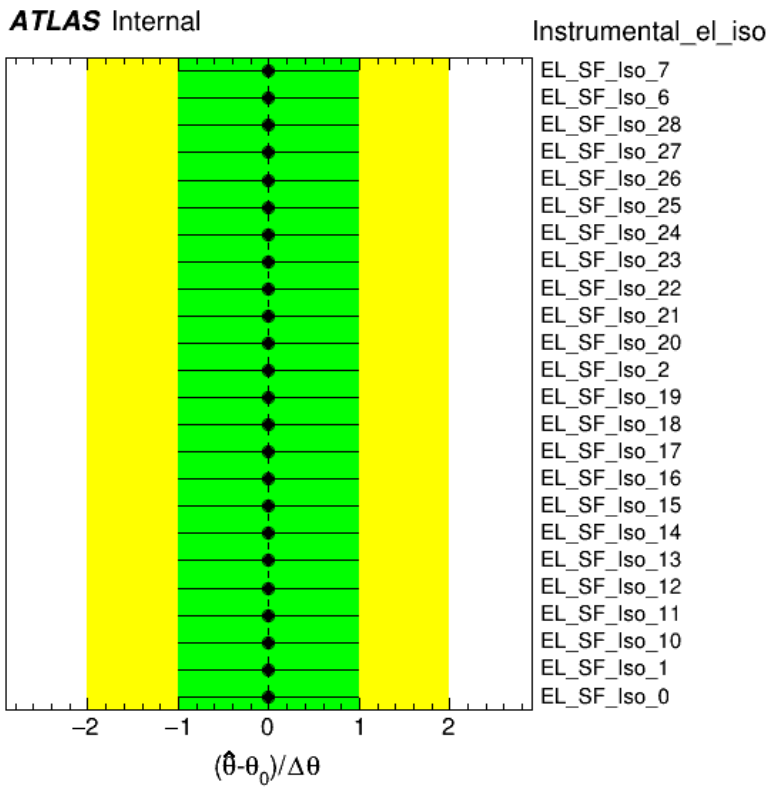

Figure 5.18: Nuisance parameter pulls and constraints for Electron isolation in the Asimov fit.

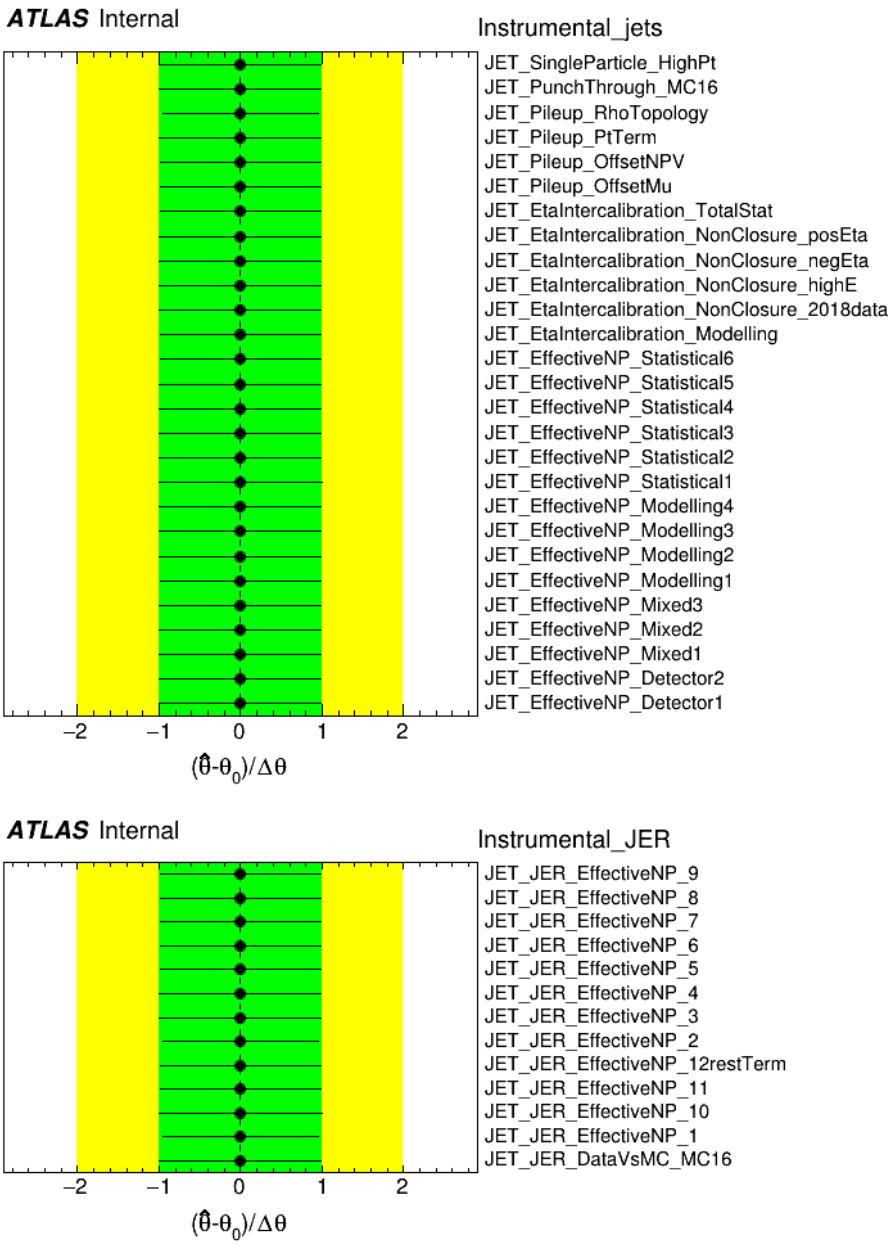

Figure 5.19: Nuisance parameter pulls and constraints for the groups of uncertainties Jets and Jets energy resolution in the Asimov fit.

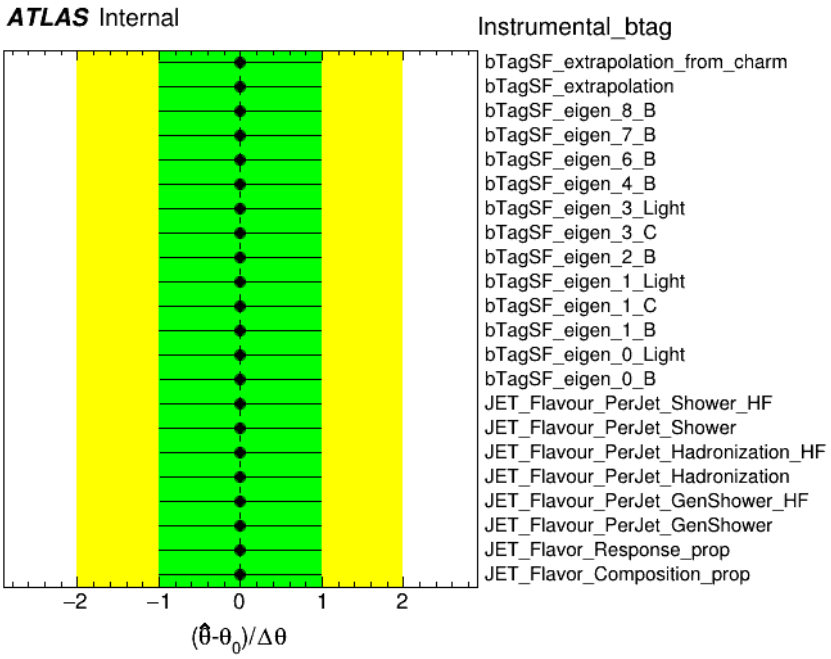

Figure 5.20: Nuisance parameter pulls and constraints for Jets flavour in the Asimov fit.

5.8.2.2 Nuisance parameter ranking (effect on POI)

Figure 5.22 shows the nuisance parameter ranking for all fit parameters.

The highest-ranked uncertainties are typically those which modify the d_0 shape or yields differently for prompt- and τ-leptons or those that affect the shape or yields of the fake electron background.

The largest systematic uncertainties are related to the modelling of the $t\bar{t}$ production: $t\bar{t}$ NNLO correction, $t\bar{t}$ parton shower, and gluon recoil systematics ($t\bar{t}$ RecoilTop). Other systematics uncertainties related to the $t\bar{t}$ production are also ranked high.

The next leading systematic uncertainty is produced by the variation of fake electrons with p_T in the range between 5 and 10 GeV.

The next leading systematic uncertainty is related to the electron reconstruction efficiency.

The pile-up uncertainty also produces a large impact on the result. This is due to the residual effect on electron p_T modelling that arises due to the different behaviour of different pile-up conditions.

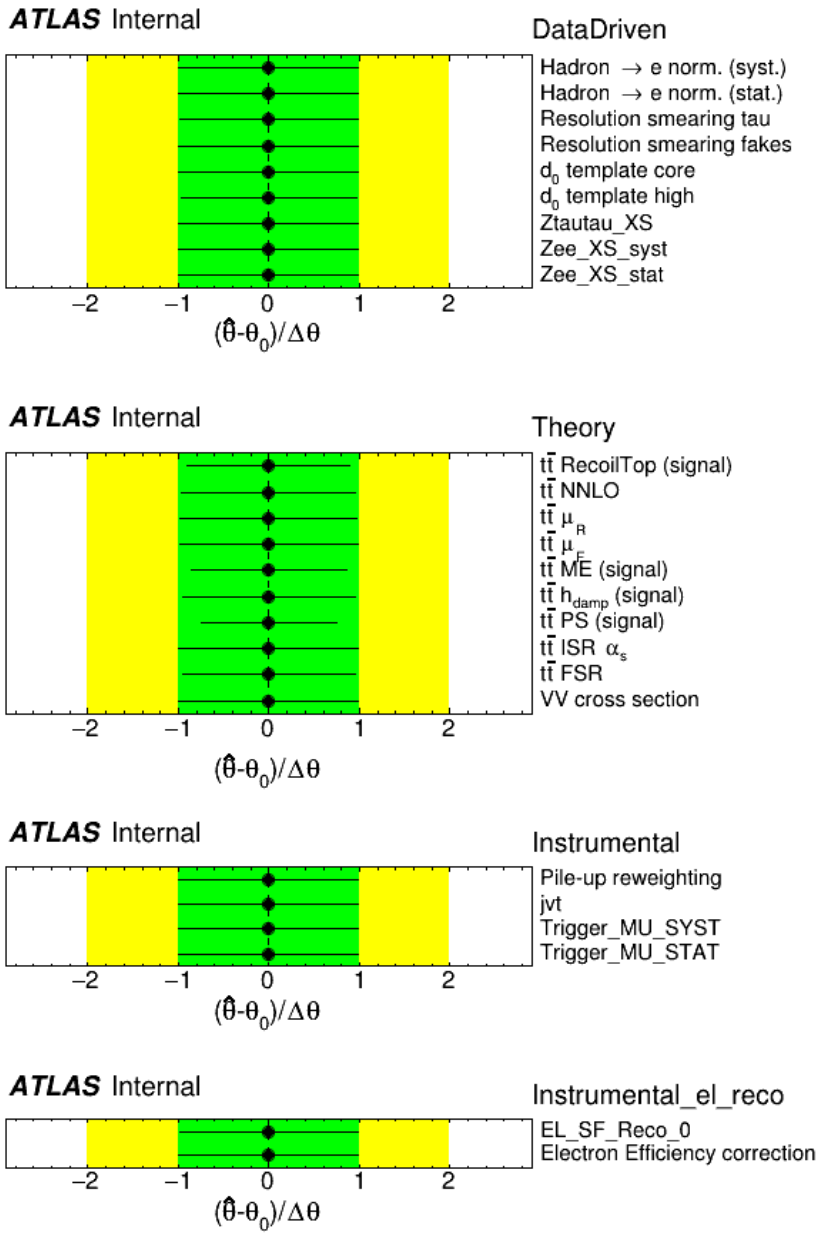

Figure 5.21: Nuisance parameter pulls and constraints for Asimov fit inclusively in electron p_T.

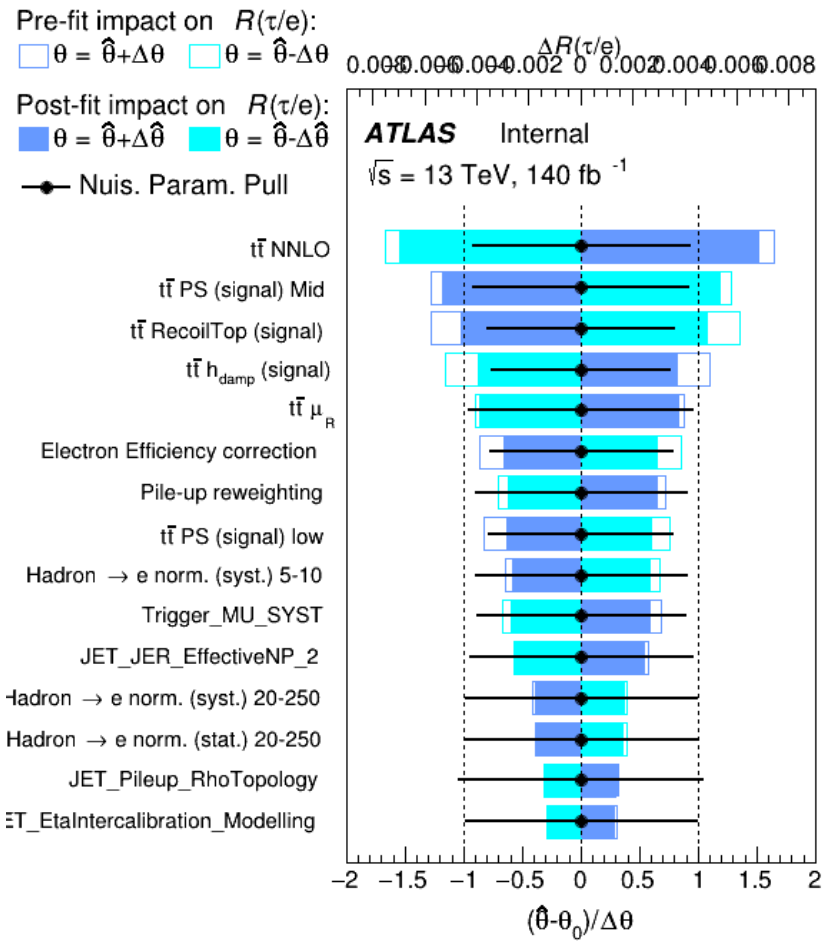

Figure 5.22: Nuisance parameter ranking of all fit parameters for Asimov fit.

5.9 Results

5.9.1 Blinding Procedure

The parameter of interest was blinded such that the result could not be biased by the analysers while checking the robustness of the fit and sensitivity. At the as time of submission was the analysis paper was awaiting publication and could not be included in the thesis. The paper is now published [1], with the result unblinded. There have been changes to some areas of the analysis since the work presented in the thesis that affect the final value of $R(\tau/e)$ and its uncertainty, therefore the result from the work presented in this thesis and the final result from the paper will be presented.

5.9.2 Prefit Results

This section shows the distributions for the input to the fit. The yields refer to the number of observed events for each process, in this case before the fit is performed. The yields will change post-fit as the fit will adjust the Monte Carlo to match the data better. The data/MC plots show a comparison of the distribution of the impact parameter, d_0, for each channel and transverse momenta bin, before the fit.

5.9.2.1 Yields

Tables 5.31 and 5.32 show the prefit yields for the ee and μe channels. This is summarised in the pie charts shown in Figure 5.36. It can be seen that the largest contributions in the medium to high p_T bins come from prompt electrons from the decay of a top quark to a W-boson and the intermediate electrons that result from the decay of a top quark to a W-boson to a τ lepton to an electron. In the low p_T bin the contribution of these events is of a similar level. The next largest contribution comes from fake electrons (from hadron decay and photon conversion). The proportion of fake events is higher in the lower p_T bins.

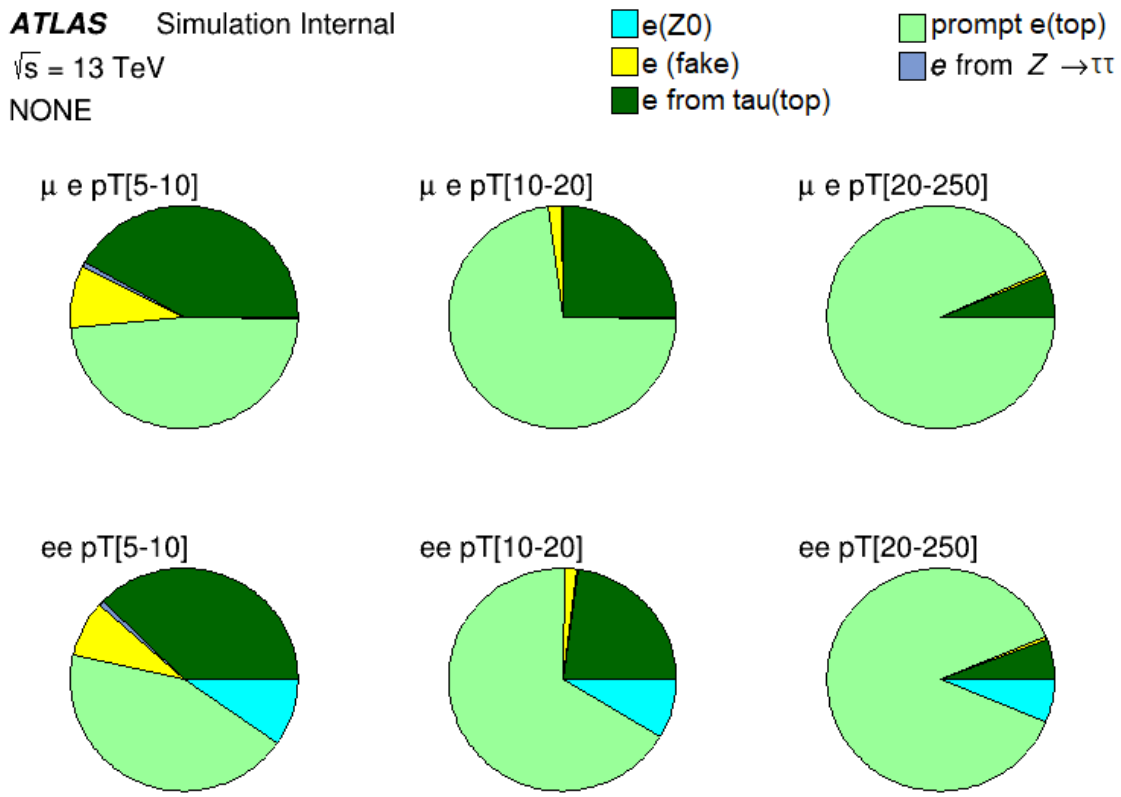

Figure 5.23: Prefit signal region composition It can be seen the signal of prompt and intermediate electrons makes up the majority of the events, with a small contribution from background events.

	μe $p_T = [7-10]$ GeV	μe $p_T = [10-20]$ GeV	μe $p_T = [20-250]$ GeV
prompt e(top)	1310 ± 80	13300 ± 800	182000 ± 10000
e from τ(top)	1130 ± 80	4530 ± 270	12300 ± 800
e(fake)	400 ± 40	528 ± 21	1480 ± 130
$e(Z^0)$	0 (0)	0 (0)	0 (0)
prompt e (not from Z or t)	5 ± 2	23 ± 7	180 ± 50
e from $Z^0 \to \tau\bar{\tau}$	23 ± 1	80 ± 2	131 ± 3
Total	2800 ± 150	18300 ± 1000	196000 ± 11000
Data	2768	18783	196552

Table 5.31: Yields of the analysis for the μe channel

	$ee\ p_T = [7-10]$ GeV	$ee\ p_T = [10-20]$ GeV	$ee\ p_T = [20-250]$ GeV
prompt $e(top)$	1230 ± 90	11900 ± 700	162000 ± 9000
tt(tau)	1050 ± 70	4050 ± 250	10800 ± 800
e(fake)	320 ± 50	430 ± 17	1180 ± 90
e(Z0)	326 ± 4	1871 ± 15	13900 ± 110
prompt e (not from Z or t)	12 ± 4	58 ± 17	550 ± 170
e from $Z^0 \to \tau\tau$	24 ± 1	77 ± 2	125 ± 3
Total	2930 ± 170	18300 ± 900	188000 ± 10000
Data	2928	19047	189945

Table 5.32: Yields of the analysis for the ee channel

5.9.2.2 Data/MC Plots

The data/MC plots show a comparison of the distribution of the impact parameter, d_0, for each channel and transverse momenta bin, before the fit. Good agreement with data and MC is seen in Figure 5.24. It can be seen, however, that the agreement becomes poor at higher values of d_0. The χ^2, ndf and probability for each channel and p_T bin are shown in Table 5.33. From Figure 5.24 and Table 5.33 it can be seen that the χ^2 for MC and data is particularly poor for the medium p_T bin. This poor χ^2 is addressed further in the post-fit results.

Lepton Channel	p_T bin	χ^2	NDF	Probability
e-e	7-10 GeV	3.3	8	0.91
	10-20 GeV	10.7	8	0.22
	20-250 GeV	4.3	8	0.83
$\mu - e$	7-10 GeV	7.7	8	0.46
	10-20 GeV	16.1	8	0.04
	20-250 GeV	8.0	8	0.43

Table 5.33: Pre-fit χ^2, number of degrees of freedom and probability for each channel and p_t bin.

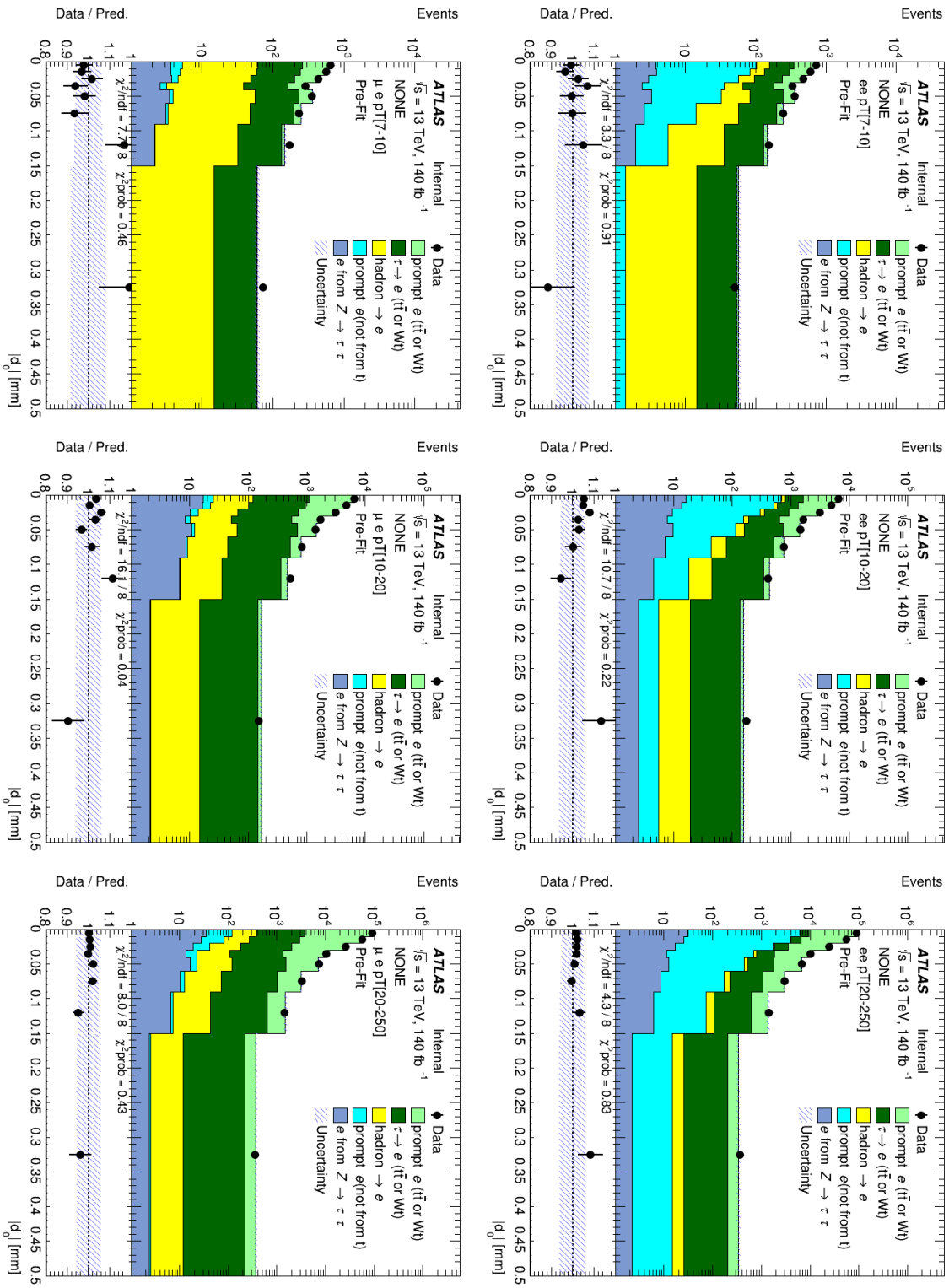

Figure 5.24: Distributions of d_0 for the ee-channel (top) and μe-channel (bottom) before the fit.

5.9.3 Postfit Results

This section presents the post-fit results including the post-fit data/MC agreement, the breakdown of the uncertainties on $R(\tau/e)$, and the discussion of the nuisance parameters and their impact on $R(\tau/e)$. The data/MC plots show a comparison of the distribution of the impact parameter, d_0, for each channel and transverse momenta bin, before the fit. The breakdown of uncertainties shows the contribution of each type of systematic to the overall uncertainty of the analysis. The discussion of the impact of the nuisance parameters on the measurement of $R(\tau/e)$ aims to highlight and explain the systematics in the analysis that contribute the most to the systematic uncertainty.

5.9.3.1 Analysis of (blinded) fit to data

The nuisance parameter pulls for different groups of systematic uncertainties are shown in Figures 5.25, 5.26, 5.28 and 5.30. In particular, Figure 5.28 shows the pulls related to various scale factor modification of electron reconstruction, identification, and isolation. The normalization parameter $C(t\bar{t})$ which controls the overall normalization of $t\bar{t}$ and Wt processes is extracted as 1.023 ± 0.055. It should be noted that this analysis is not designed to extract the unfolded top cross-section. Therefore a measurement of the top cross-section is not claimed with this value but a normalization of simulation to data. The factor $R(\mu e)$ applied to the events in μe sample is found to be 0.981 ± 0.010. It is consistent with unity within two standard deviations.

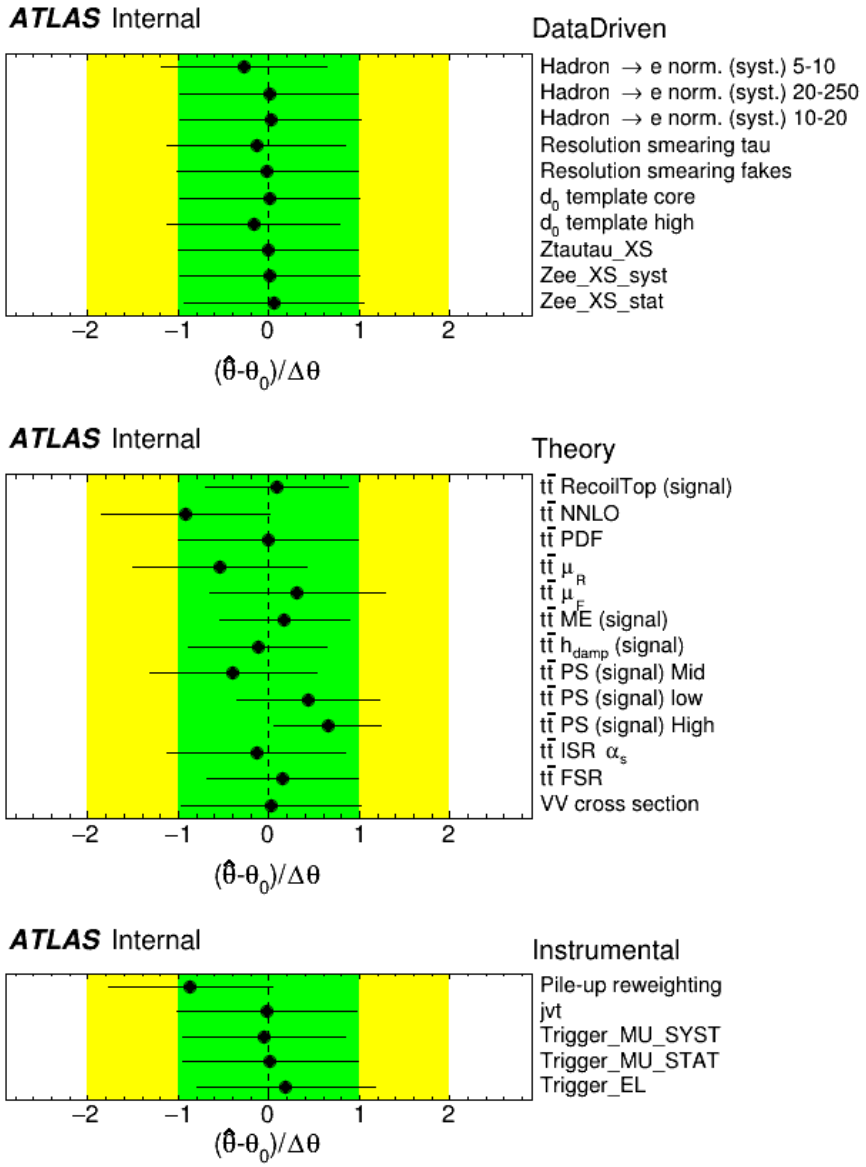

Figure 5.25: Nuisance parameter pulls and constraints for the groups of uncertainties: DataDriven (top), Theory (middle), and Other Instrumental (bottom) in fit to data.

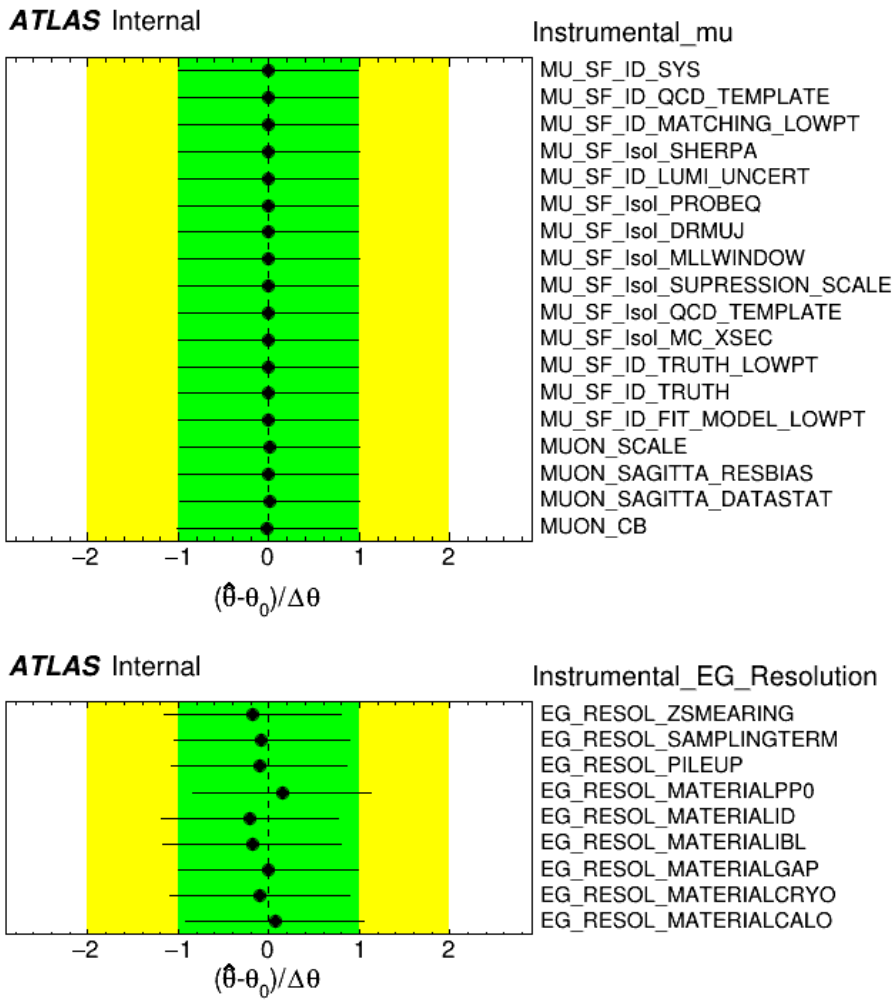

Figure 5.26: Nuisance parameter pulls and constraints for the groups of uncertainties: Muons (top) and Electron resolution (bottom) in fit to data.

The fit parameter covariance matrix is shown in Figure 5.32 with a threshold of 20% for the minimum threshold. There are no significant changes with respect to the Asimov fit shown in Fig. 5.13. The effect of each nuisance parameter on $R(\tau/e)$ pre- and post-fit and the ranking by largest post-fit effect is shown in Figure 5.33. The ordering of the ranking plot is very consistent with that of the Asimov fit, implying that there are no major issues with the fit to data.

Several parameters are pulled in the fit. Those related to the theory uncertainties and electron identification are reduced significantly if the fit is performed inclusively in p_T rather than in three p_T bins. The corresponding pulls are shown in figure 5.34.

5.9.4 Post-fit data/MC agreement

The obtained value of $R(\tau/e)$ for the analysis outlined in this analysis was found to be 1.034 ± 0.023. This value is different than that presented in the paper [1] where $R(\tau/e) = 0.975 \pm 0.024$, as several minor changes were made to the analysis as part of the approval procedure for publication, which did not begin in earnest until after the completion of the PhD. A detailed breakdown of the uncertainties is given in Table 5.34.

The data/MC plots show a comparison of the distribution of the impact parameter, d_0, for each channel and transverse momenta bin, before the fit. There is overall good agreement between data and MC post-fit, as shown in figure 5.35. It can be seen, however, that the agreement becomes poorer at higher values of d_0, similarly to the pre-fit distributions. However, it can be seen by comparing the pre- and post-fit d_0 distributions that there is an improvement in agreement post-fit for these higher d_0 values. Table 5.35 shows the value of χ^2/ndf for the comparison of data and MC. Overall, the agreement between data and MC improves after the fit. Like in the pre-fit results, from Figure 5.35 and Table 5.35 it can be seen that the χ^2 for MC and data is particularly poor for the medium p_T bin. In the e-e channel, this χ^2 is somewhat improved, however the χ^2 is still poor for the $\mu - e$ channel. The poor data/MC agreement for this p_T region is likely due to the lower statistics for this region. In comparison to the analysis comparing $\tau - \mu$, this region has 4 times fewer statistics in the $\tau - e$ analysis. There are also 2 times fewer statistics for the 20-250 GeV p_T region compared to the $\tau - \mu$ analysis. When testing with an Asmiov dataset with more statistics in these regions it was found the systematics were reduced.

Tables 5.37 and 5.36 show the post-fit yields in the six regions.

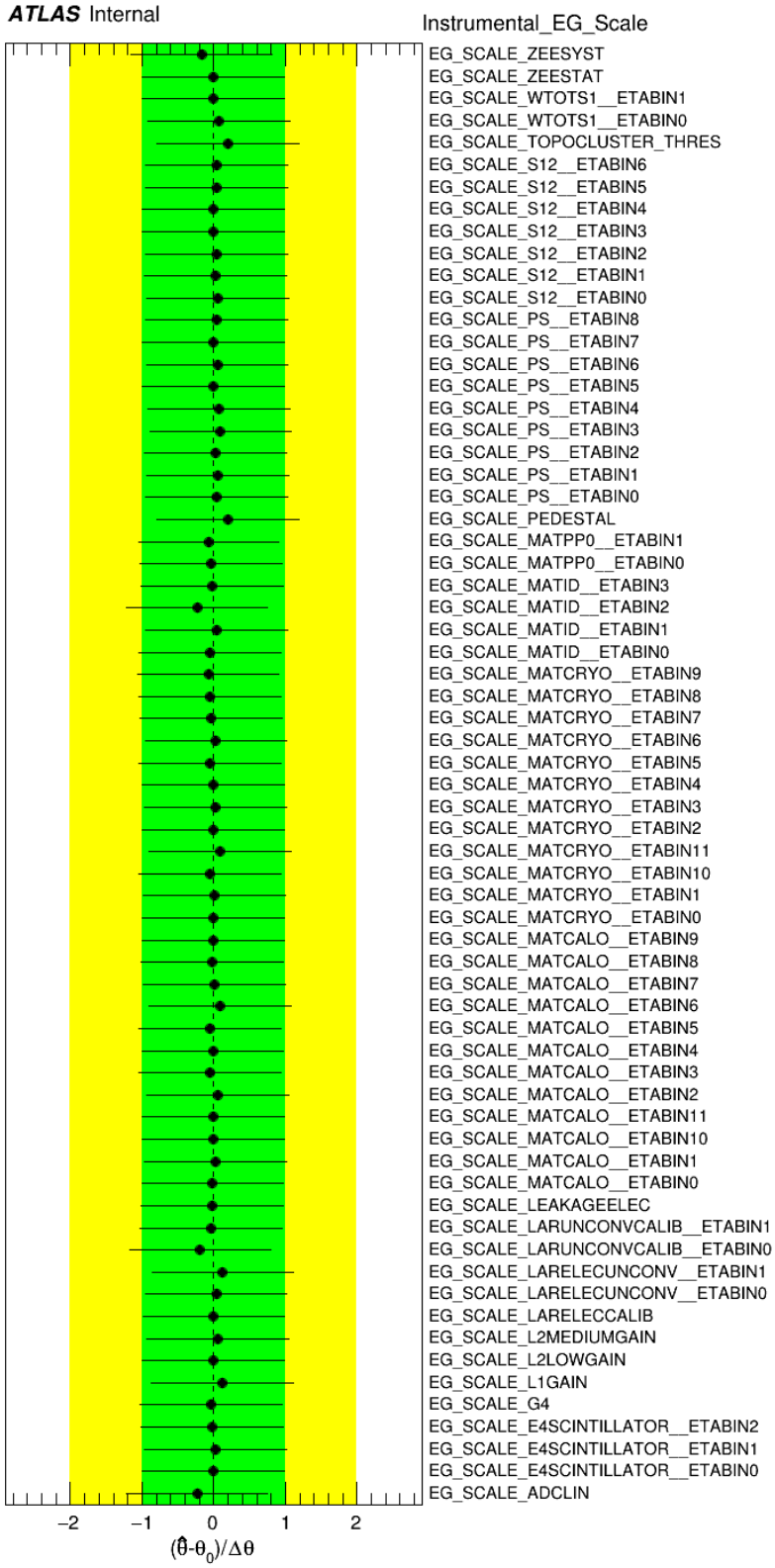

Figure 5.27: Nuisance parameter pulls and constraints for Electron scale in fit to data.

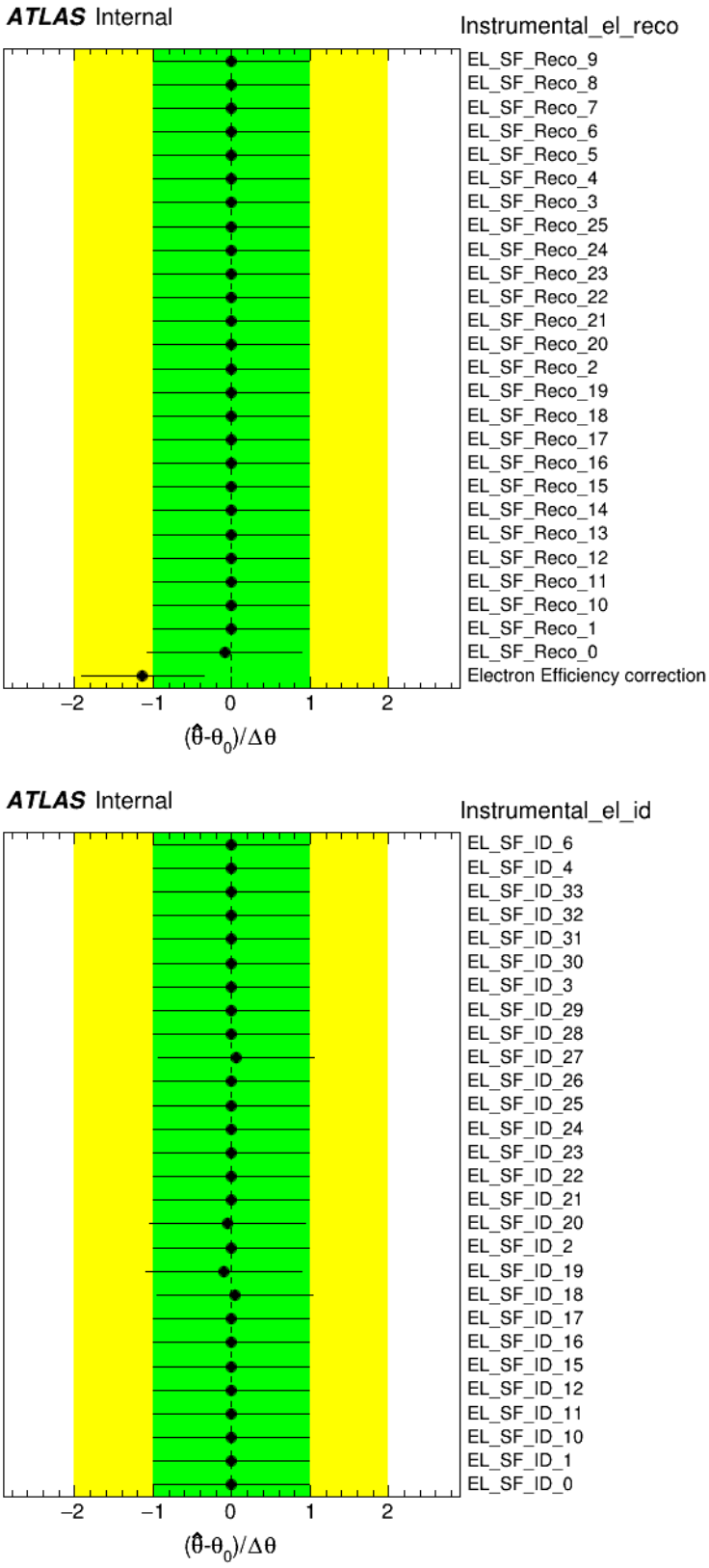

Figure 5.28: Nuisance parameter pulls and constraints for the groups of uncertainties: Electron reconstruction (top) and Electron identification (bottom) in fit to data.

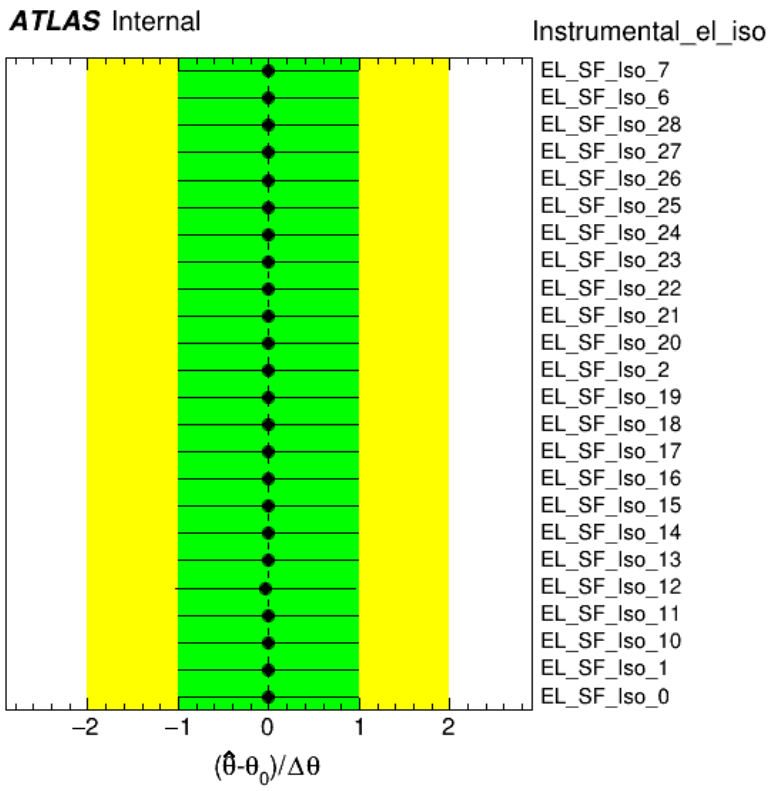

Figure 5.29: Nuisance parameter pulls and constraints for Electron isolation in fit to data.

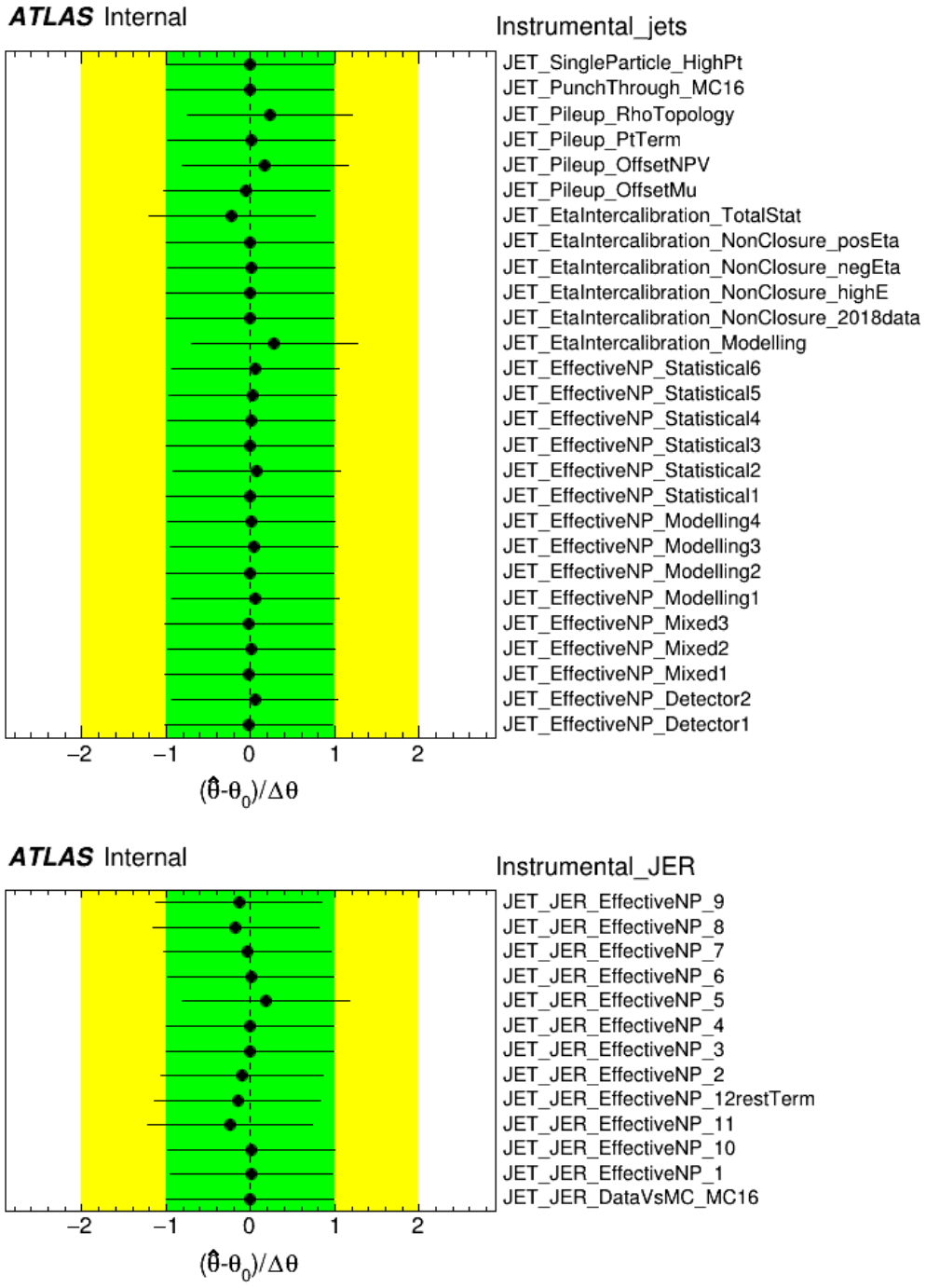

Figure 5.30: Nuisance parameter pulls and constraints for the groups of uncertainties Jets (top) and Jets energy resolution (bottom) in fit to data.

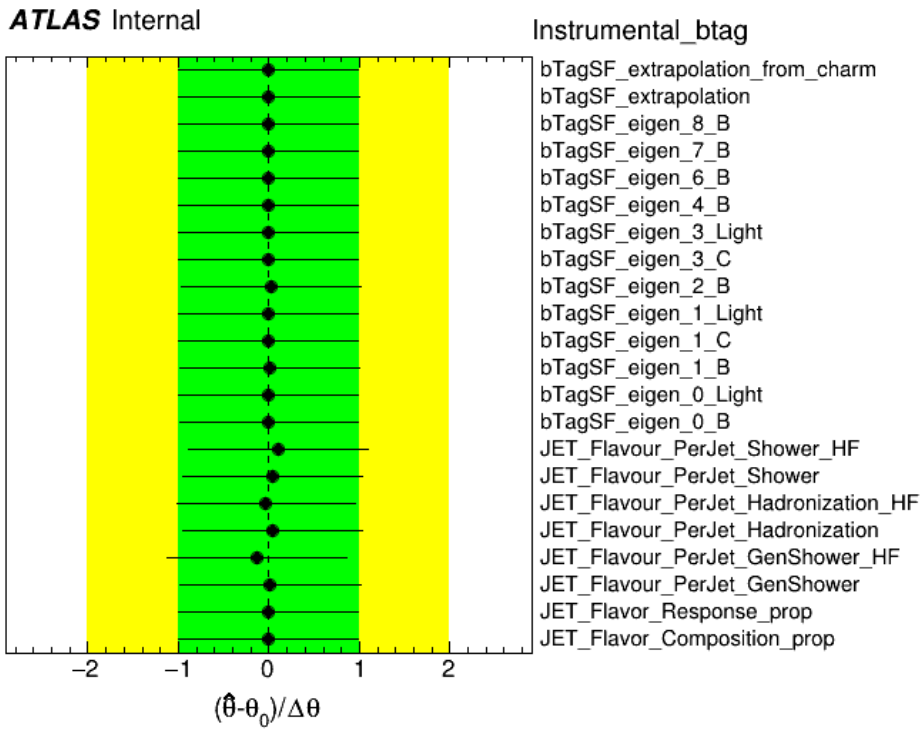

Figure 5.31: Nuisance parameter pulls and constraints for Jets flavour in fit to data.

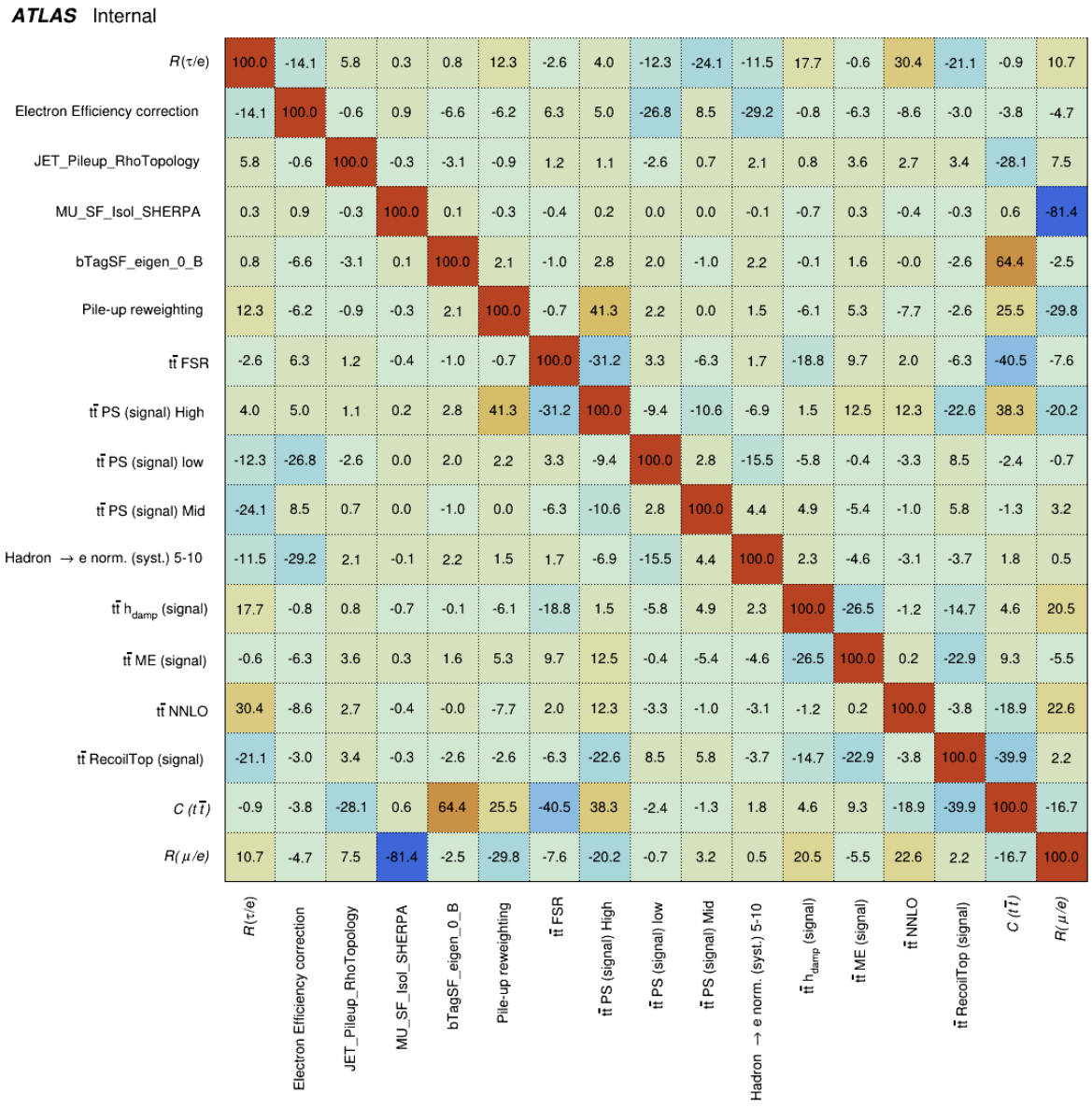

Figure 5.32: Fit parameter correlation matrix for fit to data.

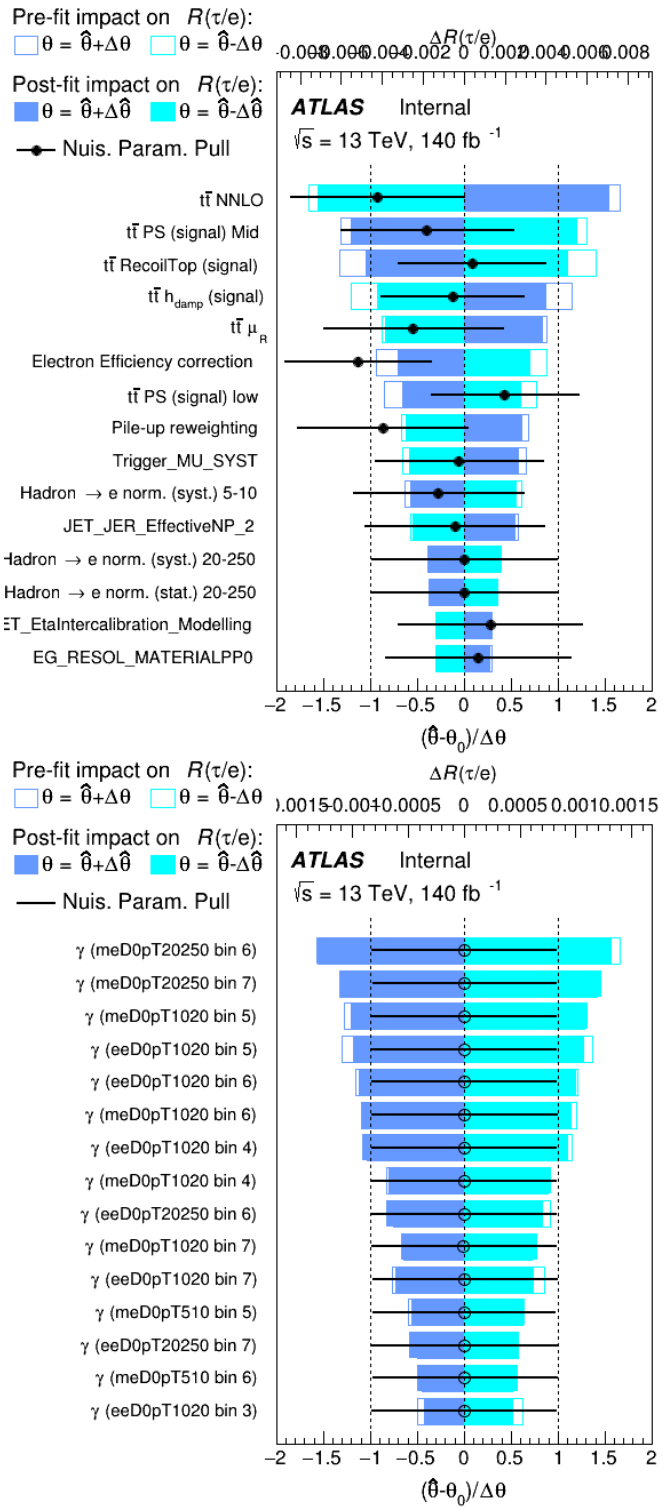

Figure 5.33: Nuisance parameter ranking for systematic uncertainties for fit to data. The top plot shows the 15 most significant uncertainties while the bottom shows only those from MC statistics (none of which rank in the top 15 most important systematic uncertainties in the analysis)

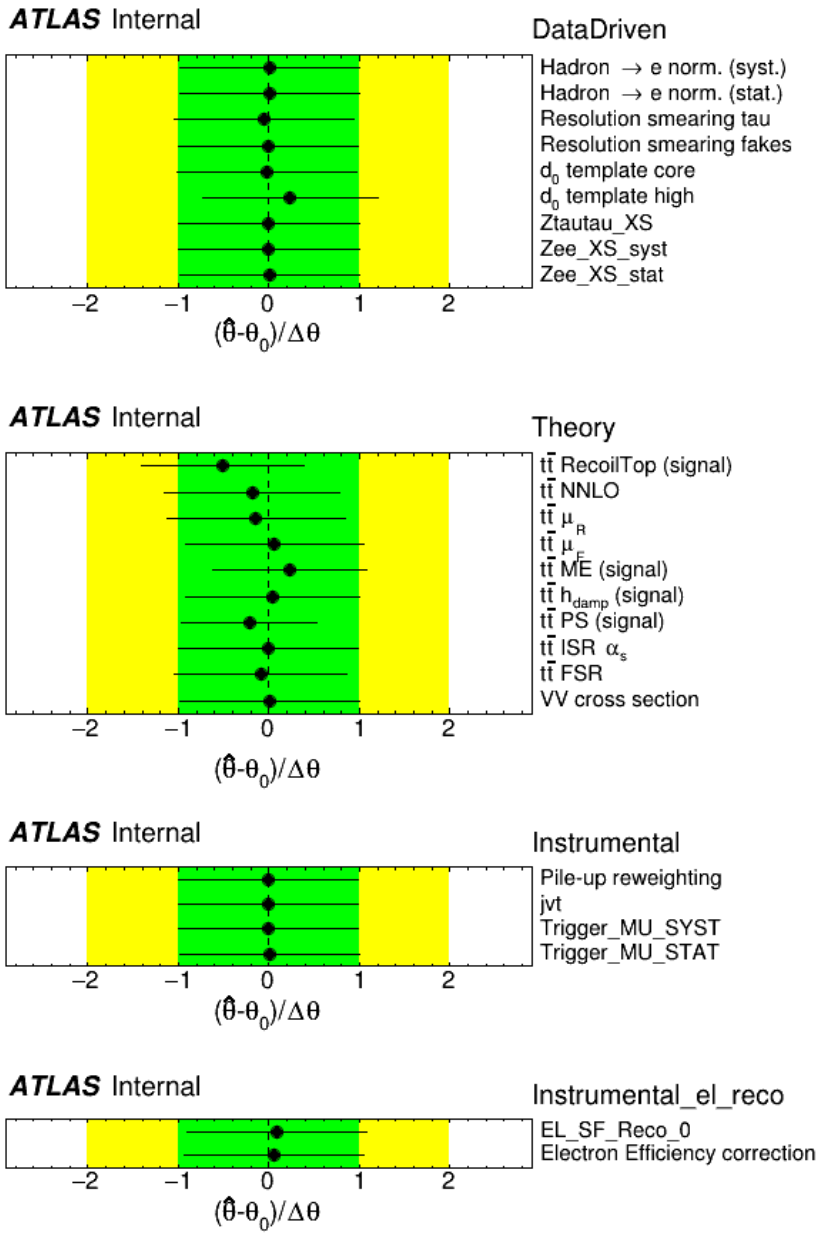

Figure 5.34: Nuisance parameter pulls and constraints for fit to data inclusively in electron p_T.

Uncertainty group	$\Delta R(\tau/e)$
Data statistics	0.0124
Systematics total	0.0197
- Data-driven	0.0041
- Theory	0.0119
- Electrons resolution	0.0025
- Electrons scale	0.0027
- Electrons reconstruction	0.0031
- Electrons identification	0.0011
- Electrons isolation	0.0002
- Muons	0.0004
- Jets	0.0027
- Jets energy resolution	0.0031
- Jets flavour	0.0015
- Instrumental other	0.0045
- Normalisation factors	0.0025
- Limited MC statistics	0.0031
$BR(W \to \tau\nu \to e\nu\nu\nu)$	0.0022
Total uncertainty	0.0234

Table 5.34: Breakdown of uncertainties in fit to data.

Lepton Channel	p_T bin	χ^2	NDF	Probability
e-e	7-10 GeV	3.0	8	0.93
	10-20 GeV	9.1	8	0.33
	20-250 GeV	4.1	8	0.85
$\mu - e$	7-10 GeV	6.4	8	0.60
	10-20 GeV	15.0	8	0.06
	20-250 GeV	7.9	8	0.44

Table 5.35: Post-fit χ^2,number of degrees of freedom and probability for each channel and p_t bin.

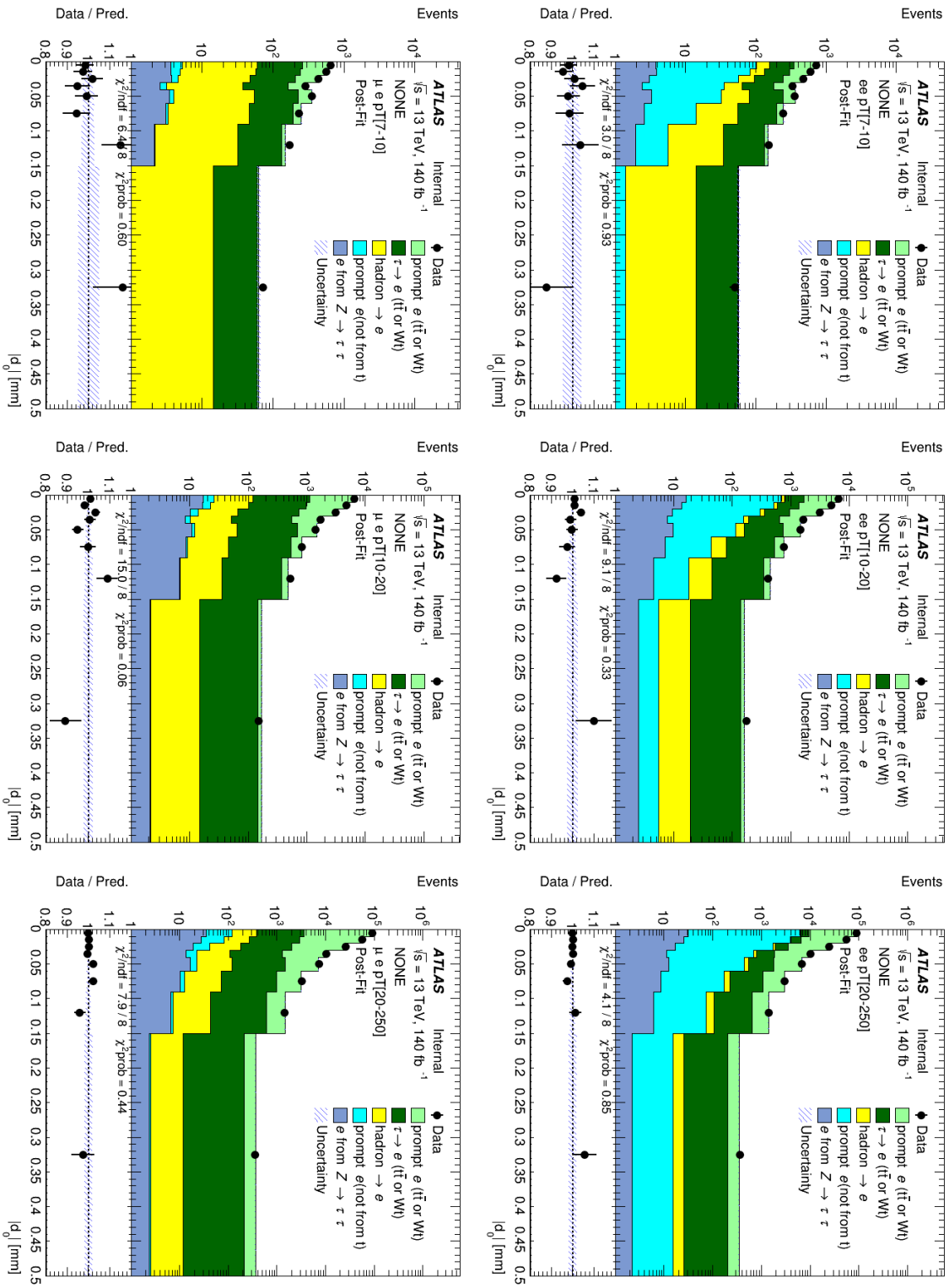

Figure 5.35: Distributions of d_0 for the ee-channel (top) and μe-channel (bottom) after the fit.

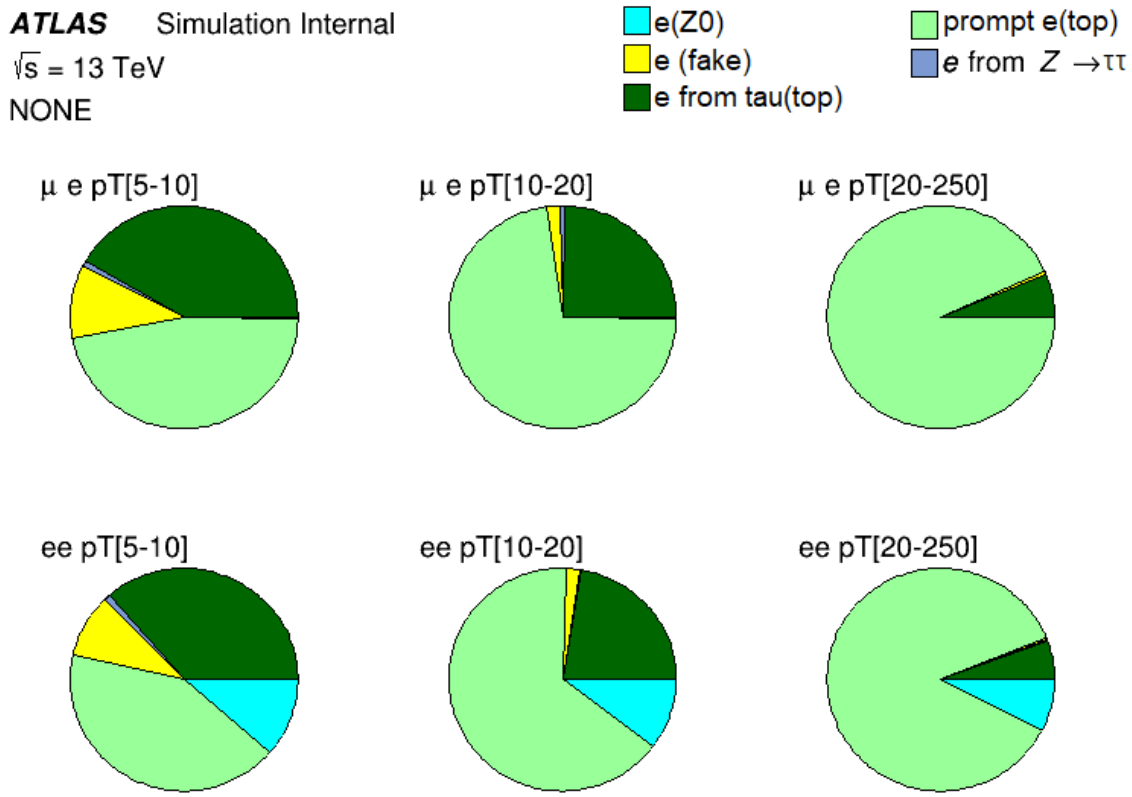

Figure 5.36: Post-fit signal region composition It can be seen the signal of prompt and intermediate electrons makes up the majority of the events, with a small contribution from background events.

	μe $p_T = [7-10]$ GeV	μe $p_T = [10-20]$ GeV	μe $p_T = [20-250] GeV$
prompt $e(top)$	1300 ± 30	13630 ± 130	183300 ± 500
tt(tau)	1150 ± 40	4640 ± 100	12210 ± 330
e(fake)	290 ± 40	374 ± 13	820 ± 60
e(Z0)	0 (0)	0 (0)	0 (0)
prompt e (not from Z or t)	5 ± 2	23 ± 7	180 ± 50
e from $Z^0 \to \tau\tau$	25 ± 1	88 ± 1	143 ± 1
Total	2780 ± 40	18760 ± 110	196700 ± 400
Data	2768	18783	196552

Table 5.36: Yields in the μe channel after the fit to data.

	$ee\ p_T = [7-10]$ GeV	$ee\ p_T = [10-20]$ GeV	$eep_T = [20-250]$ GeV
prompt $e(top)$	1248 ± 31	12310 ± 100	163800 ± 500
tt(tau)	1078 ± 34	4190 ± 100	10780 ± 320
e(fake)	280 ± 40	364 ± 12	780 ± 60
e(Z0)	326 ± 3	1873 ± 14	13910 ± 110
prompt e (not from Z or t)	12 ± 3	60 ± 17	570 ± 160
e from $Z^0 \to \tau\tau$	24 ± 1	77 ± 1	125 ± 1
Total	2960 ± 40	18880 ± 110	190000 ± 400
Data	2928	19047	189945

Table 5.37: Yields in the ee channel after the fit to data.

5.10 Conclusion

This section presented the measurement of $R(\tau/e)$ as an investigation into Lepton Flavour Universality violation. In the Standard Model, it is assumed $R(\tau/e) = 1$, however this is only an assumption and therefore needs to be tested. This was done by measuring the ratio of the branching fractions of $Br(W \to \tau)$ and $Br(W \to e)$ from the decay of top quarks. This was done using a 'tag and probe' method, utilising the decay of $t\bar{t}$ pairs by using one lepton from the decay of one of the quarks in the pair as the tag to select events on, and the other as a probe to perform physics analysis. Because of the $t\bar{t}$ pair, the tag and probe leptons can then be swapped and reused, such that both leptons can be the tag or probe, provided they pass the selection criteria. Prompt decays, decays that occur straight from a W-boson decay ($W \to e\nu_e$) and intermediate decays, decays that occur and then decay further ($W \to \tau\nu_\tau \to e\nu_e\nu_\tau$) are differentiated from each other based on their transverse momentum (p_T) and impact parameter (distance from the primary vertex, d_0).

$R(\tau/e)$ was found to be 1.033 ± 0.023 following the method outlined in this thesis. $R(\tau/e)$ was found to be 0.975 ± 0.024 after the full paper approval process at ATLAS [1].

$R(\tau/e)$ was found to be in agreement with the Standard Model prediction and therefore in disagreement with the tension with the Standard Model previously measured by LEP [13]. This result is consistent with the measurement recently performed by CMS [22], with the CMS

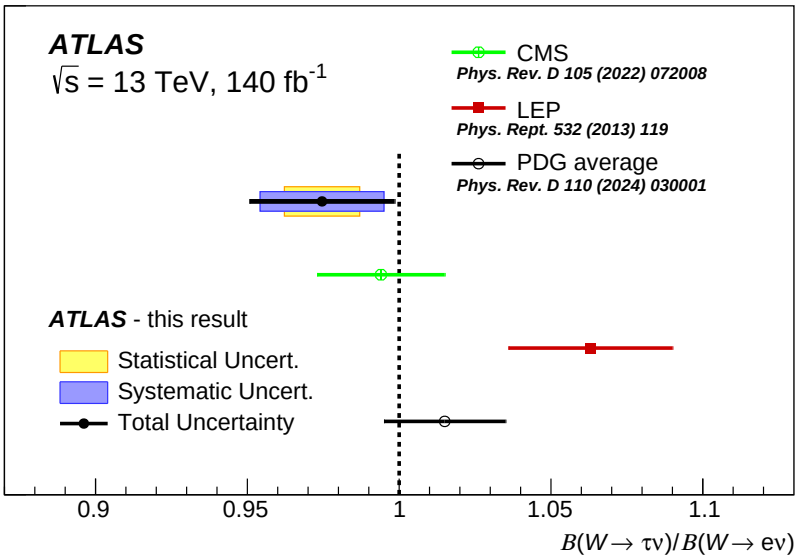

Figure 5.37: Results for all analyses measuring LFU with $Br(W \to \tau)/Br(W \to e)$, including the final paper result of this analysis [1]. It also includes the PDG average [76].

measurement being slightly more precise than the analysis outlined in this thesis. Further improvements to this analysis could include repeating the analysis with data from Run-3, making use of the higher statistics found with this higher centre-of-mass energy of 13.6 TeV and instantaneous luminosity at its peak of approximately 2.4×10^{34} cm^{-2} [99] as well as hardware improvements to the ATLAS detector, in particular to the ATLAS trigger system, allowing for more accurate data. This is likely to help improve accuracy with the electron events due to phenomena such as photon conversion in the detector that contribute towards fake leptons. The methodology for the estimation of fake leptons in this analysis is also a novel approach, and could be generalised to use in other analyses.

Chapter 6

Summary

The thesis details two projects worked on during my PhD. The first was the qualification task, which aimed to measure the efficiency of hard scatter identification at ATLAS with isolated leptons. This was done by developing methods for extracting misidentified Hard Scatter events. The first method was by estimating the position of the vertices in a particle event and then comparing these positions to the 'true' position of the event. This method was done with Release 21, an older version of ATLAS software. This method was found to find high misidentification of events in Z^0 decay events, and very low misidentification in $t\bar{t}$ decays. Another method was then developed as a comparison, also in release 21 which used a particular software package that would fit the vertices in an event to the true vertex. In this method, similar results to the estimation method were found. This method was also developed for release 22. This method in release 22 found that misidentification was low in all events. For the main physics analysis, the analysis aimed to measure the ratio of the branching ratios of the decay of W bosons to τ leptons and electrons, $R(\tau/e) = Br(W \to \tau\nu_\tau)/Br(W \to e\nu_e)$. These W bosons came from the decay of top or anti-top quarks. This was done due to the very large amount of top and anti-top pairs produced in the LHC, and the almost 100% probability these top and anti-top quarks will decay to W bosons. The majority of my work focused on the background estimations, which aimed to correct the affect of Drell-Yann processes on the analysis, as well as 'fake' leptons. The analysis of fake leptons in particular was a novel technique, which analysed the origin of leptons from different processes and used this to scale events based on these origins. After background processes were taken into account, the fit of $R(\tau/e) = Br(W \to \tau\nu_\tau)/Br(W \to e\nu_e)$ was performed. $R(\tau/e)$ was found to be 1.033 ± 0.023 following the method outlined in this thesis.

Appendix A

List of MC Samples

The list of MC samples used in this analysis are shown in Tables A.1 and A.2. In all cases, MC16a was used for 2015 and 2016 sample, MC16d for 2017 sample and MC16e for 2018 sample. For each sample we specify the p-tag used. and the cross-section used for the normalisation. The values of cross-sections are taken from the file
`/cvmfs/atlas.cern.ch/repo/sw/database/GroupData/dev/AnalysisTop/TopDataPreparation/XSection-MC16-13TeV.data`.
The last columns states whether full (FS) or fast (AF) simulation was used.

Table A.1: Top MC Samples

Sample	DSID	p-tag	Cross-section (pb)	Simulation
$t\bar{t}$ (di-leptons) Powheg + Pythia8	410472	4514	76.95	FS
$t\bar{t}$ (non all-hadronic) Powheg + Pythia8	410470	4514	396.87	FS
$t\bar{t}$ (non all-hadronic) Powheg + Pythia8	410470	4514	396.87	AF
$t\bar{t}$ Powheg + Herwig 7.2.1	600666, 600667	4514	320.1, 76.88	FS
$t\bar{t}$ Powheg + Pythia8 hdamp	410480, 410482	4514	320.00, 76.94	AF
$t\bar{t}$ (di-leptons) Powheg + Pythia8 pthard =1	601491	4514	76.92	AF
$t\bar{t}$ (di-leptons) top recoil	601357	4514	76.93	AF
$t\bar{t}+W$ aMC@NLO	410155	4514	0.55	FS
$t\bar{t}+Z(\nu\nu)$ aMC@NLO	410156	4514	0.15	FS
$t\bar{t}+Z(q\bar{q})$ aMC@NLO	410157	4514	0.53	FS
$t\bar{t}+l\bar{l}$ aMC@NLO	410218–410220	4514	0.037	FS
$t\bar{t}+H$ Powheg + Pythia8	346344,346345	4514	0.22,0.05	FS
Wt inclusive Powheg + Pythia8	410646,410647	4514	37.94, 37.91	FS
Wt di-leptons Powheg + Pythia8	410648,410649	4514	4.00, 3.99	FS
Wt di-leptons Powheg + Pythia8	410648,410649	4514	4.00, 3.99	AF
Wt di-leptons Powheg + Herwig	411038,411039	4514	4.00, 3.99	AF
Wt inclusive Powheg + Pythia8 - DS	410654,410655	4514	36.93, 37.66	FS
Wt di-leptons Powheg + Pythia8 - DS	410656,410656	4514	3.89, 3.97	FS

Table A.2: Background MC Samples

Sample	DSID	p-tag	Simulation
W + jets Sherpa 2.2.11	700338 – 700349	4514	FS
l^+l^- + jets Sherpa 2.2.11	700320 – 700334	4514	FS
l^+l^- + jets (low mass) Sherpa 2.2.11	700467 – 700472	4514	FS
l^+l^- + jets (Madgraph5+Pythia8)	363123 – 363170	4512	FS
$ZZ \to q\bar{q}l\bar{l}$ Sherpa	363356	4512	FS
$WZ \to q\bar{q}l\bar{l}$ Sherpa	363358	4512	FS
$WW \to q\bar{q}l\nu$ Sherpa	363359,363360	4512	FS
$ZW \to q\bar{q}l\nu$ Sherpa	363489	4512	FS
$VV \to 4\ l$ Sherpa	364250	4512	FS
$VV \to 3\ l + \nu$ Sherpa	364253	4512	FS
$VV \to 2\ l + \nu\nu$ Sherpa	364254	4512	FS
Single t, s-channel Powheg + Pythia8	410644,410645	4514	FS
Single t, t-channel Powheg + Pythia8	410658,410659	4514	FS

Appendix B

Fit parameters for the Z^0 correction factor fits

NAME	VALUE	ERROR
m (MeV)	9.08318e+04	2.25721e+01
s (MeV)	1.92333e+03	2.85725e+01
nbkg	7.57734e+04	3.36581e+02
nsig	3.39264e+04	2.67328e+02
χ^2/ndf	2.88	

Table B.1: Fit parameters for the fit of $Z^0 \rightarrow ee$ data

NAME	VALUE	ERROR
m (MeV)	9.07349e+04	2.42123e+01
s (MeV)	1.88286e+03	3.09559e+01
nbkg	7.33059e+04	3.29022e+02
nsig	2.96113e+04	2.54092e+02
χ^2/ndf	22.5	

Table B.2: Fit parameters for the fit of $Z^0 \rightarrow ee$ MC

NAME	VALUE	ERROR
m (MeV)	9.07038e+04	1.95015e+01 1
s (MeV)	2.02728e+03	2.42615e+01
nbkg	1.18487e+05	4.21767e+02
nsig	4.98020e+04	3.30474e+02
χ^2/ndf	4.67	

Table B.3: Fit parameters for the fit of $Z^0 \rightarrow \mu\mu$ MC

NAME	VALUE	ERROR
m (MeV)	9.08068e+04	1.81073e+01
s (MeV)	1.99290e+03	2.29190e+01
nbkg	1.23236e+05	4.31421e+02
nsig	5.52973e+04	3.43817e+02
χ^2/ndf	37.0	

Table B.4: Fit parameters for the fit of $Z^0 \rightarrow \mu\mu$ data

NAME	VALUE	ERROR
m (MeV)	8.91953e+04	1.42285e+02
m2 (MeV)	9.15078e+04	5.22401e+01
s (MeV)	1.58516e+03	6.71813e+01
nbkg	7.58252e+04	3.35715e+02
nsig	3.38746e+04	2.66005e+02
χ^2/ndf	2.91	

Table B.5: Fit parameters for the fit of $Z^0 \rightarrow ee$ data using two voigt profiles

NAME	VALUE	ERROR
m (MeV)	9.08747e+04	5.79986e+02
m2 (MeV)	9.06787e+04	2.35707e+02
s (MeV)	1.88066e+03	3.10717e+01
nbkg	7.33041e+04	3.35827e+02
nsig	2.96110e+04	2.62864e+02
χ^2/ndf	22.2	

Table B.6: Fit parameters for the fit of $Z^0 \rightarrow ee$ MC using two voigt profiles

Appendix C

Alternative MC Samples

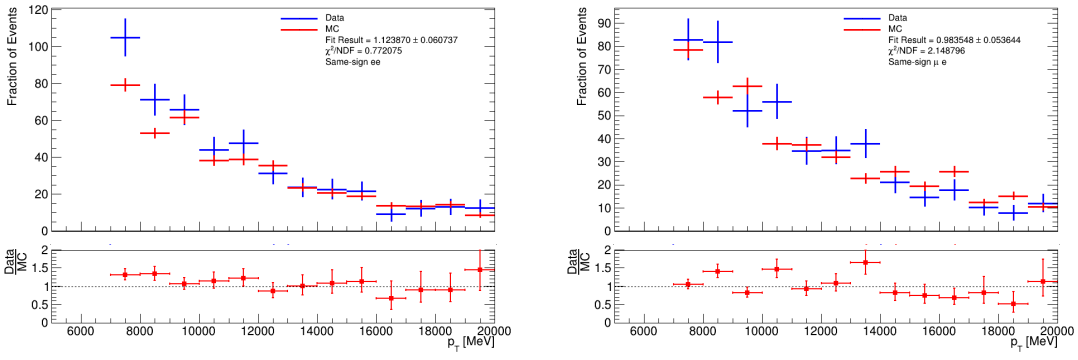

Figure C.1: Comparison of distributions of p_T in same-sign ee (left) and μe (right) events in data and simulation for the full dataset of alternative MC sample 600666-67.

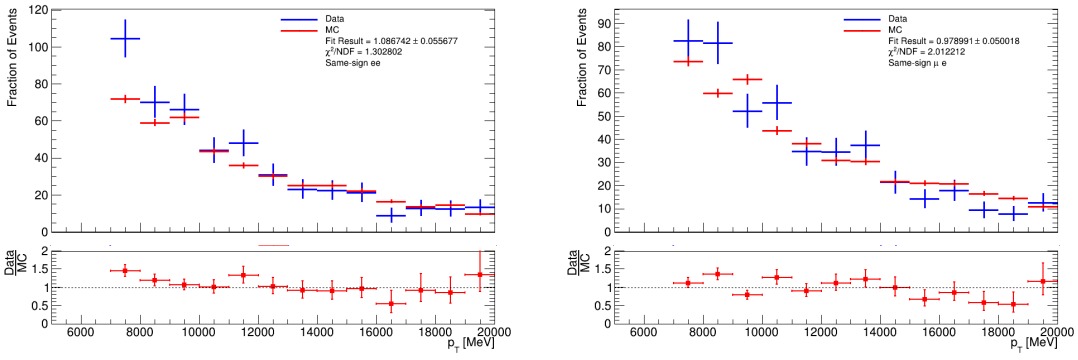

Figure C.2: Comparison of distributions of p_T in same-sign ee (left) and μe (right) events in data and simulation for the full dataset of alternative MC sample 410480-82.

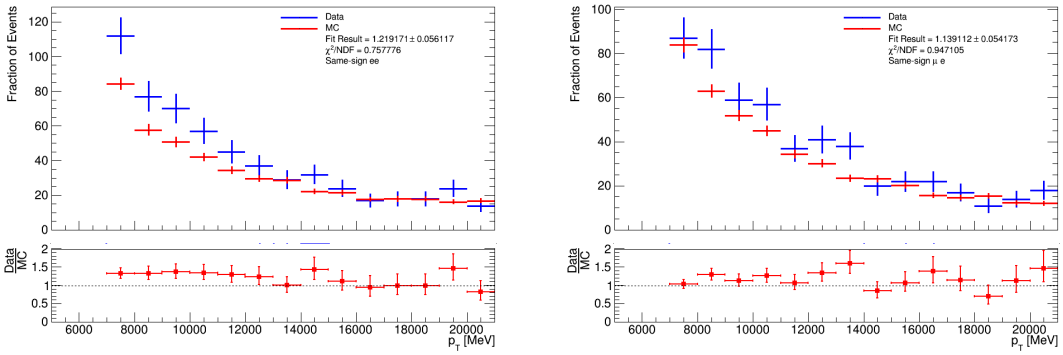

Figure C.3: Comparison of distributions of p_T in same-sign ee (left) and μe (right) events in data and simulation for the full dataset of nominal MC sample with no scaling applied.

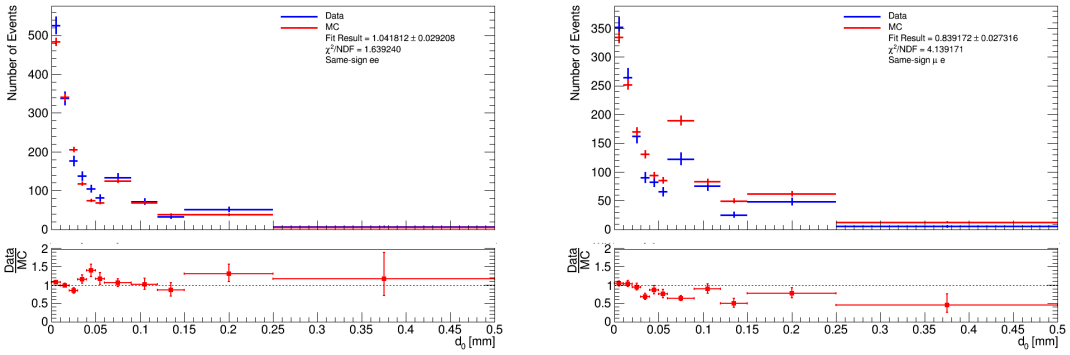

Figure C.4: Comparison of distributions of d_0 in same-sign ee (left) and μe (right) events in data and simulation for the full dataset of alternative MC sample 600666-67.

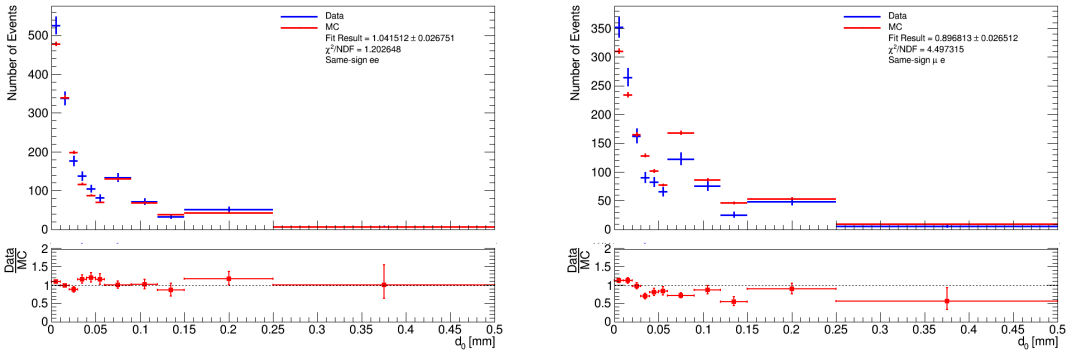

Figure C.5: Comparison of distributions of d_0 in same-sign ee (left) and μe (right) events in data and simulation for the full dataset of alternative MC sample 410480-82.

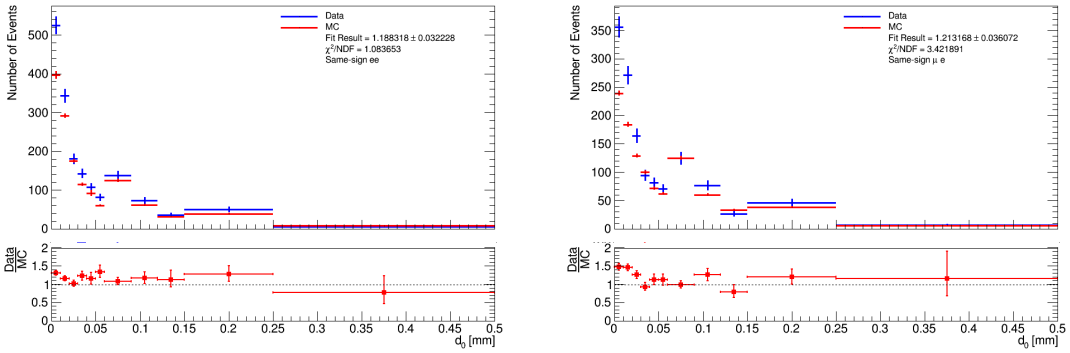

Figure C.6: Comparison of distributions of d_0 in same-sign ee (left) and μe (right) events in data and simulation for the full dataset of nominal MC sample with no scaling applied.

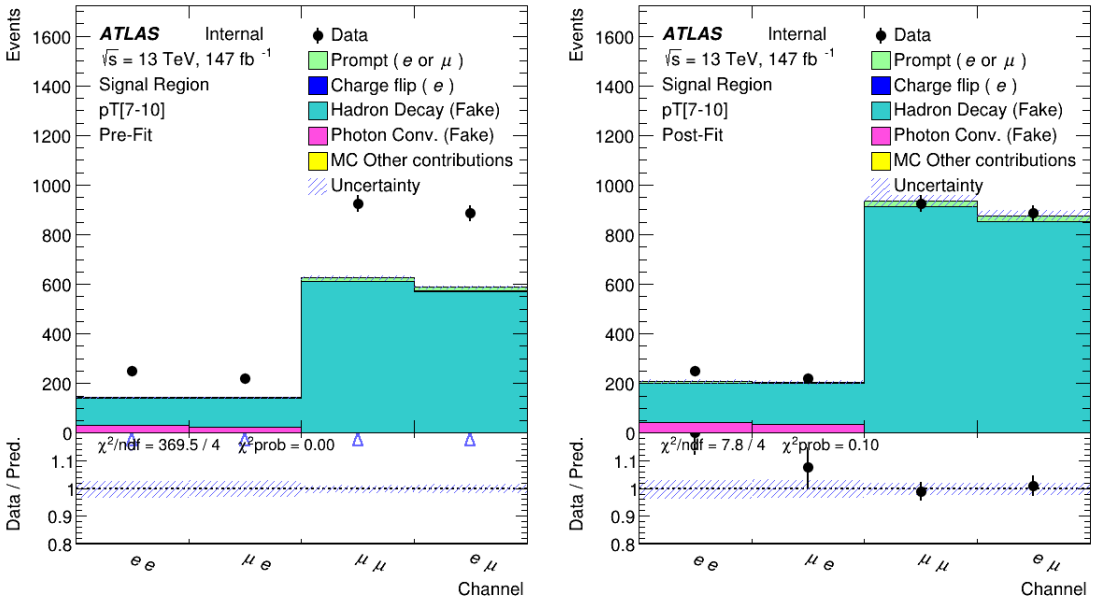

Figure C.7: Prefit (left) and postfit (right) plots in the same-sign control region showing the data and alternative MC 410480-82 sample agreement for the 5-10 GeV p_T bin for each decay channel ee, μe, $\mu\mu$ and $e\mu$. The post-fit result shows the calculated scale factors improve the data-MC agreement when applied.

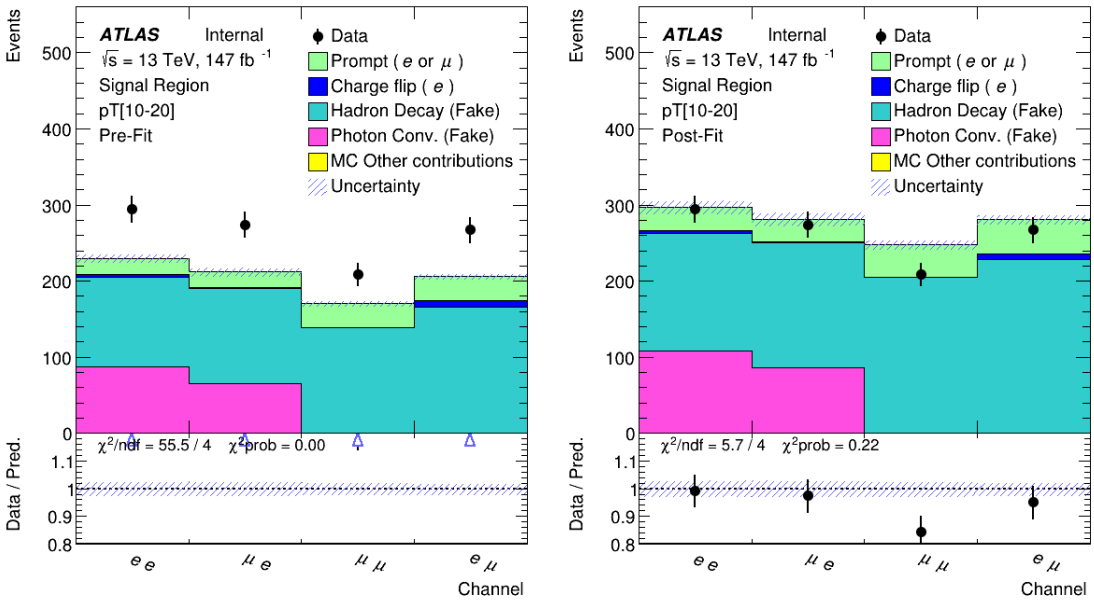

Figure C.8: Prefit (left) and postfit (right) plots in the same-sign control region showing the data and alternative MC 410480-82 sample agreement for the 10-20 GeV p_T bin for each decay channel ee, μe, $\mu\mu$ and $e\mu$. The post-fit result shows the calculated scale factors improve the data-MC agreement when applied.

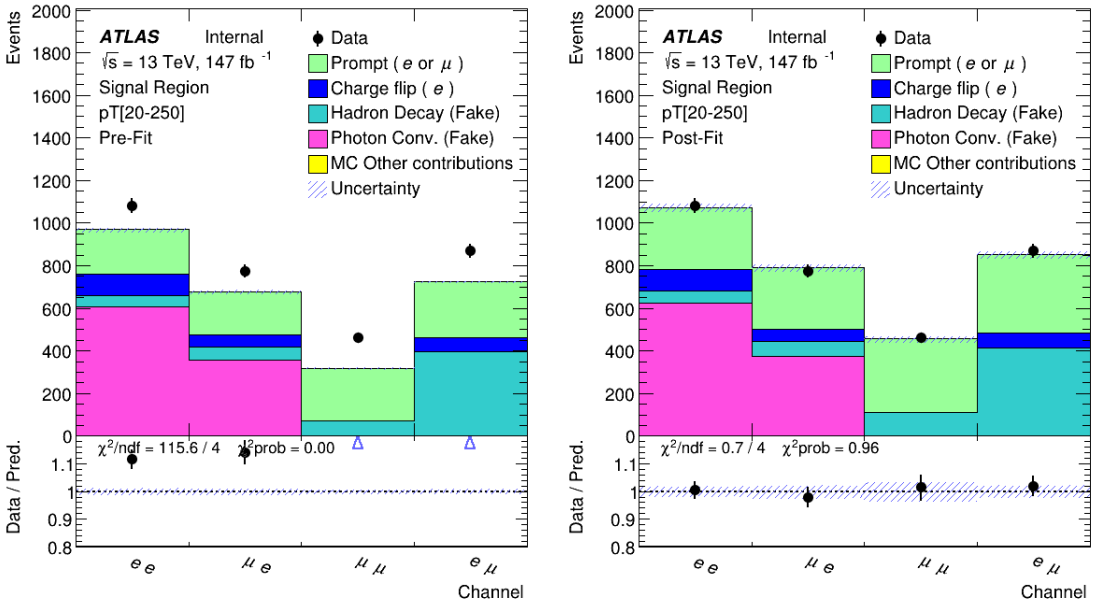

Figure C.9: Prefit (left) and postfit (right) plots in the same-sign control region showing the data and alternative MC 410480-82 sample agreement for the 20-250 GeV p_T bin for each decay channel ee, μe, $\mu\mu$ and $e\mu$. The post-fit result shows the calculated scale factors improve the data-MC agreement when applied.

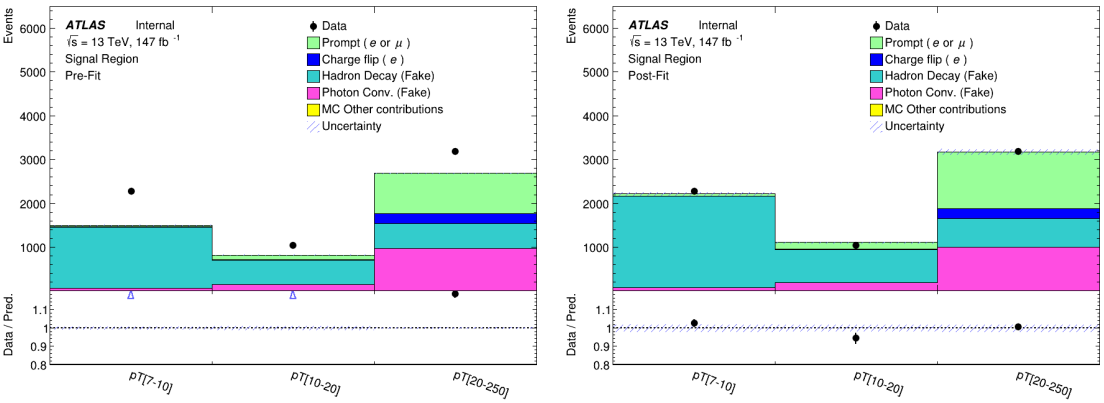

Figure C.10: Prefit (left) and postfit (right) summary plots in the same-sign control region showing the data and alternative MC 410480-82 sample agreement for all p_T bins for each decay channel ee, μe, $\mu\mu$ and $e\mu$. The post-fit result shows the calculated scale factors improve the data-MC agreement when applied.

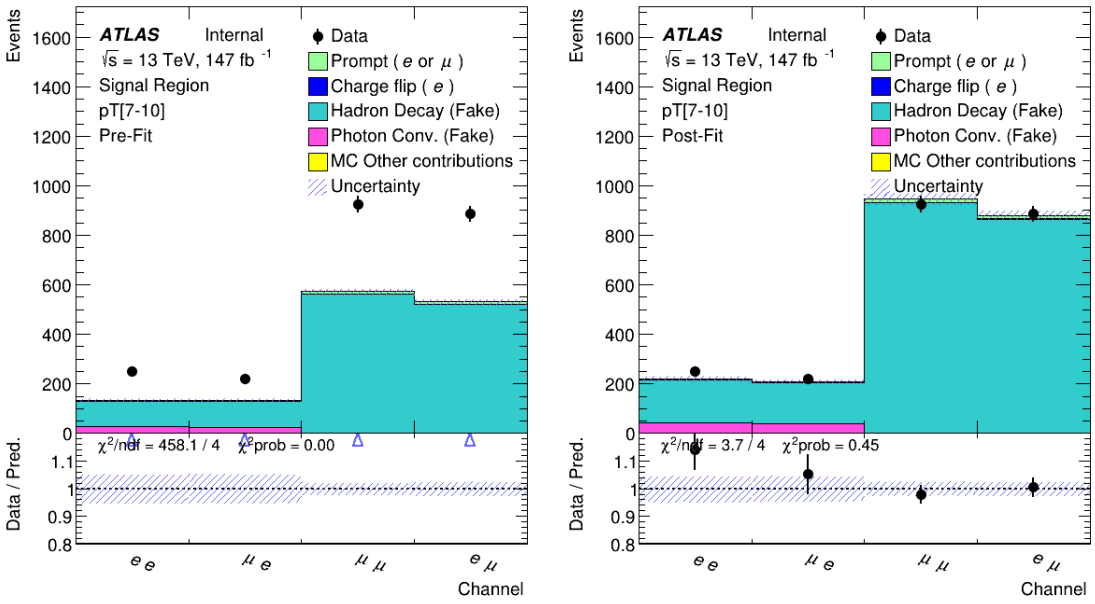

Figure C.11: Prefit (left) and postfit (right) plots in the same-sign control region showing the data and alternative MC 600666-67 sample agreement for the 5-10 GeV p_T bin for each decay channel ee, μe, $\mu\mu$ and $e\mu$. The post-fit result shows the calculated scale factors improve the data-MC agreement when applied.

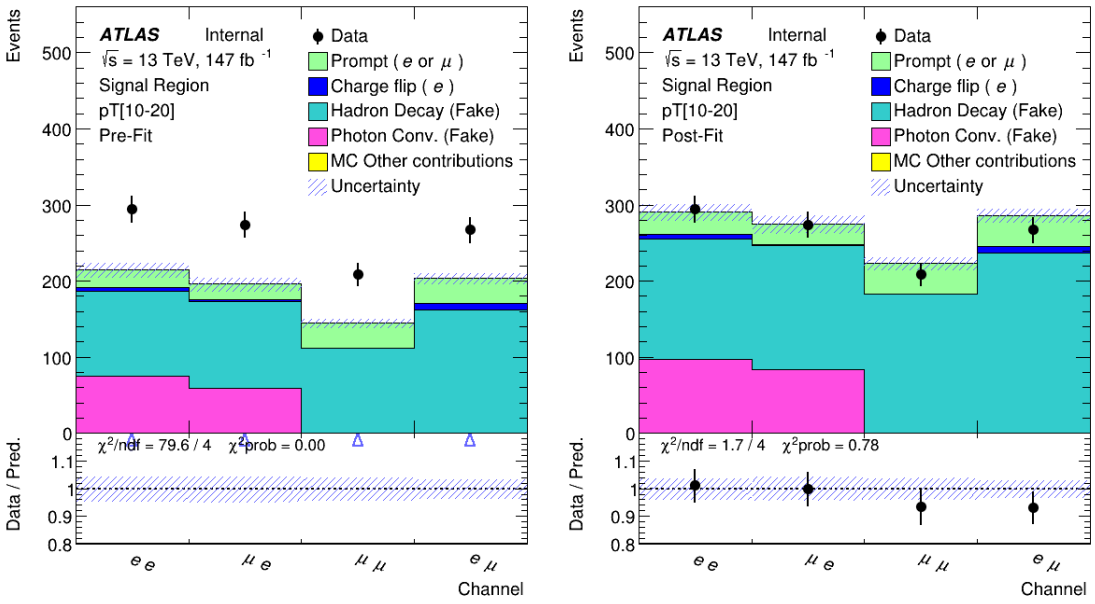

Figure C.12: Prefit (left) and postfit (right) plots in the same-sign control region showing the data and alternative MC 600666-67 sample agreement for the 10-20 GeV p_T bin for each decay channel ee, μe, $\mu\mu$ and $e\mu$. The post-fit result shows the calculated scale factors improve the data-MC agreement when applied.

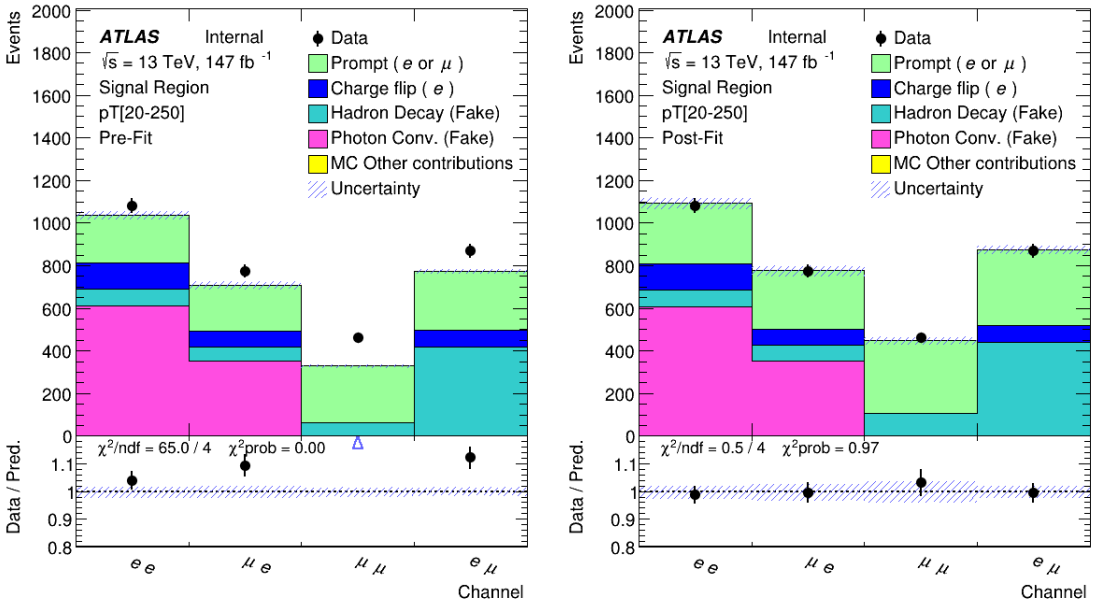

Figure C.13: Prefit (left) and postfit (right) plots in the same-sign control region showing the data and alternative MC 600666-67 sample agreement for the 20-250 GeV p_T bin for each decay channel ee, μe, $\mu\mu$ and $e\mu$. The post-fit result shows the calculated scale factors improve the data-MC agreement when applied.

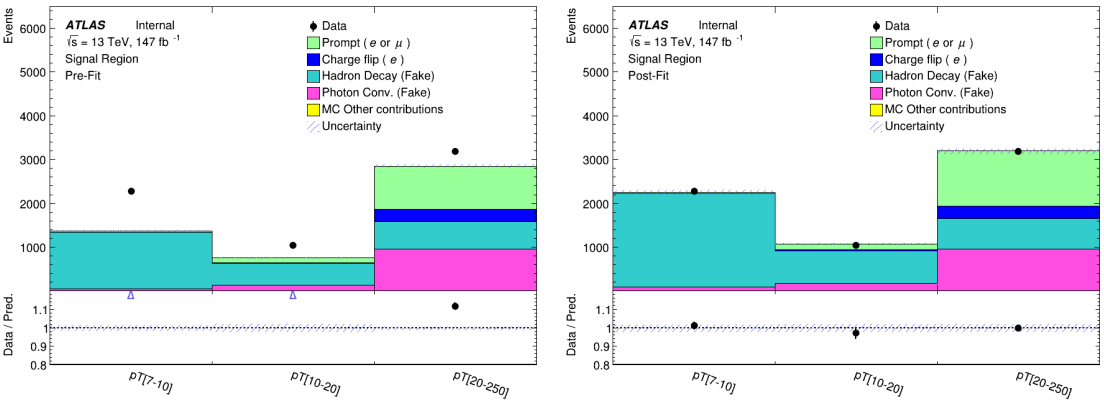

Figure C.14: Prefit (left) and postfit (right) summary plots in the same-sign control region showing the data and alternative MC 600666-67 sample agreement for all p_T bins for each decay channel ee, μe, $\mu\mu$ and $e\mu$. The post-fit result shows the calculated scale factors improve the data-MC agreement when applied.

Appendix D

Good Run Lists

Events are selected using TOPQ1 derivation in the main `Physics` stream. This derivation contains all events that have at least one lepton with $p_T > 20$ GeV.

All data samples from 2015-2018 with the ptag p4513 were used.

Year	GRL File	$\int Ldt\, fb^{-1}$
2015	`data15_13TeV/20170619/physics_25ns_21.0.19.xml`	3.2
2016	`data16_13TeV/20180129/physics_25ns_21.0.19.xml`	33.0
2017	`data17_13TeV/20180619/physics_25ns_Triggerno17e33prim.xml`	44.3
2018	`data18_13TeV/20190318/physics_25ns_Triggerno17e33prim.xml`	58.5

Table D.1: GRLs for each year and their corresponding integrated luminosity used in this analysis.

Standard ATLAS top group MC16a, MC16d and MC16e samples were used.

Appendix E

Simulation Samples

E.0.1 $t\bar{t}$

The production of $t\bar{t}$ events was modelled using the POWHEGBOX v2 [89], [90], [91], [92] generator at NLO with the NNPDF 3.0 NLO [100] PDF set and the h_{damp} parameter The events were interfaced to PYTHIA 8.230 [101] to model the parton shower, hadronisation, and underlying event, with parameters set according to the A14 tune [88] and using the NNPDF 2.3 LO set of PDFs [102]. The decays of bottom and charm hadrons were performed by EVTGEN 1.6.0 [103].

The impact of using a different parton shower and hadronisation model was evaluated by comparing the nominal $t\bar{t}$ sample with another event sample produced with the POWHEG V2 [89–92] generator using the NNPDF 3.0 NLO [100] parton distribution function (PDF). Events in the latter sample were interfaced with Herwig 7.2.1 [70, 93, 94], using the HERWIG[7.2] default set of tuned parameters [70, 94, 104] and the CT14 PDF set [105]. The decays of bottom and charm hadrons were simulated using the EVTGEN 1.6.0 program [103].

E.0.1.1 W t-channel single top

The associated production of top quarks with W bosons (tW) was modelled by the POWHEG V2 [90–92, 106] generator at NLO in QCD using the five-flavour scheme and the NNPDF 3.0 NLO set of PDFs [100]. The diagram removal scheme [107] was used to remove interference and overlap with $t\bar{t}$ production. The events were interfaced to PYTHIA 8.230 [101] using the A14 tune [88] and the NNPDF 2.3 LO set of PDFs [102].

E.0.1.2 ttV

The production of ttV events was modelled using the MGNLO 2.3.3 [108] generator at NLO with the NNPDF 3.0 NLO [100] parton distribution function (PDF). The events were interfaced to PYTHIA[8.210] [101] using the A14 tune [88] and the NNPDF 2.3 LO [100] PDF set. The decays of bottom and charm hadrons were simulated using the EVTGEN 1.2.0 program [103].

E.0.1.3 $t\bar{t}H$

The production of $t\bar{t}H$ events was modelled using the POWHEG V2 [89–92, 109] generator at NLO with the NNPDF 3.0 NLO [100] PDF set. The events were interfaced to PYTHIA 8.230 [101] using the A14 tune [88] and the NNPDF 2.3 LO [100] PDF set. The decays of bottom and charm hadrons were performed by EVTGEN 1.6.0 [103].

E.0.1.4 V+jets

The production of V+jets ($V = Z, W$) was simulated with the SHERPA 2.2.11 [71] generator using next-to-leading-order (NLO) matrix elements (ME) for up to two partons, and leading-order (LO) matrix elements for up to four partons calculated with the Comix [110] and OPENLOOPS [111–113] libraries. They were matched with the SHERPA parton shower [114] using the MEPSatNLO prescription [115–118] using the set of tuned parameters developed by the SHERPA authors. The NNPDF 3.0 nNLO set of PDFs [100] was used and the samples were normalised to a next-to-next-to-leading-order (NNLO) prediction [119].

E.0.1.5 Z+jets

The alternative Z+jets production for systematics studies of electron efficiency was simulated with MGNLO 2.2.2 [108], using LO-accurate matrix elements (ME) with up to four final-state partons. The ME calculation employed the NNPDF 3.0 NLO set of PDFs [100] (H_T-sliced) / NNPDF 2.3 LO set of PDFs [102] (N_{parton}-sliced). Events were interfaced to PYTHIA 8.186 [120] for the modelling of the parton shower, hadronisation, and underlying event. The overlap between matrix element and parton shower emissions was removed using the CKKW-L merging procedure [121, 122]. The A14 tune [88] of PYTHIA 8 was used with the NNPDF 2.3 LO PDF set [102]. The decays of bottom and charm hadrons were performed by EVTGEN 1.2.0 [103]. The Z+jets

samples were normalised to a next-to-next-to-leading-order (NNLO) prediction [119].

E.0.1.6 Dibosons

Samples of diboson final states (VV) were simulated with the SHERPA 2.2.1 or 2.2.2 [71] generator depending on the process,

E.0.1.7 s and t-channel single top

Both s- and t-channel single top production can also produce di-lepton events with at least one fake lepton. Single-top t-channel production was modelled using thePOWHEG V2 [90–92, 123] generator at NLO in QCD using the four-flavour scheme and the corresponding NNPDF 3.0 NLO set of PDFs [100]. The events were interfaced with PYTHIA 8.230 [101] using the A14 tune [88] and the NNPDF 2.3 LO set of PDFs [102].

Single-top s-channel production was modelled using the POWHEG V2 [90–92, 124] generator at NLO in QCD in the five-flavour scheme with the NNPDF 3.0 NLO [100] parton distribution function (PDF) set. The events were interfaced with PYTHIA 8.230 [101] using the A14 tune [88] and the NNPDF 2.3 LO PDF set.

Bibliography

[1] ATLAS Collaboration. *Test of lepton flavour universality in W-boson decays into electrons and -leptons using pp collisions at* $\sqrt{s} = 13$ *TeV with the ATLAS detector*. en. arXiv:2412.11989 [hep-ex]. Dec. 2024. DOI: 10.48550/arXiv.2412.11989. URL: http://arxiv.org/abs/2412.11989 (visited on 12/23/2024).

[2] *The Standard Model*. en. June 2023. URL: https://home.cern/science/physics/standard-model (visited on 07/19/2023).

[3] ATLAS Collaboration. "Observation of a new particle in the search for the Standard Model Higgs boson with the ATLAS detector at the LHC". In: *Phys. Lett. B* 716 (2012), p. 1. DOI: 10.1016/j.physletb.2012.08.020. arXiv: 1207.7214 [hep-ex].

[4] The CMS Collaboration. "Observation of a new boson at a mass of 125 GeV with the CMS experiment at the LHC". In: *Physics Letters B* 716.1 (Sept. 2012). arXiv:1207.7235 [hep-ex], pp. 30–61. ISSN: 03702693. DOI: 10.1016/j.physletb.2012.08.021. URL: http://arxiv.org/abs/1207.7235 (visited on 02/19/2024).

[5] DONUT Collaboration. "Observation of Tau Neutrino Interactions". In: *Physics Letters B* 504.3 (Apr. 2001). arXiv:hep-ex/0012035, pp. 218–224. ISSN: 03702693. DOI: 10.1016/S0370-2693(01)00307-0. URL: http://arxiv.org/abs/hep-ex/0012035 (visited on 04/08/2024).

[6] S. Abachi. "Observation of the Top Quark". en. In: *Physical Review Letters* 74.14 (Apr. 1995). arXiv:hep-ex/9503003, pp. 2632–2637. ISSN: 0031-9007, 1079-7114. DOI: 10.1103/PhysRevLett.74.2632. URL: http://arxiv.org/abs/hep-ex/9503003 (visited on 04/08/2024).

[7] The CDF Collaboration. "Observation of Top Quark Production in Pbar-P Collisions". In: *Physical Review Letters* 74.14 (Apr. 1995). arXiv:hep-ex/9503002, pp. 2626–2631. ISSN: 0031-9007, 1079-7114. DOI: 10.1103/PhysRevLett.74.2626. URL: http://arxiv.org/abs/hep-ex/9503002 (visited on 04/08/2024).

[8] SNO Collaboration. "Measurement of the rate of $\nu_e + d \rightarrow p + p + e^-$ interactions produced by 8B solar neutrinos at the Sudbury Neutrino Observatory". en. In: *Physical Review Letters* 87.7 (July 2001). arXiv:nucl-ex/0106015, p. 071301. ISSN: 0031-9007, 1079-7114. DOI: 10.1103/PhysRevLett.87.071301. URL: http://arxiv.org/abs/nucl-ex/0106015 (visited on 04/08/2024).

[9] Sheldon L. Glashow. "Partial-symmetries of weak interactions". en. In: *Nuclear Physics* 22.4 (Feb. 1961), pp. 579–588. ISSN: 0029-5582. DOI: 10.1016/0029-5582(61)90469-2. URL: https://www.sciencedirect.com/science/article/pii/0029558261904692 (visited on 07/19/2023).

[10] LHCb collaboration et al. "Test of lepton universality in beauty-quark decays". en. In: *Nature Physics* 18.3 (Mar. 2022). arXiv:2103.11769 [hep-ex], pp. 277–282. ISSN: 1745-2473, 1745-2481. DOI: 10.1038/s41567-021-01478-8. URL: http://arxiv.org/abs/2103.11769 (visited on 07/19/2023).

[11] LHCb Collaboration. "Measurement of lepton universality parameters in $B^+ \rightarrow K^+\ell^+\ell^-$ and $B^0 \rightarrow K^{*0}\ell^+\ell^-$ decays". In: *Physical Review D* 108.3 (Aug. 2023). Publisher: American Physical Society, p. 032002. DOI: 10.1103/PhysRevD.108.032002. URL: https://link.aps.org/doi/10.1103/PhysRevD.108.032002 (visited on 12/24/2024).

[12] G. Aad et al. "Test of the universality of and lepton couplings in W-boson decays with the ATLAS detector". en. In: *Nature Physics* 17.7 (July 2021). Number: 7 Publisher: Nature Publishing Group, pp. 813–818. ISSN: 1745-2481. DOI: 10.1038/s41567-021-01236-w. URL: https://www.nature.com/articles/s41567-021-01236-w (visited on 08/03/2023).

[13] S. Schael et al. "Electroweak Measurements in Electron-Positron Collisions at W-Boson-Pair Energies at LEP". In: *Phys. Rept.* 532 (2013), pp. 119–244. DOI: 10.1016/j.physrep.2013.07.004. arXiv: 1302.3415 [hep-ex].

[14] A. Tumasyan et al. "Precision measurement of the W boson decay branching fractions in proton-proton collisions at $\sqrt{s} = 13$ TeV". In: *Phys. Rev. D* 105 (7 Apr. 2022), p. 072008. DOI: 10.1103/PhysRevD.105.072008. URL: https://link.aps.org/doi/10.1103/PhysRevD.105.072008.

[15] Stuart Raby. *Introduction to the standard model and beyond : quantum field theory, symmetries and phenomenology*. eng. Edition: 1st ed. ISBN: 9781108644129 Place: Cambridge Publication Title: Introduction to the standard model and beyond : quantum field theory, symmetries and phenomenology. 2021.

[16] S. S. Schweber. *QED and the men who made it: Dyson, Feynman, Schwinger, and Tomonaga*. eng. Princeton series in physics. Princeton, N.J.: Princeton University Press, 1994. ISBN: 978-0-691-03327-3.

[17] H. David Politzer. "Reliable Perturbative Results for Strong Interactions?" en. In: *Physical Review Letters* 30.26 (June 1973), pp. 1346–1349. ISSN: 0031-9007. DOI: 10.1103/PhysRevLett.30.1346. URL: https://link.aps.org/doi/10.1103/PhysRevLett.30.1346 (visited on 07/19/2023).

[18] CMS and ATLAS Collaborations. *Combination of measurements of the top quark mass from data collected by the ATLAS and CMS experiments at $\sqrt{s} = 7$ and 8 TeV*. en. arXiv:2402.08713 [hep-ex]. Feb. 2024. URL: http://arxiv.org/abs/2402.08713 (visited on 04/08/2024).

[19] G. Aad et al. "Observation of a new particle in the search for the Standard Model Higgs boson with the ATLAS detector at the LHC". In: *Physics Letters B* 716.1 (Sept. 2012), pp. 1–29. ISSN: 0370-2693. DOI: 10.1016/j.physletb.2012.08.020. URL: https://www.sciencedirect.com/science/article/pii/S037026931200857X (visited on 02/19/2024).

[20] Raymond Davis, Don S. Harmer, and Kenneth C. Hoffman. "Search for Neutrinos from the Sun". In: *Physical Review Letters* 20.21 (May 1968). Publisher: American Physical Society, pp. 1205–1209. DOI: 10.1103/PhysRevLett.20.1205. URL: https://link.aps.org/doi/10.1103/PhysRevLett.20.1205 (visited on 12/12/2023).

[21] Jae-hyeon Park. "Lepton non-universality at LEP and charged Higgs". en. In: *Journal of High Energy Physics* 2006.10 (Oct. 2006), pp. 077–077. ISSN: 1029-8479. DOI: 10.

1088/1126-6708/2006/10/077. URL: http://stacks.iop.org/1126-6708/2006/i=10/a=077?key=crossref.8ea8f97ab70b458d5481530fdff7d765 (visited on 08/03/2023).

[22] Armen Tumasyan et al. "Precision measurement of the W boson decay branching fractions in proton-proton collisions at $\sqrt{s}$ = 13 TeV". In: *Phys. Rev. D* 105.7 (2022), p. 072008. DOI: 10.1103/PhysRevD.105.072008. arXiv: 2201.07861 [hep-ex].

[23] M. Tanabashi et al. "Review of Particle Physics". en. In: *Physical Review D* 98.3 (Aug. 2018), p. 030001. ISSN: 2470-0010, 2470-0029. DOI: 10.1103/PhysRevD.98.030001. URL: https://link.aps.org/doi/10.1103/PhysRevD.98.030001 (visited on 08/03/2023).

[24] *Evidence for production of single top quarks and first direct measurement of —Vtb— at DØ - Fall 2006*. URL: https://www-d0.fnal.gov/Run2Physics/top/public/fall06/singletop/plain_english_summary.html (visited on 07/19/2023).

[25] Nicola Cabibbo. "Unitary Symmetry and Leptonic Decays". en. In: *Physical Review Letters* 10.12 (June 1963), pp. 531–533. ISSN: 0031-9007. DOI: 10.1103/PhysRevLett.10.531. URL: https://link.aps.org/doi/10.1103/PhysRevLett.10.531 (visited on 08/03/2023).

[26] Makoto Kobayashi and Toshihide Maskawa. "CP.Violation in the Renormalizahle Theory of Weak Interaction". en. In: (). URL: https://profchristophberger.com/wp-content/uploads/2015/02/kob73.pdf.

[27] Silvan S. Schweber. *QED and the Men Who Made It: Dyson, Feynman, Schwinger, and Tomonaga*. en. Google-Books-ID: DmvdDwAAQBAJ. Princeton University Press, May 2020. ISBN: 978-0-691-21328-6.

[28] Mark Thomson. *Modern particle physics*. eng. Cambridge: University Press, 2013. ISBN: 978-1-139-52536-7.

[29] BABAR Collaboration et al. "Evidence for an Excess of $\overline{B} \to D^{(*)}\tau^{-}\overline{\nu}_{\tau}$ Decays". In: *Physical Review Letters* 109.10 (Sept. 2012). Publisher: American Physical Society, p. 101802. DOI: 10.1103/PhysRevLett.109.101802. URL: https://link.aps.org/doi/10.1103/PhysRevLett.109.101802 (visited on 11/11/2024).

[30] G. Caria et al. "Measurement of $\mathscr{R}(D)$ and $\mathscr{R}(D^*)$ with a Semileptonic Tagging Method". In: *Phys. Rev. Lett.* 124 (16 Apr. 2020), p. 161803. DOI: 10.1103/PhysRevLett.124.161803. URL: https://link.aps.org/doi/10.1103/PhysRevLett.124.161803.

[31] R. Aaij et al. "Measurement of the Ratios of Branching Fractions $\mathscr{R}(D^*)$ and $\mathscr{R}(D^0)$". In: *Phys. Rev. Lett.* 131 (11 Sept. 2023), p. 111802. DOI: 10.1103/PhysRevLett.131.111802. URL: https://link.aps.org/doi/10.1103/PhysRevLett.131.111802.

[32] Stephen Myers. *The LEP Collider, from design to approval and commissioning*. Tech. rep. Series: John Adams' memorial lecture. Geneva: CERN, 1991. DOI: 10.5170/CERN-1991-008. URL: https://cds.cern.ch/record/226776 (visited on 12/12/2023).

[33] "Electroweak measurements in electron–positron collisions at W-boson-pair energies at LEP". In: *Physics Reports*. Electroweak Measurements in Electron-Positron Collisions at W-Boson-Pair Energies at LEP 532.4 (Nov. 2013), pp. 119–244. ISSN: 0370-1573. DOI: 10.1016/j.physrep.2013.07.004. URL: https://www.sciencedirect.com/science/article/pii/S0370157313002706 (visited on 02/19/2024).

[34] Atlas Collaboration. *Precise test of lepton flavour universality in W-boson decays into muons and electrons in pp collisions at $\sqrt{s} = 13$ TeV with the ATLAS detector*. en. Mar. 2024. URL: https://arxiv.org/abs/2403.02133v1 (visited on 06/01/2024).

[35] *The ATLAS Experiment at the CERN Large Hadron Collider - IOPscience*. URL: https://iopscience.iop.org/article/10.1088/1748-0221/3/08/S08003 (visited on 02/19/2024).

[36] Esma Mobs. "The CERN accelerator complex in 2019. Complexe des accélérateurs du CERN en 2019". In: (2019). General Photo. URL: https://cds.cern.ch/record/2684277.

[37] Michael Benedikt et al. *LHC Design Report*. Tech. rep. Series: CERN Yellow Reports: Monographs. Geneva: CERN, 2004. DOI: 10.5170/CERN-2004-003-V-3. URL: https://cds.cern.ch/record/823808 (visited on 02/20/2024).

[38] Oliver Sim Brüning et al. *LHC Design Report*. Tech. rep. Series: CERN Yellow Reports: Monographs. Geneva: CERN, 2004. DOI: 10.5170/CERN-2004-003-V-2. URL: https://cds.cern.ch/record/815187 (visited on 02/20/2024).

[39] Oliver Sim Brüning et al. *LHC Design Report*. Tech. rep. Series: CERN Yellow Reports: Monographs. Geneva: CERN, 2004. DOI: 10.5170/CERN-2004-003-V-1. URL: https://cds.cern.ch/record/782076 (visited on 02/20/2024).

[40] Roger Bailey et al. "The LEP collider". fr. In: *Comptes Rendus. Physique* 3.9 (2002), pp. 1107–1120. ISSN: 1878-1535. DOI: 10.1016/S1631-0705(02)01402-0. URL: https://comptes-rendus.academie-sciences.fr/physique/articles/10.1016/S1631-0705(02)01402-0/ (visited on 12/24/2024).

[41] *LHC upgrades during LS2*. en. Apr. 2024. URL: https://home.cern/press/2022/lhc-upgrades-during-ls2 (visited on 05/04/2024).

[42] "The ALICE experiment at the CERN LHC". en. In: (2008).

[43] The Cms Collaboration et al. "The CMS experiment at the CERN LHC". en. In: *Journal of Instrumentation* 3.08 (Aug. 2008), S08004–S08004. ISSN: 1748-0221. DOI: 10.1088/1748-0221/3/08/S08004. URL: https://iopscience.iop.org/article/10.1088/1748-0221/3/08/S08004 (visited on 12/24/2024).

[44] "The LHCb Detector at the LHC". en. In: (2008).

[45] Riccardo Maria Bianchi and ATLAS Collaboration. "ATLAS experiment schematic illustration". General Photo. 2022. URL: https://cds.cern.ch/record/2837191.

[46] Sascha Mehlhase. "ATLAS detector slice (and particle visualisations)". In: (2021). URL: https://cds.cern.ch/record/2770815.

[47] Joao Pequenao. "Computer generated image of the ATLAS inner detector". 2008. URL: https://cds.cern.ch/record/1095926.

[48] ATLAS Collaboration. "Experiment Briefing: Keeping the ATLAS Inner Detector in perfect alignment". General Photo. 2020. URL: https://cds.cern.ch/record/2723878.

[49] ATLAS Collaboration. "Operation and performance of the ATLAS semiconductor tracker in LHC Run 2". en. In: *Journal of Instrumentation* 17.01 (Jan. 2022). arXiv:2109.02591 [physics], P01013. ISSN: 1748-0221. DOI: 10.1088/1748-0221/17/01/P01013. URL: http://arxiv.org/abs/2109.02591 (visited on 12/26/2024).

[50] Joao Pequenao. "Computer Generated image of the ATLAS calorimeter". 2008. URL: https://cds.cern.ch/record/1095927.

[51] Joao Pequenao. "Computer generated image of the ATLAS Muons subsystem". 2008. URL: https://cds.cern.ch/record/1095929.

[52] Ana Maria Rodriguez Vera and Joao Antunes Pequenao. "ATLAS Detector Magnet System". General Photo. 2021. URL: https://cds.cern.ch/record/2770604.

[53] ATLAS Collaboration. "The ATLAS Experiment at the CERN Large Hadron Collider". In: *JINST* 3 (2008), S08003. DOI: 10.1088/1748-0221/3/08/S08003.

[54] *ApprovedPlotsDAQ ¡ AtlasPublic ¡ TWiki*. URL: https://twiki.cern.ch/twiki/bin/view/AtlasPublic/ApprovedPlotsDAQ (visited on 12/24/2024).

[55] Johannes Elmsheuser and Alessandro Di Girolamo. "Overview of the ATLAS distributed computing system". en. In: *EPJ Web of Conferences* 214 (2019). Ed. by A. Forti et al., p. 03010. ISSN: 2100-014X. DOI: 10.1051/epjconf/201921403010. URL: https://www.epj-conferences.org/10.1051/epjconf/201921403010 (visited on 04/08/2024).

[56] C Leggett et al. "The Athena Control Framework in Production, New Developments and Lessons Learned". en. In: (). URL: https://cds.cern.ch/record/865624/files/p456.pdf.

[57] *AnalysisBase ¡ AtlasProtected ¡ TWiki*. URL: https://twiki.cern.ch/twiki/bin/view/AtlasProtected/AnalysisBase (visited on 05/04/2024).

[58] Christian Gütschow. "Monte Carlo for the LHC". en. In: (). URL: https://www.hep.ucl.ac.uk/postgrad/teaching/lhc/MC_2017.pdf.

[59] ATLAS Collaboration. "Electron reconstruction and identification in the ATLAS experiment using the 2015 and 2016 LHC proton-proton collision data at $\sqrt{s}$ = 13 TeV". In: *The European Physical Journal C* 79.8 (Aug. 2019). arXiv:1902.04655 [hep-ex, physics:physics], p. 639. ISSN: 1434-6044, 1434-6052. DOI: 10.1140/epjc/s10052-019-7140-6. URL: http://arxiv.org/abs/1902.04655 (visited on 02/19/2024).

[60] ATLAS Collaboration. *Muon reconstruction and identification efficiency in ATLAS using the full Run 2 pp collision data set at* $\sqrt{s} = 13$ *TeV*. arXiv:2012.00578 [hep-ex]. Aug. 2021. DOI: 10.1140/epjc/s10052-021-09233-2. URL: http://arxiv.org/abs/2012.00578 (visited on 02/19/2024).

[61] G. Aad et al. "Electron and photon performance measurements with the ATLAS detector using the 2015–2017 LHC proton-proton collision data". en. In: *Journal of Instrumentation* 14.12 (Dec. 2019), P12006–P12006. ISSN: 1748-0221. DOI: 10.1088/1748-0221/14/12/P12006. URL: https://iopscience.iop.org/article/10.1088/1748-0221/14/12/P12006 (visited on 02/19/2024).

[62] *Track Reconstruction Performance of the ATLAS Inner Detector at \sqrts=13 TeV*. Place: Geneva. 2015. URL: https://cds.cern.ch/record/2037683 (visited on 02/19/2024).

[63] *Vertex Reconstruction Performance of the ATLAS Detector at "= 13 TeV"*. Place: Geneva. 2015. URL: https://cds.cern.ch/record/2037717 (visited on 02/19/2024).

[64] Matteo Cacciari, Gavin P. Salam, and Gregory Soyez. "The anti-k_t jet clustering algorithm". en. In: *Journal of High Energy Physics* 2008.04 (Apr. 2008). arXiv:0802.1189 [hep-ph], pp. 063–063. ISSN: 1029-8479. DOI: 10.1088/1126-6708/2008/04/063. URL: http://arxiv.org/abs/0802.1189 (visited on 12/24/2024).

[65] ATLAS Collaboration. *Jet energy scale and resolution measured in proton-proton collisions at* $\sqrt{s} = 13$ *TeV with the ATLAS detector*. arXiv:2007.02645 [hep-ex]. Aug. 2021. DOI: 10.1140/epjc/s10052-021-09402-3. URL: http://arxiv.org/abs/2007.02645 (visited on 02/19/2024).

[66] *Performance of missing transverse momentum reconstruction with the ATLAS detector using proton–proton collisions at* $\sqrt{s} = 13$*TeV The European Physical Journal C*. URL: https://link.springer.com/article/10.1140/epjc/s10052-018-6288-9 (visited on 02/19/2024).

[67] *Luminosity determination in pp collisions at $$\sqrt{s}=13$$ TeV using the ATLAS detector at the LHC — The European Physical Journal C*. URL: https://link.springer.com/article/10.1140/epjc/s10052-023-11747-w (visited on 12/24/2024).

[68] GEANT4 Collaboration, S. Agostinelli, et al. "GEANT4 – a simulation toolkit". In: *Nucl. Instrum. Meth. A* 506 (2003), p. 250. DOI: 10.1016/S0168-9002(03)01368-8.

[69] Torbjorn Sjostrand, Stephen Mrenna, and Peter Z. Skands. "A Brief Introduction to PYTHIA 8.1". In: *Comput. Phys. Commun.* 178 (2008), pp. 852–867. DOI: 10.1016/j.cpc.2008.01.036. arXiv: 0710.3820 [hep-ph].

[70] Johannes Bellm et al. "Herwig 7.2 release note". In: *Eur. Phys. J. C* 80.5 (2020), p. 452. DOI: 10.1140/epjc/s10052-020-8011-x. arXiv: 1912.06509 [hep-ph].

[71] Enrico Bothmann et al. "Event generation with Sherpa 2.2". In: *SciPost Phys.* 7.3 (2019), p. 034. DOI: 10.21468/SciPostPhys.7.3.034. arXiv: 1905.09127 [hep-ph].

[72] Simone Alioli et al. "A general framework for implementing NLO calculations in shower Monte Carlo programs: the POWHEG BOX". en. In: *Journal of High Energy Physics* 2010.6 (June 2010), p. 43. ISSN: 1029-8479. DOI: 10.1007/JHEP06(2010)043. URL: https://doi.org/10.1007/JHEP06(2010)043 (visited on 12/24/2024).

[73] Johan Alwall et al. "MadGraph/MadEvent v4: the new web generation". en. In: *Journal of High Energy Physics* 2007.09 (Sept. 2007), pp. 028–028. ISSN: 1029-8479. DOI: 10.1088/1126-6708/2007/09/028. URL: http://stacks.iop.org/1126-6708/2007/i=09/a=028?key=crossref.117225e2f8529215c57d62b23454782e (visited on 12/24/2024).

[74] *Files · 21.2 · atlas / athena · GitLab*. en. May 2024. URL: https://gitlab.cern.ch/atlas/athena/-/tree/21.2?ref_type=heads (visited on 05/04/2024).

[75] *Files · 22.0 · atlas / athena · GitLab*. en. May 2023. URL: https://gitlab.cern.ch/atlas/athena/-/tree/22.0?ref_type=heads (visited on 05/04/2024).

[76] S. Navas et al. "Review of Particle Physics". en. In: *Physical Review D* 110.3 (Aug. 2024), p. 030001. ISSN: 2470-0010, 2470-0029. DOI: 10.1103/PhysRevD.110.030001. URL: https://link.aps.org/doi/10.1103/PhysRevD.110.030001 (visited on 12/23/2024).

[77] *RecommendedIsolationWPs ¡ AtlasProtected ¡ TWiki*. URL: https://twiki.cern.ch/twiki/bin/view/AtlasProtected/RecommendedIsolationWPs (visited on 05/04/2024).

[78] *MuonSelectionToolR21 Atlas TWiki*. URL: https://twiki.cern.ch/twiki/bin/view/Atlas/MuonSelectionToolR21 (visited on 05/04/2024).

[79] *TopRecoObjTwikiModel ¡ AtlasProtected ¡ TWiki*. URL: https://twiki.cern.ch/twiki/bin/view/AtlasProtected/TopRecoObjTwikiModel#Jets (visited on 05/04/2024).

[80] *Tracking/TrkVertexFitter/TrkVertexAnalysisUtils/TrkVertexAnalysisUtils · 21.2 · atlas / athena · GitLab*. en. June 2018. URL: https://gitlab.cern.ch/atlas/athena/-/tree/21.2/Tracking/TrkVertexFitter/TrkVertexAnalysisUtils/TrkVertexAnalysisUtils (visited on 02/26/2024).

[81] Georges Aad et al. "Test of the universality of τ and μ lepton couplings in W-boson decays with the ATLAS detector". In: *Nature Phys.* 17.7 (2021), pp. 813–818. DOI: 10.1038/s41567-021-01236-w. arXiv: 2007.14040 [hep-ex].

[82] R. L. Workman et al. "Review of Particle Physics". In: *PTEP* 2022 (2022), p. 083C01. DOI: 10.1093/ptep/ptac097.

[83] *The Drell-Yan process - IOPscience*. URL: https://iopscience.iop.org/article/10.1088/0034-4885/45/11/002/pdf (visited on 12/23/2024).

[84] *Geant4*. en. URL: https://geant4.web.cern.ch// (visited on 04/10/2024).

[85] *PubComLaTeX ¡ AtlasProtected ¡ TWiki*. URL: https://twiki.cern.ch/twiki/bin/viewauth/AtlasProtected/PubComLaTeX (visited on 05/04/2024).

[86] *TRExFitter documentation*. URL: https://trexfitter-docs.web.cern.ch/trexfitter-docs/ (visited on 02/26/2024).

[87] Johan Alwall et al. "MadGraph 5 : Going Beyond". In: *JHEP* 06 (2011), p. 128. DOI: 10.1007/JHEP06(2011)128. arXiv: 1106.0522 [hep-ph].

[88] ATLAS Collaboration. *ATLAS Pythia 8 tunes to 7 TeV data*. ATL-PHYS-PUB-2014-021. 2014. URL: https://cds.cern.ch/record/1966419.

[89] Stefano Frixione, Giovanni Ridolfi, and Paolo Nason. "A positive-weight next-to-leading-order Monte Carlo for heavy flavour hadroproduction". In: *JHEP* 09 (2007), p. 126. DOI: 10.1088/1126-6708/2007/09/126. arXiv: 0707.3088 [hep-ph].

[90] Paolo Nason. "A new method for combining NLO QCD with shower Monte Carlo algorithms". In: *JHEP* 11 (2004), p. 040. DOI: 10.1088/1126-6708/2004/11/040. arXiv: hep-ph/0409146.

[91] Stefano Frixione, Paolo Nason, and Carlo Oleari. "Matching NLO QCD computations with parton shower simulations: the POWHEG method". In: *JHEP* 11 (2007), p. 070. DOI: 10.1088/1126-6708/2007/11/070. arXiv: 0709.2092 [hep-ph].

[92] Simone Alioli et al. "A general framework for implementing NLO calculations in shower Monte Carlo programs: the POWHEG BOX". In: *JHEP* 06 (2010), p. 043. DOI: 10.1007/JHEP06(2010)043. arXiv: 1002.2581 [hep-ph].

[93] M. Bähr et al. "Herwig++ physics and manual". In: *Eur. Phys. J. C* 58 (2008), p. 639. DOI: 10.1140/epjc/s10052-008-0798-9. arXiv: 0803.0883 [hep-ph].

[94] Johannes Bellm et al. "Herwig 7.0/Herwig++ 3.0 release note". In: *Eur. Phys. J. C* 76.4 (2016), p. 196. DOI: 10.1140/epjc/s10052-016-4018-8. arXiv: 1512.01178 [hep-ph].

[95] J. Magro, L. Serkin, G. Panizzo, M. Faraj. *tt Reweighting Reloaded: a fresh new look at tt parton-kinematics reweighting to NNLO distributions*. URL: https://indico.cern.ch/event/940116/contributions/3950096/attachments/2082894/3498732/Pinamonti_30jul2020_topModelling.pdf.

[96] *Run 2 Top PDF recommendations*. URL: https://twiki.cern.ch/twiki/bin/viewauth/AtlasProtected/TopMCPDFReccommendations.

[97] Jon Butterworth et al. "PDF4LHC recommendations for LHC Run II". In: *J. Phys. G* 43 (2016), p. 023001. DOI: 10.1088/0954-3899/43/2/023001. arXiv: 1510.03865 [hep-ph].

[98] Glen Cowan et al. "Asymptotic formulae for likelihood-based tests of new physics". In: *The European Physical Journal C* 71.2 (Feb. 2011). ISSN: 1434-6052. DOI: 10.1140/epjc/s10052-011-1554-0. URL: http://dx.doi.org/10.1140/epjc/s10052-011-1554-0.

[99] ATLAS Collaboration. "The ATLAS Trigger System for LHC Run 3 and Trigger performance in 2022". en. In: *Journal of Instrumentation* 19.06 (June 2024). arXiv:2401.06630 [hep-ex], P06029. ISSN: 1748-0221. DOI: 10.1088/1748-0221/19/06/P06029. URL: http://arxiv.org/abs/2401.06630 (visited on 12/26/2024).

[100] Richard D. Ball et al. "Parton distributions for the LHC run II". In: *JHEP* 04 (2015), p. 040. DOI: 10.1007/JHEP04(2015)040. arXiv: 1410.8849 [hep-ph].

[101] Torbjörn Sjöstrand et al. "An introduction to PYTHIA 8.2". In: *Comput. Phys. Commun.* 191 (2015), p. 159. DOI: 10.1016/j.cpc.2015.01.024. arXiv: 1410.3012 [hep-ph].

[102] Richard D. Ball et al. "Parton distributions with LHC data". In: *Nucl. Phys. B* 867 (2013), p. 244. DOI: 10.1016/j.nuclphysb.2012.10.003. arXiv: 1207.1303 [hep-ph].

[103] D. J. Lange. "The EvtGen particle decay simulation package". In: *Nucl. Instrum. Meth. A* 462 (2001), p. 152. DOI: 10.1016/S0168-9002(01)00089-4.

[104] Johannes Bellm et al. "Herwig 7.1 Release Note". In: (2017). arXiv: 1705.06919 [hep-ph].

[105] Sayipjamal Dulat et al. "New parton distribution functions from a global analysis of quantum chromodynamics". In: *Phys. Rev. D* 93.3 (2016), p. 033006. DOI: 10.1103/PhysRevD.93.033006. arXiv: 1506.07443 [hep-ph].

[106] Emanuele Re. "Single-top Wt-channel production matched with parton showers using the POWHEG method". In: *Eur. Phys. J. C* 71 (2011), p. 1547. DOI: 10.1140/epjc/s10052-011-1547-z. arXiv: 1009.2450 [hep-ph].

[107] Stefano Frixione et al. "Single-top hadroproduction in association with a W boson". In: *JHEP* 07 (2008), p. 029. DOI: 10.1088/1126-6708/2008/07/029. arXiv: 0805.3067 [hep-ph].

[108] J. Alwall et al. "The automated computation of tree-level and next-to-leading order differential cross sections, and their matching to parton shower simulations". In: *JHEP* 07 (2014), p. 079. DOI: 10.1007/JHEP07(2014)079. arXiv: 1405.0301 [hep-ph].

[109] Heribertus B. Hartanto et al. "Higgs boson production in association with top quarks in the POWHEG BOX". In: *Phys. Rev. D* 91.9 (2015), p. 094003. DOI: 10.1103/PhysRevD.91.094003. arXiv: 1501.04498 [hep-ph].

[110] Tanju Gleisberg and Stefan Höche. "Comix, a new matrix element generator". In: *JHEP* 12 (2008), p. 039. DOI: 10.1088/1126-6708/2008/12/039. arXiv: 0808.3674 [hep-ph].

[111] Federico Buccioni et al. "OpenLoops 2". In: *Eur. Phys. J. C* 79.10 (2019), p. 866. DOI: 10.1140/epjc/s10052-019-7306-2. arXiv: 1907.13071 [hep-ph].

[112] Fabio Cascioli, Philipp Maierhöfer, and Stefano Pozzorini. "Scattering Amplitudes with Open Loops". In: *Phys. Rev. Lett.* 108 (2012), p. 111601. DOI: 10.1103/PhysRevLett.108.111601. arXiv: 1111.5206 [hep-ph].

[113] Ansgar Denner, Stefan Dittmaier, and Lars Hofer. "COLLIER: A fortran-based complex one-loop library in extended regularizations". In: *Comput. Phys. Commun.* 212 (2017), pp. 220–238. DOI: 10.1016/j.cpc.2016.10.013. arXiv: 1604.06792 [hep-ph].

[114] Steffen Schumann and Frank Krauss. "A parton shower algorithm based on Catani–Seymour dipole factorisation". In: *JHEP* 03 (2008), p. 038. DOI: 10.1088/1126-6708/2008/03/038. arXiv: 0709.1027 [hep-ph].

[115] Stefan Höche et al. "A critical appraisal of NLO+PS matching methods". In: *JHEP* 09 (2012), p. 049. DOI: 10.1007/JHEP09(2012)049. arXiv: 1111.1220 [hep-ph].

[116] Stefan Höche et al. "QCD matrix elements + parton showers. The NLO case". In: *JHEP* 04 (2013), p. 027. DOI: 10.1007/JHEP04(2013)027. arXiv: 1207.5030 [hep-ph].

[117] S. Catani et al. "QCD Matrix Elements + Parton Showers". In: *JHEP* 11 (2001), p. 063. DOI: 10.1088/1126-6708/2001/11/063. arXiv: hep-ph/0109231.

[118] Stefan Höche et al. "QCD matrix elements and truncated showers". In: *JHEP* 05 (2009), p. 053. DOI: 10.1088/1126-6708/2009/05/053. arXiv: 0903.1219 [hep-ph].

[119] Charalampos Anastasiou et al. "High-precision QCD at hadron colliders: Electroweak gauge boson rapidity distributions at next-to-next-to leading order". In: *Phys. Rev. D* 69 (2004), p. 094008. DOI: 10.1103/PhysRevD.69.094008. arXiv: hep-ph/0312266.

[120] T. Sjöstrand, S. Mrenna, and P. Skands. "A brief introduction to PYTHIA 8.1". In: *Comput. Phys. Commun.* 178 (2008), pp. 852–867. DOI: 10.1016/j.cpc.2008.01.036. arXiv: 0710.3820 [hep-ph].

[121] Leif Lönnblad. "Correcting the Colour-Dipole Cascade Model with Fixed Order Matrix Elements". In: *JHEP* 05 (2002), p. 046. DOI: 10.1088/1126-6708/2002/05/046. arXiv: hep-ph/0112284.

[122] Leif Lönnblad and Stefan Prestel. "Matching tree-level matrix elements with interleaved showers". In: *JHEP* 03 (2012), p. 019. DOI: 10.1007/JHEP03(2012)019. arXiv: 1109.4829 [hep-ph].

[123] Rikkert Frederix, Emanuele Re, and Paolo Torrielli. "Single-top t-channel hadroproduction in the four-flavour scheme with POWHEG and aMC@NLO". In: *JHEP* 09 (2012), p. 130. DOI: 10.1007/JHEP09(2012)130. arXiv: 1207.5391 [hep-ph].

[124] Simone Alioli et al. "NLO single-top production matched with shower in POWHEG: s- and t-channel contributions". In: *JHEP* 09 (2009), p. 111. DOI: 10.1088/1126-6708/2009/09/111. arXiv: 0907.4076 [hep-ph]. Erratum: in: *JHEP* 02 (2010), p. 011. DOI: 10.1007/JHEP02(2010)011.